Linear disturbance evolution in the semi-infinite Stokes layer and related flows

Alexander Ramage

School of Mathematics

Cardiff University

Doctor of Philosophy

2017

Abstract

The stability of the semi-infinite Stokes layer is explored. This is the flow generated in a semi-infinite region of otherwise stationary fluid by the sinusoidal oscillation of a bounding plate and is described by an exact solution to the Navier–Stokes equations.

A linear stability analysis is carried out, based on Floquet theory, that reduces the disturbance equations to an eigenvalue problem that determines the asymptotic temporal behaviour of disturbances. This method is also applied to the finite Stokes layer (being the flow in a channel bounded by oscillating plates) and modifications incorporating a mean flow.

Linear disturbances are simulated numerically and intriguing features of the spatial/temporal evolution are reproduced and expanded on. Consistency between the linear stability analysis and the simulations is demonstrated, as is evidence suggesting some disturbances exhibit temporal growth at every spatial location (absolute instabilities).

Through modification of Briggs' method, the conditions for absolute instability in temporally periodic flows are discussed. It is shown that the Stokes layer is indeed subject to absolute instability by appealing to the symmetries of the flow. This approach provides further insight into the spatial/temporal evolution of disturbances.

Finally, the Stokes layer is modified by a low-amplitude, high-frequency oscillation to approximate the noise associated with the mechanical generation of plate motion in experiments. It is shown that the introduction of noise can be dramatically destabilising and can have a significant effect on the disturbance evolution. In cases where the flow is subject to a high level of noise, the spatial/temporal evolution of the disturbance holds little resemblance to the evolution of disturbances in the pure Stokes layer.

Declaration

This work has not been submitted in substance for any other degree or award at this or any other university or place of learning, nor is being submitted concurrently in candidature for any degree or other award.

Signed _____ (candidate) Date _____

Statement 1

This thesis is being submitted in partial fulfilment of the requirements for the degree of PhD.

Signed _____ (candidate) Date _____

Statement 2

This thesis is the result of my own independent work/investigation, except where otherwise stated, and the thesis has not been edited by a third party beyond what is permitted by Cardiff University's Policy on the Use of Third Party Editors by Research Degree Students. Other sources are acknowledged by explicit references. The views expressed are my own.

Signed _____ (candidate) Date _____

Statement 3

I hereby give consent for my thesis, if accepted, to be available for photocopying and for inter-library loan, and for the title and summary to be made available to outside organisations.

Signed _____ (candidate) Date _____

Statement 4: Previously approved bar on access

I hereby give consent for my thesis, if accepted, to be available for photocopying and for inter-library loans after expiry of a bar on access previously approved by the Academic Standards & Quality Committee.

Signed _____ (candidate) Date _____

Acknowledgements

First, I wish to thank my supervisor, Dr Christopher Davies. Not only has he provided the guidance, encouragement and multiple *light-bulb* moments necessary to make this Thesis possible but he instilled in me the passion for the subject without which this work would have been doomed. From the intense discussions at the very edge of my understanding to the long conversations about music, politics and cats, every meeting has been indispensable in getting me to the end of this project.

I would also like to thank my second supervisor Dr. Nikos Savva, who's constructive advice has been well-timed and indispensable, and Dr. Tom Thomas who's correspondence has helped to focus and direct the current work.

I would also like to extend my thanks to my fellow post-grad students. In particular, Sally Hill for helping to create an office dynamic that was an excellent balance of productivity and distraction.

Despite having never met face-to-face, I would like to thank Michael Togneri, who's code and Thesis served as the starting point of this work.

I would like to thank my family and friends for always nodding patiently at my enthusiastic response when asked how my work is going. A gratitude from the very bottom of my heart goes to Beth Pretty for her infinite support and the exciting world she provided outside of my own head.

Finally, to EPSRC, whose financial assistance made this work possible.

This work was performed using the computational facilities of the Advanced Research Computing @ Cardiff (ARCCA) Division, Cardiff University.

Contents

Introduction

The experiments of Osborne Reynolds on the behaviour of fluid in pipes are generally considered to be the genesis of hydrodynamic stability theory (Drazin, 2002). In this field, the study of disturbance evolution in steady, hydrodynamic flows has developed from these early empirical observations through numerous theoretical results and into numerical methods for predicting the onset of instability and for simulation of perturbation development (Schmid & Henningson, 2001; Criminale *et al.* , 2003). As the modelling and analytic methods have developed, the study of inviscid fluid has evolved into the viscous regime and, though linear theory is better established, there is increasing development of nonlinear models (which will not be explored in this work). It has, in general, been the study of steady (independent of time), spatially homogeneous flows that have received the most attention due to the feasibility of solution methods. However, the exponential rate of technological improvement means that sophisticated numerical methods can now be deployed in many more cases, such as the temporally periodic flows that are explored herein.

Hydrodynamic stability theory

Hydrodynamic flows appear frequently in nature. In fact, the two particular fluids best described by hydrodynamics (water and air) are ubiquitous. The study of hydrodynamics can therefore be motivated by both a desire to better understand observed, natural behaviour and in developing technologies that utilise hydrodynamic properties. For instance, the study of hydrodynamics incorporates the dynamics of boats and submarines moving through water and of aeroplanes moving through the air. Both of these examples greatly contribute to modern life and for this reason it is important to ensure that such technologies are as efficient as possible. This is a particularly pertinent issue when

considering the best ways to reduce carbon emissions or reliance on fossil fuels. Take, for example, aeroplane flight. There is currently no way of powering aeroplanes except for each plane burning its own fuel, and this is a significant contributor to global carbon emissions. It would therefore be useful to improve the efficiency of planes so that less fuel is burnt. First, the aerodynamics can be investigated to reduce what is known as form drag (the drag associated with the shape of the plane), but there is also a drag associated with the boundary layer over the plane's surface known as skin friction (Carpenter *et al.* , 2007). This can be investigated by studying the stability of more idealised boundary layers and a robust reduction in skin friction would reduce drag. This in turn improves efficiency and reduces carbon emissions.

During his famous experiments, Osborne Reynolds observed that in some cases fluids behave in an orderly, easily predictable manner whereas by modifying the flow in some way, for instance by increasing the speed, a more chaotic behaviour is induced. It was found that this change in behaviour depended on a single variable: the eponymous Reynolds number, Re (Drazin, 2002). The subsequent research into this area of applied mathematics has focused largely on the stability of hydrodynamic flows by perturbing said flows to see if they return to the unperturbed state (stable) or if they diverge from the original flow to some other state (unstable). If the latter is true, often the resulting flow is chaotic and difficult to describe in a deterministic manner even though the dynamics are still subject to the same laws (Tennekes & Lumley, 1972). Chaotic flows, referred to as turbulence, are notoriously difficult to understand for this reason, yet the early development of unstable perturbations provides great insight into hydrodynamic flows (Criminale *et al.* , 2003). This insight can be utilised in many ways, such as holding off transition to turbulence (sometimes indefinitely). It is important not to confuse the study of hydrodynamic instability with the study of turbulence, as the development of an unstable perturbation to full transition is a complex problem (Schmid & Henningson, 2001), but a fascination with turbulence can motivate an interest in hydrodynamic stability theory, the latter being better represented in an idealised mathematical setting.

The study of the stability of steady, shear flows is generally characterised by the Orr–Sommerfeld equation. This equation is derived from the Navier–Stokes equations governing fluid flow by adding a perturbation to a basic state (known to satisfy the Navier–Stokes equations) and then linearising about the unperturbed state. Fixing the wavenumber of this disturbance then results in an ordinary differential equation (ODE) that can be

cast as an eigenvalue problem. This derivation and the subsequent solution for a variety of basic states is well established so will not be covered in the present work. However, it is worth noting that much of the current work has a strong analogy with the steady case. Readers interested in the derivation and solution of the Orr–Sommerfeld equation are directed to Drazin (2002) for an overview. More details are provided in Schmid & Henningson (2001) and Criminale *et al.* (2003).

Periodic flows

The present work is concerned with the study of unsteady (time dependent) flows that are temporally periodic. Some theoretical results for steady flows have been extended to time-dependent flows in general (Conrad & Criminale, 1965) but the assumption of periodicity provides a logical starting point for the study of more general time-dependence. Introduction of periodic wall motion has been shown, in some cases, to reduce drag in turbulent boundary layers (Quadrio & Ricco, 2010; Duque-Daza *et al.* , 2012; Touber & Leschziner, 2012) so the study of such flows contains the potential for insight into the structures of much more complicated flows. Further examples include respiration (producing a periodic flow) and in particular respiratory aids (for which growing disturbances would be incredibly damaging), and the agitation of solutions in laboratories dealing with chemical reactions of biological systems to promote mixing (Blennerhassett & Bassom, 2007).

Another example of flow periodicity is so-called secondary instability theory. This involves performing a linear stability analysis on a flow to deduce the wavenumber and frequency of the least stable mode. This disturbance is then incorporated into the basic state at some finite amplitude so that a second linear stability analysis can be performed (Herbert, 1988; Pier, 2003). This new basic state thus has a time dependence characterised by the frequency of this disturbance. This is a particularly interesting example as it shows that many of the methods explored herein have the potential to provide insight into the disturbance evolution of steady flows.

The stability of Stokes layers

As one of the few problems with an exact solution to the Navier–Stokes equations, a convenient starting point for the study of time-periodic flows is the Stokes layer generated in a semi-infinite region of fluid by the in-plane oscillation of a bounding plate. The framework for hydrodynamic stability theory of periodic flows has so far been conducted through this paradigm example (Hall, 1978; Blennerhassett & Bassom, 2002) and some simple variations such as the finite Stokes layer generated between two parallel plates oscillating in phase with one another (Blennerhassett & Bassom, 2006), the study of a mean flow modified by such wall motion (Thomas *et al.* , 2011) and even three-dimensional periodic motion formed by the superposition of two Stokes layers orthogonal to one another (Blennerhassett & Bassom, 2007).

The approach taken by these studies is to derive a stability equation by perturbing a solution to the Navier–Stokes equations and linearising about the undisturbed state. The streamwise (direction of wall motion) wavenumber of this disturbance is fixed and the resulting partial differential equation (PDE) contains coefficients that are periodic in time. Floquet's theorem suggests the form the solution will take and a harmonic decomposition of the periodic term reveals a coupling between disturbances with frequencies harmonic to that of the basic state.

There is an alternative approach to studying the stability characteristics of any time-dependent flow that is sometimes referred to as frozen flow analysis. This method consists of solving the Orr–Sommerfeld equation (the stability equation for steady, parallel flows) for a basic state in which the time dependence is treated as a parameter, i.e. the flow is frozen at some time t_0, a stability analysis is performed on this basic state and this process is repeated for a finite set of times. The Orr–Sommerfeld equation deduces the asymptotic behaviour of a disturbance as $t \to \infty$ so a method founded on the assumption that instantaneous behaviour can be deduced from these asymptotics requires the careful consideration of how temporally local characteristics impact global behaviour. Furthermore, the freezing of the flow can only be justified for $Re \gg 1$, whereas a finite Re is required to locate the threshold between stability and instability. Despite these shortcomings, frozen flow analysis has long been used to study the behaviour of disturbances in time-dependent flows. This is partly because numerical solution to the Orr–Sommerfeld equation is well established and relatively inexpensive, but also because in some cases it

provides a real insight into the mechanisms of instability provided the growth-rates can be appropriately *stitched* together and interpreted.

The present work will not be concerned with the details of the frozen flow method and instead will seek to compile and extend work based on the Floquet approach. A comparison of these two approaches for the Stokes layer is given in Luo & Wu (2010). It could be argued that the computationally demanding eigenvalue problem derived by this method is needlessly expensive because, due to the large instantaneous growth within each period, it is expected that nonlinear effects become significant before the completion of a single period (i.e the linear problem never sees the periodicity). However, as with any linear stability theory, the early behaviour of small disturbances is an informative part of the transition process and has the potential to be insightful and significant to the dynamics at later stages. Linear theory also provides a feasible solution method when the underlying nonlinear system is difficult to solve. Furthermore, if experimentally observed behaviour is picked up by a linear model (as is often the case) this suggests that the underlying mechanisms are linear to a large extent. For this reason, the linear framework has the potential to deepen the understanding of the system.

Comparison with experiments

The stability results of Blennerhassett & Bassom (2002), being the first time the Floquet formulation was applied to the Stokes layer with a large enough Re for instability to be observed, reported that only stable disturbances exist for any Re below the critical value of $Re_c \sim 707.84$ for the semi-infinite Stokes layer. This is at odds with the observations of experiments which suggest a value closer to $Re_c \sim 300$ (Clamen & Minton, 1977; Eckmann & Grotberg, 1991; Hino *et al.* , 1976; Akhaven *et al.* , 1991). This discrepancy of over 50% suggests that the theory was not able to predict anything meaningful about the physical flow it is intended to describe. Some possible explanations for this include the early onset of linear saturation, wall roughness, the confined geometry of the experiments or the noise induced by the mechanical motion of the plate. In the interest of addressing this discrepancy, Blennerhassett & Bassom (2006) considered Stokes layers generated in channels and pipes. This was partially successful in reducing Re_c but only by up to 20%.

Although it is difficult to quantify, experiments report noise in the generation of the

wall motion (or pressure gradient) of around 1% (sometimes up to 3%) of the amplitude of the fundamental oscillation. This suggests that even though the Stokes layer is of great interest as a paradigm example in an idealised mathematical setting, it is possibly not particularly representative of the flows generated in these experiments. For this reason, a modification to the basic state that includes low-amplitude noise (described by high-frequency harmonic oscillation superimposed over the fundamental Stokes layer) was investigated by Thomas *et al.* (2015) and found to have a drastic effect on the stability of the flow. Although it is difficult to ascertain the exact form of noise in experiments, it was found that a noise level of 1% of the fundamental could reduce the critical Reynolds number to around that observed in experiments. This suggests that the Floquet method may indeed be capable of predicting physical behaviour, a conclusion that could be better supported by some experimental studies in which the noise is induced to more closely match the theoretical model.

Absolute instability

In addition to the reduction in Re_c, the flow investigated by Thomas *et al.* (2015) provided examples of instabilities that grow at every spatial location (Thomas, 2016). Instabilities of this form (called absolute instabilities) are of particular interest because they are self amplifying. If an unstable disturbance is not absolutely unstable it is convectively unstable and any region of interest in the flow domain will eventually return to the undisturbed state as the growing disturbance is convected downstream. The observation of absolute instability provides an opportunity to further develop the theory of the stability of time-periodic flows by taking the formulation of Brevdo & Bridges (1997) for predicting the onset of absolute instability in periodic media and applying it to the flow in question.

The theoretical approach to predicting the onset of absolute instability (Briggs, 1964) will be adapted for the periodicity of the flow. The characteristics of disturbance evolution for the pure Stokes layer can then be explored in this framework to search for evidence of absolute instability. The same concepts can then be used to confirm that the cases of the Stokes layer with noise that appear subject to absolute instability are indeed so. In addition to this, simulation of the disturbance evolution by solution of the linearised Navier–Stokes equations will provide a set of results against which to validate

the theoretical predictions.

Thesis structure

Presented in Chapter 1 is a collection and extension of the work so far on the linear stability analysis of Stokes layers. Starting in two-dimensions the stability equations are derived for flows of general temporal form before committing to the finite Stokes layer in a channel. It will then be shown how this method can be generalised to incorporate a mean flow aligned with the direction of wall motion. The method by which neutral curves can be constructed will then be discussed and results will be compared with existing work (Blennerhassett & Bassom, 2002, 2006; Thomas *et al.* , 2011). Finally, the three-dimensional problem will be considered and it will be shown in what instances this problem can be reduced to two-dimensions in a manner analogous to Squire's theorem (Squire, 1933).

Chapter 2 is concerned with the numerical methods used to simulate the linearised Navier–Stokes equations. Using the velocity-vorticity formulation of Davies & Carpenter (2001), a solver is derived for the case of a single streamwise wavenumber for comparison with the results of the previous chapter. Presented next are two methods by which the response of the system to an impulse is determined. First, a spectral method is implemented as a natural extension of the single wavenumber case, then a finite-difference method is described. These solvers were derived through modification of the code written by Togneri (2011) (Togneri & Davies, 2011) and further developed by Duval (2012) and the results will be discussed in the following chapter.

In Chapter 3, the relationship between the eigenvalue problem and the simulations is explored through the behaviour of disturbances generated by an impulse. The growth-rates of disturbances as found by each method are compared and found to be in good agreement. There is also a discussion of the qualitative features of the disturbance evolution. This includes providing some evidence that the flow is subject to absolute instability.

In Chapter 4 the leading-order behaviour of disturbances is explored with a specific focus on the temporal behaviour at fixed streamwise locations and the evolution of the disturbance maximum. A set of criteria for absolute instability is found by consideration of the former. This criteria is analogous to that found for steady flows (Briggs, 1964).

In Chapter 5, these criteria are explored by adapting the numerical method used to solve the stability problem (Chapter 1) for locating cusp maps in the complex plane for the semi-infinite Stokes layer. The characteristics of the absolutely unstable modes found in this manner are compared against the simulation results of Chapter 3 and it is confirmed that the cusp map method is capable of predicting the onset of absolute instability.

Chapter 6 presents the linear stability of a Stokes layer modified by high-frequency, low-amplitude noise (Thomas *et al.* , 2015). The eigenvalue solver is reformulated for flows of this form and an inspection of the spatial/temporal characteristics of disturbances in this regime is carried out. A parametric study is conducted using the simulation methods presented in Chapter 2 to provide insight into the effect that noise can have on the disturbance evolution. The cusp map method developed in Chapter 4 is then applied to this flow to explore the disturbance evolution at fixed spatial locations.

The thesis is concluded with a summary of the work presented and suggestions for future work in the field. The significance of the work is also discussed.

Note that throughout this work, the real and imaginary parts of a variable will be denoted with subscript r and i, respectively. For instance $\mu = \mu_r + i\mu_i$ and $\alpha = \alpha_r + i\alpha_i$. In the cases where this subscript notation is not suitable, $\mathfrak{Re}\{\bullet\}$ and $\mathfrak{Im}\{\bullet\}$ will denote the real and imaginary parts, respectively. Also, unless otherwise stated, the complex conjugate of some number z will be denoted by $\bar{z}$.

Chapter 1

Linear stability theory for time-periodic flows

Introduction

While the study of the stability of steady solutions to the Navier–Stokes equations has been developed gradually since Reynolds' experiment in 1883, it has only been recently that similar methods have been adapted for time-dependent flows (Conrad & Criminale, 1965; Von Kerczek & Davis, 1974; Hall, 1978; Blennerhassett & Bassom, 2002, 2006; Thomas *et al.* , 2011). The present study will focus on time-periodic flows through the application of Floquet theory to derive an appropriate stability equation analogous to the Orr–Sommerfeld equation in steady theory (Drazin, 2002).

So far, research into the stability of periodic flows has focused primarily on Stokes layers. These are flows induced by the oscillation of boundaries or pressure gradients in various configurations such as channels, pipes (Blennerhassett & Bassom, 2006) or the semi-infinite boundary layer (Blennerhassett & Bassom, 2002). Such flows are of particular interest as many such arrangements have exact solutions to the Navier–Stokes equations and so techniques can be developed to appropriately deal with periodicity. These techniques can then be adapted for any periodic flow.

There are also some generalisations that can be made so that the theory presented in this chapter is as broad as is appropriate at each stage. Initially, the stability of any unsteady flow will be considered. Interest will then be restricted to a Stokes layer for which the fluid would be stationary in the absence of the wall motion. It will then be shown

that if the fluid is moving with some mean velocity (Thomas *et al.* , 2011) the method can easily be adapted for this problem in such a way that the flow with no mean velocity is considered as a special case. Initially, it will be assumed that this mean flow is aligned along the direction of oscillation. It will later be shown that the three-dimensional problem in which the mean flow is oblique to the direction of oscillation can be reduced to an aligned problem through results analogous to Squire's theorem (Squire, 1933). This means that no further computational effort is required for this generalisation.

The reason for the recent surge in research in this area is due, at least in part, to advances in computational resources. In fact, though the Floquet formulation was introduced by Hall (1978), it was only found that the semi-infinite Stokes layer was stable for $Re < 160$ and that the flow stabilises as $Re \to \infty$. It was not until Blennerhassett & Bassom (2002) were able to push the theory to higher (finite) Re that instability was found, the critical Reynolds number was estimated as $Re_c \sim 707.84$ (Blennerhassett & Bassom, 2002), and a portion of the neutral curve was traced.

In Section 1.1, the stability of two-dimensional shear flows will be discussed, starting with general results for any time-dependent flow and then considering the specifics of a temporally periodic flow. Section 1.2 will then derive a numerical method for solving the stability problems that arise for periodic flows while Section 1.3 describes the construction of neutral curves to visually represent stability characteristics. Having developed all of the necessary tools, some important results for the semi-infinite Stokes layer are reported in Section 1.4 to be discussed further in other chapters. Finally, the work will be generalised to three-dimensions in Section 1.5

1.1 Stability equations for 2D, unsteady, shear flows

In this section the stability equations for a two-dimensional (2D) time-dependent shear flow will be derived. Without committing to any particular geometry, fluid motion will be restricted to the x-direction and the velocity will depend only on time and the y-direction. That is, the flow considered will be parallel and unsteady. The assumption of a parallel flow is also made in the derivation of the Orr–Sommerfeld equation for steady flows, and while many flows satisfy this condition exactly others are well approximated.

For instance, consider the Blasius boundary layer. This steady flow is not parallel as there is motion in the wall-normal direction which results in a boundary layer thickness

that grows with distance from the leading edge of the plate. However, at large distances from the leading edge the real flow is well approximated in the parallel regime. The Orr–Sommerfeld equation can therefore provide insight into the stability of the flow in this region, and the growth of the boundary layer can even be approximately incorporated by considering how a locally defined Reynolds number changes with distance from the leading edge.

Unlike the Blasius boundary layer, the Stokes layer is truly parallel. However, since the generalisation of a Stokes layer modified by a mean flow is of interest later, this issue still needs some consideration. For instance, in the finite Stokes layer (the flow generated in a channel by the in-plane oscillation of the bounding plates in phase with each other) the mean flow will take the form of Poiseuille flow. Both of these flows are parallel so the soon-to-be-derived equations are appropriate. However, in the semi-infinite Stokes layer the mean flow will take the form of the Blasius boundary layer and, due to non-parallel effects, the ratio of the Blasius boundary layer thickness to the Stokes layer thickness (a significant parameter in the stability equations) changes with distance from the leading edge of the plate. As for the Blasius boundary layer itself, a careful consideration of how the flow develops will allow for a meaningful stability analysis, but this example serves as a disclaimer that there are flow configurations in which the following analysis cannot naïvely be applied.

This section is concerned with the stability of flows that can be expressed in the form

$$\boldsymbol{U} = \Big(U(y,t), 0, 0\Big). \tag{1.1.1}$$

As with steady flows, it is convenient to recast the Navier–Stokes equations in terms of nondimensional parameters so there are several scaling choices to be made depending on the nature of the flow. These issues will be discussed now so as to improve clarity later on.

1.1.1 A discussion on scaling

Consider the dimensional Navier–Stokes equations governing the evolution of the dimensional velocity $\boldsymbol{u}^*$ and pressure p^* of a fluid with viscosity μ coupled with the incom-

pressibility condition,

$$\rho\left(\frac{\partial \boldsymbol{u}^*}{\partial t} + \boldsymbol{u}^* \cdot \nabla \boldsymbol{u}^*\right) = -\nabla p^* + \mu \Delta \boldsymbol{u}^*, \tag{1.1.2a}$$

$$\nabla \cdot \boldsymbol{u}^* = 0. \tag{1.1.2b}$$

The exact nature of the nondimensionalisation depends on the structure of the flow but dos not alter the underlying physics. For instance, Conrad & Criminale (1965) scale time using a combination of velocity and lengthscales whereas Von Kerczek & Davis (1974) use a timescale associated with the unsteady basic state to imply a lengthscale. Once rescaled, the difference between these approaches comes down to whether the unsteady terms ($\partial \boldsymbol{u}/\partial t$) are of comparative size to the viscous terms ($\Delta \boldsymbol{u}$) or the inertial terms ($\boldsymbol{u} \cdot \nabla \boldsymbol{u}$).

Since the flow is time-dependent it will be assumed that a characteristic time exists which will be denoted t_0. For oscillatory flows $t_0 = 1/\omega$ would be appropriate, where ω is the frequency of oscillation. The nondimensional parameters are thus defined using the characteristic length $\delta_s = \sqrt{2\mu t_0/\rho}$ and velocity U_0 as

$$x = \frac{x^*}{\delta_s}, \quad y = \frac{y^*}{\delta_s}, \quad z = \frac{z^*}{\delta_s}, \tag{1.1.3a}$$

$$u = \frac{u^*}{U_0}, \quad v = \frac{v^*}{U_0}, \quad w = \frac{w^*}{U_0}, \tag{1.1.3b}$$

$$\tau = \frac{t}{t_0}, \quad p = p^* \frac{\delta_s}{\mu U_0}, \tag{1.1.3c}$$

where the absence of the superscript $*$ has been used to denote nondimensional quantities.

There is generally no natural pressure scaling and a choice must be made between p as defined above and $p = p^*/\rho U_0^2$. It will be assumed that pressure is scaled with the viscous terms and the appropriately interpreted results should be independent of this choice. In fact both choices result in identical stability equations once the pressure is removed.

Resetting (1.1.2) in nondimensional variables (1.1.3) gives

$$\frac{\partial \boldsymbol{u}}{\partial \tau} + Re\, \boldsymbol{u} \cdot \nabla \boldsymbol{u} = \frac{1}{2}\left[-\nabla p + \Delta \boldsymbol{u}\right], \tag{1.1.4a}$$

$$\nabla \cdot \boldsymbol{u} = 0, \tag{1.1.4b}$$

where Re is the Reynolds number, defined as

$$Re = U_0\sqrt{\frac{t_0}{2\nu}} = \frac{U_0\delta_s}{2\nu}. \tag{1.1.5}$$

Here, $\nu = \mu/\rho$ is the kinematic viscosity. Any other choice of nondimensionalisation may give variations on (1.1.4) or alternative definitions of Re, but the correctly interpreted results should be independent of these choices.

1.1.2 Disturbance equations

The nondimensional Navier–Stokes equations (1.1.4) will be taken and it will be assumed that the solution consists of a basic state $\boldsymbol{U}$, which solves (1.1.4) and has the form (1.1.1), plus a small perturbation, that is

$$\boldsymbol{u} = \boldsymbol{U} + \epsilon\Big(u_p(x,y,z,\tau), v_p(x,y,z,\tau), w_p(x,y,z,\tau)\Big), \tag{1.1.6a}$$

$$p = P + \epsilon p_p, \tag{1.1.6b}$$

where $\epsilon > 0$ is a measure of the size of the perturbation. Assuming that $\epsilon \ll 1$ justifies linearising the equations in ϵ, giving the disturbance equations

$$\frac{1}{Re}\frac{\partial u_p}{\partial \tau} + U\frac{\partial u_p}{\partial x} + \frac{\partial U}{\partial y}v_p = -\frac{1}{2}\frac{\partial p_p}{\partial x} + \frac{1}{2Re}\left[\frac{\partial^2 u_p}{\partial x^2} + \frac{\partial^2 u_p}{\partial y^2} + \frac{\partial^2 u_p}{\partial z^2}\right], \tag{1.1.7a}$$

$$\frac{1}{Re}\frac{\partial v_p}{\partial \tau} + U\frac{\partial v_p}{\partial x} = -\frac{1}{2}\frac{\partial p_p}{\partial y} + \frac{1}{2Re}\left[\frac{\partial^2 v_p}{\partial x^2} + \frac{\partial^2 v_p}{\partial y^2} + \frac{\partial^2 v_p}{\partial z^2}\right], \tag{1.1.7b}$$

$$\frac{1}{Re}\frac{\partial w_p}{\partial \tau} + U\frac{\partial w_p}{\partial x} = -\frac{1}{2}\frac{\partial p_p}{\partial z} + \frac{1}{2Re}\left[\frac{\partial^2 w_p}{\partial x^2} + \frac{\partial^2 w_p}{\partial y^2} + \frac{\partial^2 w_p}{\partial z^2}\right], \tag{1.1.7c}$$

$$\frac{\partial u_p}{\partial x} + \frac{\partial v_p}{\partial y} + \frac{\partial w_p}{\partial z} = 0. \tag{1.1.7d}$$

Through manipulation, these can be combined into the following two equations

$$\left[\frac{1}{Re}\frac{\partial}{\partial \tau} + U\frac{\partial}{\partial x}\right]\nabla^2 v_p - U''\frac{\partial v_p}{\partial x} - \frac{1}{2Re}\nabla^2 v_p = 0, \tag{1.1.8a}$$

$$\left[\frac{1}{Re}\frac{\partial}{\partial \tau} + U\frac{\partial}{\partial x}\right]\eta_p - \frac{1}{2Re}\nabla^2 \eta_p = U'\frac{\partial v_p}{\partial z}, \tag{1.1.8b}$$

where $'$ denotes differentiation with respect to y and η_p is the perturbation vorticity in the y-direction defined as

$$\eta_p = \frac{\partial u_p}{\partial z} - \frac{\partial w_p}{\partial x}. \tag{1.1.9}$$

Now, assuming normal-mode solutions of the form

$$\Big(v_p(x,y,z,\tau), \eta_p(x,y,z,\tau)\Big) = \Big(\hat{v}(y,\tau), \hat{\eta}(y,\tau)\Big)\mathrm{e}^{i(\alpha x+\beta z)}, \tag{1.1.10}$$

reveals the Orr–Sommerfeld-like equation

$$\left[\left(\frac{\partial}{\partial\tau} + i\alpha ReU\right)\left(\partial_y^2 - k^2\right) - i\alpha ReU'' - \frac{1}{2}\left(\partial_y^2 - k^2\right)^2\right]\hat{v} = 0, \tag{1.1.11}$$

and the Squire-like equation

$$\left[\frac{\partial}{\partial\tau} + i\alpha ReU - \frac{1}{2}\left(\partial_y^2 - k^2\right)\right]\hat{\eta} = i\beta U'\hat{v}, \tag{1.1.12}$$

where $k = \sqrt{\alpha^2+\beta^2}$. Although these equations differ from the Orr–Sommerfeld and Squire equations which arise in the steady case, the natural analogy between the two means that for the present work these names will be adopted for equations (1.1.11) and (1.1.12) which will thus be referred to as the OS equation and the Squire equation, respectively.

In the special case of a two-dimensional disturbance (for which $\beta = 0$ and $\hat{\eta} = 0$) the Squire equation becomes trivial and the OS equation becomes

$$\left[\left(\frac{\partial}{\partial\tau} + i\alpha_{2D}Re_{2D}\,U\right)\left(\partial_y^2 - \alpha_{2D}^2\right) - i\alpha_{2D}Re_{2D}\,U'' - \frac{1}{2}\left(\partial_y^2 - \alpha_{2D}^2\right)^2\right]\hat{v} = 0. \tag{1.1.13}$$

This equation will be used for comparison later.

Boundary conditions

The boundary conditions for this problem are found by considering the requirements that there is no flow through physical boundaries (no-penetration) and that the velocity of the fluid at any boundary is equal to the velocity of the boundary (no-slip). For unbounded domains there is also the condition that all perturbation quantities vanish in the far-field.

To demonstrate how these conditions manifest, let y_0 be the wall-normal location of some boundary. Due to the parallel assumption made earlier, all boundaries will exist at a fixed wall-normal location. In primitive variables, the no-penetration condition is given by

$$v_p(x, y_0, z, \tau) = 0. \tag{1.1.14}$$

The no-slip condition gives

$$u_p(x, y_0, z, \tau) = 0,$$
$$w_p(x, y_0, z, \tau) = 0.$$

The basic state already moves at the velocity of any boundary due to no-slip, hence the perturbation quantities must vanish. The final disturbance equations (1.1.11) and (1.1.12) are only concerned with the wall-normal velocity $\hat{v}$ and vorticity $\hat{\eta}$, so the boundary conditions need to be expressed solely in terms of these variables.

In the normal mode form (1.1.10) the no-penetration condition (1.1.14) becomes

$$\hat{v}(y_0, \tau) = 0. \tag{1.1.16}$$

Now, for the no-slip conditions, it is convenient to use the normal-mode decomposition on u_p and w_p, i.e.

$$\Big(u_p(x, y, z, \tau), w_p(x, y, z, \tau)\Big) = \Big(\hat{u}(y, \tau), \hat{w}(y, \tau)\Big) \mathrm{e}^{i(\alpha x + \beta z)}, \tag{1.1.17}$$

so that the no-slip conditions (1.1.15) become

$$\hat{u}(y_0, \tau) = 0, \tag{1.1.18a}$$
$$\hat{w}(y_0, \tau) = 0. \tag{1.1.18b}$$

Making the normal-mode assumption in the continuity equation (1.1.7d) gives

$$i\alpha\hat{u} + \hat{v}' + i\beta\hat{w} = 0, \tag{1.1.19}$$

where $'$ denotes differentiation with respect to y. Then, since $\hat{u}$ and $\hat{w}$ vanish at y_0, this

gives

$$\hat{v}'(y_0, \tau) = 0. \tag{1.1.20}$$

Similarly, making the normal-mode assumption in the definition of vorticity (1.1.9) gives

$$\hat{\eta} = i\beta\hat{u} - i\alpha\hat{w}. \tag{1.1.21}$$

Evaluating this at y_0 yields

$$\hat{\eta}(y_0, \tau) = 0. \tag{1.1.22}$$

The same arguments then hold in an unbounded regime except instead of evaluating the variables at an appropriate $y = y_0$, the limit is taken as $y \to \infty$. It follows that the boundary conditions required to solve the disturbance equations (1.1.11) and (1.1.12) are

$$\hat{v}, \hat{v}', \hat{\eta} = 0 \tag{1.1.23}$$

at physical boundaries or in the far-field (whichever is appropriate).

1.1.3 Squire's theorem for time-dependent flows

In the steady case, there is a well established relationship between 2D and 3D disturbances (Squire, 1933). When locating the onset of instability this relationship reveals that only 2D disturbances need be considered. It will now be shown that the same result holds for unsteady flows.

Since $\hat{v}$ appears in (1.1.12) but $\hat{\eta}$ is absent from (1.1.11), there are two families of solutions;

- **OS modes** that satisfy (1.1.11) and force a particular solution to (1.1.12).
- **Squire modes** that satisfy the homogeneous form of (1.1.12) (i.e. $\hat{v} = 0$).

Therefore the growth or decay of disturbances with $\hat{v} \neq 0$ can be described by (1.1.11) and for disturbances with $\hat{v} = 0$ the homogeneous form of the Squire equation,

$$\left[\frac{\partial}{\partial\tau} + i\alpha ReU - \frac{1}{2}\left(\partial_y^2 - k^2\right)\right]\hat{\eta} = 0, \tag{1.1.24}$$

describes the disturbance evolution.

Damped Squire modes

Consider the case $\hat{v} = 0$ so that disturbance evolution is described by the homogeneous Squire equation (1.1.24). It will be shown that all solutions to (1.1.24) are damped (i.e. decay as $\tau \to \infty$) so only OS modes become unstable.

In order to deduce whether Squire modes ever become unstable, some definition of stability must be used. The disturbance, η, is considered stable if

$$\frac{\partial}{\partial \tau}\left(\iiint_V |\eta|^2 \, \mathrm{d}V \right) < 0, \tag{1.1.25}$$

where V is the flow domain. The integral is a measure of the magnitude of the disturbance over V so put simply (1.1.25) states that the size of the disturbance decreases with increasing τ.

Multiply the equation (1.1.24) by $\bar{\eta}$ (the complex conjugate of η) and integrate over the wall-normal domain Ω_y (i.e. for the semi-infinite Stokes layer $\Omega_y = [0, \infty)$). This results in

$$\int_{\Omega_y} \frac{\partial \eta}{\partial \tau} \bar{\eta} \, \mathrm{d}y + i\alpha Re \int_{\Omega_y} U|\eta|^2 \, \mathrm{d}y - \frac{1}{2} \int_{\Omega_y} \frac{\partial^2 \eta}{\partial y^2} \bar{\eta} \, \mathrm{d}y + \frac{k^2}{2} \int_{\Omega_y} |\eta|^2 \, \mathrm{d}y = 0. \tag{1.1.26}$$

Through integration by parts it can be deduced that

$$\int_{\Omega_y} \frac{\partial^2 \eta}{\partial y^2} \bar{\eta} \, \mathrm{d}y = \left[\bar{\eta} \frac{\partial \eta}{\partial y} \right]_{\Omega_y} - \int_{\Omega_y} |\eta'|^2 \, \mathrm{d}y. \tag{1.1.27}$$

Now, making use of the condition that $\eta \to 0$ at the end-points of the domain (which must also hold for $\bar{\eta}$), (1.1.26) can be rewritten as

$$\int_{\Omega_y} \frac{\partial \eta}{\partial \tau} \bar{\eta} \, \mathrm{d}y + i\alpha Re \int_{\Omega_y} U|\eta|^2 \, \mathrm{d}y + \frac{1}{2} \int_{\Omega_y} \left(|\eta'|^2 + k^2 |\eta|^2 \right) \mathrm{d}y = 0. \tag{1.1.28}$$

Taking the real part of this expression gives

$$\mathfrak{Re}\left\{ \int_{\Omega_y} \frac{\partial \eta}{\partial \tau} \bar{\eta} \, \mathrm{d}y \right\} = -\frac{1}{2} \int_{\Omega_y} \left(|\eta'|^2 + k^2 |\eta|^2 \right) \mathrm{d}y. \tag{1.1.29}$$

Using the fact that integration and differentiation are linear, and that $\mathfrak{Re}\{z\} = (z + \bar{z})/2$ for

any $z \in \mathbb{C}$,

$$\Re\mathfrak{e}\left\{\int_{\Omega_y} \frac{\partial \eta}{\partial \tau}\bar{\eta}\,\mathrm{d}y\right\} = \int_{\Omega_y} \Re\mathfrak{e}\left\{\frac{\partial \eta}{\partial \tau}\bar{\eta}\right\}\mathrm{d}y = \frac{1}{2}\int_{\Omega_y}\left(\frac{\partial \eta}{\partial \tau}\bar{\eta} + \frac{\partial \bar{\eta}}{\partial \tau}\eta\right)\mathrm{d}y. \tag{1.1.30}$$

By the product rule it is readily confirmed that

$$\frac{\partial \eta}{\partial \tau}\bar{\eta} + \frac{\partial \bar{\eta}}{\partial \tau}\eta = \frac{\partial \eta\bar{\eta}}{\partial \tau} = \frac{\partial}{\partial \tau}|\eta|^2. \tag{1.1.31}$$

Thus, (1.1.29) can be written as

$$\begin{aligned}\frac{\partial}{\partial \tau}\int_{\Omega_y}|\eta|^2\,\mathrm{d}y &= -\frac{1}{2}\int_{\Omega_y}\left(|\eta'|^2 + k^2|\eta|^2\right)\mathrm{d}y,\\ &< 0.\end{aligned}$$

Finally, by integrating over the streamwise (x) and spanwise (z) directions, the stability condition (1.1.25) is satisfied since integration preserves inequalities. Hence, all Squire modes are damped. Therefore, to find an unstable 3D disturbance only the OS modes described by (1.1.11) need be considered.

Squire Transform

Consider a 3D disturbance described by the (three-dimensional) OS equation (1.1.11). This forces a particular solution to the Squire equation (1.1.12) but the growth can be found by considering only (1.1.11). It has been shown that Squire modes are damped so the OS equation describes all 3D disturbances that become unstable. The OS equation (1.1.11) will be compared with the OS equation governing the evolution of a 2D disturbance (1.1.13). This is the only equation governing the evolution of 2D disturbances since in two dimensions the Squire equation is trivial. It is evident from this comparison that the 3D (1.1.11) and 2D (1.1.13) OS equations yield identical solutions if

$$\alpha_{2D} = k, \tag{1.1.33a}$$

$$\alpha_{2D}Re_{2D} = \alpha Re. \tag{1.1.33b}$$

It then follows that

$$Re_{2D} = \frac{\alpha}{k}Re \leq Re. \tag{1.1.34}$$

This means that for any three-dimensional OS mode there exists an equivalent (i.e. same growth-rate) 2D disturbance at a lower Reynolds number. It follows that, since only OS modes become unstable, any time-dependent shear flow is subjected to 2D instabilities at a lower Re than 3D instabilities. This transformation describes a relationship between the 2D and 3D cases and it is shown in Thomas *et al.* (2010) that this relationship holds for a selection of simulated disturbances.

In order to illustrate the significance of this result, consider the critical Reynolds number, Re_c. This is defined as the largest value of Re below which all disturbances are stable. That is, a value of Re marginally greater than Re_c yields at least one unstable disturbance whereas a value marginally lower than Re_c yields only stable disturbances. Implicit in this definition is the assumption that (at least initially) an increase in Re is associated with destabilisation. This is consistent with the observations of Osborne Reynolds (after whom the Reynolds number is named). There are many flows that have been studied (for instance the Blasius boundary layer) for which a further increase in Re can be associated with stabilisation, but even in this case the onset of instability is reached by increasing Re past Re_c.

It was shown above that an unsteady, parallel flow is subjected to 2D instabilities at a lower Re than 3D instabilities. The direct result of this is that the critical Reynolds number Re_c must correspond to a two-dimensional disturbance. Therefore, when investigating the onset of instability only 2D disturbances need be considered through the two-dimensional OS equation

$$\left[\left(\frac{\partial}{\partial\tau}+i\alpha Re\,\bar{U}\right)\left(\partial_y^2-\alpha^2\right)-i\alpha Re\,\bar{U}''-\frac{1}{2}\left(\partial_y^2-\alpha^2\right)^2\right]\hat{v}=0. \tag{1.1.35}$$

The extension of Squire's theorem to the periodic regime was already shown by Von Kerczek & Davis (1974) by appealing to the disturbance equations in primitive variable form (i.e. four equations in u, v, w and p). By reducing the problem to the OS and Squire equations, the work above provides an alternative approach that utilises the classification of OS and Squire modes in a manner akin to Schmid & Henningson (2001). It will be seen later that an analogous process can be used when investigating the stability of three-dimensional boundary layers.

1.2 The linear stability of the finite Stokes layer

In this section, a linear stability analysis of a two-dimensional oscillatory flow will be described. Consider the finite Stokes layer, being the flow in a channel generated by oscillatory wall motion, as in Blennerhassett & Bassom (2006). The channel geometry has been chosen since this is a more natural setting for the application of the Chebyshev methods that will be used. Also, it was shown by Blennerhassett & Bassom (2006) that the results for a wide enough channel are virtually indistinguishable from those in the semi-infinite regime. The stability of the semi-infinite Stokes layer can then be studied using a solver designed for the finite Stokes layer in a channel with sufficiently large channel width.

1.2.1 The finite Stokes layer

Consider a fluid in a channel with channel half-width l so that the boundaries of the channel are located at $y = \pm l$ and have infinite extent in the x and z directions. Let the otherwise stationary fluid be subjected to the in-phase sinusoidal oscillation of both boundaries in the streamwise x-direction. This flow has an exact solution to the Navier–Stokes equations, and is called the finite Stokes layer.

Let U_0 be the amplitude of oscillation and ω be the frequency of oscillation so that the dimensional wall motion will have the form $U_0\cos(\omega t)$. This flow can be nondimensionalised using U_0 as the velocity scale and $1/\omega$ as the timescale. As alluded to earlier this results in the lengthscale

$$\delta_s = \sqrt{\frac{2\nu}{\omega}}, \tag{1.2.1}$$

called the Stokes layer thickness. The resulting nondimensional velocity profile (in the streamwise direction) can be written as

$$U(y,\tau) = \Re\mathfrak{e}\left\{\frac{\cosh[(1+i)y]}{\cosh[(1+i)h]}e^{i\tau}\right\}, \tag{1.2.2}$$

where τ is the nondimensional time such that U oscillates with a period of 2π in τ. This nondimensional flow has a wall oscillation amplitude of 1 and a Stokes layer thickness of 1, resulting in the additional parameter h which is the nondimensional channel half-width. If l is the dimensional channel half-width then the nondimensional channel half-width can be written as $h = l/\delta_s$, i.e. h is the ratio of the channel half-width to the Stokes

layer thickness. The Reynolds number associated with this flow is

$$Re = \frac{U_0}{\sqrt{2\nu\omega}}. \tag{1.2.3}$$

There are now two key parameters in this nondimensional flow: the nondimensional channel half-width h and the Reynolds number Re. Since care has been taken to ensure scalings are consistent with those used to derive the disturbance equations in Section 1.1, the stability of this flow can be investigated using the stability equation (1.1.35).

1.2.2 Application of Floquet theory

The 2D disturbance can be expressed in terms of a stream function ψ_p,

$$(u_p, v_p) = \left(\frac{\partial \psi_p}{\partial y}, -\frac{\partial \psi_p}{\partial x}\right), \tag{1.2.4}$$

so that the continuity equation is automatically satisfied. Assume the stream function has normal mode form $\psi_p(x,y,\tau) = \hat{\psi}(y,\tau)\mathrm{e}^{i\alpha x}$ as in (1.1.10) but with $\beta = 0$ since only 2D disturbances are of interest for deducing the onset of instability. This results in the equation

$$\left[\left(\frac{\partial}{\partial \tau} + i\alpha Re\, U\right)\mathcal{L} - i\alpha Re\, U'' - \frac{1}{2}\mathcal{L}^2\right]\hat{\psi} = 0, \tag{1.2.5}$$

where $\mathcal{L} = \partial_y^2 - \alpha^2$. This is a variation on (1.1.35), which has been compacted using $\mathcal{L}$. Also, this is an equation for the stream function $\hat{\psi}$ rather than $\hat{v}$, but it can easily be confirmed that both disturbance variables are governed by the same equation. This particular form of the stability equation is directly comparable to those used by Blennerhassett & Bassom (2002, 2006), Hall (1978) and Thomas *et al.* (2011, 2014).

The periodicity of the operator in (1.2.5) suggests the application of Floquet's theorem. This theorem was originally developed for ordinary differential equations (ODEs) with periodic operators but is easily adapted to partial differential equations (PDEs) that are periodic in one variable, such as (1.2.5). This adaptation is made either by considering a spatial discretisation of the problem or by assuming such an extension as an ansatz. Discretisation results in a vector ODE in τ for which Floquet's theorem is entirely appropriate while the ansatz extension simply suggests that the y-dependence should be incorporated into the solution in the same manner as it would be for a vector.

It makes no practical difference which approach is taken since the problem will be

discretised later. The ansatz argument is therefore applied so that the formulation can be continued and the discretisation will be discussed later.

Floquet's theorem states that the solution to a problem with a periodic operator can be written as a periodic function (with the same period as the operator) multiplied by an exponential function allowing for growth or decay. This is essentially the normal-mode form for periodic operators. The solution $\hat{\psi}$ to (1.2.5) is therefore written in the form

$$\hat{\psi} = e^{\mu\tau}\psi(y,\tau) + c.c. \tag{1.2.6}$$

where ψ is 2π-periodic in τ, the complex number μ is called the Floquet exponent and *c.c.* denotes the complex conjugate. The growth or decay of a disturbance is found from the real part of μ, i.e. a disturbance grows for $\mu_r > 0$ and decays for $\mu_r < 0$.

Functions of this form (i.e. the product of a periodic function with an exponential) will be referred to as *quasi-periodic* with the *quasi-period* referring to the period of the periodic component. This term can usually have a variety of meanings but for the entirety of this work it will be used solely to described any function that can be described in a similar manner to (1.2.6). When $\mu \in \mathbb{R}$, this is simply an amplifying periodic function, but $\mu_i \neq 0$ introduces subtler behaviour in which there is a phase-shift as well as amplification each quasi-period. This behaviour will be discussed in more detail when appropriate.

The resulting stability problem is an eigenvalue problem in μ,

$$\frac{\partial}{\partial\tau}\mathcal{L}\psi = \left[\frac{1}{2}\mathcal{L} - \mu - i\alpha ReU\right]\mathcal{L}\psi + i\alpha ReU''\psi. \tag{1.2.7}$$

The periodic function ψ can then be decomposed into harmonics

$$\psi(y,\tau) = \sum_{n=-\infty}^{\infty} \psi_n(y)e^{in\tau}. \tag{1.2.8}$$

Since the basic state is periodic, each harmonic is coupled with those on either side of it. This can be shown by writing the basic state as

$$U(y,\tau) = u_1(y)e^{i\tau} + u_{-1}(y)e^{-i\tau}, \tag{1.2.9}$$

with u_1 and u_{-1} being complex conjugates of each other. For the Stokes layer in a channel

$$u_1(y) = \frac{\cosh[(1+i)y]}{2\cosh[(1+i)h]}. \tag{1.2.10}$$

By substituting (1.2.8) and (1.2.9) into the stability equation (1.2.7) and comparing coefficients of $\exp(in\tau)$, an infinite system of coupled equations is constructed where, for each n,

$$\Big[\mathcal{L} - 2(\mu + in)\Big]\mathcal{L}\psi_n = 2i\alpha Re\Big[u_1\big(\mathcal{L} - 2i\big)\psi_{n-1} + u_{-1}\big(\mathcal{L} + 2i\big)\psi_{n+1}\Big]. \tag{1.2.11}$$

This makes the coupling of the different harmonics quite clear through the appearance of $\psi_{n\pm1}$. This infinite system of equations can be truncated and the resulting system can be solved numerically using spectral methods.

1.2.3 Numerical method

Following the pseudospectral techniques of Trefethen (2000), the differential operators will be approximated using Chebyshev collocation on the domain $[-h, h]$. This problem will be formulated in physical space, so the eigenvectors represent the values of the function at each collocation point (an alternative method is for the eigenvectors to contain the Chebyshev coefficients and the relationship between these two approaches will be discussed later).

By letting $\boldsymbol{\psi}_n$ be the vector containing the function values of $\psi_n(y)$ on the Chebyshev mesh, the following pseudospectral differential operators can be defined

$$\mathcal{L} \rightarrow \boldsymbol{L} = \boldsymbol{\mathcal{D}}_2 - \alpha^2 \boldsymbol{I}, \tag{1.2.12a}$$

$$\frac{1}{2}\left(\frac{\partial^4}{\partial y^4} - 2\alpha^2\frac{\partial^2}{\partial y^2} + \alpha^4\right) \rightarrow \boldsymbol{V} = \frac{1}{2}\left(\boldsymbol{\mathcal{D}}_4 - 2\alpha^2\boldsymbol{\mathcal{D}}_2 + \alpha^4\boldsymbol{I}\right), \tag{1.2.12b}$$

$$\boldsymbol{M} = \boldsymbol{L}^{-1}\boldsymbol{u_1}(\boldsymbol{L} - 2i\boldsymbol{I}), \tag{1.2.12c}$$

where $\boldsymbol{u}_1$ is a square matrix containing the values of u_1 at each mesh point along the diagonal. Also appearing are $\boldsymbol{I}$, being the identity matrix of relevant size, and finally $\boldsymbol{\mathcal{D}}_2$ and $\boldsymbol{\mathcal{D}}_4$ which are the matrix approximations to the second and fourth derivatives, respectively.

For each n this gives

$$-i\alpha Re\bar{\boldsymbol{M}}\boldsymbol{\psi}_{n+1} + \left(\boldsymbol{L}^{-1}\boldsymbol{V} - in\boldsymbol{I}\right)\boldsymbol{\psi}_n - i\alpha Re\boldsymbol{M}\boldsymbol{\psi}_{n-1} = \mu\boldsymbol{\psi}_n, \tag{1.2.13}$$

where $\bar{\boldsymbol{M}}$ is the complex conjugate of $\boldsymbol{M}$. The inverted matrix $\boldsymbol{L}^{-1}$ is introduced to ensure that $\mu\boldsymbol{\psi}_n$ appears alone on the right-hand side. It can be assumed that $\boldsymbol{L}^{-1}$ exists and is well defined since it is implicit that this matrix operator only acts in a space where the boundary conditions are satisfied.

The no-penetration condition gives rise to homogeneous boundary conditions and the no-slip condition shows up as the derivative also vanishing at the boundaries,

$$\psi_n(\pm h) = \psi_n'(\pm h) = 0. \tag{1.2.14}$$

These conditions are implemented the same way as Blennerhassett & Bassom (2006), using the techniques of Trefethen (2000). It is observed that in order for each ψ_n to vanish at the boundary the top and bottom rows of the derivative matrices can simply be dropped. The derivative condition is implemented by observing that each $\psi_n(y)$ can therefore be written in the form $(h^2 - y^2)g_n(y)$ and the condition on the derivatives demands that $g_n(\pm h) = 0$. This is then built into $\boldsymbol{\mathcal{D}}_4$ by transforming from ψ_n to g_n and then back again so that the removal of the top and bottom rows enforces both boundary conditions (Trefethen, 2000).

It now remains to truncate the system by assuming that $\psi_n = 0$ for all $|n| > N$. Some value of N for which results become insensitive to the choice of a larger N was found empirically by Blennerhassett & Bassom (2002) to be $0.8\alpha Re$ for neutral conditions.

The system can be written in the block tridiagonal matrix form

$$\begin{pmatrix}
\boldsymbol{C}_{-N} & \boldsymbol{B}^* & \boldsymbol{0} & \dots & \dots & \dots & \boldsymbol{0} \\
\boldsymbol{B} & \boldsymbol{C}_{-N+1} & \boldsymbol{B}^* & \boldsymbol{0} & \dots & \dots & \boldsymbol{0} \\
\boldsymbol{0} & \boldsymbol{B} & \boldsymbol{C}_{-N+2} & \boldsymbol{B}^* & \boldsymbol{0} & & \vdots \\
\vdots & \ddots & \ddots & \ddots & \ddots & \ddots & \vdots \\
\vdots & & \boldsymbol{0} & \boldsymbol{B} & \boldsymbol{C}_{N-2} & \boldsymbol{B}^* & \boldsymbol{0} \\
\boldsymbol{0} & \dots & \dots & \boldsymbol{0} & \boldsymbol{B} & \boldsymbol{C}_{N-1} & \boldsymbol{B}^* \\
\boldsymbol{0} & \dots & \dots & \dots & \boldsymbol{0} & \boldsymbol{B} & \boldsymbol{C}_N
\end{pmatrix}
\begin{pmatrix}
\boldsymbol{\psi}_{-N} \\ \boldsymbol{\psi}_{-N+1} \\ \boldsymbol{\psi}_{-N+2} \\ \vdots \\ \boldsymbol{\psi}_{N-2} \\ \boldsymbol{\psi}_{N-1} \\ \boldsymbol{\psi}_N
\end{pmatrix}
= \mu
\begin{pmatrix}
\boldsymbol{\psi}_{-N} \\ \boldsymbol{\psi}_{-N+1} \\ \boldsymbol{\psi}_{-N+2} \\ \vdots \\ \boldsymbol{\psi}_{N-2} \\ \boldsymbol{\psi}_{N-1} \\ \boldsymbol{\psi}_N
\end{pmatrix}, \tag{1.2.15}$$

where $\mathbf{0}$ is the zero matrix of appropriate size and

$$\boldsymbol{C}_n = \boldsymbol{L}^{-1}\boldsymbol{V} - in\boldsymbol{I},$$
$$\boldsymbol{B} = -i\alpha Re\boldsymbol{M},$$
$$\boldsymbol{B}^* = -i\alpha Re\bar{\boldsymbol{M}}.$$

All constituent blocks are square and of the size $(K-1)\times(K-1)$ where K is the number of mesh points used in the discretisation, so each vector $\boldsymbol{\psi}_n$ is of length $(K-1)$. A choice of $K = 100$ is sufficient resolution to find neutral points.

The vector $\boldsymbol{\phi}$ can now be defined as

$$\boldsymbol{\phi}^T = \left(\boldsymbol{\psi}_{-N}^T, \boldsymbol{\psi}_{1-N}^T, \ldots, \boldsymbol{\psi}_{N-1}^T, \boldsymbol{\psi}_N^T\right) \tag{1.2.17}$$

so that defining $\boldsymbol{A}$ as the matrix in (1.2.15) leaves an eigenvalue problem

$$\boldsymbol{A}\boldsymbol{\phi} = \mu\boldsymbol{\phi}, \tag{1.2.18}$$

where $\boldsymbol{A}$ is a sparse, block tridiagonal matrix with $(2N+1)(K-1)$ rows and columns. The eigenvalues μ and eigenvectors $\boldsymbol{\phi}$ are then found using the sparse matrix eigenvalue routine, eigs, in Matlab.

From the Floquet normal form (1.2.6) and harmonic decomposition (1.2.8) it can be seen that for any eigenvalue μ, $\mu \to \mu \pm ik$ results in an identical expression when $k \in \mathbb{N}$ since k simply shifts n by an integer value, having no effect on the infinite sum. For this reason, only values of μ satisfying $\mu_i \in [-1/2, 1/2]$ need be considered. Furthermore, the oscillatory flow has the additional feature that the flow reverses direction each half-period (antiperiodicity). This symmetry suggests that positive and negative μ_i correspond to left and right travelling waves which only differ by a time delay of half a period, so μ can be restricted to the region $\mu_i \in [0, 1/2]$.

Separation of even and odd modes

The problem (1.2.5) only contains even derivatives and the basic state in the channel is symmetric in the wall-normal co-ordinate y. Solutions can therefore be separated into even (symmetric around the channel centre) and odd (anti-symmetric) modes. Even

modes are expected to be the most unstable (Blennerhassett & Bassom, 2002, 2006). One of the useful properties of Chebyshev polynomials is that they alternate between even and odd, so it should be possible to utilise this property to solve only for even disturbances, thereby reducing the size of the problem.

Although the problem is solved in physical space, i.e. the eigenvector $\boldsymbol{\psi}$ contains the values of the stream function at a discrete number of spatial locations, there is a strong link between this formulation and that in Chebyshev space where the eigenvector contains the coefficients of each Chebyshev polynomial, this will be called $\boldsymbol{v}$. This relationship arises from the evaluation of $\boldsymbol{\psi}$ at collocation points and can be expressed as

$$\boldsymbol{\psi} = D_0 \boldsymbol{v}, \tag{1.2.19}$$

with each entry of the matrix D_0 defined by

$$(D_0)_{mn} = T_m(y_n/h) = \cos\Big(m\cos^{-1}(y_n/h)\Big) \quad \text{for} \quad n = 0,\ldots,K, \tag{1.2.20}$$

where T_m is the m^{th} Chebyshev polynomial as adapted for the domain $[-h,h]$. When m is even, T_m is an even function in y and when m is odd, T_m is odd. Any even (odd) function can be constructed entirely from even (odd) Chebyshev polynomials. This property will now be exploited.

To illustrate the manner in which even and odd modes can be separated let $\boldsymbol{C}$ denote some matrix approximation to a derivative operator (containing only even derivative matrices). The eigenvalue problem can be written as

$$\boldsymbol{C}\boldsymbol{\psi} = \mu\boldsymbol{\psi}, \tag{1.2.21}$$

and using (1.2.19) this can be written as

$$\tilde{\boldsymbol{C}}\boldsymbol{v} = \mu\boldsymbol{v}, \tag{1.2.22}$$

where $\tilde{\boldsymbol{C}} = D_0^{-1}\boldsymbol{C}D_0$. The problem in physical space can thus be transformed into Chebyshev space to better interpret whether contributions to the solution are even or odd.

Due to the symmetries of the problem, any terms in $\tilde{\boldsymbol{C}}$ that correspond to interaction between even and odd elements of $\boldsymbol{v}$ can be eliminated and, by reordering the elements

of $\boldsymbol{v}$ (and $\tilde{\boldsymbol{C}}$ accordingly), the problem can be written as

$$\left(\begin{array}{c|c} \tilde{\boldsymbol{C}}_{even} & \boldsymbol{0} \\ \hline \boldsymbol{0} & \tilde{\boldsymbol{C}}_{odd} \end{array}\right)\left(\begin{array}{c} v_0 \\ v_2 \\ v_4 \\ \vdots \\ \hline v_1 \\ v_3 \\ v_5 \\ \vdots \end{array}\right) = \mu \left(\begin{array}{c} v_0 \\ v_2 \\ v_4 \\ \vdots \\ \hline v_1 \\ v_3 \\ v_5 \\ \vdots \end{array}\right). \tag{1.2.23}$$

Thus, the even (odd) sub-problem is found by considering only $\tilde{\boldsymbol{C}}_{even}$ ($\tilde{\boldsymbol{C}}_{odd}$). The most unstable eigenvalues can be found by considering only the even subproblem and so, by performing this process on all the constituent blocks of $\boldsymbol{A}$ before construction, the size of the problem is quartered. By performing this routine before computing the eigenvalues, both time and computational expense are saved without sacrificing any accuracy.

1.2.4 Eigenvalues and validation

The first check that can be made on the eigenvalue solver is that for any eigenvalue μ, $\mu \pm ik$ are also eigenvalues for $k \in \mathbb{N}$. This means that when μ_i is plotted against μ_r (imaginary and real parts of μ, respectively) there should be an infinite number of eigenvalues at each growth-rate μ_r before μ is restricted as described above. The complex eigenvalues for stable and unstable cases are plotted in Figure 1.1, confirming that this characteristic holds. Due to the symmetry of this problem it is also expected that for any eigenvalue μ the complex conjugate is also an eigenvalue. This is also confirmed in Figure 1.1.

A comparison between the least stable (or most unstable) modes found by Blennerhassett & Bassom (2006) and those found in the present study is given in Table 1.1. In most cases the values are indistinguishable to 5 significant figures.

1.2.5 Aligned composite flow in a channel

Consider the periodic flow in a channel consisting of a purely oscillatory flow U_s (the Stokes layer generated by the channel walls oscillating in phase with one another) superimposed on a steady mean flow U_b (Poiseuille flow) in the same direction as the oscilla-

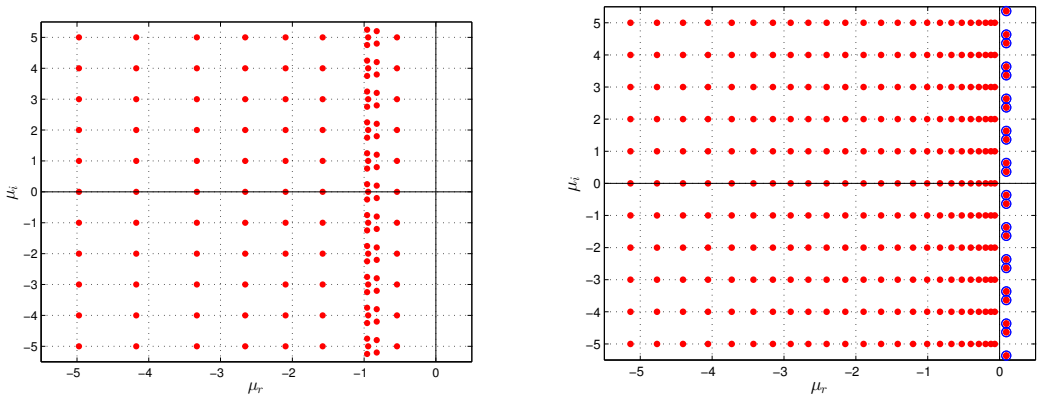

(a) *(b)*

Figure 1.1: Floquet eigenvalues for the finite Stokes layer in a channel with wavenumber $\alpha = 0.3$. The stable case (a) is for $Re = 570$ and $h = 8$, the unstable case (b) is for $Re = 800$ and $h = 16$. Note that (b) should be virtually indistinguishable from the semi-infinite Stokes layer at the same α and Re (Blennerhassett & Bassom, 2006).

Parameters			B&B	Present Study
α	h	Re		
0.3	8	0.1	(-0.08833, 0.00000)	(-0.08833, 0.00000)
0.3	8	570	(-0.54130, 0.00000)	(-0.54130, 0.00000)
0.3	16	0.1	(-0.05249, 0.00000)	(-0.05249, 0.00000)
0.3	16	570	(-0.06572, 0.00000)	(-0.06572, 0.00000)
0.3	16	750	(-0.06695, 0.00000)	(-0.06695, 0.00000)
0.3	16	800	(0.08238, 0.34583)	(0.08238, 0.34582)
0.38	16	847.5	(0.67616, 0.14881)	(0.67620, 0.14880)

Table 1.1: Comparison of least stable (most unstable) modes with those presented by Blennerhassett & Bassom (2006) (B&B). Complex numbers $x + iy$ are represented as vectors (x, y). All cases used $K = 100$ and are rounded to 5 decimal places for comparison with B&B. The cases depicted in Figure 1.1 are shaded.

tion. This is the flow considered in Thomas *et al.* (2011).

For the channel, in the special case where there is no mean flow, the basic state converges to that of a semi-infinite Stokes layer as the channel width increases. Hence, a solver developed for a channel geometry contains results for a semi-infinite geometry as a limiting case. It is, however, important to note that the semi-infinite problem with a mean flow would require reformulation in the semi-infinite geometry since Poiseuille flow does not approach the Blasius boundary layer as the channel width is increased.

Basic state

Consider the flow regime in which a fluid, located between two plates of infinite extent, has a mean flow in some direction and is also subjected to the in-phase oscillation of the plates in this direction. This is an aligned composite flow since the flow consists of two components (the steady mean flow and unsteady oscillation) aligned in the same direction. Each flow component has an exact solution to the Navier–Stokes equations: the mean component is described by Poiseuille flow and the oscillatory component is the finite Stokes layer already discussed.

First, consider the mean flow in the absence of the wall oscillation. Let $U_{b,0}$ be the velocity at the centre of the channel and l be the channel half-width. The flow can be nondimensionalised using these characteristic values resulting in the nondimensional Poiseuille flow velocity profile

$$f(y) = 1 - y^2, \tag{1.2.24}$$

where y is the wall-normal co-ordinate and f is the velocity in the streamwise direction (the velocity in the other directions being zero). This nondimensional flow has a channel half-width of 1 and a velocity of 1 in the centre of the channel. The Reynolds number associated with this flow, based on these scalings, is

$$Re_b = \frac{U_{b,0} l}{\nu}. \tag{1.2.25}$$

Now, consider the oscillatory flow in the absence of the mean flow which has already been discussed. For this section, let $U_{s,0}$ be the amplitude of oscillation. The resulting nondimensional velocity profile is the same as (1.2.2),

$$g(y,\tau) = \mathfrak{Re}\left\{\frac{\cosh[(1+i)y]}{\cosh[(1+i)h]} e^{i\tau}\right\}. \tag{1.2.26}$$

Again, note the additional parameter h which is the nondimensional channel half-width. The Reynolds number associated with this flow component is

$$Re_s = \frac{U_{s,0}}{\sqrt{2\nu\omega}}. \tag{1.2.27}$$

Now consider the composite flow. The natural lengthscale for periodic flows is the Stokes layer thickness δ_s based on the frequency of oscillation, and it has already been

shown that when nondimensionalising the problem using this lengthscale, the parameter $h = l/\delta_s$ is introduced. The Stokes layer thickness will also be used as the characteristic lengthscale of the composite flow so the mean flow profile (1.2.24) must be rescaled to correspond to a channel half-width of h. The nondimensional composite velocity profile will be a linear combination of these profiles, $f(y/h)$ and $g(y,\tau)$.

To write an expression for the nondimensional composite flow, define the characteristic velocity as $U_{b,0} + U_{s,0}$. The velocity profile can be written as

$$U(y,\tau) = \frac{U_{b,0}}{U_{b,0}+U_{s,0}} f(y/h) + \frac{U_{s,0}}{U_{b,0}+U_{s,0}} g(y,\tau). \tag{1.2.28}$$

Much as h is the ratio of the lengths associated with each flow component, the ratio of the velocities can be defined so that this velocity profile can be written as

$$U(y,\tau) = \gamma_b f(y/h) + \gamma_s g(y,\tau), \tag{1.2.29}$$

where

$$\gamma_b = \frac{\Gamma}{1+\Gamma} = 1 - \gamma_1 \in [0,1], \tag{1.2.30a}$$

$$\gamma_s = \frac{1}{1+\Gamma} \in [0,1], \tag{1.2.30b}$$

$$\text{for} \quad \Gamma = \frac{U_{b,0}}{U_{s,0}} \in [0,\infty). \tag{1.2.30c}$$

Note that when $\Gamma = 0$ the velocity profile is simply that of the finite Stokes layer already discussed. As $\Gamma \to \infty$ the velocity profile U approaches Poiseuille flow in a channel with half-width h.

There are now three key parameters in this nondimensional flow: the ratio of lengthscales associated with each flow component, h; the ratio of the velocity scales associated with each component, Γ; and the Reynolds number. The Reynolds number associated with this flow will be of a similar form to (1.2.3) since the same time and length scales have been used for the nondimensionalisation. This yields a composite Reynolds number that can be written in terms of the Reynolds numbers associated with each flow component (1.2.25) and (1.2.27);

$$Re = \frac{U_{b,0}+U_{s,0}}{\sqrt{2\nu\omega}} = \frac{Re_b}{2h} + Re_s. \tag{1.2.31}$$

The flow has now been nondimensionalised in such a way that the stability equation (1.2.7) is appropriate.

Floquet theory

The stability analysis of this flow is similar to that already described except that the mean flow needs to be incorporated. The stream function, as the subject of the stability equation (1.2.7), is again decomposed into harmonics ψ_n, (1.2.8). For a fully steady flow (approached as $\Gamma \to \infty$) each ψ_n can be found independently of the others and for the correctly interpreted scalings this unsurprisingly recovers the Orr–Sommerfeld equation at a selection of frequencies.

When the periodic component is non-zero there is the same harmonic coupling as shown for the purely oscillatory case. The periodic component of the basic state takes the form

$$g(y,\tau) = u_1(y)\mathrm{e}^{i\tau} + u_{-1}(y)\mathrm{e}^{-i\tau}, \tag{1.2.32}$$

with u_1 and u_{-1} being complex conjugates of each other and u_1 given in (1.2.10). Through harmonic decomposition and comparing coefficients of $\mathrm{e}^{in\tau}$, the infinite system of coupled equations is now given, for each n, by

$$\Big[\mathcal{L} - 2(\mu + in)\Big]\mathcal{L}\psi_n - 2i\alpha\gamma_b Re\Big[f\mathcal{L} - \frac{1}{h^2}f''\Big]\psi_n \\ = 2i\alpha\gamma_s Re\Big[u_1\big(\mathcal{L} - 2i\big)\psi_{n-1} + u_{-1}\big(\mathcal{L} + 2i\big)\psi_{n+1}\Big]. \tag{1.2.33}$$

Note that in the special case $\gamma_b = 0$, this is identical to the equation (1.2.11) for the purely oscillatory case.

Numerical Method

The numerical methods for the aligned composite flow are identical to those for the purely oscillatory flow considered earlier, except that the additional term introduced by the presence of the mean flow requires the definition of an addition matrix operator,

$$\boldsymbol{P} = \gamma_b \boldsymbol{L}^{-1}\left(\boldsymbol{U}_b\boldsymbol{L} - \boldsymbol{\mathcal{D}}_2\boldsymbol{U}_b\right), \tag{1.2.34}$$

where $\boldsymbol{U}_b$ contains the values of $f(y/h)$ along the diagonal. The composite flow also requires the definition of $\boldsymbol{M}$ to be modified to

$$\boldsymbol{M} = \gamma_s \boldsymbol{L}^{-1} \boldsymbol{u_1} (\boldsymbol{L} - 2i\boldsymbol{I}). \tag{1.2.35}$$

For each n this gives

$$-i\alpha Re\bar{\boldsymbol{M}}\boldsymbol{\psi}_{n+1} + \left(\boldsymbol{L}^{-1}\boldsymbol{V} - in\boldsymbol{I} - i\alpha Re\boldsymbol{P}\right)\boldsymbol{\psi}_n - i\alpha Re\boldsymbol{M}\boldsymbol{\psi}_{n-1} = \mu\boldsymbol{\psi}_n, \tag{1.2.36}$$

where $\boldsymbol{L}$ is as defined in (1.2.12) and $\bar{\boldsymbol{M}}$ is again the complex conjugate of $\boldsymbol{M}$. The boundary conditions are implemented in the same manner as before and it is observed that the system has the same structure as for the purely oscillatory case. Once truncated, the system can again be written in the matrix form (1.2.15) with a modified definition of the diagonal terms to incorporate the matrix $\boldsymbol{P}$,

$$\boldsymbol{C}_n = \boldsymbol{L}^{-1}\boldsymbol{V} - in\boldsymbol{I} - i\alpha Re\boldsymbol{P}. \tag{1.2.37}$$

With regards to the truncation, it was found empirically by Thomas *et al.* (2011) that $N = 0.8\gamma_s \alpha Re$ was sufficiently large for neutral conditions. As an unphysical parameter, the inappropriate choice of N can introduce spurious results. As $N \to \infty$, the full system is approached and so the value of N is selected so that the selection of a larger N has little to no effect on the eigenvalues μ. It was found in this study that a choice of $N = 0.8\gamma\alpha Re$ was more effective, where $\gamma = \max(\gamma_b, \gamma_s)$.

Having appropriately modified definition of the matrix $\boldsymbol{A}$, the stability of the aligned composite flow can be deduced by solving the eigenvalue problem (1.2.18). Since the basic state has retained the symmetry in the wall-normal domain, the size of the problem can again be reduced by solving only the even subproblem.

It is important to note that the introduction of the mean flow breaks the antiperiodicity of the oscillatory flow component. That is, when time is shifted by half a period the velocity profile does not simply reverse direction. Therefore, for the aligned composite flow, values of μ satisfying $\mu_i \in [-1/2, 1/2]$ are considered, whereas previously eigenvalues existed in complex conjugate pairs meaning $\mu_i < 0$ could be discarded.

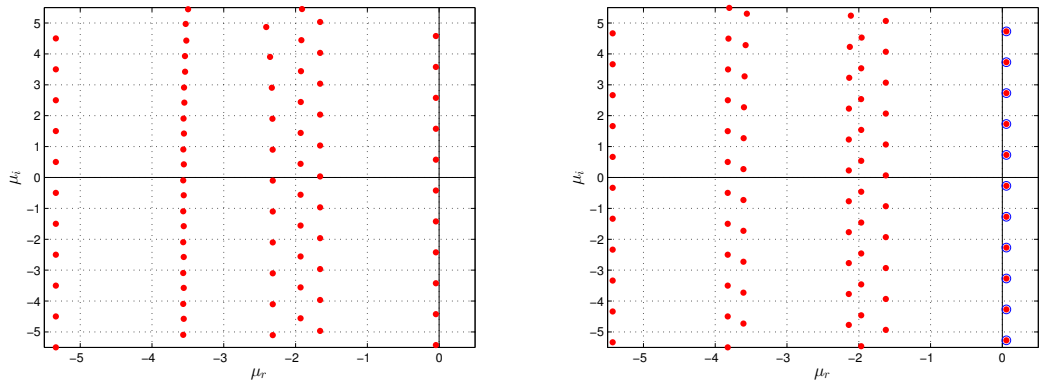

(a) *(b)*

Figure 1.2: Floquet eigenvalues for the finite Stokes layer modified by an aligned mean flow (Poiseuille flow). Diagrams correspond to wavenumber $\alpha = 0.3$, channel half-width $h = 6$ and velocity ratio $\Gamma = 0.5$. The stable case (a) is for $Re = 520$, the unstable case (b) is for $Re = 540$.

Results

Direct comparison is not possible with the work of Thomas *et al.* (2011) since this paper does not present any individual eigenvalues. Thus, validation will be properly conducted later using neutral curves for confirmation. However, the eigenvalues of two cases known to be stable and unstable from Thomas *et al.* (2011) are presented in Figure 1.2. Since the stability characteristics and the pattern in μ_i are as expected it will be tentatively assumed that the present study is in agreement with Thomas *et al.* (2011).

1.3 Growth-rate contours and neutral curves

Described above is a method for finding the eigenvalues μ corresponding to flow parameters Re, Γ, h and disturbance parameter α. For this section, the parameters Γ and h will be fixed (so a specific member of the family of flows described above is being considered) and $\mu(\alpha, Re)$ will denote the least stable eigenvalue for the particular choice of α and Re.

Of fundamental importance to hydrodynamic stability theory is the classification of disturbances as stable or unstable and for this reason neutral curves are an indispensable tool. A neutral curve is found by plotting the zero-growth contour (corresponding to $\mu_r = 0$) in the (α, Re)-plane. It is useful in finding the critical Reynolds number (below which no instability occurs) and in deducing, for any choice of α and Re, whether a disturbance grows or decays. The problem will be generalised to finding any growth-

rate contour of which the neutral curve is a special case.

In order to construct a contour of growth-rate μ_{crit}, roots of the equation

$$F(\alpha, Re) = \Re\mathfrak{e}\{\mu(\alpha, Re)\} - \mu_{crit} \tag{1.3.1}$$

must be found. Letting $\mu_{crit} = 0$ makes these roots correspond to neutral points. The obvious choice of method to achieve this is Newton's method due to its quadratic convergence and relatively straight-forward implementation. One drawback of Newton's method is the requirement of a fairly good initial guess and once a point on the curve has been found this can be used as the initial guess for the next point. However, an accurate starting point is first required.

1.3.1 Initialisation

Bisection method for initial point

The first point on the contour will be found by a bisection method. First, the Reynolds number is chosen to be fixed at some Re_0 for which there exists at least one α yielding $F(\alpha, Re_0) > 0$. Some wavenumber α_0 is chosen so that $F(\alpha_0, Re_0)$ can be found. Then, for

$$\alpha_i = \alpha_{i-1} + \Delta\alpha,$$

where $i \geq 1$ and $\Delta\alpha$ is fixed at the beginning, $F(\alpha_i, Re_0)$ is calculated until some $i = j$ is reached for which $F(\alpha_j, Re_0)$ has opposite sign to $F(\alpha_0, Re_0)$.

Since the root of F must be somewhere between α_0 and α_j, the curve of F is approximated between these points as a straight line and F is calculated at the approximate root. Base on the sign of F at this location, either $F(\alpha_0, Re_0)$ or $F(\alpha_j, Re_0)$ is discarded so that the process can be repeated on a smaller interval to find a better approximation to the root. This process of bisection is then repeated until the root is found to within a chosen accuracy, thus providing a starting point for the contour curve.

Although much of the process is automated, the selection of Re_0 and α_0 can be time consuming for a curve of completely unknown shape. The sign of $\Delta\alpha$ is also an important parameter that requires some exploration to find. Fortunately, for the problem of interest, a selection of neutral curves are plotted in Thomas *et al.* (2011) from which these starting parameters can be estimated. For previously unpublished curves this ini-

tialisation can be more difficult but ball-park figures can be found by comparison with curves corresponding to similar parameters.

Rescaling the problem

Due to the very different scales of α and Re ($\alpha \sim 0.1$ and $Re \sim 100$), it is convenient to rescale these parameters, which can be considered the independent variables of the root-finding problem. Defining a characteristic value of α as a_c and a characteristic value of Re as r_c, an alternative independent variable $\boldsymbol{x}$ will be defined as

$$\boldsymbol{x} = (x, y) = \left(\frac{\alpha}{a_c}, \frac{Re}{r_c}\right) \tag{1.3.2}$$

so that the problem is transformed to a root-finding problem in $\boldsymbol{x}$ of the function

$$F(\boldsymbol{x}) = g(\boldsymbol{x}) - \mu_{crit}, \tag{1.3.3}$$

where g is used to denote the growth-rate and is related to μ by

$$g(x, y) = \mathfrak{Re}\Big\{\mu(a_c x, r_c y)\Big\}, \tag{1.3.4}$$

from which it can be seen that

$$\frac{\partial g}{\partial x} = a_c \mathfrak{Re}\left\{\frac{\partial \mu}{\partial \alpha}\right\}, \tag{1.3.5a}$$

$$\frac{\partial g}{\partial y} = r_c \mathfrak{Re}\left\{\frac{\partial \mu}{\partial Re}\right\}, \tag{1.3.5b}$$

which will be useful later. The letters x and y in this section should not be confused with the spatial co-ordinates used in the rest of this work. In this section, x and y will only be used in this context, while outside of this section they will only describe the spatial directions.

The problem with using Newton's method to find roots of (1.3.3) is that Newton's method requires the same number of equations as variables and (1.3.3) is a single equation in two variables. It is possible to resolve this by fixing either x or y (as for the bisection), finding the roots of F at this value and then making a step in the fixed variable and repeating. Though this is a mathematically robust method it fails when the contour has

a turning point with respect to the variable being stepped forward. It is for this reason that pseudo-arclength continuation will be used (Kelley, 2005). The basic idea is that by fixing some measure of the distance between consecutive points on the contour (for instance, arclength) a second equation is introduced and so Newton's method can be used in two-dimensions to find the roots of the resulting system.

1.3.2 Arclength

Arclength is a measure of the distance of any point on a curve from some starting point. The starting point for this problem has already been found using bisection and will be denoted $\boldsymbol{x}_0$. For subsequent steps the same process is carried out with the previous point relabelled as $\boldsymbol{x}_0$. Letting s represent arclength and $\dot{\boldsymbol{x}}$ denote differentiation of $\boldsymbol{x}$ with respect to s,

$$\|\dot{\boldsymbol{x}}\|^2 = |\dot{x}|^2 + |\dot{y}|^2 = 1. \tag{1.3.6}$$

For this problem, an approximation to this normalisation equation will be $N = 0$ where

$$N(\boldsymbol{x}, s) = \dot{\boldsymbol{x}}_0^T(\boldsymbol{x} - \boldsymbol{x}_0) - (s - s_0). \tag{1.3.7}$$

This will provide the additional equation for the root-finding problem. Since s is a measure of distance from $\boldsymbol{x}_0$, which is relabelled at each point in this process, the term $(s - s_0)$ can be replaced with δs. This will be set as a parameter in advance. The only unknown in (1.3.7) is $\dot{\boldsymbol{x}}_0$, which will be calculated using (1.3.3) and (1.3.6) as follows.

For any $\boldsymbol{x}$ on the contour, it must hold that

$$F(\boldsymbol{x}) = g(\boldsymbol{x}) - \mu_{crit} = 0, \tag{1.3.8}$$

which can be differentiated with respect to s to give

$$\frac{\partial g}{\partial x}\dot{x} + \frac{\partial g}{\partial y}\dot{y} = 0. \tag{1.3.9}$$

This can be written as

$$a_c \mathfrak{Re}\left\{\frac{\partial \mu}{\partial \alpha}\right\}\dot{x} + r_c \mathfrak{Re}\left\{\frac{\partial \mu}{\partial Re}\right\}\dot{y} = 0 \tag{1.3.10}$$

using (1.3.5) and then rearranged to give

$$\dot{x} = -\left(\frac{r_c}{a_c}\right)\frac{\Re\mathfrak{e}\left\{\frac{\partial\mu}{\partial Re}\right\}}{\Re\mathfrak{e}\left\{\frac{\partial\mu}{\partial\alpha}\right\}}\dot{y}. \tag{1.3.11}$$

Using this expression, (1.3.6) can be written entirely in terms of $\dot{y}$, which can in turn be rearranged to give

$$\dot{y} = \frac{\pm 1}{\sqrt{1+\left(\frac{r_c}{a_c}\right)\left[\frac{\Re\mathfrak{e}\{\partial\mu/\partial\alpha\}}{\Re\mathfrak{e}\{\partial\mu/\partial Re\}}\right]^2}}. \tag{1.3.12}$$

The choice of $\pm$ will dictate the direction moved in, so provided only one is chosen for all points the curve will not double back on itself.

Between (1.3.11) and (1.3.12), an expression $\dot{\boldsymbol{x}}$ can be written (and hence $\dot{\boldsymbol{x_0}}$) once the appropriate derivatives of μ have been calculated.

1.3.3 A means of finding the necessary derivatives

The derivatives $\partial\mu/\partial\alpha$ and $\partial\mu/\partial Re$ will be found following Bridges & Morris (1983). First, the eigenvalue problem (1.2.18) will be written as

$$(\boldsymbol{A}-\mu\boldsymbol{I})\boldsymbol{\phi} = \boldsymbol{0}, \tag{1.3.13}$$

for eigenvalue μ and eigenvector $\boldsymbol{\phi}$. For each eigenvalue μ, there exist both right and left eigenvectors defined by

$$(\boldsymbol{A}-\mu\boldsymbol{I})\boldsymbol{\phi}_r = \boldsymbol{0}, \tag{1.3.14a}$$

$$\boldsymbol{\phi}_l^T(\boldsymbol{A}-\mu\boldsymbol{I}) = \boldsymbol{0}, \tag{1.3.14b}$$

where $\boldsymbol{\phi}_r$ is the right eigenvector and $\boldsymbol{\phi}_l$ is the left eigenvector. The Matlab routine eigs, used to find μ, is also used to find both eigenvectors. Differentiation with respect to each parameter gives

$$\frac{\partial(\boldsymbol{A}-\mu\boldsymbol{I})}{\partial\alpha}\boldsymbol{\phi}_r + (\boldsymbol{A}-\mu\boldsymbol{I})\frac{\partial\boldsymbol{\phi}_r}{\partial\alpha} = \boldsymbol{0}, \tag{1.3.15a}$$

$$\frac{\partial(\boldsymbol{A}-\mu\boldsymbol{I})}{\partial Re}\boldsymbol{\phi}_r + (\boldsymbol{A}-\mu\boldsymbol{I})\frac{\partial\boldsymbol{\phi}_r}{\partial Re} = \boldsymbol{0}. \tag{1.3.15b}$$

Left multiplication by $\boldsymbol{\phi}_l^T$ will, from (1.3.14b), eliminate the second term in both these expressions, giving

$$\boldsymbol{\phi}_l^T \left(\frac{\partial \boldsymbol{A}}{\partial \alpha} - \frac{\partial \mu}{\partial \alpha} \boldsymbol{I} \right) \boldsymbol{\phi}_r = \boldsymbol{0}, \tag{1.3.16a}$$

$$\boldsymbol{\phi}_l^T \left(\frac{\partial \boldsymbol{A}}{\partial Re} - \frac{\partial \mu}{\partial Re} \boldsymbol{I} \right) \boldsymbol{\phi}_r = \boldsymbol{0}, \tag{1.3.16b}$$

which can be rearranged to give the derivatives of μ,

$$\frac{\partial \mu}{\partial \alpha} = \frac{\boldsymbol{\phi}_l^T \frac{\partial \boldsymbol{A}}{\partial \alpha} \boldsymbol{\phi}_r}{\boldsymbol{\phi}_l^T \boldsymbol{I} \boldsymbol{\phi}_r}, \tag{1.3.17a}$$

$$\frac{\partial \mu}{\partial Re} = \frac{\boldsymbol{\phi}_l^T \frac{\partial \boldsymbol{A}}{\partial Re} \boldsymbol{\phi}_r}{\boldsymbol{\phi}_l^T \boldsymbol{I} \boldsymbol{\phi}_r}. \tag{1.3.17b}$$

In order to calculate the derivatives of $\boldsymbol{A}$. Each constituent block can be differentiated with respect to α and Re. The derivative of $\boldsymbol{A}$ with respect to Re is given by

$$\frac{\partial \boldsymbol{A}}{\partial Re} = \begin{pmatrix} (\boldsymbol{C}_{-N})_{Re} & (\boldsymbol{B}^*)_{Re} & \boldsymbol{0} & \dots & \dots & \dots & \boldsymbol{0} \\ (\boldsymbol{B})_{Re} & (\boldsymbol{C}_{-N+1})_{Re} & (\boldsymbol{B}^*)_{Re} & \boldsymbol{0} & \dots & \dots & \boldsymbol{0} \\ \boldsymbol{0} & (\boldsymbol{B})_{Re} & (\boldsymbol{C}_{-N+2})_{Re} & (\boldsymbol{B}^*)_{Re} & \boldsymbol{0} & & \vdots \\ \vdots & \ddots & \ddots & \ddots & \ddots & \ddots & \vdots \\ \vdots & & \boldsymbol{0} & (\boldsymbol{B})_{Re} & (\boldsymbol{C}_{N-2})_{Re} & (\boldsymbol{B}^*)_{Re} & \boldsymbol{0} \\ \boldsymbol{0} & \dots & \dots & \boldsymbol{0} & (\boldsymbol{B})_{Re} & (\boldsymbol{C}_{N-1})_{Re} & (\boldsymbol{B}^*)_{Re} \\ \boldsymbol{0} & \dots & \dots & \dots & \boldsymbol{0} & (\boldsymbol{B})_{Re} & (\boldsymbol{C}_N)_{Re} \end{pmatrix}$$

and the derivative of $\boldsymbol{A}$ with respect to α is, similarly, given by

$$\frac{\partial \boldsymbol{A}}{\partial \alpha} = \begin{pmatrix} (\boldsymbol{C}_{-N})_{\alpha} & (\boldsymbol{B}^*)_{\alpha} & \boldsymbol{0} & \dots & \dots & \dots & \boldsymbol{0} \\ (\boldsymbol{B})_{\alpha} & (\boldsymbol{C}_{-N+1})_{\alpha} & (\boldsymbol{B}^*)_{\alpha} & \boldsymbol{0} & \dots & \dots & \boldsymbol{0} \\ \boldsymbol{0} & (\boldsymbol{B})_{\alpha} & (\boldsymbol{C}_{-N+2})_{\alpha} & (\boldsymbol{B}^*)_{\alpha} & \boldsymbol{0} & & \vdots \\ \vdots & \ddots & \ddots & \ddots & \ddots & \ddots & \vdots \\ \vdots & & \boldsymbol{0} & (\boldsymbol{B})_{\alpha} & (\boldsymbol{C}_{N-2})_{\alpha} & (\boldsymbol{B}^*)_{\alpha} & \boldsymbol{0} \\ \boldsymbol{0} & \dots & \dots & \boldsymbol{0} & (\boldsymbol{B})_{\alpha} & (\boldsymbol{C}_{N-1})_{\alpha} & (\boldsymbol{B}^*)_{\alpha} \\ \boldsymbol{0} & \dots & \dots & \dots & \boldsymbol{0} & (\boldsymbol{B})_{\alpha} & (\boldsymbol{C}_N)_{\alpha} \end{pmatrix},$$

where subscripts have been used to denote partial differentiation. The derivative blocks

can be constructed using the definition of each block:

$$\boldsymbol{B} = -i\alpha Re\boldsymbol{M} \Rightarrow \begin{cases} (\boldsymbol{B})_{Re} = -i\alpha\boldsymbol{M}, \\ (\boldsymbol{B})_{\alpha} = -iRe\left[\boldsymbol{M} + \alpha(\boldsymbol{M})_{\alpha}\right], \end{cases}$$

and similarly,

$$\begin{aligned} (\boldsymbol{B}^*)_{Re} &= -i\alpha\bar{\boldsymbol{M}}, \\ (\boldsymbol{B}^*)_{\alpha} &= -iRe\Big[\bar{\boldsymbol{M}} + \alpha(\bar{\boldsymbol{M}})_{\alpha}\Big]. \end{aligned}$$

The derivatives of $\boldsymbol{M}_{\alpha}$ can be found by writing,

$$\begin{aligned} \boldsymbol{M} = \gamma_s\boldsymbol{L}_{-1}u_1(\boldsymbol{L} - 2i\boldsymbol{I}) &\Rightarrow \boldsymbol{L}\boldsymbol{M} = \gamma_s u_1(\boldsymbol{L} - 2i\boldsymbol{I}), \\ &\Rightarrow \boldsymbol{L}(\boldsymbol{M})_{\alpha} + (\boldsymbol{L})_{\alpha}\boldsymbol{M} = \gamma_s u_1(\boldsymbol{L})_{\alpha}, \\ &\Rightarrow (\boldsymbol{M})_{\alpha} = \boldsymbol{L}^{-1}\left[\gamma_s u_1(\boldsymbol{L})_{\alpha} - (\boldsymbol{L})_{\alpha}\boldsymbol{M}\right], \end{aligned}$$

where $(\boldsymbol{L})_{\alpha} = -2\alpha\boldsymbol{I}$ comes directly from the definition. Taking the complex conjugate gives an expression for $(\bar{\boldsymbol{M}})_{\alpha}$.

Similarly, for each n,

$$\begin{aligned} \boldsymbol{C}_n = \boldsymbol{L}^{-1}\boldsymbol{V} - in\boldsymbol{I} - i\alpha Re\boldsymbol{P} &\Rightarrow (\boldsymbol{C}_n)_{Re} = -i\alpha\boldsymbol{P}, \\ \boldsymbol{L}\boldsymbol{C}_n = \boldsymbol{V} - in\boldsymbol{L} - i\alpha Re\boldsymbol{L}\boldsymbol{P} &\Rightarrow \boldsymbol{L}(\boldsymbol{C}_n)_{\alpha} = (\boldsymbol{V})_{\alpha} - (\boldsymbol{L})_{\alpha}\boldsymbol{L}^{-1}\boldsymbol{V} - iRe\left[\alpha\boldsymbol{L}(\boldsymbol{P})_{\alpha} + \boldsymbol{L}\boldsymbol{P}\right], \\ &\Rightarrow (\boldsymbol{C}_n)_{\alpha} = \boldsymbol{L}^{-1}\left[(\boldsymbol{V})_{\alpha} - (\boldsymbol{L})_{\alpha}\boldsymbol{L}\boldsymbol{V}\right] - iRe\left[\alpha(\boldsymbol{P})_{\alpha} + \boldsymbol{P}\right], \end{aligned}$$

where

$$\begin{aligned} \boldsymbol{P} = \gamma_b\boldsymbol{L}_{-1}\left[U_m\boldsymbol{L} + \frac{2}{h^2}\boldsymbol{I}\right] &\Rightarrow \boldsymbol{L}\boldsymbol{P} = \gamma_b\left[U_m\boldsymbol{L} + \frac{2}{h^2}\boldsymbol{I}\right], \\ &\Rightarrow \boldsymbol{L}(\boldsymbol{P})_{\alpha} = \gamma_b U_m(\boldsymbol{L})_{\alpha} - (\boldsymbol{L})_{\alpha}\boldsymbol{P}, \\ &\Rightarrow (\boldsymbol{P})_{\alpha} = \boldsymbol{L}^{-1}\left[\gamma_b U_m(\boldsymbol{L})_{\alpha} - (\boldsymbol{L})_{\alpha}\boldsymbol{P}\right], \end{aligned}$$

and

$$(\boldsymbol{V})_{\alpha} = 2\alpha\Big[\alpha^2\boldsymbol{I} - \boldsymbol{\mathcal{D}}_2\Big].$$

Much of the detail is missing from the differentiation of each of these blocks, but the

general approach is demonstrated.

The appropriate derivatives of $\boldsymbol{A}$ can thus be used to define $\dot{\boldsymbol{x}}$ (and hence $\dot{\boldsymbol{x}}_0$) in (1.3.7). Again, the problem can also be reduced in size by considering only the even subproblem.

1.3.4 Pseudo-arclength continuation

Since N is now defined for the next point on the contour, the problem can be recast as finding $\boldsymbol{x}$ for which

$$\boldsymbol{H}(\boldsymbol{x},s)=\begin{pmatrix}F(\boldsymbol{x})\\ N(\boldsymbol{x},s)\end{pmatrix}=\begin{pmatrix}g(\boldsymbol{x})-\mu_{crit}\\ \dot{\boldsymbol{x}}_0^T(\boldsymbol{x}-\boldsymbol{x}_0)-\delta s\end{pmatrix}=\begin{pmatrix}0\\0\end{pmatrix}, \tag{1.3.22}$$

a problem perfectly suited to Newton's method. From this, the Jacobean of the system can be calculated,

$$\boldsymbol{J_H}(\boldsymbol{x},s)=\begin{pmatrix}\frac{\partial F}{\partial x} & \frac{\partial F}{\partial y}\\ \frac{\partial N}{\partial x} & \frac{\partial N}{\partial y}\end{pmatrix}=\begin{pmatrix}a_c\,\mathfrak{Re}\left\{\frac{\partial\mu}{\partial\alpha}\right\} & r_c\,\mathfrak{Re}\left\{\frac{\partial\mu}{\partial\mathfrak{Re}}\right\}\\ \dot{x}_0 & \dot{y}_0\end{pmatrix}. \tag{1.3.23}$$

An iterative process is initiated with $\boldsymbol{x}^0=\boldsymbol{x}_0$, and each subsequent iteration is calculated by

$$\boldsymbol{x}^{i+1}=\boldsymbol{x}^i-\left[\boldsymbol{J_H}(\boldsymbol{x}^i,s)\right]^{-1}\boldsymbol{H}(\boldsymbol{x}^i,s) \tag{1.3.24}$$

using the backslash operator in Matlab. The iteration is stopped once the difference of subsequent $\boldsymbol{x}^i$ is below a given threshold and the resulting approximation to the root of $\boldsymbol{H}$ is labelled $\boldsymbol{x}$. The location of the contour can then be stored in terms of α and Re (found from $\boldsymbol{x}$) and for the next point $\boldsymbol{x}$ is relabelled $\boldsymbol{x}_0$ and $\dot{\boldsymbol{x}}_0$ is found at this new location. This process is continued until the desired length of the contour is plotted.

Improving efficiency

One easy way to improve the speed of convergence is with a closer initial guess. One way to achieve this is to use the following tangent predictor to initialise Newton's iteration,

$$\boldsymbol{x}^0=\boldsymbol{x}_0+\dot{\boldsymbol{x}}_0\delta s, \tag{1.3.25}$$

which is a first order accurate approximation in δs. Higher order polynomial approximations can also be used but this requires more points being stored along the path and the

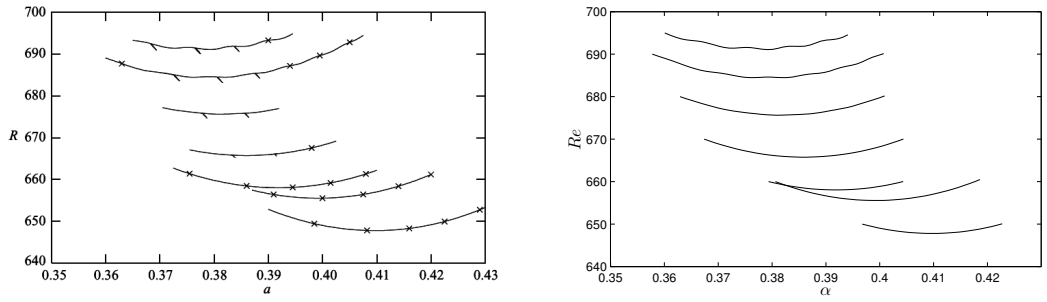

(a) *(b)*

Figure 1.3: Comparison of neutral curves found by Blennerhassett & Bassom (2006) (a) and those found in the present study (b). The curves correspond to $h = 5, 5.5, 6, 6.5, 7, 7.5, 8$ from the bottom curve ($h = 5$) to the top ($h = 8$). There appears to be excellent agreement. In Blennerhassett & Bassom (2006), the Reynolds number is denoted as R (rather than Re) and the wavenumber is denoted as a (rather than α). The axes of (a) are labelled accoridng to this notation.

calculation of higher order derivatives. The method is quadratically convergent so only a slightly improved guess is required. Thus, the tangent predictor will be used.

An additional improvement on efficiency is through the secant method. This involves approximating $\dot{\boldsymbol{x}}$ rather than performing the expensive calculations described above. Letting $\boldsymbol{x}_{-1}$ denote the point on the contour found before $\boldsymbol{x}_0$, if

$$D\boldsymbol{x} = \frac{\boldsymbol{x}_0 - \boldsymbol{x}_{-1}}{\delta s} \tag{1.3.26}$$

then $\dot{x}$ can be approximated by

$$\dot{x} = \frac{D\boldsymbol{x}}{\|D\boldsymbol{x}\|}. \tag{1.3.27}$$

This can be used in both the tangent predictor and in the expression for N (which requires updating as $\boldsymbol{x}_0$ is updated).

1.3.5 Validation

For comparison with existing results, consider neutral conditions ($\mu_{crit} = 0$). The method described above was used to reproduce figures by Blennerhassett & Bassom (2006) and Thomas *et al.* (2011). These are shown in Figure 1.3 and Figure 1.4, respectively. Some of the curves do not cover the same extent but it is clear that there is good agreement where they overlap. This coupled with the agreement of individual eigenvalues presented in Table 1.1 suggests a valid model.

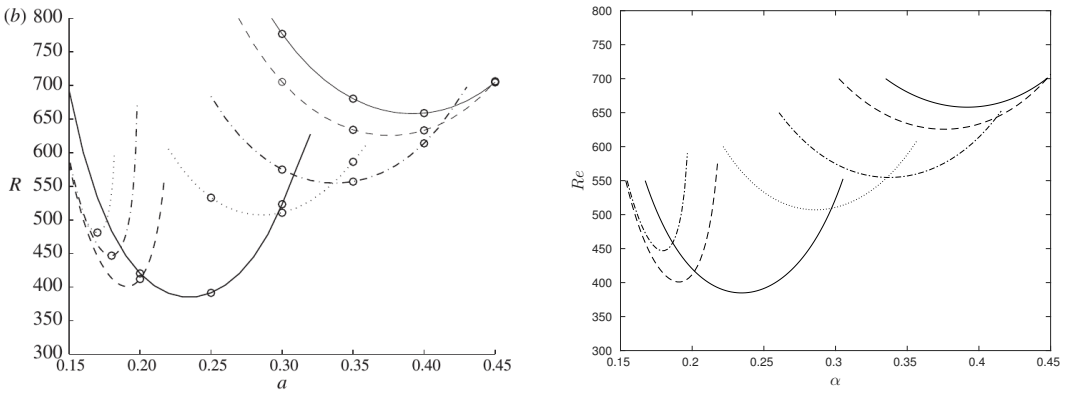

(a) *(b)*

Figure 1.4: Comparison of neutral curves found by Thomas et al. *(2011) (a) and those found in the present study (b).* $\Gamma h = 0, 0.5, 2, 5, 10, 30, 50, , \infty$ *and* $h = 6$*. The uppermost curve corresponds to* $\Gamma = 0$ *and* Γh *increases as critical conditions move to smaller wavenumbers. The curve for* $\Gamma h = \infty$ *does not appear in (b). In Thomas* et al. *(2011), the Reynolds number is denoted as R (rather than Re) and the wavenumber is denoted as a (rather than* α*).*

One feature of the curves from Blennerhassett & Bassom (2006) not observed in the reproductions is the existence of small protrusions from the neutral curve (marked as lines or crosses in Figure 1.3). This is due to a conscious decision to set δs too large to pick up on these small-scale features. However, a small investigation has confirmed the ability of the method to recognise these intriguing features which will be discussed in Section 1.4.

To more clearly show the superb agreement, Figure 1.5 shows a superposition of the two graphs in Figure 1.3 and Figure 1.4. The neutral curves of the present method are represented by lines and those of the previous studies, Blennerhassett & Bassom (2006) and Thomas *et al.* (2011), are represented by crosses. The data points of these studies were extracted from the figures using the online resource "WebPlotDigitizer" (Rohatgi, 2010) and it can clearly be seen that where the extent of the curves overlap the agreement is excellent.

The significance of this validation should not be overlooked because, although this merely shows the ability of the present eigenvalue solver to reproduce existing results, the fact that research in this area is still so recent and novel means that there are few studies conducted using this method. In addition to validating the present solver, Figure 1.5 also represents an independent validation of the work of Blennerhassett & Bassom (2006) and Thomas *et al.* (2011) because, though based on the same formulation, the

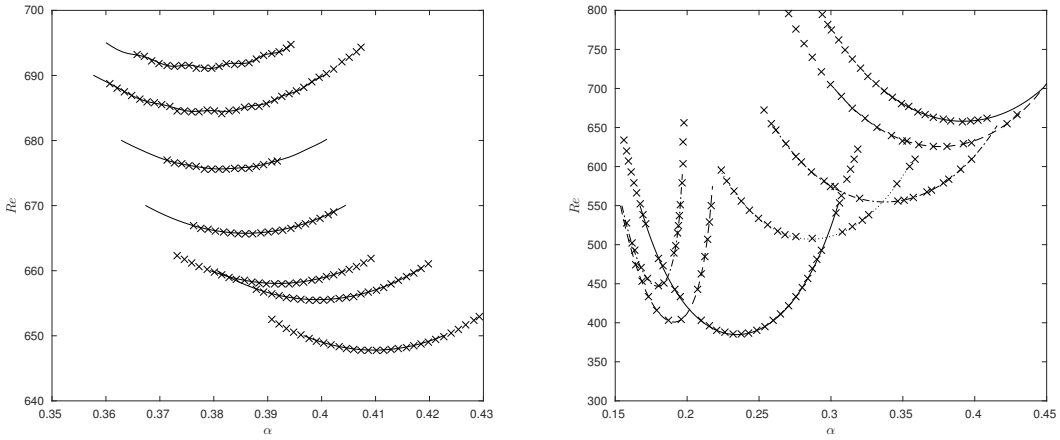

(a) *(b)*

Figure 1.5: Neutral curves generated by the present method (lines) are directly compared with data points from previous work (crosses). In (a), the neutral curves are for the finite Stokes layer with different nondimensional channel widths (see Figure 1.3). In (b), the neutral curves are for the the aligned composite flow with $h = 6$ and different choices of Γh (see Figure 1.4). Data is extracted from the original papers by the "WebPlotDigitizer" (Rohatgi, 2010).

present solver was developed entirely independently of those against which it is compared. Although there have been other studies using a similar formulation (Atobe, 2014) this approach remains largely unexplored so this validation against previous results is non-trivial and the extent of the agreement is extremely gratifying.

Note that there are several studies on pulsate flow in channels (Pier & Schmid, 2017; Tsigklifis & Lucey, 2017) that utilise this formulation and explore additional effects such as nonlinearity or compliant surfaces. These basic states utilise alternative methods of nondimensionalisation and are derived in slightly different ways but yield essentially the same flows as considered here and in Thomas *et al.* (2011).

1.4 Some results for the Semi-infinite Stokes layer

Outside of this chapter, the present study is concerned primarily with the stability of the semi-infinite Stokes layer so consider now the case with $\Gamma = 0$ and $h = 16$. These values are chosen so that there is no steady mean flow and the channel is wide enough for the flow to closely resemble the semi-infinite case, respectively.

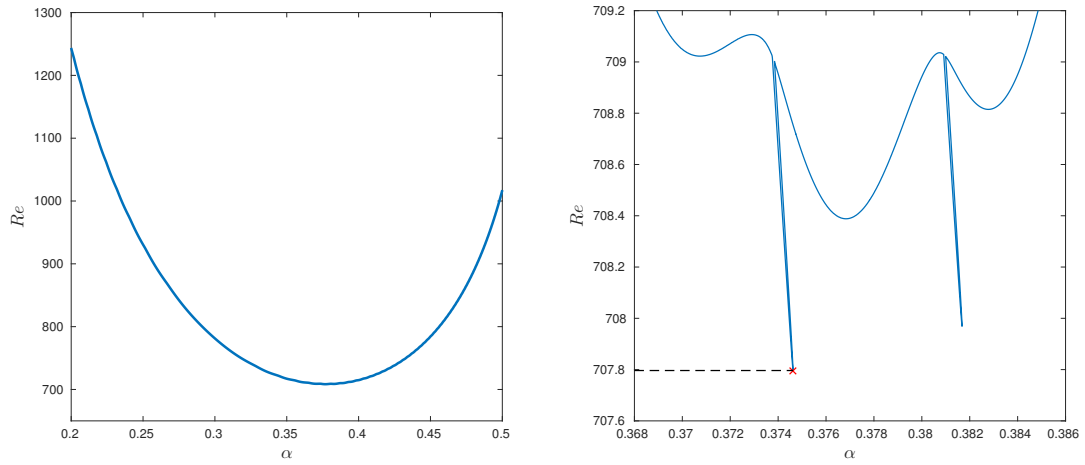

(a) *(b)*

Figure 1.6: Neutral curve for the semi-infinite Stokes layer ($h = 16$) with no mean flow ($\Gamma = 0$). The region below the curve indicates stability while that above (or inside) the curve represents instability. In (a) the curve is shown for the wavenumbers expected to be most unstable and in (b) the lowest point of this curve is shown at a smaller scale, revealing small-scale protrusions from the curve. This plot is used to identify the critical Reynolds number $Re_c = 707.796$.

1.4.1 Neutral curve

The first neutral curve for the semi-infinite Stokes layer is reported in Blennerhassett & Bassom (2002) and reproduced at two scales in Figure 1.6.

In Figure 1.6a, the curve covers wavenumbers in the region $0.2 \leq \alpha \leq 0.5$, which is where the most unstable disturbances are expected to lie. The curve was extended to marginally higher values of α but with further increases in α the eigenvalue method began to fail so this segment of the curve could not be reported with confidence. The failure of the eigenvalue problem at larger α is reported in Kong & Luo (2016) and in the present study the eigenvalues displayed a somewhat random behaviour which made it impossible to follow the curve any further. In Figure 1.6b, the lower tip of the neutral curve is shown, revealing the small-scale protrusions reported by Blennerhassett & Bassom (2002) and marked on Figure 1.3.

The critical Reynolds number calculated here of $Re_c = 707.796$ is marginally smaller than the value reported in Blennerhassett & Bassom (2002) of 707.84. This minor discrepancy appears to be due to the greater resolution used to produce Figure 1.6b than the equivalent figure in Blennerhassett & Bassom (2002), where a selection of neutral conditions appeared to be joined by straight lines, with higher resolution at the start of each

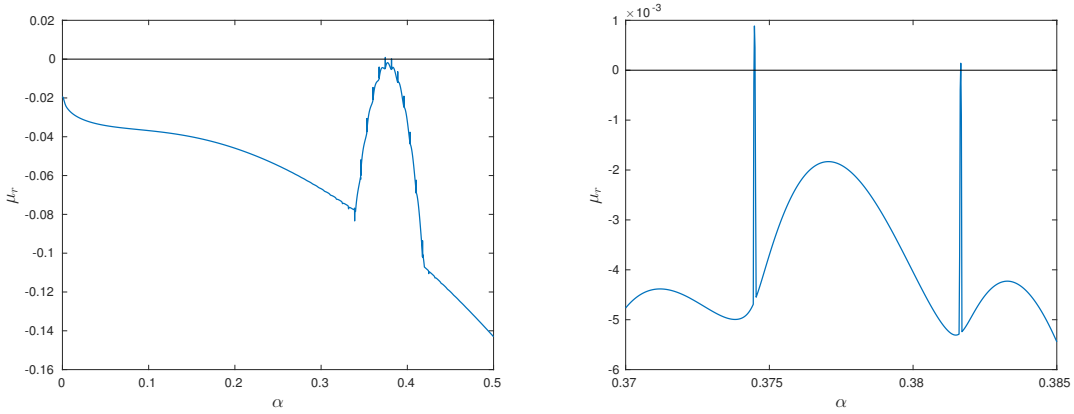

(a) *(b)*

Figure 1.7: The growth-rate μ_r corresponding to a range of α at $Re = 708$. In (a) the growth-rate is shown for $0 \leq \alpha \leq 0.5$ and in (b) the small-scale features at the tip of the curve are shown. This value of Re was chosen since it is between the tips of the neutral curve fingers at $Re_c = 707.8$ and the main body of the neutral curve above $Re = 708.4$ seen in Figure 1.6b. This reveals a growth-rate curve itself subject to small-scale protrusions. For this value of Re one finger clearly passes into the unstable region $\mu_r > 0$ and another marginally passes into this region. The main body of this curve remains in the stable region $\mu_r < 0$.

finger and relatively small resolution along the fingers themselves. This discrepancy is of little consequence for the following work since a value of Re_c given to one decimal place ($Re_c \sim 707.8$) is accurate enough for the current purposes.

1.4.2 Small-scale protrusions (fingers)

The existence of the *fingers* in Figure 1.6b shows that the current method is capable of picking up these intriguing features in the same locations as Blennerhassett & Bassom (2002), indicating that these are physical attributes rather than a numerical artefact. The critical Reynolds number of $Re_c = 707.8$ deduced from Figure 1.6b corresponds to the tip of one such finger and it is noted that for values of Re marginally greater than Re_c the only unstable modes correspond to these protrusions. This is shown in Figure 1.7, where the growth-rate μ_r is plotted against the wavenumber α for $Re = 708$. There are two fingers that protrude into the unstable region while all other modes are stable.

In order to shed some light on the formation of these protrusions, the movement of eigenvalues in the complex plane as α is increased will be considered for fixed $Re = 708$. The values of α that will be considered will be those spanning the most unstable of the two fingers shown in Figure 1.7. Eight plots are shown in Figure 1.8 that demonstrate the

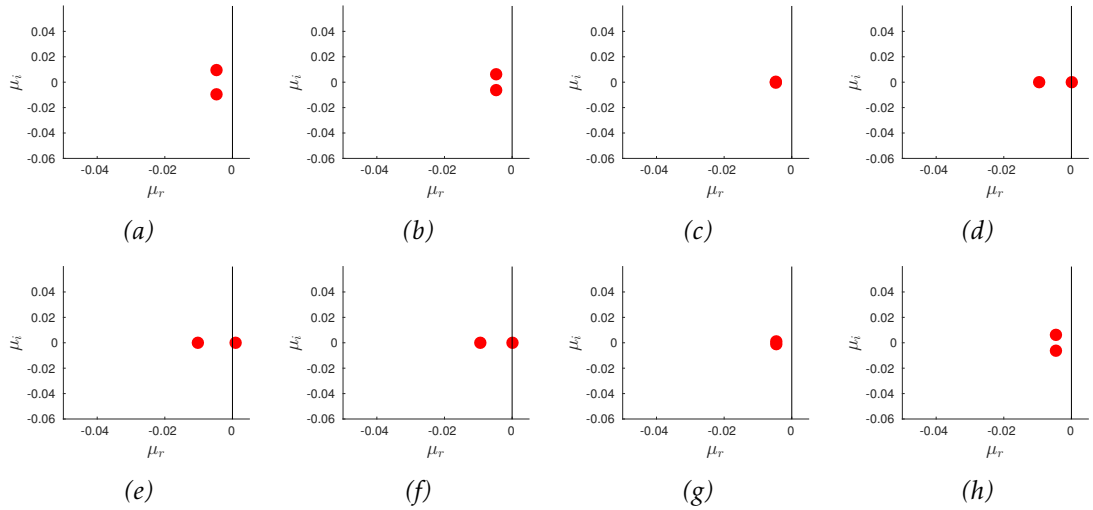

Figure 1.8: Tracing eigenvalues across the protruding finger for $Re = 708$ as α is increased. Plot (a) denotes the least stable eigenvalues at this Re when $\alpha = 0.3744047$ and for each of (b)-(h) α is incremented by 0.0000199. In (a) the complex conjugate pairs are established. These move closer to the real line in (b) and lie on top of each other in (c). This single eigenvalue then splits into two that move in opposite directions along the real line in (d) with one crossing into the unstable region $\mu_r > 0$ and achieving maximum growth in (e). These eigenvalues move closer again in (f), lie practically on top of one another in (g) and leave the real line again (in complex conjugate pairs) in (h). All axis are scaled the same and the vertical line indicates the imaginary axis. This figure is directly comparable to Figure B.2.

behaviour across the finger. These plots reveal that at the beginning of the protrusion the complex conjugate eigenvalues have collapsed into each other on the real axis. This then separates back into two eigenvalues that move in opposite directions along the real axis before moving back to a single point and breaking away from the real axis in complex conjugate pairs again. Notice that it is while the two eigenvalues move apart from one another along the real axis that the least stable of the two becomes unstable.

While these fingers are an intriguing feature of the eigenvalue problem, the three states of complex conjugate eigenvalues, repeated real eigenvalues, and two real eigenvalues are fairly generic and encountered in many settings. In Appendix B, it is shown that similar features can be reproduced in a dramatically simplified setting.

1.4.3 Eigenvector structure

The eigenvalues associated with a range of wavenumbers have been utilised to construct neutral curves, the growth-rate curve for $Re = 708$, and investigate the intriguing fingers protruding from each of these. The eigenvalues, however, provide no information on the

intracyclic behaviour of the disturbances. For completeness, the eigenvectors will now be considered.

In the steady case (described by the Orr–Sommerfeld equation), the eigenvectors found through an analogous process are the discrete representations of the wall-normal dependence of each mode. In the periodic case, the eigenvector $\boldsymbol{\phi}$, as found by the numerical method, consists of a concatenation of such spatial vectors corresponding to different harmonics. In order to derive meaning from $\boldsymbol{\phi}$ this vector must be broken up into vectors for each constituent harmonic $\boldsymbol{\psi}_n$. The temporal variation is then found by calculating

$$\boldsymbol{\psi}(\tau) = \sum_{n=-N}^{N} \boldsymbol{\psi}_n \mathrm{e}^{in\tau} \tag{1.4.1}$$

for a selection of τ with values chosen to ensure the curves are well resolved. Notice that $\boldsymbol{\psi}(\tau)$ has a periodicity of 2π. The term 'eigenvector' will generally be used to refer to $\boldsymbol{\psi}(\tau)$, being the discrete approximation to the eigenfunction $\psi(y,\tau)$, rather than the vector $\boldsymbol{\phi}$ found when solving the eigenvalue problem since $\boldsymbol{\phi}$ has little physical meaning on its own. If $\boldsymbol{\phi}$ is being referred to this will be made explicit.

In general, the eigenvectors for all Re and α considered have similar features. Consider $Re = 710$ and $\alpha = 0.38$ for demonstrative purposes. These values were chosen so that the disturbance is unstable and within a neighbourhood of the most unstable mode at this Re. An unstable mode for this α was selected and the corresponding eigenvector is investigated in Figure 1.9.

The temporal variation of $\psi(y,\tau)$ is illustrated in Figure 1.9b at a fixed wall-normal location y_0 (selected as the location of greatest magnitude when $\tau = 0$). This figure shows significant changes in amplitude across a single cycle. Such behaviour could be explored further using a frozen flow analysis to find instantaneous growth-rates. For instance, in Tsigklifis & Lucey (2017) this behaviour is explored for pulsatile flow in a compliant channel and is referred to as modal transient growth. This form of growth can theoretically result in nonlinear effects becoming significant even in flows that are asymptotically stable. Note that the linearity of the problem means that if $\psi(y,\tau)$ is an eigenfunction of the problem, then so too is any constant multiple $A\psi(y,\tau)$. When extracting the eigenvectors from the problem for Figure 1.9, the vector is therefore normalised by dividing every element by the vector magnitude.

In Figure 1.9c and Figure 1.9d the wall-normal variation of the eigenvector is shown

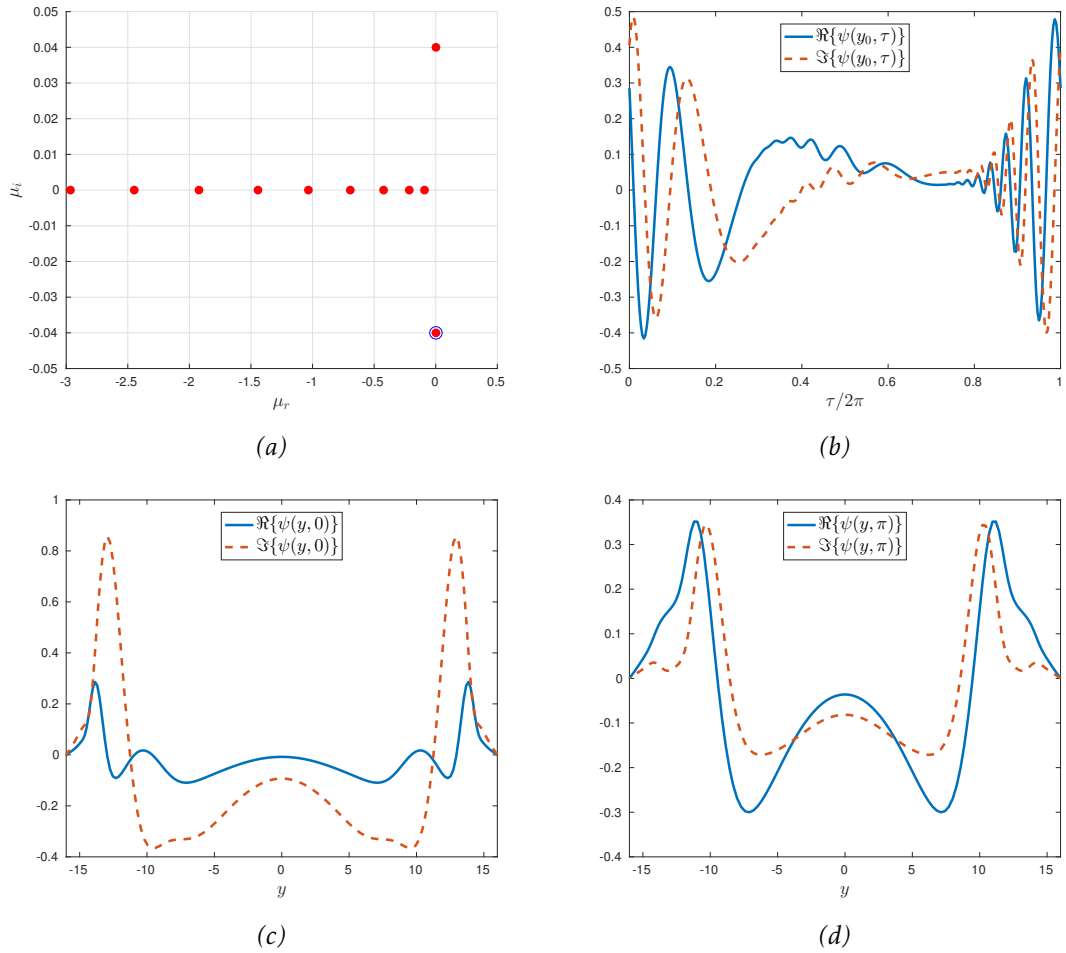

Figure 1.9: In (a) the eigenvalues for $Re = 710$ and $\alpha = 0.38$ are plotted on the complex plane with the most unstable being $\mu = 0.004884 - 0.040132i$ and indicated with a circle. The wall-normal location of maximum amplitude was found at $\tau = 0$, being $y_0 \approx -13.86$, and the variation of ψ with τ at this location is shown in (b), revealing significant growth and decay within a single period of wall motion. The spatial dependence of ψ is given for $\tau = 0$ and $\tau = \pi$ in (c) and (d), respectively. At both times, the greatest variation is near the walls and ψ has relatively low magnitude in the channel centre.

at the start ($\tau = 0$) and middle ($\tau = \pi$) of a period of wall motion. In both cases ψ has greatest amplitude and shows greatest variation near the channel walls. In both cases the magnitude at the channel centre $y = 0$ is non-zero which means that the finite configuration is still having an influence on the disturbance even though the eigenvalues remain essentially unchanged when larger channels are taken.

The form the disturbance takes will be of the periodic eigenvector multiplied by some complex number each period. This number is the Floquet multiplier $\exp(\mu 2\pi)$ and in general amplifies the eigenvector as well as performing a phase shift.

Thus concludes a brief review of the hydrodynamic stability of the semi-infinite Stokes layer. Further interpretation and insight will be provided later when the results can be directly compared against other methods.

1.5 The linear stability of 3D, unsteady, shear flows

The previous section is concerned with the stability of unsteady shear flows with motion in only one direction. In this section, the results will be generalised to include the stability of flows with motion in both the streamwise x-direction and the spanwise z-direction. In particular, it will be shown that composite flows consisting of an oscillatory component and a mean flow at some angle to it can be reduced to an aligned composite flow like that described in Section 1.2. This will reveal that the aligned case in this family of flows is subject to instability at lower Re than any unaligned case.

This section is concerned with the stability of flows that can be expressed in the form

$$\boldsymbol{U} = \Big(U_x(y,\tau), 0, U_z(y,\tau)\Big). \tag{1.5.1}$$

The derivation of the disturbance equations is similar to the two-dimensional case in Section 1.1. In particular, the Navier–Stokes equations will be nondimensionalised in the same way, implicitly assuming that there is a natural timescale from which a lengthscale can be deduced. This is a reasonable assumption since the flow is assumed to be unsteady. For a Stokes layer this lengthscale and timescale are the Stokes layer thickness (1.2.1) and the reciprocal of the frequency, respectively.

1.5.1 Three-dimensional disturbance equations

First, the disturbance equations will be derived for an unsteady flow of unspecified temporal form in a similar manner to the 2D case. Taking the nondimensional Navier–Stokes equations (1.1.4) and assuming a solution consisting of a basic state of the form (1.5.1) that satisfies (1.1.4) plus a small perturbation gives

$$\boldsymbol{u} = \boldsymbol{U} + \epsilon\Big(u_p(x,y,z,\tau), v_p(x,y,z,\tau), w_p(x,y,z,\tau)\Big), \tag{1.5.2a}$$

$$p = P + \epsilon p_p, \tag{1.5.2b}$$

where $\epsilon > 0$ is a small parameter.

The resulting equations are then linearised in ϵ, giving the following disturbance equations

$$\frac{1}{Re}\frac{\partial u_p}{\partial \tau} + U_x\frac{\partial u_p}{\partial x} + U_x' v_p + U_z\frac{\partial w_p}{\partial z} = -\frac{1}{2}\frac{\partial p_p}{\partial x} + \frac{1}{2Re}\left[\frac{\partial^2 u_p}{\partial x^2} + \frac{\partial^2 u_p}{\partial y^2} + \frac{\partial^2 u_p}{\partial z^2}\right], \tag{1.5.3a}$$

$$\frac{1}{Re}\frac{\partial v_p}{\partial \tau} + U_x\frac{\partial v_p}{\partial x} + U_z\frac{\partial v_p}{\partial z} = -\frac{1}{2}\frac{\partial p_p}{\partial y} + \frac{1}{2Re}\left[\frac{\partial^2 v_p}{\partial x^2} + \frac{\partial^2 v_p}{\partial y^2} + \frac{\partial^2 v_p}{\partial z^2}\right], \tag{1.5.3b}$$

$$\frac{1}{Re}\frac{\partial w_p}{\partial \tau} + U_x\frac{\partial w_p}{\partial x} + U_z' v_p + U_z\frac{\partial w_p}{\partial z} = -\frac{1}{2}\frac{\partial p_p}{\partial z} + \frac{1}{2Re}\left[\frac{\partial^2 w_p}{\partial x^2} + \frac{\partial^2 w_p}{\partial y^2} + \frac{\partial^2 w_p}{\partial z^2}\right], \tag{1.5.3c}$$

$$\frac{\partial u_p}{\partial x} + \frac{\partial v_p}{\partial y} + \frac{\partial w_p}{\partial z} = 0. \tag{1.5.3d}$$

Through manipulation, these can be combined into the following two equations

$$\left[\frac{1}{Re}\frac{\partial}{\partial \tau} + U_x\frac{\partial}{\partial x} + U_z\frac{\partial}{\partial z}\right]\nabla^2 v_p - \left[U_x''\frac{\partial}{\partial x} + U_z''\frac{\partial}{\partial x}\right]v_p - \frac{1}{2Re}\nabla^2\nabla^2 v_p = 0, \tag{1.5.4a}$$

$$\left[\frac{1}{Re}\frac{\partial}{\partial \tau} + U_x\frac{\partial}{\partial x} + U_z\frac{\partial}{\partial z}\right]\eta_p - \frac{1}{2Re}\nabla^2\eta_p = \left[U_x'\frac{\partial}{\partial z} - U_z'\frac{\partial}{\partial x}\right]v_p, \tag{1.5.4b}$$

where η_p is the perturbation vorticity in the y-direction as defined by (1.1.9). Assuming normal-mode solutions of the form (1.1.10) yields the three-dimensional OS equation,

$$\left[\left(\frac{\partial}{\partial \tau} + iRe\left(\alpha U_x + \beta U_z\right)\right)\left(\partial_y^2 - k^2\right) - iRe\left(\alpha U_x'' + \beta U_z''\right) - \frac{1}{2}\left(\partial_y^2 - k^2\right)^2\right]\hat{v} = 0, \tag{1.5.5}$$

and the three-dimensional Squire equation,

$$\left[\frac{\partial}{\partial \tau} + iRe\left(\alpha U_x + \beta U_z\right) - \frac{1}{2}\left(\partial_y^2 - k^2\right)\right]\hat{\eta} = i\left(\beta U_x' - \alpha U_z'\right)\hat{v}, \tag{1.5.6}$$

where $k = \sqrt{\alpha^2 + \beta^2}$. Note that these equations are described as three-dimensional due to the 3D basic state whereas in Section 1.1 references to three-dimensionality were with regards to the disturbance. In this section, the 2D problem is that concerned with both a 2D basic state and a 2D disturbance (since Squires theorem applies) whereas the 3D problem is that concerned with both a 3D basic state and a 3D disturbance.

The boundary conditions again come from no-penetration, no-slip and that the disturbance decays in the free-stream if the geometry of the flow is not bounded (as for the 2D case in Section 1.1).

Since $\hat{v}$ appears in (1.5.6) but $\hat{\eta}$ is absent from (1.5.5), the solutions can again be decomposed into two families: OS modes ($v \neq 0$) satisfy (1.5.6) and force a solution to (1.5.6) while Squire modes ($v = 0$) satisfy the homogeneous form of the 3D Squire equation

$$\left[\frac{\partial}{\partial \tau} + iRe\,(\alpha\, U_x + \beta\, U_z) - \frac{1}{2}\left(\partial_y^2 - k^2\right)\right]\hat{\eta} = 0. \tag{1.5.7}$$

For better comparison with the 2D case, it is useful to rewrite α and β in terms of k. This can be done by defining the wavevector in the (x,z)-plane

$$\boldsymbol{\alpha} = (\alpha, \beta). \tag{1.5.8}$$

Then, letting θ be the angle between $\boldsymbol{\alpha}$ and the x-direction, through simple trigonometry the following identities must hold

$$\theta = \arctan\left(\frac{\beta}{\alpha}\right), \tag{1.5.9a}$$

$$\alpha = k\cos(\theta), \tag{1.5.9b}$$

$$\beta = k\sin(\theta). \tag{1.5.9c}$$

Using (1.5.9a) to define θ and (1.5.9b), (1.5.9c) in the three-dimensional OS equation (1.5.5) yields

$$\left[\left(\frac{\partial}{\partial \tau} + ikRe\mathcal{U}\right)\left(\partial_y^2 - k^2\right) - ikRe\mathcal{U}'' - \frac{1}{2}\left(\partial_y^2 - k^2\right)^2\right]v = 0, \tag{1.5.10}$$

where $\hat{v}$ has been replaced with v for convenience and

$$\mathcal{U} = U_x\cos\theta + U_z\sin\theta. \tag{1.5.11}$$

This can be compared with the 2D equation (1.1.13) and the similarities are clear; both are identical when $U_x \to \mathcal{U}$ and $\alpha \to k$. Thus, the three-dimensional OS modes governed by (1.5.5) can be investigated by considering only the OS modes of the 2D velocity profile $\mathcal{U}$, which can be physically interpreted as the 3D flow resolved along the wavevector (α, β).

Similarly, if the relations (1.5.9b), (1.5.9c) are used in the homogeneous Squire equation (1.5.7) and the definition of $\mathcal{U}$ (1.5.11) is used, the homogeneous Squire equation

becomes

$$\left[\frac{\partial}{\partial\tau} + ikRe\mathcal{U} - \frac{1}{2}\left(\partial_y^2 - k^2\right)\right]\hat{\eta} = 0. \tag{1.5.12}$$

This equation describes the behaviour of all disturbances for which $\hat{v} = 0$ and is identical to the homogeneous Squire equation for 2D flows (1.1.24) when it is applied to $\mathcal{U}$. It has been shown that all solutions to (1.1.24) are damped, so it follows that all solutions to (1.5.12) are damped. The stability of a 3D flow is therefore described entirely by (1.5.10).

1.5.2 Linear stability of unaligned composite flows

Consider a flow consisting of an oscillatory flow modified by a mean flow at some angle to it (3D, unaligned composite flow). The established results can be used to construct an equivalence between the 3D and 2D cases. Let $U_s(y,\tau)$ and $U_b(y)$ be the velocity profiles of each component, respectively. Let U_s be aligned with the x-direction and U_b be at an angle ϕ from it. The basic state $\boldsymbol{U}$ can then be written as

$$\boldsymbol{U} = (U_s + U_b\cos\phi, 0, U_b\sin\phi), \tag{1.5.13}$$

which, after trigonometric manipulation, gives the following expression for the composite velocity profile that appears in (1.5.10)

$$\mathcal{U} = U_s\cos\theta + U_b\cos(\phi - \theta). \tag{1.5.14}$$

The basic state consists of two flows, each with their own natural scalings. If each flow component is taken separately, the following Reynolds numbers can be defined

$$Re_s = \frac{U_{s,0}}{\sqrt{2\nu\omega}} \quad \text{and} \quad Re_b = \frac{U_{b,0}l}{\nu}, \tag{1.5.15}$$

where l is the lengthscale of the steady flow component and $U_{s,0}$, $U_{b,0}$ are the velocity-scales associated with each component. The notation is the same as in Section 1.2 but no geometry has yet been settled on while also recalling the difficulties that arise if U_b is not truly parallel.

As for the case of aligned composite flow, the characteristic timescale and lengthscale used to nondimensionalise this problem will be those associated with the oscillatory flow component, namely the reciprocal of the oscillation frequency $1/\omega$ and the Stokes layer

thickness δ_s, respectively. Remember that scaling lengths with δ_s introduces the parameter $h = l/\delta_s$ (the ratio of the lengthscales of each flow).

In this setting, the choice of velocity scale is not immediately apparent so the amplitude of oscillation $U_{s,0}$ will be used. This approach is also appropriate for aligned composite flow but was not used above for consistency with Thomas *et al.* (2011). Using this velocity scale gives

$$U_s(y,\tau) = g(y,\tau), \tag{1.5.16a}$$

$$U_b(y) = \frac{U_{b,0}}{U_{s,0}} f(y/h), \tag{1.5.16b}$$

as the expressions for each flow component in this setting, where f and g are the nondimensional profiles of each flow component. The ratio of velocities can be rewritten in terms of the Reynolds numbers (1.5.15),

$$\begin{aligned}
\frac{U_{b,0}}{U_{s,0}} &= \frac{\nu Re_b}{\sqrt{2\nu\omega} l Re_s}, \\
&= \frac{Re_b}{l Re_s}\sqrt{\frac{\nu}{2\omega}}, \\
&= \frac{Re_b}{Re_s}\frac{\delta_s}{2l}, \quad \text{since} \quad \delta_s = \sqrt{\frac{2\nu}{\omega}}, \\
&= \frac{Re_b}{2hRe_s}.
\end{aligned}$$

The mean flow can then be rewritten as

$$U_b(y) = \frac{Re_b}{2hRe_s} f(y/h), \tag{1.5.18}$$

and thus (1.5.14) becomes

$$\mathcal{U} = g(y,\tau)\cos\theta + \frac{Re_b}{2hRe_s} f(y/h)\cos(\phi - \theta). \tag{1.5.19}$$

The stability of a 3D disturbance (with wavevector at angle θ to the x-direction) to a 3D composite flow (as defined for the current work) is therefore described by the two-dimensional OS equation

$$\left[\left(\frac{\partial}{\partial\tau} + ikRe_s\mathcal{U}\right)\left(\partial_y^2 - k^2\right) - ikRe_s\mathcal{U}'' - \frac{1}{2}\left(\partial_y^2 - k^2\right)^2\right] v = 0, \tag{1.5.20}$$

where $k = |\boldsymbol{\alpha}|$ and $\mathcal{U}$ is given by (1.5.19).

Restrictions on θ and ϕ

Consider now what restrictions can be placed on θ and ϕ without loss of generality. First, notice that letting $\cos\theta \to -\cos\theta$ in (1.5.19) is equivalent to letting $g(y,\tau) \to -g(y,\tau)$. Due to the oscillatory nature of g this in turn is equivalent to taking a time shift of half a period. Any time shift leaves the asymptotic behaviour unaltered so letting $\cos\theta \to -\cos\theta$ has no affect on the stability of the flow.

Consider the effect that $\mathcal{U} \to -\mathcal{U}$ has on the equation (1.5.20),

$$\left[\left(\frac{\partial}{\partial\tau} - ikRe_s\mathcal{U}\right)\left(\partial_y^2 - k^2\right) + ikRe_s\mathcal{U}'' - \frac{1}{2}\left(\partial_y^2 - k^2\right)^2\right]v = 0. \tag{1.5.21}$$

Notice that this equation can equivalently be interpreted as a reversal of the direction of the wavenumber k and is also the complex conjugate of (1.5.20).

Taking the complex conjugate of (1.5.21) recovers the same operator as (1.5.20), but this time applied to $\bar{v}$,

$$\left[\left(\frac{\partial}{\partial\tau} + ikRe_s\mathcal{U}\right)\left(\partial_y^2 - k^2\right) - ikRe_s\mathcal{U}'' - \frac{1}{2}\left(\partial_y^2 - k^2\right)^2\right]\bar{v} = 0, \tag{1.5.22}$$

The magnitudes of v and $\bar{v}$ will always be equal so complex conjugation (and thus changing the sign of $\mathcal{U}$ or k) does not affect the stability characteristics of the flow.

According to these arguments, for any fixed $\cos\theta$ and $\cos(\phi-\theta)$, the following cases are accounted for:

$$\mathcal{U} = \pm\left[\pm g(y,\tau)\cos\theta + \frac{Re_b}{2hRe_s}f(y/h)\cos(\phi-\theta)\right]. \tag{1.5.23}$$

It may therefore be assumed that the trigonometric terms are positive without any loss of generality so the angles can be restricted to

$$-\frac{\pi}{2} \le \phi \le \frac{\pi}{2} \quad \text{and} \quad -\frac{\pi}{2} \le \phi - \theta \le \frac{\pi}{2}.$$

Composite flow transform

Now, in analogy with Squire's theorem (Squire, 1933), a transform will be used to equate the 3D and 2D problems. Consider the 2D problem, described by (1.5.20) and (1.5.19)

when the flow components are aligned in the streamwise direction ($\phi = 0$) and the wavevector is also in this direction ($\theta = 0$),

$$\left[\left(\frac{\partial}{\partial\tau} + i\tilde{\alpha}\widetilde{Re}_s\widetilde{U}\right)\left(\partial_y^2 - k^2\right) - i\tilde{\alpha}\widetilde{Re}_s\widetilde{U}'' - \frac{1}{2}\left(\partial_y^2 - \tilde{\alpha}^2\right)^2\right]\tilde{v} = 0, \tag{1.5.24}$$

where the wavevector $\tilde{\boldsymbol{\alpha}} = (\tilde{\alpha}, 0)$ and

$$\widetilde{U} = g(y,\tau) + \frac{\widetilde{Re}_b}{2h\widetilde{Re}_s} f(y/h). \tag{1.5.25}$$

The general case (1.5.20) is completely equivalent to (1.5.24) (i.e. $v = \tilde{v}$) when the following relationships hold:

$$Re_s\mathcal{U} = \widetilde{Re}_s\widetilde{U}, \tag{1.5.26a}$$

$$k = \tilde{\alpha}. \tag{1.5.26b}$$

By comparing the expressions for $\mathcal{U}$ and $\widetilde{U}$, (1.5.26a) yields

$$\widetilde{Re}_s = Re_s\cos\theta, \tag{1.5.27a}$$

$$\widetilde{Re}_b = Re_b\cos(\phi - \theta). \tag{1.5.27b}$$

It can therefore be concluded that $Re_s \geq \widetilde{Re}_s$ and $Re_b \geq \widetilde{Re}_b$ since $0 \leq \cos\theta, \cos(\phi - \theta) \leq 1$. Also, equality only holds when $\theta = \phi = 0$ so the lowest values of both Re_s and Re_b correspond to the aligned case. This means that any solution to the unaligned problem can be recast as an equivalent solution to the aligned problem with lower Reynolds numbers.

This has shown that a composite flow consisting of an oscillatory component and a steady mean flow can always be reduced to the case in which both flow components are aligned in the same direction, as is the wavevector $\boldsymbol{\alpha}$. Therefore, finding neutral conditions for the two-dimensional case as in Thomas *et al.* (2011) provides neutral conditions for the entire family of composite flows. Note that this result can easily be extended to other 3D flows. For instance, by letting both U_s and U_b have an oscillatory temporal variation, the stability of the flow generated above a plate moving in elliptic or circular paths can be reduced to a 2D problem (Blennerhassett & Bassom, 2007).

If a particular member of this family of flows is considered (by fixing $\phi \neq 0$), the sta-

bility analysis can be performed by resolving the problem in the direction of the wavevector (i.e. angle θ from the x-direction) and performing a 2D stability analysis in this direction. The flow resolved in this direction will be of the form of an aligned composite flow (already discussed) with both Reynolds numbers (Re_b and Re_s) strictly smaller than those in the original setting.

Summary

This Chapter has been concerned with the derivation and numerical solution of the equations describing disturbance evolution in a time-periodic flow. The disturbance equations were derived starting with a two-dimensional flow with general time-dependence in Section 1.1. It was shown that Squire's theorem holds for such flows, meaning that the onset of instability can be explored by considering only two-dimensional disturbances.

Taking the special case of temporally periodic flows, the Floquet approach and numerical methods were illustrated for the finite Stokes layer in Section 1.2. The results were compared against those of Blennerhassett & Bassom (2006) with excellent agreement. The same approach was then applied to a composite flow consisting of steady and oscillatory components aligned in the same direction.

In Section 1.3, the means by which neutral curves could be constructed by arclength continuation was described and by plotting such curves in several cases further comparison was made against existing results (Blennerhassett & Bassom, 2002; Thomas *et al.* , 2011). Some results were discussed for the semi-infinite Stokes layer with no mean flow in Section 1.4. In particular, the finger-like features were highlighted and discussed.

In Section 1.5, the problem was generalised to unaligned composite flows utilising a result analogous to Squire's theorem. It was shown that any unaligned composite flow can be transformed to an aligned case at lower Reynolds numbers so the 2D problem is subject to instability at lower Re than the 3D problem.

Chapter 2

Numerical methods for the linear simulation of disturbance evolution

Introduction

As with the study of other flows, the study of a periodic flow benefits from linear simulation of the governing equations in addition to the solution of the stability equations described above. Comparison of these methods allows for validation and for further insight into the disturbance evolution. To this end Thomas *et al.* (2011) directly compared Floquet and simulation results in the case of a single wavenumber. Additionally, Thomas *et al.* (2014) investigated the details of wavepacket evolution for a better understanding of how the Floquet theory of Blennerhassett & Bassom (2002) relates to experimental observations.

In this chapter, the code originally designed by Togneri (2011) (Togneri & Davies, 2011) and further developed by Duval (2012) is adapted for application to the Stokes layer. Originally designed for a linear, deterministic model of sublayer streak formation in a turbulent boundary layer, the code has been modified for the different demands of this flow. One feature of the original code left unchanged is the semi-infinite wall-normal domain, so comparison with the stability analysis will be for a channel with nondimensional half-width $h = 16$ which is expected to give indistinguishable results. There will also be no mean flow because, as discussed earlier, this breaks down the relationship between the wide channel and the semi-infinite cases.

Adapting the code for the oscillatory Stokes layer should be relatively straightfor-

ward, but there are certain issues that arise in such a configuration. For instance, the flow no longer has a well-defined upstream and downstream since the fluid moves equally in both directions over a period. This means that disturbances can be found in both streamwise directions of the initial excitation. The effect of this is that a very large streamwise domain is needed so as to avoid the computationally enforced boundary conditions infiltrating the region of interest. In order to keep the dynamics well resolved, this large domain requires many points, making this problem much larger than for steady boundary layers.

For a direct comparison with Floquet theory the problem will first be formulated for a fixed wavenumber α in Section 2.2. The problem in which the basic state responds to an impulse that is localised in space will then be formulated in both wavenumber space (spectral method, Section 2.3) and in physical space (finite-difference method, Section 2.4). Comparison of results will be presented in Chapter 3.

2.1 Governing equations

Following from Chapter 1, it will immediately be assumed that time will be scaled with the frequency of oscillation (giving the nondimensional time $\tau = \omega t$) and all lengths will be scaled using the Stokes layer thickness defined in (1.2.1). Velocities are scaled using U_0 which is the amplitude of oscillation. Solving the (nondimensional) Navier–Stokes equations with oscillatory boundary condition $U_S(0,\tau) = \cos(\tau)$ gives a nondimensional analytic solution for the semi-infinite Stokes layer

$$\boldsymbol{U}_S(y,\tau) = \Big(U_S(y,\tau), 0\Big) = \Big(\mathrm{e}^{-y}\cos(\tau - y), 0\Big), \tag{2.1.1}$$

where y is the wall-normal co-ordinate.

The evolution of 2D perturbations to this flow are considered, i.e. the flow is taken to have the form

$$\boldsymbol{U} = (U_S, 0) + (u, v). \tag{2.1.2}$$

The perturbation quantities u and v will be found using the velocity-vorticity formulation devised by Davies & Carpenter (2001). The problem will be discretised in space using compact finite-difference schemes as described by Lele (1992) and temporally using an Adams-Bashforth predictor-corrector scheme. The following derivatives of U_S

will be important:

$$U_S = \mathrm{e}^{-y}\cos(\tau - y), \tag{2.1.3a}$$

$$U_S' = \mathrm{e}^{-y}\left(\sin(\tau - y) - \cos(\tau - y)\right), \tag{2.1.3b}$$

$$U_S'' = -2\mathrm{e}^{-y}\sin(\tau - y), \tag{2.1.3c}$$

where $'$ denotes differentiation with respect to y.

Following Davies & Carpenter (2001), begin with the nondimensional Navier–Stokes equations coupled with the incompressibility condition, as seen in (1.1.4),

$$\frac{\partial \boldsymbol{U}}{\partial \tau} + Re\,\boldsymbol{U}\cdot\nabla\boldsymbol{U} = \frac{1}{2}\left[-\nabla P + \Delta\boldsymbol{U}\right], \tag{2.1.4a}$$

$$\nabla\cdot\boldsymbol{U} = 0. \tag{2.1.4b}$$

The curl of these equations is then taken, utilising the properties

$$\nabla\cdot\boldsymbol{U} = 0, \tag{2.1.5a}$$

$$\nabla\cdot\boldsymbol{\Omega} = 0, \tag{2.1.5b}$$

$$\boldsymbol{\Omega} = \nabla\times\boldsymbol{U} \Rightarrow \Delta\boldsymbol{U} = -\nabla\times\boldsymbol{\Omega}. \tag{2.1.5c}$$

Here, (2.1.5a) is the incompressibility condition, (2.1.5b) is the solenoidal property of vorticity, and (2.1.5c) is the definition of vorticity followed by the curl of this definition.

The equations governing disturbance evolution can be manipulated using these conditions to deduce a velocity-vorticity formulation as discussed in detail in Davies & Carpenter (2001). Only the two-dimensional problem is of interest here, but a brief overview of this formulation in three dimensions will be given.

First, the six solution variables (three velocity components and three vorticity components) are categorised into *primary variables* and *secondary variables*. The governing equations are then recast in terms of the primary variables. This results in two vorticity transport equations (one in each of the two directions parallel to the wall) and an equation for the wall-normal velocity. The vorticity transport equations are found by taking the curl of (2.1.4a) and projecting this equation along the x and z directions. The equation for the wall-normal velocity v is found from the condition (2.1.5c). In this way

the Navier–Stokes equations are recast as three equations for the three primary variables. The secondary variables can then be calculated from the primary variables whenever they are of specific interest.

In Thomas *et al.* (2014) the same method is applied in two dimensions. In this case the primary variables are the single component of vorticity

$$\zeta = \frac{\partial u}{\partial y} - \frac{\partial v}{\partial x}, \tag{2.1.6}$$

and the wall-normal velocity v. The only secondary variable in the two dimensional formulation is the streamwise velocity u. The evolution of these variables can then be described by a vorticity transport equation for ζ and a Poisson equation in v. The secondary variable u can be calculated from these whenever it is of interest. The perturbation equations are manipulated in this manner to yield

$$\frac{1}{Re}\frac{\partial \zeta}{\partial \tau} + U_S\frac{\partial \zeta}{\partial x} + U_S''v = \frac{1}{2Re}\left(\frac{\partial^2}{\partial x^2} + \frac{\partial^2}{\partial y^2}\right)\zeta, \tag{2.1.7a}$$

$$\left(\frac{\partial^2}{\partial x^2} + \frac{\partial^2}{\partial y^2}\right)v = -\frac{\partial \zeta}{\partial x}, \tag{2.1.7b}$$

$$u = -\int_y^\infty \left(\zeta + \frac{\partial v}{\partial x}\right)\mathrm{d}y, \tag{2.1.7c}$$

where nonlinear terms, i.e. those with u, v or ζ multiplied by one another, have been neglected. The derivation of these governing equations has been brief so the interested reader is directed to Davies & Carpenter (2001) for a more detailed derivation and the evidence that this formulation is completely equivalent to the Navier–Stokes equations once the boundary conditions are incorporated appropriately.

These partial differential equations require boundary conditions in the wall-normal y-direction which are usually dictated by no-slip and no-penetration (as described in Section 1.1). Exactly how these conditions appear in this formulation will be considered later. It will also be assumed that, for any variable f, $\lim_{y\to\infty} f = 0$. That is the disturbance does not extend infinitely far from the wall. Note that it is implicit in the derivation of (2.1.7c) that this condition holds for u. For the finite-difference formulation, boundary conditions in the streamwise x-direction are also required and will be discussed later.

Since disturbances decay in the far-field, the semi-infinite domain $y \in [0, \infty)$ can con-

veniently be mapped to a finite domain $\xi \in [0,1]$ by the transform

$$\xi = \frac{l}{y+l}. \tag{2.1.8}$$

The stretching factor l is chosen so that there are enough points near the wall ($\xi = 1$) to fully resolve the disturbance and enough points as $\xi \to 0$ to resolve the decay of the disturbance in this limit. Notice that this transform reverses the direction of the domain with $y = 0$ corresponding to $\xi = 1$ and $y \to \infty$ equivalent to $\xi \to 0$.

Derivatives and integrals of any variable f along the wall-normal direction can thus be written with respect to the transformed co-ordinate,

$$\frac{\partial f}{\partial y} = -\frac{\xi^2}{l}\frac{\partial f}{\partial \xi}, \tag{2.1.9a}$$

$$\frac{\partial^2 f}{\partial y^2} = \frac{\xi^4}{l^2}\frac{\partial^2 f}{\partial \xi^2} + \frac{2\xi^3}{l^2}\frac{\partial f}{\partial \xi}, \tag{2.1.9b}$$

$$\int_0^\infty f \,\mathrm{d}y = l\int_0^\infty \frac{f}{\xi^2}\,\mathrm{d}\xi. \tag{2.1.9c}$$

2.2 Single wavenumber simulation

Before considering a spatially localised excitation to the flow described above, a Fourier decomposition in the streamwise x-direction will be made. The reasons for this simplification are:

- The consideration of a single wavenumber in isolation is directly comparable to the Floquet analysis of Chapter 1.
- The computational time taken is drastically reduced by the removal of the streamwise extent of the domain.
- Problems can arise from the inlet/outlet conditions in the streamwise domain. This often quite delicate consideration is absent from the single wavenumber problem.
- By decomposing the impulse into Fourier modes, a selection of single-wavenumber solutions can be weighted and reassembled for a full spatial description. More detail of this will be given in Section 2.3.

2.2.1 Problem formulation

As with the normal-mode assumption made in Section 1.1, it will be assumed that the disturbance has streamwise wavenumber α so $\partial/\partial x \to i\alpha$. The governing equations (2.1.7) then become

$$\frac{1}{Re}\frac{\partial \zeta}{\partial \tau} + i\alpha U_S \zeta + U_S'' v = \frac{1}{2Re}\left(\frac{\partial^2}{\partial y^2} - \alpha^2\right)\zeta, \tag{2.2.1a}$$

$$\left(\frac{\partial^2}{\partial y^2} - \alpha^2\right) v = -i\alpha\zeta, \tag{2.2.1b}$$

$$u = -\int_y^\infty (\zeta + i\alpha v)\,\mathrm{d}y. \tag{2.2.1c}$$

The vorticity transport equation (2.2.1a) and the Poisson equation (2.2.1b) are solved for ζ and v, respectively, while u only needs calculating if it is of specific interest so can be thought of as a secondary variable.

The variables ζ, u and v are all subject to the condition that

$$\lim_{y\to\infty} \zeta(y,\tau), u(y,\tau), v(y,\tau) = 0, \quad \forall \tau. \tag{2.2.2}$$

This is already implicit in the definition of u given in (2.2.1c) and in (2.1.7c).

Conditions at the wall are given by the no-slip and no-penetration conditions as the wall undergoes a small localised vertical displacement $\eta(\tau)$ used to excite the flow. When linearised about the undisplaced wall location, these conditions take the form

$$u(0,\tau) = -U_S'(0,\tau)\eta(\tau), \tag{2.2.3a}$$

$$v(0,\tau) = \frac{\partial \eta}{\partial \tau}(\tau). \tag{2.2.3b}$$

The conditions required on η are that $\eta(0) = 0$ so that the excitation can be gently ramped up from the unperturbed flow, and that the impulse lasts for only a small time. Taking these considerations into account, η is chosen to take the form

$$\eta(\tau) = A(1 - \mathrm{e}^{-\sigma\tau^2})\mathrm{e}^{-\sigma\tau^2}, \tag{2.2.4a}$$

$$\frac{\partial \eta}{\partial \tau}(\tau) = 2\sigma\tau A(2\mathrm{e}^{-\sigma\tau^2} - 1)\mathrm{e}^{-\sigma\tau^2}, \tag{2.2.4b}$$

where A is some (non-zero) measure of amplitude, and σ describes the temporal spread

of η. Following Thomas *et al.* (2014), σ is to be chosen so that the impulse is significant for less than one twentieth of a period. Since η can be thought of as only being significant during the time interval $\tau = 1/\sqrt{\sigma}$ we will choose $\sigma \approx 10$. Generally $A = 1$ will be taken since the problem is linear so different choices of A do not change the disturbance characteristics.

Since the vorticity ζ is the subject of the transport equation (2.2.1a), the no-slip condition will have to be imposed as a vorticity condition. By letting $y \to 0$ in the equation for u (2.2.1c) and using the boundary condition (2.2.3a) to evaluate u at the wall, the integral constraint

$$\int_0^\infty \zeta \, \mathrm{d}y = U_S'(0,\tau)\eta(\tau) - i\alpha \int_0^\infty v \, \mathrm{d}y \tag{2.2.5}$$

is introduced. This is fully equivalent to the no-slip condition on u and provides closure for solving (2.2.1a).

2.2.2 Numerical method

Spatial schemes

Presented below is an overview of the spatial schemes used in the wall-normal direction, as derived by Togneri (2011). The wall-normal direction is currently the only spatial dimension and only the second y-derivative appears in the governing equations. The wall-normal co-ordinate will be discretised into K nodes, evenly spaced in ξ, and the second y-derivative will be approximated using a stencil of three adjacent points.

The usual stencils (Lele, 1992; Togneri, 2011) can be used to derive discrete approximations of derivatives with respect to ξ. The relationship between ξ and y (2.1.8) and their derivatives (2.1.9) can be used to derive the following fourth order scheme

$$\frac{1}{10}\left[\frac{f_{k+1}''}{(k+1)^3} + \frac{f_{k-1}''}{(k-1)^3}\right] + \frac{f_k''}{k^3} = \frac{6\Delta\xi^2}{5l^2}\left[(k-1)f_{k-1} - 2kf_k + (k+1)f_{k+1}\right] + O(\Delta\xi^4), \tag{2.2.6}$$

where f_k denotes any of the variables evaluated at node k and f_k'' denotes the second y-derivative in the same location. Recalling the reversal of the domain under the mapping (2.1.8), f_0 is the variable evaluated in the limit $y \to \infty$ while f_K is the value of the variable at the wall $y = 0$. The scheme for evenly spaced nodes from which this is derived is given later in Section 2.4 and the transformation into the semi-infinite domain is described fully by Togneri (2011).

A scheme by which the integral of a variable over the entire spatial domain can be computed is also required. Consider the following scheme for evenly spaced nodes,

$$\frac{f_1 - f_0}{\Delta\xi} = \frac{1}{24}\left[9\dot{f}_0 + 19\dot{f}_1 - 5\dot{f}_2 + \dot{f}_3\right] + O(\Delta\xi^4), \tag{2.2.7a}$$

$$\frac{f_{k+1} - f_k}{\Delta\xi} = \frac{1}{24}\left[-\dot{f}_{k-1} + 13\dot{f}_k + 13\dot{f}_{k+1} - \dot{f}_{k+2}\right] + O(\Delta\xi^4), \tag{2.2.7b}$$

$$\frac{f_K - f_{K-1}}{\Delta\xi} = \frac{1}{24}\left[9\dot{f}_K + 19\dot{f}_{K-1} - 5\dot{f}_{K-2} + \dot{f}_{K-3}\right] + O(\Delta\xi^4), \tag{2.2.7c}$$

where $\dot{}$ is used to denote differentiation with respect to ξ. This is equivalent to the integral scheme

$$\int_{\xi_0}^{\xi_1} f \,\mathrm{d}\xi = \frac{1}{24\Delta\xi}\left[9f_0 + 19f_1 - 5f_2 + f_3\right] + O(\Delta\xi^4), \tag{2.2.8a}$$

$$\int_{\xi_k}^{\xi_{k+1}} f \,\mathrm{d}\xi = \frac{1}{24\Delta\xi}\left[-f_{k-1} + 13f_k + 13f_{k+1} - f_{k+2}\right] + O(\Delta\xi^4), \tag{2.2.8b}$$

$$\int_{\xi_{K-1}}^{\xi_K} f \,\mathrm{d}\xi = \frac{1}{24}\left[9f_K + 19f_{K-1} - 5f_{K-2} + f_{K-3}\right] + O(\Delta\xi^4). \tag{2.2.8c}$$

The integral across the y domain of some function g can be written in terms of ξ using (2.1.9),

$$\int_z^\infty g(y)\,\mathrm{d}y = \int_0^\xi \frac{l g(\xi)}{\xi^2}\,\mathrm{d}\xi =: G(\xi). \tag{2.2.9}$$

Integration over the entire domain is therefore given by $G(1)$ or G_K, which can be written as

$$G_K = (G_K - G_{K-1}) + (G_{K-1} - G_{K-2}) + \ldots + (G_{k+1} - G_k) + \ldots + (G_1 - G_0). \tag{2.2.10}$$

Using the definition of G,

$$G_{k+1} - G_k = \int_{\xi_k}^{\xi_{k+1}} \frac{l g(\xi)}{\xi^2}\,\mathrm{d}\xi, \tag{2.2.11}$$

so the integration scheme (2.2.8) can be used to approximate $G_{k+1} - G_k$ for each k in terms of g. These can be summed to give

$$\begin{aligned} G_K = \frac{l}{24\Delta\xi}\left[9\frac{g_K}{K^2} + 19\frac{g_{K-1}}{(K-1)^2} - 5\frac{g_{K-2}}{(K-2)^2} + \frac{g_{K-3}}{(K-3)^2}\right] + \\ \frac{l}{24\Delta\xi}\left[-\frac{g_K}{K^2} + 13\frac{g_{K-1}}{(K-1)^2} + 13\frac{g_{K-2}}{(K-2)^2} - \frac{g_{K-3}}{(K-3)^2}\right] + \ldots \\ + \frac{l}{24\Delta\xi}\left[\frac{g_3}{9} - 5\frac{g_2}{4} + 19g_1\right]. \end{aligned} \tag{2.2.12}$$

Finally, collecting coefficients of each g_k gives

$$G(1) = \sum_{k=1}^{K} d_k g_k, \tag{2.2.13}$$

where

$$d_1 = \frac{31l}{24\Delta\xi}, \tag{2.2.14a}$$
$$d_2 = \frac{5l}{24\Delta\xi}, \tag{2.2.14b}$$
$$d_3 = \frac{25l}{216\Delta\xi}, \tag{2.2.14c}$$
$$d_k = \frac{1}{k^2\Delta\xi}, \quad \text{for } k = 4,\ldots,K-4, \tag{2.2.14d}$$
$$d_{K-3} = \frac{25l}{24(K-3)^2\Delta\xi}, \tag{2.2.14e}$$
$$d_{K-2} = \frac{5l}{6(K-2)^2\Delta\xi}, \tag{2.2.14f}$$
$$d_{K-1} = \frac{31l}{24(K-1)^2\Delta\xi}, \tag{2.2.14g}$$
$$d_K = \frac{l}{3K^2\Delta\xi}. \tag{2.2.14h}$$

Thus concludes the description of the relevant spatial schemes. This is an overview and the interested reader is directed to Duval (2012) and Togneri (2011) for more details.

Poisson equation

The vorticity transport equation (2.2.1a) is the first to be solved at each time-step but the methods of solving both (2.2.1a) and (2.2.1b) are strongly related and it is more straightforward to solve the Poisson equation (2.2.1b). For this reason, the method of solving the Poisson equation will be described first so that the approach taken can then be adapted for the vorticity transport equation.

Consider the Poisson equation (2.2.1b). This equation holds at every spatial location, so at the k^{th} node we can write

$$v_k'' - \alpha^2 v_k = -i\alpha\zeta_k \tag{2.2.15}$$

and, since the VTE is solved first, ζ_k is known for all k. Note that the Poisson operator has no time dependence so it is not necessary to label the time-step as all variables

correspond to the same time instance.

Take this equation at three adjacent nodes. With reference to the left-hand side of (2.2.6), a linear combination of these is taken, giving

$$\frac{1}{10}\left[\frac{v''_{k+1}}{(k+1)^3}+\frac{v''_{k-1}}{(k-1)^3}\right]+\frac{v''_k}{k^3}-\alpha^2\left[\frac{1}{10}\left(\frac{v_{k+1}}{(k+1)^3}+\frac{v_{k-1}}{(k-1)^3}\right)+\frac{v_k}{k^3}\right] = -i\alpha\left[\frac{1}{10}\left(\frac{\zeta_{k+1}}{(k+1)^3}+\frac{\zeta_{k-1}}{(k-1)^3}\right)+\frac{\zeta_k}{k^3}\right]. \quad (2.2.16)$$

The second derivative scheme (2.2.6) can then be used to replace all terms involving the second derivative. The differential problem is then replaced by an algebraic problem, given by

$$\frac{6\Delta\xi^2}{5l^2}[(k-1)v_{k-1}-2kv_k+(k+1)v_{k+1}]-\alpha^2\left[\frac{1}{10}\left(\frac{v_{k+1}}{(k+1)^3}+\frac{v_{k-1}}{(k-1)^3}\right)+\frac{v_k}{k^3}\right] = -i\alpha\left[\frac{1}{10}\left(\frac{\zeta_{k+1}}{(k+1)^3}+\frac{\zeta_{k-1}}{(k-1)^3}\right)+\frac{\zeta_k}{k^3}\right]. \quad (2.2.17)$$

By collecting coefficients of v at each node and multiplying through by k^3, this equation can be written as

$$\left[\frac{6k^3\Delta\xi^2(k-1)}{5l^2}-\alpha^2\frac{k^3}{10(k-1)^3}\right]v_{k-1}+\left[-\frac{12k^4\Delta\xi^2}{5l^2}-\alpha^2\right]v_k+ \left[\frac{6k^3\Delta\xi^2(k+1)}{5l^2}-\alpha^2\frac{k^3}{10(k+1)^3}\right]v_{k+1}=-i\alpha\left[\frac{k^3}{10}\left(\frac{\zeta_{k+1}}{(k+1)^3}+\frac{\zeta_{k-1}}{(k-1)^3}\right)+\zeta_k\right]. \quad (2.2.18)$$

This describes the relationship between the values of v three adjacent nodes with a right-hand side that is already known from solving the vorticity transport equation. This problem can be expressed as a tridiagonal matrix problem with $v_0 = 0$ and $v_K = \partial\eta/\partial\tau$.

$$\begin{pmatrix} \epsilon_1 & \theta_1 & & & & & \\ \delta_2 & \epsilon_2 & \theta_2 & & & & \\ & \ddots & \ddots & \ddots & & & \\ & & \ddots & \ddots & \ddots & & \\ & & & \ddots & \ddots & \ddots & \\ & & & & \delta_{K-2} & \epsilon_{K-2} & \theta_{K-2} \\ & & & & & \delta_{K-1} & \epsilon_{K-1} \end{pmatrix}\begin{pmatrix} v_1 \\ v_2 \\ \vdots \\ \vdots \\ \vdots \\ v_{K-2} \\ v_{K-1} \end{pmatrix}=\begin{pmatrix} r_1 \\ r_2 \\ \vdots \\ \vdots \\ \vdots \\ r_{K-2} \\ r_{K-1} \end{pmatrix}, \quad (2.2.19)$$

where

$$\delta_k = \frac{6k^3\Delta\xi^2(k-1)}{5l^2} - \alpha^2\frac{k^3}{10(k-1)^3}, \tag{2.2.20a}$$

$$\epsilon_k = -\frac{12k^4\Delta\xi^2}{5l^2} - \alpha^2, \tag{2.2.20b}$$

$$\theta_k = \frac{6k^3\Delta\xi^2(k+1)}{5l^2} - \alpha^2\frac{k^3}{10(k+1)^3}, \tag{2.2.20c}$$

$$r_k = -i\alpha\left[\frac{k^3}{10}\left(\frac{\zeta_{k+1}}{(k+1)^3} + \frac{\zeta_{k-1}}{(k-1)^3}\right) + \zeta_k\right]. \tag{2.2.20d}$$

Notice that r_k is not well defined when $k = 1$ (due to division by zero). This is easily accounted for by remembering that $k = 0$ corresponds to $y \to \infty$ and that all variables vanish in this limit. It is thus already known that $\zeta_0 = 0$ so this term can be removed from the expression for r_1 to avoid this issue.

This system of equations can be solved by the Thomas algorithm for tridiagonal matrices, which is well documented and so not included here.

Vorticity transport equation

Consider the vorticity transport equation (2.2.1a) and rearrange so that only the derivative terms appear on the left-hand side,

$$\frac{\partial\zeta}{\partial\tau} - \frac{1}{2}\frac{\partial^2\zeta}{\partial y^2} = -\frac{\alpha^2}{2}\zeta - i\alpha ReU_S\zeta - ReU_S''v. \tag{2.2.21}$$

The terms on the left-hand side will be treated implicitly and the terms on the right-hand side explicitly. Let E be the collection of explicit terms,

$$E = -\frac{\alpha^2}{2}\zeta - i\alpha ReU_S\zeta - ReU_S''v. \tag{2.2.22}$$

Note that it would require no extra computational effort to treat the first term implicitly. However, in the full spatial formulation this is the second x-derivative so will be more suited to explicit treatment in Section 2.4. This term will therefore be treated explicitly for consistency.

Using superscripts to indicate time instance, at the n^{th} time-step the equation can be written as

$$\frac{\partial\zeta^n}{\partial\tau} - \frac{1}{2}\frac{\partial^2\zeta^n}{\partial y^2} = E^n. \tag{2.2.23}$$

This equation is solved at each time (in the manner described below), first using the linear predictor

$$E_p^n = 2E^{n-1} - E^{n-2}. \tag{2.2.24}$$

This predicted E^n is used as the right-hand side of (2.2.23) to predict the vorticity at this time-step,

$$\frac{\partial \zeta_p^n}{\partial \tau} - \frac{1}{2}\frac{\partial^2 \zeta_p^n}{\partial y^2} = E_p^n. \tag{2.2.25}$$

The predicted ζ_p^n is then used as the right-hand side to the Poisson equation (2.2.1b) to find the wall-normal velocity at this time-step, v^n. That is,

$$\frac{\partial^2 v^n}{\partial y^2} - \alpha^2 v^n = -i\alpha\zeta_p^n. \tag{2.2.26}$$

The solutions ζ_p^n and v^n can then be used to correct the explicit term,

$$E_c^n = -\frac{\alpha^2}{2}\zeta_p^n - i\alpha ReU_S\zeta_p^n - ReU_S''v^n. \tag{2.2.27}$$

Finally, the corrected vorticity is found by solving (2.2.23) with E_c^n on the right-hand side. The corrector steps can be iterated on for improved accuracy (Togneri, 2011) but in practise this is not necessary since the solution converges to the desired accuracy after a single corrector step.

The backwards temporal scheme

$$\frac{\partial \zeta^n}{\partial \tau} = \frac{3\zeta^n - 4\zeta^{n-1} + \zeta^{n-2}}{2\Delta\tau} + \mathcal{O}(\Delta\tau^2) \tag{2.2.28}$$

can now be used to approximate the time-derivative. It is convenient to write the problem as

$$\frac{3\zeta^n}{2\Delta\tau} - \frac{1}{2}\frac{\partial^2 \zeta^n}{\partial y^2} = \frac{4\zeta^{n-1} - \zeta^{n-2}}{2\Delta\tau} + E^n, \tag{2.2.29}$$

where E^n is used to refer to either the predicted (E_p^n) or corrected (E_c^n) explicit term at this time-step. The equation is written in this way so that all of the terms that are already known (based on information from previous time steps) appear on the right-hand side.

This equation is now of the same form as the Poisson equation. The scheme (2.2.6) is

used, following a similar process as before, so that the problem can be written as

$$\left[\frac{k^3}{10(k-1)^3}\frac{3}{2\Delta\tau}-\frac{3k^3\Delta\xi^2(k-1)}{5l^2}\right]\zeta_{k-1}^n+\left[\frac{3}{2\Delta\tau}+\frac{6k^4\Delta\xi^2}{5l^2}\right]\zeta_k^n+ \\ +\left[\frac{k^3}{10(k+1)^3}\frac{3}{2\Delta\tau}-\frac{3k^3\Delta\xi^2(k+1)}{5l^2}\right]\zeta_{k+1}^n=E_k^n+\frac{4\zeta_k^{n-1}-\zeta_k^{n-2}}{2\Delta\tau}+ \\ +\frac{k^3}{10(k-1)^3}\left(E_{k-1}^n+\frac{4\zeta_{k-1}^{n-1}-\zeta_{k-1}^{n-2}}{2\Delta\tau}\right)+\frac{k^3}{10(k+1)^3}\left(E_{k+1}^n+\frac{4\zeta_{k+1}^{n-1}-\zeta_{k+1}^{n-2}}{2\Delta\tau}\right). \quad (2.2.30)$$

for each spatial node k. This can be solved with the boundary condition that $\zeta_0^n = 0$ for all n (decay in the far-field) and closure is achieved using the no-slip integral constraint (2.2.5). This condition is approximated discretely by

$$\sum_{k=1}^{K} d_k\zeta_k^n=\iota^n=\left[U_S'(0,\tau)\eta\right]^n-i\alpha\sum_{k=1}^{K}d_k v_k^n, \quad (2.2.31)$$

where each d_k is given in (2.2.14).

Since ι^n requires information from every spatial location, the integral constraint will also require use of the predictor-corrector method. The first time the VTE is solved, the integral is predicted by projecting u and v to the current time step using the same linear predictor as used for E^n (2.2.24). In terms of the exact integrals this gives

$$\int_0^\infty \zeta_p^n\,\mathrm{d}y=-(2u_w^{n-1}-u_w^{n-2})-i\alpha\int_0^\infty(2v^{n-1}-v^{n-2})\,\mathrm{d}y, \quad (2.2.32)$$

where $u_w(\tau) = -U_S'(0,\tau)\eta(\tau)$ is the streamwise velocity at the wall. This can be rearranged to give

$$\int_0^\infty \zeta_p^n\,\mathrm{d}y=2\left(-u_w^{n-1}-i\alpha\int_0^\infty v^{n-1}\,\mathrm{d}y\right)-\left(-u_w^{n-2}-i\alpha\int_0^\infty v^{n-2}\,\mathrm{d}y\right), \quad (2.2.33)$$

or, since the integral condition must be satisfied at all previous time steps,

$$\int_0^\infty \zeta_p^n\,\mathrm{d}y\approx\iota_p^n \quad (2.2.34)$$

where $\iota_p^n = 2\iota^{n-1}-\iota^{n-1}$.

After the Poisson equation is solved the corrected value ι_c^n is recalculated from v. The secondary variable u does not need to be calculated since u_w is known for all times from the no-slip condition.

The linear system can now be written in the following form

$$\begin{pmatrix} d_1 & d_2 & d_3 & d_4 & \dots & d_{K-1} & d_K \\ b_1 & c_1 & & & & & \\ a_2 & b_2 & c_2 & & & & \\ & \ddots & \ddots & \ddots & & & \\ & & \ddots & \ddots & \ddots & & \\ & & & a_{K-2} & b_{K-2} & c_{K-2} & \\ & & & & a_{K-1} & b_{K-1} & c_{K-1} \end{pmatrix} \begin{pmatrix} \zeta_1 \\ \zeta_2 \\ \zeta_3 \\ \vdots \\ \vdots \\ \zeta_{K-1} \\ \zeta_K \end{pmatrix} = \begin{pmatrix} \iota^n \\ \rho_1 \\ \rho_2 \\ \vdots \\ \vdots \\ \rho_{K-2} \\ \rho_{K-1} \end{pmatrix}, \tag{2.2.35}$$

where d_k are given in (2.2.14), ι^n refers to either the predicted (ι_p^n) or corrected (ι_c^n) integral constraint, and

$$a_k = \frac{k^3}{10(k-1)^3}\frac{3}{2\Delta\tau} - \frac{3k^3\Delta\xi^2(k-1)}{5l^2}, \tag{2.2.36a}$$

$$b_k = \frac{3}{2\Delta\tau} + \frac{6k^4\Delta\xi^2}{5l^2}, \tag{2.2.36b}$$

$$c_k = \frac{k^3}{10(k+1)^3}\frac{3}{2\Delta\tau} - \frac{3k^3\Delta\xi^2(k+1)}{5l^2}, \tag{2.2.36c}$$

$$\begin{aligned} \rho_k = E_k^n + \frac{4\zeta_k^{n-1} - \zeta_k^{n-2}}{2\Delta\tau} + \\ + \frac{k^3}{10(k-1)^3}\left(E_{k-1}^n + \frac{4\zeta_{k-1}^{n-1} - \zeta_{k-1}^{n-2}}{2\Delta\tau}\right) + \frac{k^3}{10(k+1)^3}\left(E_{k+1}^n + \frac{4\zeta_{k+1}^{n-1} - \zeta_{k+1}^{n-2}}{2\Delta\tau}\right), \end{aligned} \tag{2.2.36d}$$

with E^n also referring to either the predicted or corrected value. This system can then be solved using a modified Thomas algorithm (Togneri, 2011) that is initiated with

$$\mu_1 = b_1, \tag{2.2.37a}$$

$$\delta_1 = d_1, \tag{2.2.37b}$$

$$\nu_1 = \rho_1, \tag{2.2.37c}$$

$$\iota_1 = \iota^n. \tag{2.2.37d}$$

Then, for $k = 2, 3, ..., K-1$,

$$\mu_k = b_k - c_{k-1}\frac{a_k}{\mu_{k-1}}, \tag{2.2.38a}$$

$$\delta_k = d_k - c_{k-1}\frac{\delta_{k-1}}{\mu_{k-1}}, \tag{2.2.38b}$$

$$\nu_k = \rho_k - \nu_{k-1}\frac{a_k}{\mu_{k-1}}, \tag{2.2.38c}$$

$$\iota_k = \iota_{k-1} - \nu_{k-1}\frac{\delta_{k-1}}{\mu_{k-1}}, \tag{2.2.38d}$$

which results in

$$\delta_{K-1}\zeta_{K-1} + d_K\zeta_K = \iota_{K-1}, \tag{2.2.39a}$$

$$\mu_{K-1}\zeta_{K-1} + c_{K-1}\zeta_K = \nu_{K-1}. \tag{2.2.39b}$$

By eliminating ζ_{K-1}, we get an expression for ζ_K,

$$\zeta_K = \frac{\iota_{K-1}\mu_{K-1} - \delta_{K-1}\nu_{K-1}}{d_K\mu_{K-1} - c_{K-1}\delta_{K-1}}, \tag{2.2.40}$$

from which each ζ_k can be calculated from ζ_{k+1} with

$$\zeta_k = \frac{\nu_k - c_k\zeta_{k+1}}{\mu_k}. \tag{2.2.41}$$

Thus concludes the methods used for solving the governing equations (2.2.1) for a disturbance with a fixed streamwise wavenumber. A means of interpreting the results will now be discussed.

2.2.3 Measuring the growth of disturbances

One of the benefits of considering each wavenumber in isolation is that the results can easily be compared against the eigenvalues of the stability equation (1.2.7). In fact, the formulation of these methods is fundamentally the same up until Floquet's theorem is used to express the solution variables in the form

$$f(y,\tau) = e^{\mu\tau}p(y,\tau), \tag{2.2.42}$$

where p is 2π-periodic in τ and f represents any variable of interest. The complex number μ is called the Floquet exponent and any growth or decay of the disturbance appears in its real part.

From the Floquet analysis it has been seen that each parameter pair (α, Re) results in multiple eigenvalues, most of which are stable. The simulation results should be a superposition of all of these modes. The least stable (or most unstable) mode is expected to become dominant after a sufficient length of time.

It is also known that for any eigenvalue μ, the complex conjugate $\bar{\mu}$ is also an eigenvalue. Inspection of the stability equation reveals that this can be interpreted as a disturbance that propagates upstream rather than downstream which is equivalent to taking a time shift of half a period, $\tau \to \tau + \pi$, due to the symmetries of the flow.

The growth-rate associated with μ and $\bar{\mu}$ are equal. So, at later times, any solution variable is expected to be well approximated by the linear superposition of these two modes, i.e.

$$f(y,\tau) \sim A_1 e^{\mu\tau} p_1(y,\tau) + A_2 e^{\bar{\mu}\tau} p_2(y,\tau), \tag{2.2.43}$$

where A_1, A_2 are constants and $\mu, \bar{\mu}$ are the dominant eigenvalues. Inspection of the stability equation (1.2.7) reveals that p_1 and p_2 are equal under conjugation and a time shift of half a period, but this information will not be made use of. Only the periodicity of these functions is used.

In order to extract the Floquet exponent μ from the simulation results consider the time-history of a chosen variable at a chosen wall-normal location. The vorticity ζ at the wall $y = 0$ will be selected. It will then be assumed that after sufficient time has passed this variable will be well approximated by

$$\zeta(0,\tau) \sim A_1 e^{\mu\tau} p_1(\tau) + A_2 e^{\bar{\mu}\tau} p_2(\tau). \tag{2.2.44}$$

Consider some reference time τ_0. The periodicity of p_1 and p_2 can be used to give the following three equations

$$\zeta(0,\tau_0) = A_1 p_1(\tau_0) e^{\mu\tau_0} + A_2 p_2(\tau_0) e^{\bar{\mu}\tau_0}, \tag{2.2.45a}$$

$$\zeta(0,\tau_0 + 2\pi) = A_1 p_1(\tau_0) e^{\mu\tau_0} e^{2\pi\mu} + A_2 p_2(\tau_0) e^{\bar{\mu}\tau_0} e^{2\pi\bar{\mu}}, \tag{2.2.45b}$$

$$\zeta(0,\tau_0 + 4\pi) = A_1 p_1(\tau_0) e^{\mu\tau_0} e^{4\pi\mu} + A_2 p_2(\tau_0) e^{\bar{\mu}\tau_0} e^{4\pi\bar{\mu}}, \tag{2.2.45c}$$

where $\zeta(0,\tau_0)$, $\zeta(0,\tau_0+2\pi)$ and $\zeta(0,\tau_0+4\pi)$ are taken from the time-history and will be abbreviated to f_0, f_1 and f_2, respectively. These expressions will be further simplified by denoting

$$B_1 = A_1 p_1(\tau_0)\mathrm{e}^{\mu\tau_0} \quad \text{and} \quad B_2 = A_2 p_2(\tau_0)\mathrm{e}^{\bar{\mu}\tau_0},$$

and this system will be solved for the Floquet multiplier $\lambda = \exp(2\pi\mu)$, leaving

$$f_0 = B_1 + B_2, \tag{2.2.46a}$$

$$f_1 = B_1\lambda + B_2\bar{\lambda}, \tag{2.2.46b}$$

$$f_2 = B_1\lambda^2 + B_2\bar{\lambda}^2, \tag{2.2.46c}$$

which we wish to solve for $\lambda = \lambda_r + i\lambda_i$. This is achieved by eliminating B_1 and B_2 and taking the real and imaginary parts of the resulting equation,

$$\mathfrak{Re}\{f_2\} = 2\lambda_r\mathfrak{Re}\{f_1\} - |\lambda|^2\mathfrak{Re}\{f_0\}, \tag{2.2.47a}$$

$$\mathfrak{Im}\{f_2\} = 2\lambda_r\mathfrak{Im}\{f_1\} - |\lambda|^2\mathfrak{Im}\{f_0\}. \tag{2.2.47b}$$

The unknowns λ_r and $|\lambda|$ are then solved for and can be expressed in their simplest forms as

$$\lambda_r = \frac{\mathfrak{Im}\{f_2/f_0\}}{2\mathfrak{Im}\{f_1/f_0\}}, \tag{2.2.48a}$$

$$|\lambda| = \sqrt{-\frac{\mathfrak{Im}\{f_2/f_1\}}{\mathfrak{Im}\{f_0/f_1\}}}. \tag{2.2.48b}$$

Finally, μ can be recovered by taking the complex logarithm of $\lambda = \exp(2\pi\mu)$ (using the principle argument in terms of cosine for convenience), giving

$$\ln(|\lambda|) + i\cos^{-1}\left(\frac{\lambda_r}{|\lambda|}\right) = 2\pi(\mu_r + i\mu_i). \tag{2.2.49}$$

Taking real and imaginary parts leaves

$$\mu_r = \frac{1}{2\pi}\ln(|\lambda|), \tag{2.2.50a}$$

$$\mu_i = \frac{1}{2\pi}\cos^{-1}\left(\frac{\lambda_r}{|\lambda|}\right). \tag{2.2.50b}$$

By this method, the Floquet exponent μ can be approximated for each point in the time-history and should converge towards the eigenvalue predicted by Floquet theory. For the first few periods of wall motion, the growth-rate measured in this way will not be at all representative of the asymptotic value since the solution will contain many modes at similar magnitudes. Then, as the more stable modes decay the convergence towards this value should become apparent.

A least squares method can also be used to find the μ that minimises the difference between the observed values and the model (2.2.44), provided a good initial guess is found by the method described above. However, this method was found to significantly underestimate the growth-rates so is not included.

2.2.4 Results and validation

In order to validate the Navier–Stokes simulation for a single wavenumber, a selection of eigenvalues were found using the Floquet eigenvalue solver. For each choice of α and Re a simulation was run for twenty periods so as to ensure sufficient convergence to the least stable mode (particularly important in the sub-critical cases). Some snapshots of the time histories are presented in Figure 2.1 in cases where the disturbance is classified as unstable ($Re = 800$), stable ($Re = 700$) and approximately neutrally stable ($Re = 714.8$). Also shown in Figure 2.1 is an example of a heavily damped mode for which the disturbance displays less oscillatory behaviour ($Re = 600$).

Noting that the plots of Figure 2.1 display the real part of the disturbance, it is clear that all but the highly damped example ($Re = 600$) display similar features to the eigenvector plotted in Figure 1.9b except for the periodic growth/decay. All disturbances indicate large instantaneous growth that is not at all representative of the asymptotic behaviour of the disturbance and in all three of these cases the size of the disturbance peaks approximately half way through each period of wall motion. The highly damped case $Re = 600$ displays two peaks per period of wall motion.

Once the time-histories had been traced for each case of interest, the above method for measuring μ could then be applied and it was generally observed that the growth-rate had converged to the predicted μ to two decimal places after twenty periods of wall motion, these results are presented in Table 2.1.

The agreement between these two methods serves to convincingly validate the model

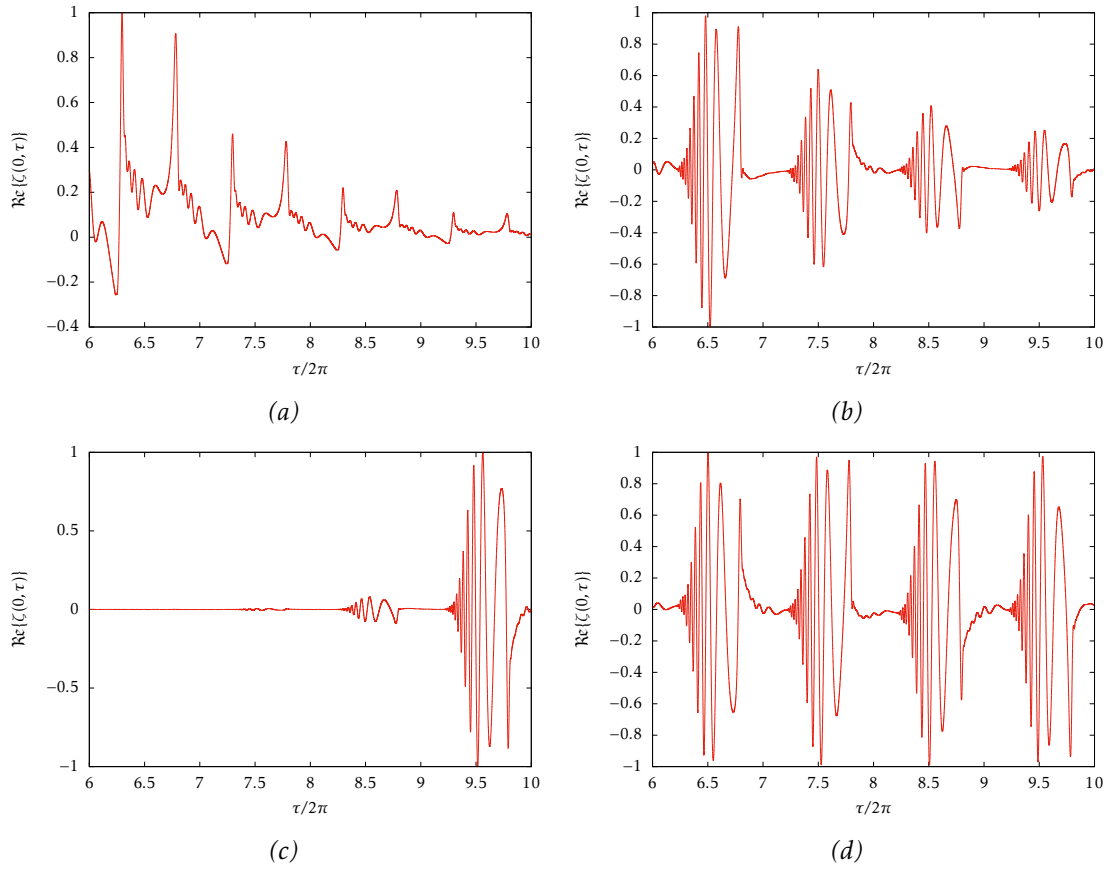

Figure 2.1: Time-histories of the real part of the vorticity at the wall for $\alpha = 0.4$. A highly damped case ($Re = 600$) is shown in (a), a stable case ($Re = 700$) in (b), an unstable case ($Re = 800$) in (c), and an approximately neutral case ($Re = 714.8$) in (d). The snapshots have been normalised so it would not be appropriate to compare the size of the disturbances in each plot.

α	Re	Predicted μ	Approximate μ
0.3	600	-0.0660 ± 0.0000i	-0.0665 ± 0.0000i
	700	-0.0668 ± 0.0000i	-0.0684 ± 0.0000i
	800	0.0824 ± 0.3458i	0.0815 ± 0.3536i
0.4	600	-0.0987 ± 0.0000i	-0.1024 ± 0.0000i
	700	-0.0710 ± 0.2491i	-0.0713 ± 0.2496i
	800	0.4048 ± 0.2384i	0.4045 ± 0.2389i

Table 2.1: Comparison of least stable (or most unstable) modes predicted by the Floquet eigenvalue solver against the growth-rates approximated from the time-histories after twenty periods of wall motion.

provided we appropriately consider what is being calculated. First, it is important to remember that even after the transient effects appear to have passed, the disturbance will still contain all the modes present for that choice of Re and α. A more accurate

representation of this function than (2.2.44) is therefore

$$\zeta(0,\tau) = \sum_{n=0}^{\infty} A_n e^{\mu_n \tau} p_n(\tau). \tag{2.2.51}$$

Clearly, to solve such a system in the same manner would require an infinite number of calculations so this is not a viable method for the extraction of growth-rates. It was deemed necessary to make the above simplification under the assumption that the most unstable mode is sufficiently dominant. Note that the closer the growth-rate of the mode with next-largest growth, the less accurate the approximated growth-rate.

An alternative interpretation of this process is to consider instead an initial value problem and represent the initial value as a vector in y which will be called $\boldsymbol{v}_0$. Then, according to Floquet theory, after a period of wall oscillation this vector will be acted on by a monodromy matrix, which will be referred to as $\boldsymbol{A}$, to give the new vector $\boldsymbol{v}_1$. The Floquet exponents can then be found as the eigenvalues of $\boldsymbol{A}$. The initial value problem can easily be related to the response to forcing by allowing transient effects to sufficiently pass before selecting $\boldsymbol{v}_0$. The passing of each time period is equivalent to additional multiplication by $\boldsymbol{A}$. For instance, the value of the vector at the 3^{rd} period can be found from $\boldsymbol{v}_0$ by $\boldsymbol{v}_3 = \boldsymbol{A}\boldsymbol{v}_2 = \boldsymbol{A}(\boldsymbol{A}\boldsymbol{v}_1) = \boldsymbol{A}(\boldsymbol{A}(\boldsymbol{A}\boldsymbol{v}_0)) = \boldsymbol{A}^3\boldsymbol{v}_0$. The time-stepping problem is therefore equivalent to performing a power iteration on $\boldsymbol{A}$ in order to converge to the dominant eigenvalue and the vectors $\boldsymbol{v}_i$ will converge to the associated eigenvector as $i \to \infty$.

At this juncture, all that is intended is a preliminary evaluation of the behaviour together with a validation of the code through comparison of the measured growth-rates against the Floquet eigenvalues. In the next chapter, a more detailed evaluation of disturbances with spatial variation will be discussed and many of the ideas touched on here will be expanded on.

2.3 Spectral method for impulse response

Now that the single wavenumber solver has been validated it is possible to reintroduce the streamwise dimension to the problem so that wavepacket evolution can be explored. This can be achieved in physical space by discretising the computational box using finite-differences, as in Thomas *et al.* (2014), but an alternative method that is more easily adapted from the single wavenumber formulation is to solve in wavenumber space. This

involves solving for a selection of wavenumbers independently and reconstructing the spatial shape of the solution by a linear combination of these solutions.

The main benefits are:

- This method lends itself to parallelisation since the evolution for each wavenumber is independent of all the others.
- The sometimes problematic streamwise boundary conditions (see Section 2.4) are not present in this formulation, replaced by an imposed periodicity.
- This method is much faster than the full-blown simulation in physical space.
- The existing code only requires a few adjustments and the inclusion of a routine to find the appropriate weightings for each wavenumber and to reconstruct the spatial form of the solution.

2.3.1 Fourier decomposition and reconstruction

Now that the streamwise direction has been reintroduced to the problem, the wall deformation used to excite the fluid requires a spatial dependence. The excitation will be localised in space with a Gaussian centred around some point x_f (usually the mid-point of the domain) with spread factor λ_f.

The x and τ dependence of the deformation $\eta(x,\tau)$ will be separated into multiplying factors, i.e. $\eta(x,\tau) = \eta_x(x)\eta(\tau)$ where $\eta(\tau)$ is the function of the wall deformation in the single wavenumber case above (2.2.4). The wall deformation is therefore described by

$$\eta(x,\tau) = A(1-\mathrm{e}^{-\sigma\tau^2})\mathrm{e}^{-\sigma\tau^2}\mathrm{e}^{-\lambda_f(x-x_f)^2}, \tag{2.3.1}$$

that is, the product of the purely temporal function $\eta(\tau)$ given in (2.2.4) with the afore mentioned Gaussian function

$$\eta_x(x) = \mathrm{e}^{-\lambda_f(x-x_f)^2}. \tag{2.3.2}$$

This will be defined on some spatial domain $x \in [0, L_x]$ and, following Thomas *et al.* (2014), L_x will initially be taken to be around $6,000$ so that the domain is large enough to observe the evolution of wavepackets for at least three periods of wall motion. Using

the discrete Fourier transform, η_x can be approximated by

$$\eta_x(x) \simeq \sum_{j=0}^{N} \hat{\eta}_j e^{i(j\Delta\alpha)x}, \tag{2.3.3}$$

where $\Delta\alpha$ imposes a periodicity of $2\pi/\Delta\alpha$ since the largest wavelength permitted by this approximation corresponds to the smallest non-zero wavenumber ($\Delta\alpha$).

Each coefficient $\hat{\eta}_j$ can be thought of as the weighting of the wavenumber $\alpha_j = j\Delta\alpha$ in η_x. In order to ensure that the solution converges to the least stable mode, N has to be chosen to ensure that α_N is larger than the wavenumber corresponding to this mode. It should be appropriate in most cases to take $\alpha_N = 0.6$ so that the wavenumbers are in the range $0 \leq \alpha \leq 0.6$. Care should be taken to increase the maximum α if necessary.

The choice of $\Delta\alpha = 0.001$ imposes a spatial periodicity of $\sim 6,300$ which, as found by Thomas *et al.* (2014), is expected to be large enough to trace the development of disturbances for up to three periods of oscillation.

In order to find the weightings $\hat{\eta}_j$, take the inverse discrete Fourier transform

$$\hat{\eta}_j = \sum_{k=0}^{M} \eta_x(k\Delta x) e^{-i(k\Delta x)\alpha_j}, \tag{2.3.4}$$

where Δx is chosen so that the solution is fully resolved. This choice directly impacts the choice of M, which is chosen to satisfy $M\Delta x = L_x$ and can be interpreted as the number of spatial nodes contained in the periodic computational box.

The relationship between the spectral parameters ($\Delta\alpha$, α_N, N) and the spatial parameters (Δx, L_x, M) is best described in terms of domain size and resolution (the largest and smallest scales, respectively). The size of the periodic domain is dictated by $\Delta\alpha$ (as mentioned above) and so L_x is chosen to be the size of this computational box ($L_x = 2\pi/\Delta\alpha$).

The smallest scales are associated with the wavenumber α_N, so the smallest wavelength is given by $2\pi/\alpha_N \sim 10$ (when $\alpha_N = 0.6$) so Δx must be chosen to ensure that these features are well resolved. In Thomas *et al.* (2014) a resolution of $\Delta x \sim 1$ is taken which here corresponds to ~ 10 nodes within each wavelength of $2\pi/\alpha_N$. This is sufficient resolution since this value of α_N has been chosen to be larger than the fastest growing mode, which will dominate the disturbance behaviour. The most unstable mode is usually located at a wavenumber < 0.4 which, for this choice of Δx, results in > 16 nodes

per wavelength. These waves are therefore well resolved. The number of Fourier modes $N = \alpha_N/\Delta\alpha$ and the number of spatial nodes in the domain $M = L_x/\Delta x$ are then fixed by these considerations.

In order to deduce the spacial variation of the disturbance, the weights $\hat{\eta}_j$ are calculated before the time-stepping begins and then the full spatial picture is constructed by

$$f(x, y, \tau) = \sum_{j=0}^{N} \hat{\eta}_j \hat{f}_j(y, \tau) \mathrm{e}^{i(j\Delta\alpha)x}, \tag{2.3.5}$$

where $\hat{f}_j$ is the velocity or vorticity found through the method described in Section 2.2 corresponding to the wavenumber $\alpha_j = j\Delta\alpha$, and f is the velocity or vorticity of the impulse response in physical space. The Fourier transforms can either be performed by writing routines for calculating the relevant summations or, more efficiently, by the FFTW (Fastest Fourier Transform in the West) library routines. Results will be discussed in Chapter 3

2.4 Impulse response with finite-differences

Presented above is a means of simulating the linear evolution of disturbances through discretisation of the governing equations. In this section, another such method will be described. The main benefit of this additional method is the reproduction of results and thus validation of each method against the other. This method was found to be incredibly sensitive to the choice of inlet and outlet boundary conditions (as will be seen in Section 3.5) and the problems arising at these locations have not been fully accounted for. It should be noted that these problems are not inherent to the formulation so more time could be taken to resolve these issues. However, the existence of an alternative, more efficient method (Section 2.3) has meant that the resolution of these issues has not been necessary for the present study.

2.4.1 Problem formulation

Consider the fully spatial governing equations (2.1.7) with the wall-normal transform (2.1.8). This section presents an alternative means of solving the same problem already discussed so all of the initial/boundary conditions used in the previous sections hold. Namely, it is assumed that all variables vanish in the far field ($y \to \infty, \xi \to 0$), that the no-

slip and no-penetration conditions apply at the wall ($y = 0, \xi = 1$) and that all variables are zero at $\tau = 0$.

In the previous scheme, the spectral discretisation in the streamwise direction imposed a periodicity on the solution. In this approach, boundary conditions will be imposed at either end of the streamwise domain. At the outlet, use will be made of the fact that a disturbance of a particular wavelength will dominate and that this can be predicted through Floquet theory (this relationship will be discussed in Chapter 3) so the following condition will be applied

$$\frac{\partial^2 f}{\partial x^2}(L_x, y, \tau) = -\alpha^2 f(L_x, y, \tau), \tag{2.4.1}$$

where $f(x, y, \tau)$ denotes any flow variable and L_x is the location of the outlet. The same condition can also be used at the inlet, but instead the homogeneous condition

$$f(0, y, \tau) = 0 \tag{2.4.2}$$

will be used since this pairing of conditions has been found to be stable (Thomas *et al.* , 2014). These boundary conditions proved problematic at large times, causing unphysical deformation at the inlet/outlet. These issues have not been fully resolved, though all combinations of these two conditions at the inlet and outlet were experimented with to reduce the problems encountered but the combination stated above was still found to be the most stable.

The only difference between this method and the spectral method described above is in the treatment of the x-direction. The boundary condition and integral constraint associated with no-slip and no-penetration will now be restated with the x-dependence incorporated since these conditions have thus far only been stated for a single Fourier component (i.e. in the single wavenumber case).

The boundary conditions on the velocity components (u, v) are again found by linearising the wall deformation about the undeformed wall, as in (2.2.3),

$$u(x, 0, \tau) = -U_S'(0, \tau)\eta(x, \tau), \tag{2.4.3a}$$

$$v(x, 0, \tau) = \frac{\partial \eta}{\partial \tau}(x, \tau). \tag{2.4.3b}$$

where $\eta(x,\tau)$ is given in (2.3.1), and from this it is readily deduced that

$$\frac{\partial \eta}{\partial \tau}(x,\tau) = 2\sigma\tau A \mathrm{e}^{-\lambda_f (x-x_f)^2}(2\mathrm{e}^{-\sigma\tau^2} - 1)\mathrm{e}^{-\sigma\tau^2}.$$

The integral constraint on the vorticity (equivalent to the no-slip condition) is written as

$$\int_0^\infty \zeta \,\mathrm{d}y = U_S'(0,\tau)\eta(x,\tau) - \int_0^\infty \frac{\partial v}{\partial x}\,\mathrm{d}y. \tag{2.4.4}$$

The problem is now properly posed with the streamwise variation fully incorporated. The numerical methods utilising a finite-difference scheme in the streamwise direction can now be developed.

First, the compact finite-difference schemes used to calculate the first and second derivatives with respect to the streamwise x-direction will be described (the streamwise derivatives in the previous formulation were calculated by multiplying the variable by $i\alpha$). It will then be seen that the vorticity transport equation (2.1.7a) is solved in a similar manner to that already described in the single wavenumber case. The method of solution of the Poisson equation (2.1.7b) is then detailed where the streamwise dependence of the differential operator means a different approach must be taken.

2.4.2 Numerical method

Spatial schemes

The finite-difference approach utilises the same wall-normal and temporal schemes described in Section 2.2 but a different streamwise discretisation is implemented. The finite-difference schemes for the first and second derivatives will be briefly described below. The interested reader is directed to Togneri (2011) for more details on these schemes.

Unlike in the wall-normal y-direction, the nodes in the streamwise x-direction are evenly spaced. This means that the compact finite-difference stencils of Lele (1992) can be used directly. It is from applying the wall-normal mapping to the schemes below that the wall-normal scheme (2.2.6) is derived.

Let the streamwise domain $[0, L_x]$ be divided into J evenly spaced nodes. The first derivative of any variable f with respect to the streamwise co-ordinate x can then be

approximated by the fourth-order scheme

$$\frac{1}{4}f'_{j+1} + f'_j + \frac{1}{4}f'_{j-1} = \frac{3}{4}\frac{f_{j+1} - f_{j-1}}{\Delta x} + \mathcal{O}(\Delta x^4) \tag{2.4.5}$$

for all interior nodes ($j = 1, ..., J-1$). Closure will be achieved using one-sided third-order schemes,

$$f'_0 + 2f'_1 = \frac{-5f_0 + 4f_1 + f_2}{2\Delta x} + \mathcal{O}(\Delta x^3), \tag{2.4.6a}$$

$$f'_J + 2f'_{J-1} = \frac{5f_J - 4f_{J-1} - f_{J-2}}{2\Delta x} + \mathcal{O}(\Delta x^3), \tag{2.4.6b}$$

where use can be made of the fact that $f_0 = 0$ to eliminate this term. The stability of high-order finite-difference schemes with lower order closure is discussed in Carpenter *et al.* (1993). The first x-derivative of a variable can the be found through the solution of the matrix problem

$$\begin{pmatrix} 1 & 2 & & & & & & \\ \frac{1}{4} & 1 & \frac{1}{4} & & & & & \\ & \ddots & \ddots & \ddots & & & & \\ & & \frac{1}{4} & 1 & \frac{1}{4} & & & \\ & & & \ddots & \ddots & \ddots & & \\ & & & & \frac{1}{4} & 1 & \frac{1}{4} & \\ & & & & & 2 & 1 & \end{pmatrix} \begin{pmatrix} f'_0 \\ f'_1 \\ \vdots \\ f'_j \\ \vdots \\ f'_{J-1} \\ f'_J \end{pmatrix} = \frac{1}{\Delta x} \begin{pmatrix} \frac{1}{2}(4f_1 + f_2) \\ \frac{3}{4}(f_2) \\ \vdots \\ \frac{3}{4}\left(f_{j+1} - f_{j-1}\right) \\ \vdots \\ \frac{3}{4}\left(f_J - f_{J-2}\right) \\ \frac{1}{2}\left(5f_J - 4f_{J-1} - f_{J-2}\right) \end{pmatrix}. \tag{2.4.7}$$

When the variable f is known at every streamwise node for the time-step of interest, the right-hand side of this equations is known. This is always the case when the predictor-corrector approach is used. This tridiagonal matrix problem can then be solved using the Thomas algorithm.

The second x-derivative is calculated at the internal points using the fourth order scheme

$$\frac{1}{10}f''_{j+1} + f''_j + \frac{1}{10}f''_{j-1} = \frac{6}{5}\frac{f_{j+1} - 2f_j + f_{j-1}}{\Delta x^2} + \mathcal{O}(\Delta x^4). \tag{2.4.8}$$

At the inlet, closure is again achieved using a one-sided third order scheme, but the boundary condition at the outlet already gives an explicit expression for the derivative

there. The system is therefore closed with

$$f_0'' + 11 f_1'' = \frac{13 f_0 - 27 f_1 + 15 f_2 - f_3}{\Delta x^2} + \mathcal{O}(\Delta x^3), \tag{2.4.9a}$$

$$f_J'' = -\alpha^2 f_J, \tag{2.4.9b}$$

where use can be made of the fact that $f_0 = 0$ to eliminate this term. The problem can then be written in matrix form as

$$\begin{pmatrix} 1 & 11 & & & & & \\ \frac{1}{10} & 1 & \frac{1}{10} & & & & \\ & \ddots & \ddots & \ddots & & & \\ & & \frac{1}{10} & 1 & \frac{1}{10} & & \\ & & & \ddots & \ddots & \ddots & \\ & & & & \frac{1}{10} & 1 & \frac{1}{10} \\ & & & & & 0 & 1 \end{pmatrix} \begin{pmatrix} f_0'' \\ f_1'' \\ \vdots \\ f_j'' \\ \vdots \\ f_{J-1}'' \\ f_J'' \end{pmatrix} = \frac{1}{\Delta x^2} \begin{pmatrix} -27 f_1 + 15 f_2 - f_3 \\ \frac{6}{5}(f_2 - 2 f_1) \\ \vdots \\ \frac{6}{5}\left(f_{j+1} - 2 f_j + f_{j-1}\right) \\ \vdots \\ \frac{6}{5}\left(f_J - 2 f_{J-1} + f_{J-2}\right) \\ -\alpha^2 f_J \end{pmatrix}. \tag{2.4.10}$$

Again, the second derivative of a variable is only calculated once that variable is known at every streamwise node, so the right-hand side is known. This system is then solved using the Thomas algorithm.

As the code of Togneri (2011) was being adapted, a range of different finite-difference schemes were investigated to minimise the unphysical edge effects. The schemes described above, being those used by Togneri (2011), were found to be the least susceptible to these problems of all those explored. However, the unphysical behaviour was not entirely eliminated.

The schemes described above are appropriate for any domain divided into evenly spaced nodes. The wall-normal scheme (2.2.6) was derived from these schemes. First, recall that the wall-normal nodes are not evenly spaced in y but are evenly spaced in ξ (the transformed wall-normal co-ordinate). The schemes (2.4.5) and (2.4.8) can be used to find the first and second ξ derivatives, respectively. The transformation (2.1.8) can then be performed to relate these ξ derivatives to the second y derivative through (2.1.9b), i.e.

$$\frac{\partial^2 f}{\partial y^2} = \frac{\xi^4}{l^2}\frac{\partial^2 f}{\partial \xi^2} + \frac{2\xi^3}{l^2}\frac{\partial f}{\partial \xi}.$$

More details on this process are provided by Togneri (2011).

Vorticity transport equation

Taking the vorticity transport equation (2.1.7a) and rearranging as before gives

$$\frac{\partial \zeta}{\partial \tau} - \frac{1}{2}\frac{\partial^2 \zeta}{\partial y^2} = \frac{1}{2}\frac{\partial^2 \zeta}{\partial x^2} - ReU_S\frac{\partial \zeta}{\partial x} - ReU_S''v, \tag{2.4.11}$$

so that the explicit terms can now be defined as

$$E = \frac{1}{2}\frac{\partial^2 \zeta}{\partial x^2} - ReU_S\frac{\partial \zeta}{\partial x} - ReU_S''v. \tag{2.4.12}$$

Notice that all x-derivatives are treated explicitly.

The predictor-corrector method is also used in this case, with the value of E at the n^{th} time-step predicted using (2.2.24) and then corrected. This means that ζ is known at every streamwise node whenever E is calculated, so the methods described above are indeed appropriate for calculating the first and second x-derivatives of ζ.

The expression for E differs from the single wavenumber case only in the inclusion of x derivatives rather than multiplication by $i\alpha$. Since all of these terms are included in E, the vorticity transport equation (2.1.7a) can again be written at his time-step as equation (2.2.23),

$$\frac{\partial \zeta^n}{\partial \tau} - \frac{1}{2}\frac{\partial^2 \zeta^n}{\partial y^2} = E^n,$$

except that now ζ^n and E^n are dependent of x as well as y. The operator is independent of x, so this problem can be solved at each spatial location in the same manner as for the single wavenumber case. The integral constraint used here is

$$\sum_{k=1}^{K} d_k \zeta_k^n = \iota^n = \left[U_S'(0,\tau)\eta\right]^n - \sum_{k=1}^{K} d_k \left(\frac{\partial v}{\partial x}\right)_k^n, \tag{2.4.13}$$

which differs from (2.2.31) only in the use of the term $\partial v/\partial x$ rather than $i\alpha v$ to fully account for the variation of the integrand with x.

The values of the explicit terms and the integral condition are again predicted at each time-step by $E_p^n = 2E^{n-1} - E^{n-2}$ and $\iota_p^n = 2\iota^{n-1} - \iota^{n-2}$. The first time (2.1.7a) is solved gives a predicted vorticity ζ_p^n which is then used to solve the Poisson equation by the method detailed below. The corrected E and ι are then calculated directly from ζ_p^n and v and the equation is solved again to find a more accurate ζ.

Poisson equation

Unlike the vorticity transport equation, the Poisson equation (2.1.7b) cannot be solved at each x-location individually. This is due to the x-dependence of the differential operator. For this reason, the approach described for the single wavenumber case (Section 2.2) cannot be applied. However, the problem can be transformed in such a way that similar methods can be deployed. This transformation is similar to the Fourier transform already seen, though it is based on sinusoids rather than exponentials.

The method described below can be thought of as a transformation into a spectral sine domain, solution in this domain, then transformation back to physical space. The relationship between sinusoids and exponentials will be exploited so that fast Fourier transform routines (from the FFTW library) can be used to perform this transformation efficiently.

To begin, apply the scheme (2.4.8) to the Poisson equation (2.1.7b) for all internal nodes $j = 1,...,J-1$. All variables are from the same time-step so the superscript n will be dropped for this section. This gives, after some rearrangement,

$$\frac{v_{j-1} - 2v_j + v_{j+1}}{\Delta x^2} + \frac{1}{12}\frac{\partial^2}{\partial y^2}\left(v_{j-1} + 10v_j + v_{j+1}\right) = F_j, \tag{2.4.14}$$

where the right-hand side F_j is given by

$$F_j = -\frac{1}{12}\left(\frac{\partial \zeta}{\partial x}\right)_{j-1} - \frac{5}{6}\left(\frac{\partial \zeta}{\partial x}\right)_j - \frac{1}{12}\left(\frac{\partial \zeta}{\partial x}\right)_{j+1}. \tag{2.4.15}$$

Following Togneri (2011), a discrete sine transform will be used so that the problem can again be reduced to a tridiagonal system. This transform requires homogeneous boundary conditions at both ends of the domain, so to apply it in this case the problem must be modified to ensure that both the subject (v) and the right-hand side (F) vanish at the inlet and outlet.

The inlet condition is already homogeneous, giving the following expression when $j = 1$,

$$\frac{-2v_1 + v_2}{\Delta x^2} + \frac{1}{12}\frac{\partial^2}{\partial y^2}(10v_1 + v_2) = F_1 = -\frac{5}{6}\left(\frac{\partial \zeta}{\partial x}\right)_1 - \frac{1}{12}\left(\frac{\partial \zeta}{\partial x}\right)_2. \tag{2.4.16}$$

A different condition is imposed at the outlet so a new variable $\tilde{v}$ will be defined that does vanish at this location. This variable will be equal to v everywhere except at the

outlet where it will satisfy

$$\frac{\tilde{v}_{J-2}-2\tilde{v}_{J-1}}{\Delta x^2}+\frac{1}{12}\frac{\partial^2}{\partial y^2}\left(\tilde{v}_{J-2}+10\tilde{v}_{J-1}\right)=F_{J-1}-\frac{v_J}{\Delta x^2}-\frac{1}{12}\frac{\partial^2 v_J}{\partial y^2}. \tag{2.4.17}$$

The problem can be recast in terms of $\tilde{v}$ provided expressions for v_J and the derivative $[\partial^2 v/\partial y^2]_J$ can be found. The Poisson equation must be satisfied at every location so writing (2.1.7b) at the outlet and applying the outlet condition $\partial^2 v_J/\partial x^2 = -\alpha^2 v_J$ gives

$$\frac{\partial^2 v_J}{\partial y^2}-\alpha^2 v_J=-\frac{\partial^2 \zeta_J}{\partial x^2}. \tag{2.4.18}$$

The variable v_J is acted on by the same differential operator seen in the single wavenumber case (2.2.15) so the same method can be used to solve this equation for v_J. This method is not detailed here since it is so similar to that already described in Section 2.2.

Using v_J found in this way, the expression at $j = J-1$ (2.4.17) can be rewritten using (2.4.18) as

$$\begin{aligned}\frac{\tilde{v}_{J-2}-2\tilde{v}_{J-1}}{\Delta x^2}+\frac{1}{12}\frac{\partial^2}{\partial y^2}\left(\tilde{v}_{J-2}+10\tilde{v}_{J-1}\right)&\\ =-\frac{1}{12}\left(\frac{\partial\zeta}{\partial x}\right)_{J-2}-\frac{5}{6}\left(\frac{\partial\zeta}{\partial x}\right)_{J-1}-\left(\frac{1}{\Delta x^2}+\frac{\alpha}{12}\right)v_J,&\end{aligned} \tag{2.4.19}$$

where the right-hand side is now known. Thus, a new function $\tilde{F}$ can be defined as being equal to F everywhere except for when $j = J-1$ where it is equal to the right-hand side of (2.4.19). Note that F is not defined at the inlet or outlet so can be set to zero at these nodes to satisfy the boundary conditions for the transform. The system can now be written as

$$\frac{\tilde{v}_{j-1}-2\tilde{v}_j+\tilde{v}_{j+1}}{\Delta x^2}+\frac{1}{12}\frac{\partial^2}{\partial y^2}\left(\tilde{v}_{j-1}+10\tilde{v}_j+\tilde{v}_{j+1}\right)=\tilde{F}_j, \tag{2.4.20}$$

where $\tilde{v}_0=\tilde{v}_J=\tilde{F}_0=\tilde{F}_J=0$. That is, the subject of the equation and the right-hand side now have homogeneous boundary conditions so the afore mentioned sine transform can be applied.

The transformation used in the streamwise direction will now be introduced. Consider the discrete expression of a smooth function g that satisfies homogeneous boundary conditions. The discrete sine transform of this function (denoted by $\breve{g}$) will be defined by

the following procedures

$$\check{g}_m = \frac{2}{J}\sum_{j=0}^{J-1} g_j \sin\left(\frac{\pi m j}{J}\right), \tag{2.4.21a}$$

$$g_j = \sum_{m=0}^{J-1} \check{g}_m \sin\left(\frac{\pi m j}{J}\right). \tag{2.4.21b}$$

This transform can be implemented by directly calculating the summations (Togneri, 2011) or, alternatively, the FFTW library can be used (Duval, 2012). This is a much faster method although it requires some careful thought about the relationship between the complex exponential transform and the sine transform.

In order to build an equivalence between these transforms, first double the size of the domain and extend the function into this new domain based on the relationship

$$g_{2J-n} = -g_n, \quad \text{for} \quad n = 0, ..., J-1, \tag{2.4.22}$$

so that the extended function is anti-symmetric about the J^{th} node and is continuous at this point since $g_J = 0$ has been assured. In the new domain, define the following complex exponential transform, which is calculated using the FFTW library,

$$\hat{g}_m = \frac{1}{2J}\sum_{j=0}^{2J-1} g_j \mathrm{e}^{-\frac{\pi i j m}{J}}, \tag{2.4.23a}$$

$$g_j = \sum_{m=0}^{2J-1} \hat{g}_m \mathrm{e}^{\frac{\pi i j m}{J}}. \tag{2.4.23b}$$

Note that the FFTW library does not divide by $2J$, this has to be applied manually.

The relationship (2.4.22) can be used to write $\hat{g}$ in the form

$$\hat{g}_m = \frac{1}{2J}\sum_{j=0}^{J-1} g_j \left(\mathrm{e}^{-\frac{\pi i j m}{J}} - \mathrm{e}^{\frac{\pi i j m}{J}}\right) = -\frac{2i}{2J}\sum_{j=0}^{J-1} g_j \sin\left(\frac{\pi j m}{J}\right) = \frac{1}{2i}\check{g}_m, \tag{2.4.24}$$

giving the relationship between the two transforms as

$$\check{g}_m = 2i\hat{g}_m, \tag{2.4.25}$$

which allows efficient calculation of the sine transform for any variable. A similar rela-

tionship also holds between the inverse transforms.

Using the domain extension (2.4.22) and the relationship (2.4.25), $\tilde{v}$ and $\tilde{F}$ at each spatial location can be expressed in the form

$$\tilde{v}_j = \sum_{m=0}^{J-1} \check{v}_m \sin\left(\frac{\pi m j}{J}\right), \tag{2.4.26a}$$

$$\tilde{F}_j = \sum_{m=0}^{J-1} \check{F}_m \sin\left(\frac{\pi m j}{J}\right). \tag{2.4.26b}$$

These expressions can now be used to transform the problem (2.4.20) into the sine domain,

$$\begin{aligned}&\left(\frac{5}{6}\frac{\partial^2}{\partial y^2} - \frac{2}{\Delta x^2}\right)\sum_{m=0}^{2J-1} \check{v}_m \sin\left(\frac{\pi m j}{J}\right) + \\ &\left(\frac{1}{\Delta x^2} + \frac{1}{12}\frac{\partial^2}{\partial y^2}\right)\sum_{m=0}^{2J-1} \check{v}_m \left[\sin\left(\frac{\pi m (j-1)}{J}\right) + \sin\left(\frac{\pi m (j+1)}{J}\right)\right] = \sum_{m=0}^{2J-1} \check{F}_m \sin\left(\frac{\pi m j}{J}\right).\end{aligned} \tag{2.4.27}$$

The terms concerning nodes $j-1$ and $j+1$ can be combined using trigonometric identities to give

$$\sin\left(\frac{\pi m (j-1)}{J}\right) + \sin\left(\frac{\pi m (j+1)}{J}\right) = 2\sin\left(\frac{\pi m j}{J}\right)\cos\left(\frac{\pi m}{J}\right). \tag{2.4.28}$$

The coefficients of $\sin(\pi m j/J)$ can be considered separately for each m due to the linear independence of sine functions with different wavenumbers. Defining

$$\sigma_m = \cos\left(\frac{\pi m}{J}\right) \tag{2.4.29}$$

then leaves

$$\left[\frac{2}{\Delta x^2}(\sigma_m - 1) + \frac{\sigma_m + 5}{6}\frac{\partial^2}{\partial y^2}\right]\check{v}_m = \hat{F}_m, \quad \text{for} \quad m = 1, \ldots, J-1. \tag{2.4.30}$$

The Poisson equation has now been reduced to a problem for which the only differential operator is the second derivative with respect to y. Therefore, for each m, the system can be solved in the established manner.

As before, the wall-normal scheme (2.2.6) is applied to the equation to replace differ-

ential terms with algebraic terms over several nodes, giving

$$k^3\left[\frac{\sigma_m-1}{5\Delta x^2(k-1)^3}+\frac{\sigma_m+5}{5}\frac{\Delta\xi^2(k-1)}{l^2}\right]\check{v}_m^{k-1}+\left[\frac{2(\sigma_m-1}{\Delta x^2}-(\sigma_m+5)\frac{2\Delta\xi^2k^2}{5l^2}\right]\check{v}_m^k+$$
$$k^3\left[\frac{\sigma_m-1}{5\Delta x^2(k+1)^2}+\frac{\sigma_m+5}{5}\frac{\Delta\xi^2(k+1}{l^2}\right]\check{v}_m^{k+1}=\check{F}_m^k+\frac{k^3}{10}\left[\frac{\check{F}_m^{k-1}}{(k-1)^3}+\frac{\check{F}_m^{k+1}}{(k+1)^3}\right]. \quad (2.4.31)$$

This can be written as the tridiagonal system

$$\begin{pmatrix}\epsilon_m^1 & \theta_m^1 & & & & & & \\ \delta_m^2 & \epsilon_m^2 & \theta_m^2 & & & & & \\ & \ddots & \ddots & \ddots & & & & \\ & & \ddots & \ddots & \ddots & & & \\ & & & \ddots & \ddots & \ddots & & \\ & & & & \delta_m^{K-2} & \epsilon_m^{K-2} & \theta_m^{K-2} & \\ & & & & & \delta_m^{K-1} & \epsilon_m^{K-1} & \end{pmatrix}\begin{pmatrix}\check{v}_m^1\\ \check{v}_m^2\\ \vdots\\ \vdots\\ \vdots\\ \check{v}_m^{K-2}\\ \check{v}_m^{K-1}\end{pmatrix}=\begin{pmatrix}r_m^1\\ r_m^2\\ \vdots\\ \vdots\\ \vdots\\ r_m^{K-2}\\ r_m^{K-1}\end{pmatrix}, \quad (2.4.32)$$

where

$$\delta_m^k=k^3\left[\frac{\sigma_m-1}{5\Delta x^2(k-1)^3}+\frac{\sigma_m+5}{5}\frac{\Delta\xi^2(k-1)}{l^2}\right], \quad (2.4.33a)$$
$$\epsilon_m^k=\left[\frac{2(\sigma_m-1}{\Delta x^2}-(\sigma_m+5)\frac{2\Delta\xi^2k^2}{5l^2}\right], \quad (2.4.33b)$$
$$\theta_m^k=k^3\left[\frac{\sigma_m-1}{5\Delta x^2(k+1)^2}+\frac{\sigma_m+5}{5}\frac{\Delta\xi^2(k+1}{l^2}\right], \quad (2.4.33c)$$
$$r_m^k=\check{F}_m^k+\frac{k^3}{10}\left[\frac{\check{F}_m^{k-1}}{(k-1)^3}+\frac{\check{F}_m^{k+1}}{(k+1)^3}\right]. \quad (2.4.33d)$$

This is solved (for each m) using the Thomas algorithm. Then, letting $v_j=\tilde{v}_j$ for $j=1,...,J-1$ while $v_0=0$ and v_J is already known (from solving the problem at the outlet) gives the solution to the Poisson equation.

Summary of the finite-difference formulation

This concludes the description of the finite-difference method in which the streamwise dependence is treated in physical space rather than in Fourier space. Aside from minor alterations to some expressions, the vorticity transport equation (2.1.7a) is solved in a similar way to that already established. The Poisson equation (2.1.7b) required some

extra attention due to the x dependence of the differential operator. In this case a sine transform was defined that reduced the problem to a tridiagonal system that could be solved in the same way as before.

Summary

This chapter has been concerned with methods by which disturbance evolution can be simulated using the linearised Navier–Stokes equations. First, a method for solving the equations when the disturbance has a single fixed wavenumber was developed and briefly validated in Section 2.2.

A means of building a full spatial response from many single wavenumber simulations was then described (spectral method) in Section 2.3. This involves taking each single wavenumber simulation as a Fourier mode and constructing the response from these spectral components using an inverse discrete Fourier transform.

A finite-difference method was described in Section 2.4 for which the x dependence is described in the physical domain. In this case it was necessary to solve the Poisson equation in the sine domain to account for the streamwise dependence of the differential operator.

While the single wavenumber case is useful for direct comparison with the Floquet eigenvalue problem, it is the wavepacket evolution triggered by a spatially localised impulse that is of particular interest. In Chapter 3, an investigation will be carried out into the impulse response of the Stokes layer. This investigation will be conducted using the spectral method due to its greater speed.

Another reason for using only the spectral method for this investigation is that for the finite-difference method unphysical behaviour originating at the inlet and outlet is observed. This numerical artefact was explored in some detail but could not be fully accounted for or corrected. Some experimentation with the formulation was undertaken to attempt to rectify this issue but the problems persisted. It was, however, found that this method was capable of picking up the early stages of the impulse response in some cases so results for the finite-difference method are also given in Chapter 3 for comparison with the spectral method. The issues at the boundaries are then discussed again once these results have been presented.

Chapter 3

Impulse response in the semi-infinite Stokes layer

Introduction

This chapter is concerned with describing and quantifying the behaviour of linear disturbances in the semi-infinite Stokes layer. In particular, the response of the system to an impulsive excitation that seeds multiple wavenumbers is investigated. This is more realistic than considering each wavenumber in isolation, which describes the evolution of disturbances with infinite periodic extent in the streamwise direction whereas the response to the localised forcing allows for variation in this direction.

For a single fixed wavenumber, if all disturbances are stable the flow returns to the unperturbed basic state whereas an unstable disturbance diverges from this basic state. The response to a spatially localised disturbance is considered unstable if the disturbance maximum grows in time and stable if the maximum exhibits temporal decay.

The introduction of spatial variation introduces the further classification of unstable disturbances as convective or absolute, based on the behaviour at fixed streamwise locations. A disturbance is convectively unstable if its maximum grows with time (i.e. is unstable) but it eventually exhibits temporal decay at any given spatial location. A disturbance displaying convective instability propagates away from the point of excitation so the flow at any spatial location returns to the unperturbed basic state. An absolute instability exhibits temporal growth at any given spatial location (in addition to the growth of the disturbance maximum). Rigorous definitions of absolute and convective instability

will be provided in Section 4.3, where a theoretical approach for locating the threshold between these classifications will be described. In this chapter these physical descriptors are sufficient for finding evidence or either type of instability to inform the work of Chapter 5.

The impulse response of the system will be investigated using the spectral simulation scheme described in Section 2.3. First, the structure of the impulse response is discussed in Section 3.1. Results are then compared directly against the behaviour predicted by the eigenvalue problem to verify that there is good agreement between the different methods: in Section 3.2 the growth of the disturbance is explored and in Section 3.3 the wavenumbers are considered. The focus of Section 3.4 is on the temporal evolution of disturbances at fixed streamwise locations so as to deduce the convective or absolute nature of instabilities. Finally, the finite-difference method described in Section 2.4 will be shown to be consistent with the spectral method in Section 3.5.

Results can be compared with those of Thomas *et al.* (2014), where wavepacket evolution in the semi-infinite Stokes layer was first investigated using linear simulation. Throughout this chapter results from Thomas *et al.* (2014) will be alluded to and expanded on.

3.1 Spatial/temporal structure of disturbances

To validate the method, simulations have been run for $Re = 600$ (Figure 3.1) and $Re = 700$ (Figure 3.2) for comparison with Thomas *et al.* (2014). The unstable case of $Re = 750$ (Figure 3.4) is also considered. Space/time contour plots have been used to indicate the regions in which the disturbance is strongest and reveal an intriguing *family-tree* structure. To the eye, these contour plots show excellent agreement with those of Thomas *et al.* (2014) so a more thorough investigation can take place.

The space/time plots are used to trace the wavepacket evolution over time. The vorticity at the wall is considered and the variation of this variable with x and τ is explored. First, a Hilbert transform is taken to calculate the envelope of the wall vorticity and then the envelope is normalised by dividing through by the maximum. Removing all values below a certain threshold, the natural logarithm is taken, showing very clearly the locations of the wavepackets. For the remainder of this work, the wavepacket envelope of a variable f (calculated through the Hilbert transform) will be indicated by $|f|$, and

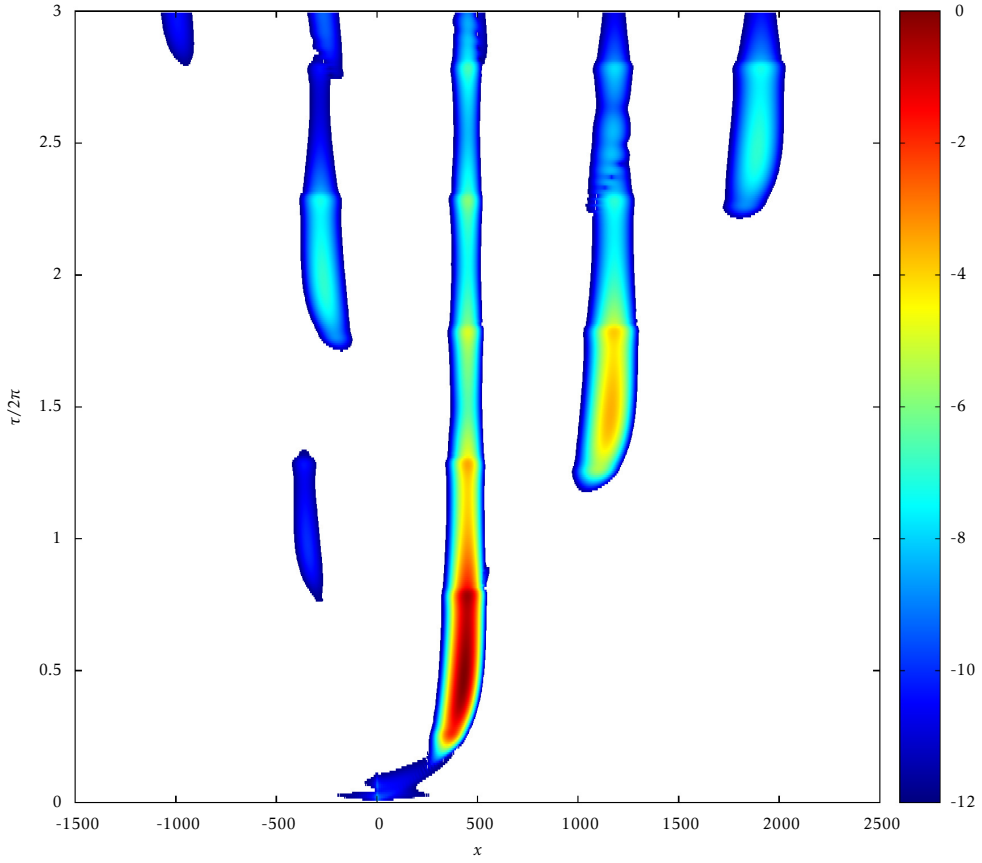

Figure 3.1: Space/time contour plot of $\log|\zeta(x,0,\tau)|$ *for* $Re = 600$*. The vorticity at the wall is taken at each time and a Hilbert transform is performed to find the envelope. The time-history of this envelope is normalised by dividing by the maximum and a threshold is selected so that any part of the disturbance below said threshold is removed. The natural logarithm is then taken. The disturbance maximum is carried downstream away from the point of excitation and overall decay is observed.*

should be distinguishable from the absolute value through context. Self-consistency was checked by reversing the initial direction of wall oscillation, giving plots that are identical up to reflection around the centre of the initial excitation, see Figure 3.3 compared with Figure 3.1. All such contour plots are constructed in the same manner.

In general, the white areas of these plots indicate that the magnitude of the disturbance envelope is below the given threshold. It should be noted, however, that when

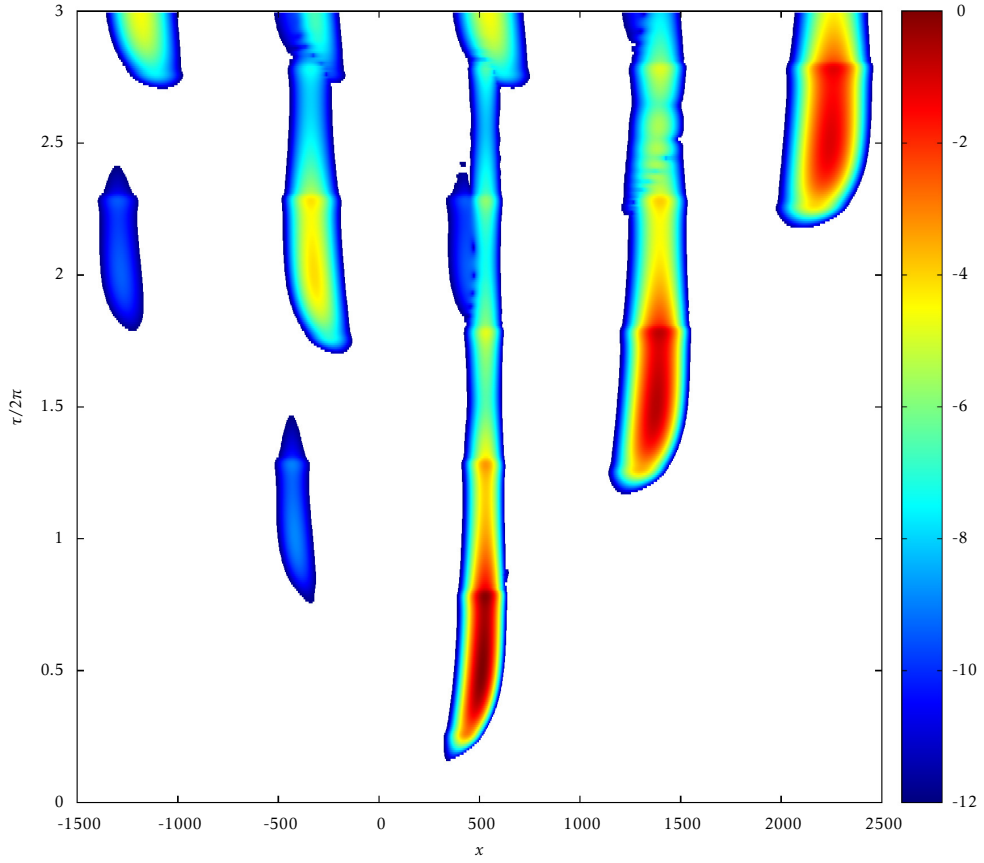

Figure 3.2: Space/time contour plot of $\log|\zeta(x,0,\tau)|$ *for* $Re = 700$*. Constructed in the same manner as Figure 3.1. The disturbance maximum is carried downstream away from the point of excitation and overall decay is observed.*

viewed in grey-scale, there may be areas contained within each wavepacket that appear to be white. This is not due to the magnitude of the envelope being below the threshold, so it is noted here that for all of the examples here there is no region within any wavepacket that drops below this threshold.

For consistency, the streamwise transform $x \to x - x_f$ is used so that the initial excitation is centred at $x = 0$. This is because in order to explore longer times, larger domains are needed and so there would be a range of values of x_f for different simulation runs. By performing this transform, all plots have consistent forcing location $x_f = 0$ so are directly

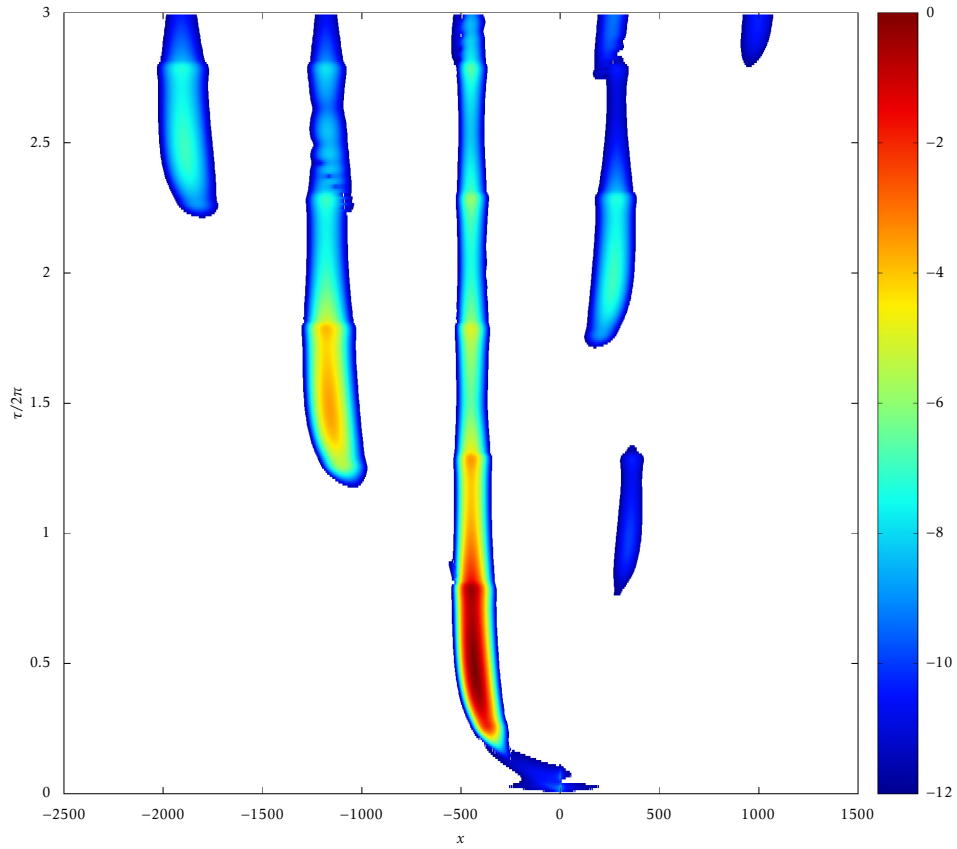

Figure 3.3: Exactly the same as Figure 3.1, except that the basic state has been shifted by half a period of wall oscillation. This is equivalent to a reversal of direction and it is clear that this plot is identical to Figure 3.1 except reflected around the point of excitation at $x = 0$.

comparable. This also results in the two streamwise directions being naturally labelled positive and negative, which is particularly practical for this oscillatory flow since upstream and downstream (as defined by the direction the bulk of the fluid is moving in) swap every half period. Generally, it was found that domains of size $L_x \sim 6,000$ were large enough to run the simulation for up to three periods of wall oscillation for the Re considered in this chapter. Larger domains of $L_x \sim 24,000$ were used to run simulations for up to ten periods and $L_x \sim 48,000$ were needed for 20 period runs. The value of L_x is controlled by changing $\Delta\alpha$, fixing the size of the periodic box as $L_x = 2\pi/\Delta\alpha$.

The immediately striking feature of the contour plots (Figure 3.1, Figure 3.2, Figure 3.4) is the multiple-wavepacket structure which is referred to as the family-tree

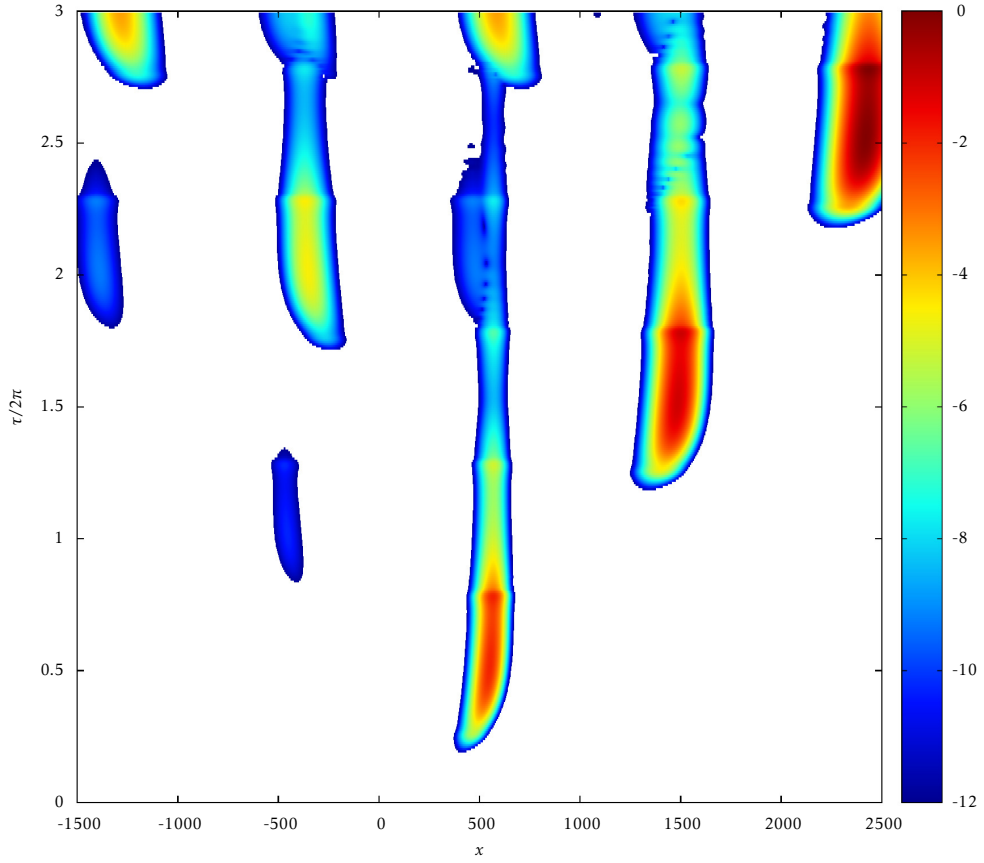

Figure 3.4: Space/time contour plot of $\log|\zeta(x,0,\tau)|$ *for* $Re = 750$*. Constructed in the same manner as Figure 3.1. The disturbance maximum is carried downstream away from the point of excitation and this maximum undergoes growth even though each individual wavepacket decays.*

structure in Thomas *et al.* (2014). The initial *mother* wavepacket births two *daughter* wavepackets, one in each streamwise direction. The dominant of the two daughter wavepackets is dictated by the initial phase of oscillation as can be seen by comparing Figure 3.1 with Figure 3.3. Each of these daughter wavepackets then birth *granddaughter* wavepackets and so on. A further observation that can be made is that each of the wavepackets appear to decay as time progresses, while the disturbance maximum is convected away from the initial point of excitation. However, the superposition of grand-

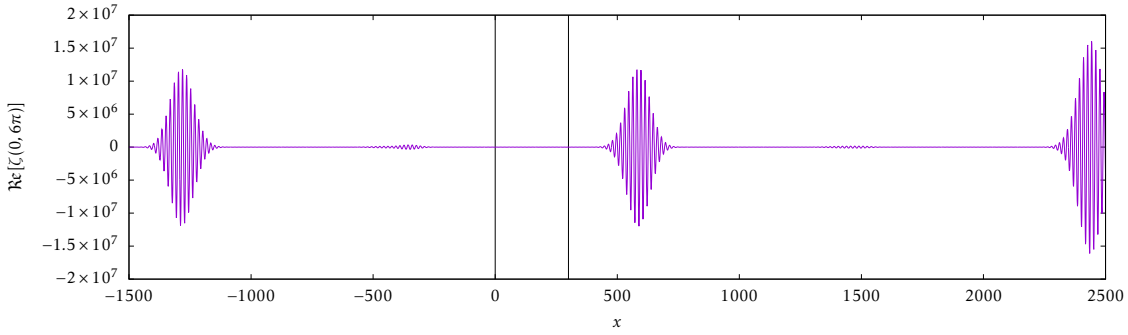

(a)

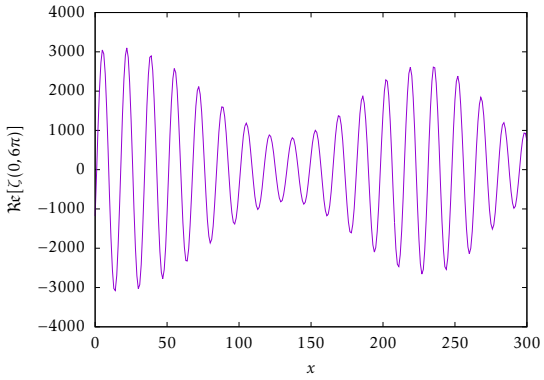

(b)

Figure 3.5: A snapshot of vorticity at the wall after three periods of wall oscillation is shown in (a) for $Re = 750$. This corresponds to the top of Figure 3.4. The comparative sizes of the wavepackets is clearer than in Figure 3.4 (since the logarithm has not been taken) as is the oscillatory nature of the solution. The vertical lines indicate a region that appears to contain no wavepacket. However, in (b) said region is shown to also display a wavelike disturbance. This shows that the wavepackets are not as isolated as the contour plot Figure 3.4 would suggest.

daughter wavepackets over their *grand-mother* wavepacket increases the amplitude of the decaying wavepacket. This is clearer for $Re = 700$ (Figure 3.2) and $Re = 750$ (Figure 3.4) than for $Re = 600$ and can be seen at the top centre of these plots.

Consider the unstable case of $Re = 750$. In Figure 3.5 the wavepackets are shown after three periods, $\tau = 6\pi$, as a companion to the contour plot Figure 3.4. This figure illustrates the correct interpretation of the contour plots by revealing the streamwise form of the disturbances. The inspection of a region that might be considered to contain no wavepacket from interpretation of Figure 3.4 shows that there is indeed a wavelike disturbance present, albeit at a much lower magnitude than the local maxima observed in Figure 3.4.

3.1.1 Family-tree structure

Some insight into the generation of daughter wavepackets can be provided by considering the wall motion. This discussion applies to all contour plots excluding the reversed plot in Figure 3.3 for which the words positive and negative can simply be swapped.

First, note that the wall moves towards positive x at the start of each period (i.e. $\tau/2\pi \in \{0, 1, 2, ...\}$) and towards negative x when halfway through each period (i.e. $\tau/2\pi \in \{0.5, 1.5, 2.5, ...\}$). At $\tau = 0$, the plate is moving with maximum speed towards positive x and this explains the convection of the mother wavepacket away from the point of excitation ($x = 0$). When $\tau/2\pi = 0.5$ the plate is moving in the opposite direction with maximum speed and this begins the process of generating the weaker of the two daughter wavepackets which takes around a quarter of a period to reach a large enough magnitude to appear in the contour plots. Similarly, when $\tau/2\pi = 1$ the generation of the stronger of the daughter wavepackets begins. This again takes around a quarter of a period to properly manifest.

This process continues and the family-tree grows in complexity as each wavepacket births two more within each period of wall oscillation. Increasingly, this results in the superposition of new wavepackets over existing wavepackets.

3.1.2 Streamwise separation of wavepackets

The timing of daughter wavepacket generation is the same for $Re = 600$ (Figure 3.1), $Re = 700$ (Figure 3.2) and $Re = 750$ (Figure 3.4) and as expected the contours suggest more unstable disturbances for higher Re. It is also observed when comparing these figures that the streamwise spacing between consecutive wavepackets is greater for larger Re. This distance, which shall be denoted by Λ, appears to be fairly constant for each simulation and the locations of local maxima at different times can be used to approximate this distance for a range of Re. This reveals a linear relationship between Re and the wavepacket spacing Λ as can be seen in Figure 3.6.

While the spectral method makes clear the manner in which a wavepacket response can be constructed from a superposition of a range of wavenumbers, it is interesting to see that running the same simulations for $\alpha \in [0.1, 0.6]$ rather than $\alpha \in [0, 0.6]$ has little to no effect on the results (so no plots are included). This is interesting since the removal of $\alpha < 0.1$ is equivalent to removing structures with wavelength > 62, which shows that

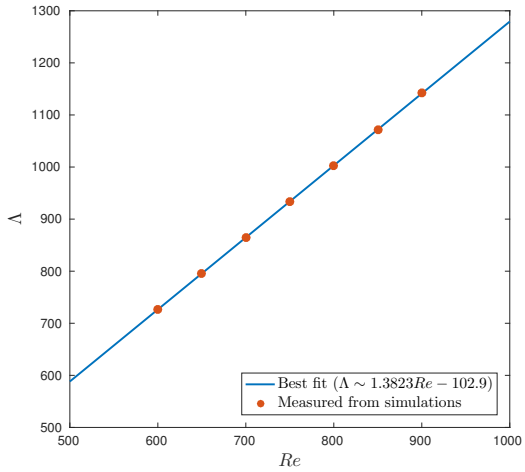

Figure 3.6: The wavepacket spacing Λ is plotted against the Reynolds number Re. The distance between local maxima was measured for $Re = 650, 700, 750, 800, 850, 900$ and the average values are plotted (•). The solid line is the linear relationship found by regression. Upper and lower deviation from the average has not been indicated in the plot as the points are large enough to cover this extent.

the wavepacket separation is not caused by long-wave modes.

This separation is consistent with what may be anticipated from the convective properties of the governing equation. A brief inspection of (4.1.1) reveals that the convective terms (in particular $\partial/\partial x$ terms) are scaled with the Reynolds number. This would suggest that during each period of wall oscillation the disturbance will have convected a distance of the order of Re. This is consistent with Figure 3.6, since $Re < \Lambda < 1.4Re$ so $\Lambda = \mathcal{O}(Re)$. More insight into the streamwise separation of wavepackets will be explored in Section 5.4.

Aside from the wavepacket spacing and the growth/decay of the disturbance maximum, all additional space/time contour plots considered demonstrated similar structure and behaviour to those shown in this chapter. The close agreement with Thomas *et al.* (2014) suggests that the present method is valid but further validation can be made by direct comparison against the Floquet eigenvalue problem. Prior to this, a quick conformation of consistency can be made by observing that the disturbances for $Re = 600, 700$ appear stable (Figure 3.1 and Figure 3.2) whereas the disturbance for $Re = 750$ appears unstable (Figure 3.4). This is consistent with the critical Reynolds number of this flow $Re_c \sim 707.8$ as first reported by Blennerhassett & Bassom (2002) and indicated in Figure 1.6b.

3.2 Temporal growth/decay of the disturbance maximum

Now that the immediately apparent qualitative features of the impulse response have been discussed and compared to existing work, a more quantitative approach can be taken. For a true impulse, every wavenumber is seeded at equal magnitude and the growth-rate associated with each Fourier mode will thus dictate the spectral make-up of the disturbance after a certain length of time. In the numerical simulations, the true impulse is approximated by a Gaussian and thus it is expected that some wavenumbers will be given more weighting than others.

There is a length of time at the start of the simulation in which the presence of multiple modes of comparative size means the disturbance is a complex superposition of many modes. Then, as the more stable modes decay, the disturbances should converge towards the least stable (or most unstable) mode. For this reason, the simulations must be run for more than three periods in order for the leading-order behaviour to become apparent and so the simulations are run for ten periods of wall oscillation in this section.

The work of Thomas *et al.* (2014) was not able to investigate such long times due to the computational expenses of the problem, but application of the spectral method in the present study has greatly improved efficiency. Furthermore, since the simulations for each wavenumber are independent of one another, the problem lends itself to parallelisation and so the Raven cluster, the supercomputer of the Advanced Research Computing @ Cardiff (ARCCA) division (Cardiff University), was utilised and the run-time of the simulations was dramatically reduced.

It was stated earlier that in the case of a spatially localised excitation, a disturbance is defined as stable or unstable based on the temporal evolution of the disturbance maximum. In fact, the temporal growth (or decay) of the disturbance maximum is dictated by the growth-rate of the most unstable mode over all real α. This is not a trivial result, though it is well established for steady flows. In Chapter 4, it will be shown that this is also the case for temporally periodic flows.

The predicted temporal growth-rate of the disturbance maximum can be found from Floquet theory by calculating the growth-rates for a range of α and selecting the most unstable. This predicted value can then be compared against values measured from the simulations. The growth-rate of a disturbance variable f can be measured at some time

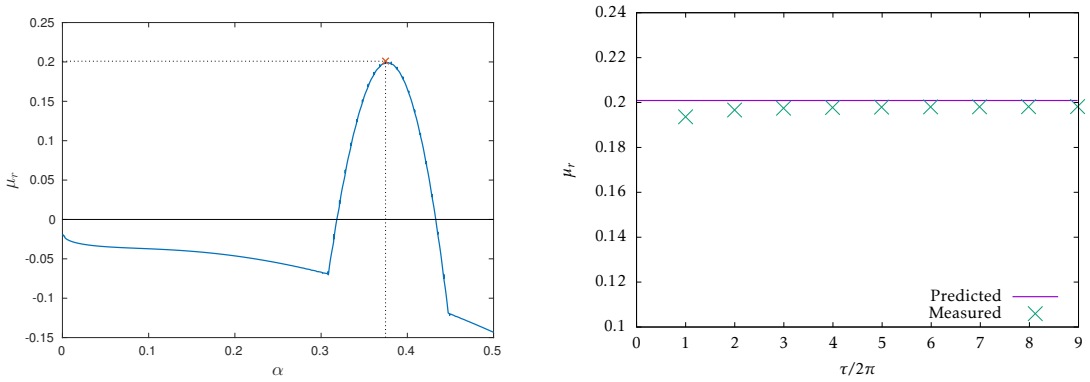

(a) *(b)*

Figure 3.7: The semi-infinite Stokes layer at $Re = 750$. In (a) the growth-rate associated with a selection of α are plotted and the one expected to be most dominant is selected ($\alpha = 0.3747$ and $\mu_r = 0.2009$). In (b) the temporal growth-rate of the disturbance maximum is calculated with (3.2.1) at the beginning of each period and compared with the predicted value.

τ using (4.3.14), i.e.

$$\mu_r(\tau) = \frac{1}{2\pi}\log\left(\sqrt{1+\frac{2\pi}{\tau}}\frac{\max_x|f(x,\tau+2\pi)|}{\max_x|f(x,\tau)|}\right). \tag{3.2.1}$$

This expression will be derived in Section 4.3 and in general the disturbance variable considered will be the vorticity at the wall, $\zeta(x,0,\tau)$.

Two cases will now be considered: an unstable case ($Re = 750$) and a stable case ($Re = 700$). In both cases, the temporal growth-rate will be extracted from the time-history of the disturbance maximum using (3.2.1). The most unstable mode for each Re can be predicted by solving the Floquet eigenvalue problem for a range of α and selecting the mode with largest μ_r. It is then anticipated that the predicted value will be an asymptote for the growth-rate as measured by (3.2.1), approached as $\tau \to \infty$.

3.2.1 Unstable case

Consider the case $Re = 750$ (larger than the critical Reynolds number of $Re_c \sim 707.8$). It can be seen from Figure 3.4 that the disturbance maximum is convected away from the point of excitation and appears to grow with time. In general, the disturbance maximum is expected to grow/decay with a temporal growth-rate μ_r that can be found either by the Floquet eigenvalue problem or by measuring the growth at a given time with (3.2.1).

The growth-rates for a range of α are shown in Figure 3.7a. According to this figure,

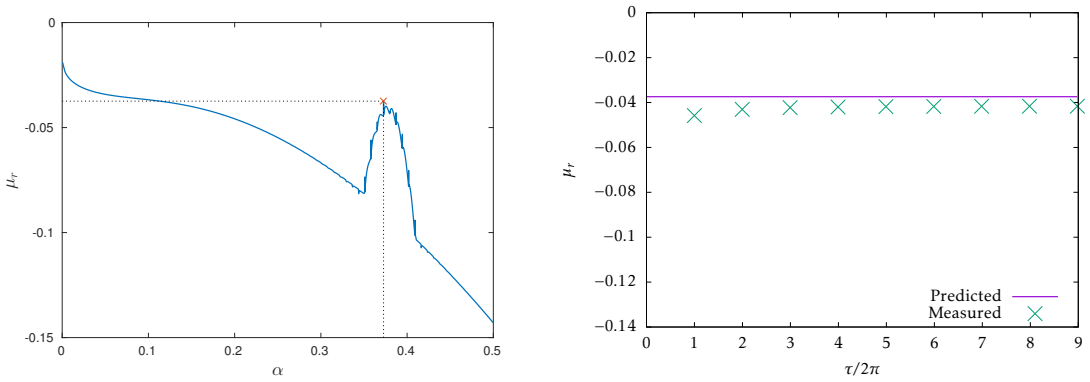

(a) *(b)*

Figure 3.8: The semi-infinite Stokes layer at $Re = 700$. In (a) the growth-rate associated with a selection of α are plotted and the mode with $\alpha = 0.3727$ and $\mu_r = -0.0374$ is selected. In (b) the temporal growth-rate of the disturbance maximum is calculated with (3.2.1) at the beginning of each period and compared with the predicted value.

the least stable mode at this Re corresponds to $\alpha = 0.3747$ and has positive growth-rate $\mu_r = 0.2009$. This value can now be compared with the temporal growth measured from the simulation results using (3.2.1). In Figure 3.8b, these values are compared and it is seen that as time progresses the difference between these values decreases. This is evidence that the growth-rate measured using (3.2.1) converges to the growth-rate predicted from Floquet theory for large times. The two methods are in good agreement in this case.

Note that the most unstable mode in Figure 3.7a appears at the tip of one of the small-scale finger-like protrusions. The relevance of this feature will be discussed in Chapter 5.

3.2.2 Stable case

Consider now the case $Re = 700$, for which the disturbance is expected to be stable since $Re < Re_c \sim 707.8$. This can be confirmed through inspection of Figure 3.2 and observing that the disturbance maximum is convected away from the point of excitation and decreases in magnitude each period. Again, the temporal growth-rate of the maximum μ_r can be measured for a selection of times with (3.2.1).

As for the unstable case, the predicted value can be extracted from the Floquet approach by measuring the growth-rate corresponding to a range of wavenumbers to deduce the growth of the least stable mode. The growth-rates for a range of α are shown in Figure 3.8a. According to this figure, the least stable mode at this Re corresponds to

$\alpha = 0$. This is problematic as the Floquet eigenvalue method breaks down when $\alpha = 0$ since in this case the basic state no longer appears in the stability equation (1.2.7). However, it will be seen in Section 4.3 that the temporal growth-rate exhibited by the disturbance maximum is not simply $\mu_r^{max} = \max_\alpha\{\mu_r\}$, but must necessarily satisfy

$$\frac{\partial \mu_r}{\partial \alpha} = 0.$$

Therefore, the local maximum indicated in Figure 3.8a is selected as the predicted temporal growth-rate of the disturbance maximum. This mode corresponds to wavenumber $\alpha = 0.3727$ and growth-rate $\mu_r = -0.0374$ and again corresponds to the tip of a finger. This value can now be compared with the growth measured from the simulation results using (3.2.1), showing a convergence towards the predicted, negative value in Figure 3.8b.

The selection of this particular mode can also be made on the grounds of the simulation results. The growth-rate of the disturbance maximum is much closer to the growth-rate associated with the local maximum than that corresponding to $\alpha = 0$. It will also be seen below that the dominant wavenumber at later times is close to the selected value of $\alpha = 0.3727$. Additional simulations were run with the lower values of α removed and were found to produce practically identical plots.

3.3 Inspection of the Fourier spectrum

In addition to the comparison of growth-rates, convergence to the dominant mode can be indicated by considering the spectral composition of the disturbance. Again, consider the wall vorticity $\zeta(x, 0, \tau)$ as a representative value for the disturbance.

Using the spectral approach, the Fourier decomposition of the physical disturbance is found directly by the simulation. For the wall vorticity, the Fourier transform at some given time τ_0 can be written in terms of the physical disturbance as

$$\hat{\zeta}(\alpha, 0, \tau_0) \simeq \sum_{j=0}^{L} \zeta(j\Delta x, 0, \tau_0) \mathrm{e}^{-i(j\Delta x)\alpha}. \tag{3.3.1}$$

As discussed earlier, this transform deconstructs the disturbance into its composite wavenumbers and so the function $|\hat{\zeta}(\alpha, 0, \tau_0)|$ (where $|\bullet|$ indicates the absolute value

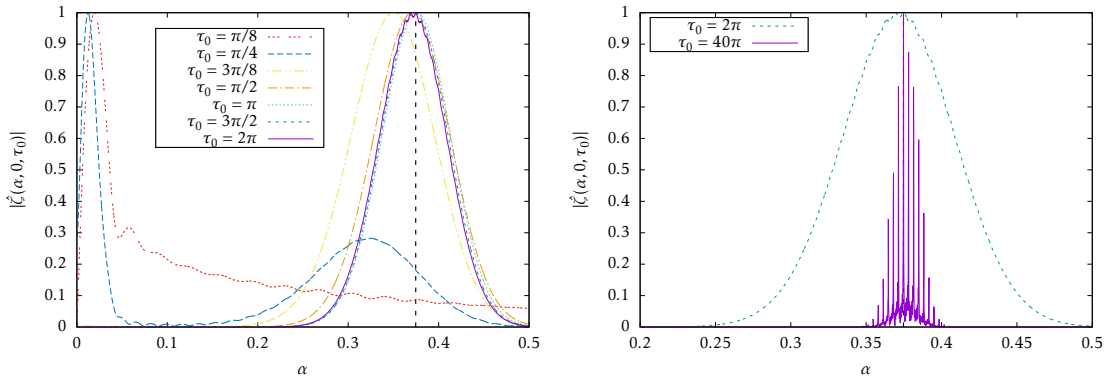

(a) *(b)*

Figure 3.9: Snapshots of the (normalised) absolute value of the Fourier transform of the wall vorticity $|\hat{\zeta}(\alpha, 0, \tau_0)|$ at $Re = 750$. In (a) the spectrum is shown for times $\tau_0 = \pi/8, \pi/4, 3\pi/8, \pi/2, \pi, 3\pi/2, 2\pi$ (not an equal time increment) while (b) is a direct comparison between the curves for $\tau_0 = 2\pi$ and $\tau_0 = 40\pi$. These curves indicate that the peak of the spectrum is very close to the predicted dominant wavenumber of $\alpha = 0.3747$ (see Figure 3.7a). By the end of the simulation the peak of the spectrum coincides with this predicted value to the accuracy of this plot.

rather than the envelope found through the Hilbert transform) describes the relative dominance of the wavenumber α. Of particular interest in this section is the location of the maximum, which indicates the most dominant wavenumber at this time, and the band of significant amplitude around this maximum.

In each case, $|\hat{\zeta}(\alpha, 0, \tau_0)|$ can be normalised (divided by some constant) so that the maximum value is 1. This normalisation is implemented for all times since the change in amplitude as time progresses has already been discussed in Section 3.2 (so is not of interest in this section).

Consider first the unstable case $Re = 750$. Floquet theory has predicted a dominant wavenumber of $\alpha = 0.3747$, see Figure 3.7a. The absolute value of the Fourier transform of the wall vorticity is plotted for several time instances in Figure 3.9. There is evidence of convergence to the predicted value (indicated by the vertical line) within the first period of wall motion. Figure 3.9a also shows that the dominant wavenumber jumps from very low α to the vicinity of the predicted value at some early time.

In Figure 3.9b the spectrum at the end of the first period is compared with that at the end of the twentieth showing that the band of significant wavenumbers has thinned significantly. This means that the most unstable mode is becoming more dominant as time progresses. In fact, the vertical line indicating the wavenumber of the predicted

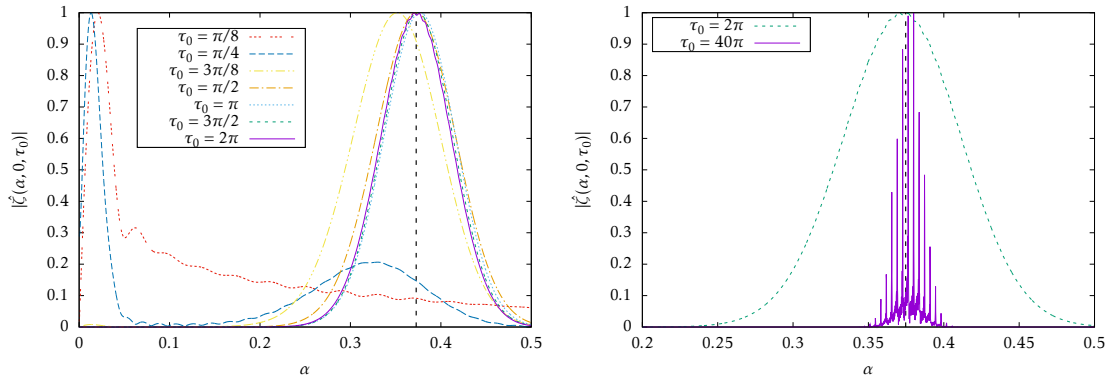

(a) *(b)*

Figure 3.10: The same as Figure 3.9 except at $Re = 700$. In (a) the spectrum is shown for times $\tau_0 = \pi/8, \pi/4, 3\pi/8, \pi/2, \pi, 3\pi/2, 2\pi$ (not an equal time increment) while (b) is a direct comparison between the curves for $\tau_0 = 2\pi$ and $\tau_0 = 40\pi$. By the end of the simulation the peak of the spectrum seems to coincide with the wavenumber corresponding to the growth-rate of the disturbance maximum $\alpha = 0.3727$ (see Figure 3.8a) and there is evidence of convergence to this α within the first period of wall motion.

dominant mode $\alpha = 0.3747$ is obscured by the peak in the spectrum at this location.

Notice that the spectrum after twenty periods of wall motion is more sensitive to α, with several peaks within the band of significant magnitude. At this point, no attempt will be made to explain this feature. It is instead noted that these multiple peaks could either be a numerical artefact or related to the fingers protruding from the growth-rate curve. This feature will be revisited at the end of Chapter 5.

Consider now the stable case of $Re = 700$. The equivalent plots are shown in Figure 3.10. There is again evidence of convergence towards the expected wavenumber of $\alpha = 0.3727$ (see Figure 3.8a) within the first period of oscillation. As seen in the unstable case, the spectrum has multiple peaks after twenty periods of oscillation and the band of significant magnitude is restricted to a small range of wavenumbers.

An alternative means of visualising these features would be to plot the natural logarithm of the Fourier spectrum instead of performing the normalisation. This is because the exponential growth (or decay) of a disturbance means that it can be impossible to display the Fourier spectrum for different times on the same scale. Taking the logarithm means that exponential growth would appear linear and so the curves can be directly compared on the same plots. The choice was made to instead display the normalised spectra since this approach makes the peaks much clearer. Furthermore, the

growth/decay of the disturbance maximum has already been shown to agree with Floquet theory in these two cases so the change in magnitude of the Fourier spectrum with time does not need to be explored.

3.4 Temporal growth at fixed streamwise locations

Now that the simulation results have been validated against the Floquet eigenvalue problem, an investigation into the temporal evolution of the disturbances at fixed spatial locations can be carried out.

Unlike the evolution of the disturbance maximum, the growth at a fixed spatial location cannot be extracted from the Floquet analysis in such a simple manner. Comparison of these methods involves locating cusps in the complex μ plane, which will be explored in Chapter 5.

The temporal growth of a disturbance variable f at a given time τ and spatial location x_0 will be measured using (4.3.23), i.e.

$$\Re\mathfrak{e}\{\mu_0(\tau)\} = \frac{1}{2\pi}\ln\left[-\sqrt{1+\frac{4\pi}{\tau}}\frac{\mathrm{Im}\{f(x_0,\tau+4\pi)/f(x_0,\tau+2\pi)\}}{\mathrm{Im}\{f(x_0,\tau)/f(x_0,\tau+2\pi)\}}\right], \tag{3.4.1}$$

which will be derived in Section 4.3. Again, the wall vorticity $\zeta(x,0,\tau)$ will be the disturbance variable considered.

With regards to the classification of disturbances as convective or absolute, Thomas *et al.* (2014) (having only been able to run simulations for three periods of wall oscillation) note little discernible pattern in the time-history of the disturbance at fixed x. This coupled with the convection of the disturbance maximum amounted to no clear evidence of absolute instability.

Due to the more computationally efficient spectral formulation and use of a more powerful computer, simulations can be run for longer in the present study. In the interest of producing convincing evidence of absolute instability, twenty periods of wall oscillation were used to investigate the evolution at a selection of spatial locations.

Figure 3.11a shows the logarithm of the time-history at three streamwise locations. There is a period of transient behaviour lasting around four periods of wall motion followed by growth. The spatial locations were chosen to approximately coincide with the wavepacket maxima seen in Figure 3.4. The initial transient behaviour shows why

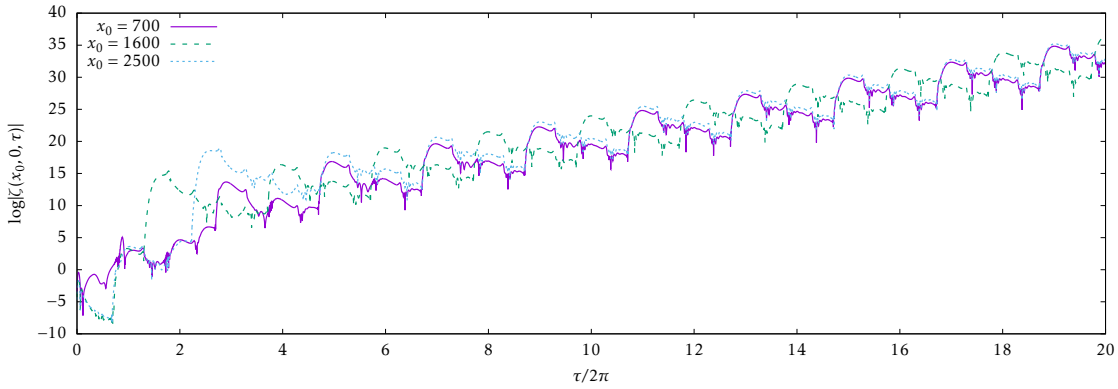

(a)

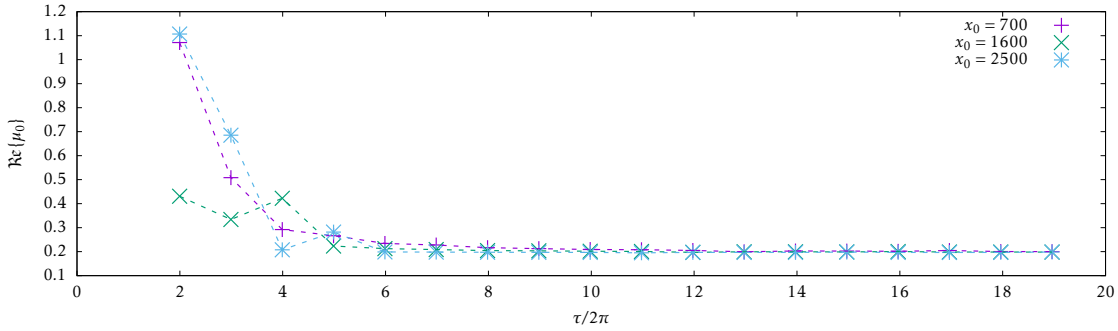

(b)

Figure 3.11: The Stokes layer at Re = 750. In (a) a snapshot of the logarithm of the wall vorticity envelope at $x = 700, 1600, 2500$ shows that after four periods of oscillation temporal growth is observed at each x. In (b) the temporal growth-rates are calculated at the beginning of each period using (3.4.1) for $x_0 = 700$ (+), $x_0 = 1600$ (×) and $x_0 = 2500$ (∗), showing convergence to a single positive value.

Thomas *et al.* (2014) could not observe clear growth after three periods of oscillation.

Figure 3.11b shows the extracted temporal growth-rates for these spatial locations at a selection of times, as measured using (3.4.1). It is apparent that as τ increases, the temporal growth-rates associated with each location seem to approach the same positive value. Since the disturbance exhibits temporal growth for each choice of x (moreover, the same temporal growth in each case), it will tentatively be assumed that the disturbance generated in the semi-infinite Stokes layer at $Re = 750$ is absolutely unstable.

Having drawn this conclusion, it is vital that the possibility of this behaviour being unphysical is ruled out. To this end several simulations were run with various choices of numerical parameters: The size of the domain L_x was increased by decreasing the wavenumber increment $\Delta\alpha$; the time step $\Delta\tau$ was halved; the number of wall-normal points K was doubled; the wall-normal stretching factor l was taken both larger and

smaller; the largest wavenumber α_{up} was increased; and a higher order time-stepping scheme was implemented. In each of these cases all other variables were fixed and it was found that this behaviour was robust. This provides evidence that this flow is subject to absolute instability in this case.

This conclusion is seemingly at odds with the structure observed in the contour plots for the first three periods of oscillation. In these plots, each wavepacket decays as τ increases and the disturbance maximum is convected away from the point of excitation (both features of convective instability). However, the observed superposition of granddaughter wavepackets over their respective grand-mother wavepackets results in an increase in the magnitude of each wavepacket every 2 periods of wall oscillation.

This is consistent with the time-history of the disturbance at fixed streamwise locations (Figure 3.11) where it is observed that the growing disturbance has a temporal quasi-period that is twice the period of the wall motion (remembering that a quasi-periodic function is defined for the purposes of this work as a periodic function multiplied by a complex exponential).

Consider some fundamental oscillation with frequency ω. In general, a waveform is considered harmonic to the fundamental if its frequency can be written as $n\omega$ for some $n \in \mathbb{N}$ or subharmonic if its frequency can be written as ω/m for some $m \in \mathbb{N}$. In the present study, the special cases of $n = 1$ and $m = 2$ will be the only cases associated with these terms. That is, a harmonic waveform has frequency ω (equal period to the fundamental) and a subharmonic waveform has frequency $\omega/2$ (twice the period of the fundamental). The meaning of these terms has been restricted in this way for brevity since only these two cases have been observed in the present study.

Additionally, disturbances undergo amplification each period so these definitions will also be naturally extended for quasi-periodic behaviour. That is, for the remainder of this work, any temporal variation with a period (or quasi-period) twice that of the underlying flow will be described as *subharmonic*. If the period (or quasi-period) is equal to that of the underlying flow the temporal variation will be described as *harmonic*. This is not to be confused with the harmonic decomposition of the disturbance (1.2.8), and it should be clear from context which meaning is intended.

The subharmonic temporal variation of each of the wavepackets can be illustrated by a contour plot for the first ten periods of wall motion (constructed in the same man-

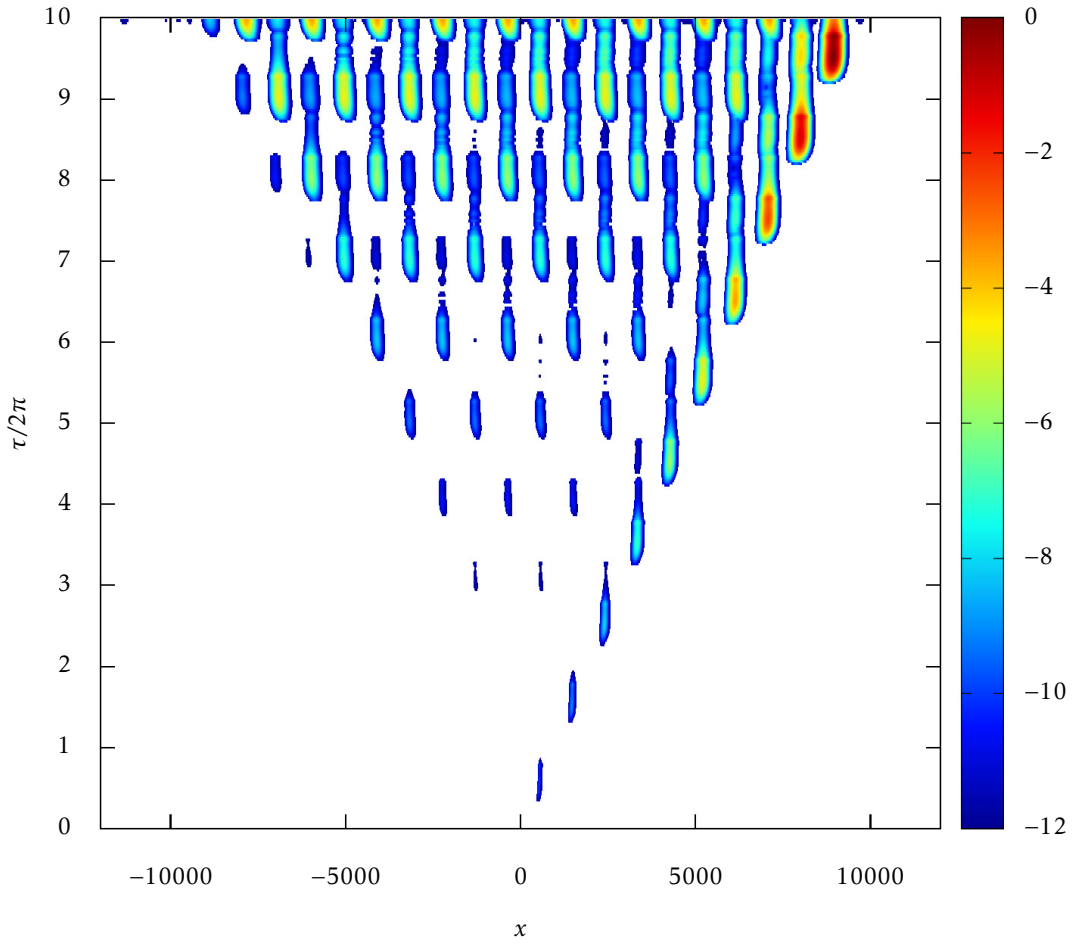

Figure 3.12: Space/time contour plot of the logarithm of the wall vorticity envelope for the semi-infinite Stokes layer at $Re = 750$ for ten periods of wall oscillation showing subharmonic temporal growth of each wavepacket. This plot is constructed in the same manner as Figure 3.1.

ner as before). This is shown in Figure 3.12. The temporal growth of each wavepacket is instantly apparent, and the convected disturbance maximum is still observed on the right-hand side of the plot.

The subharmonic variation is illustrated by the staggering of wavepackets: in two periods the wavepackets have returned to their original position (and grown) while during the interim period the wavepackets are offset. A somewhat unexpected feature of this plot is that, with the exception of the convected disturbance maximum, every wavepacket at a given time seems to be around the same magnitude. This is counter-intuitive given

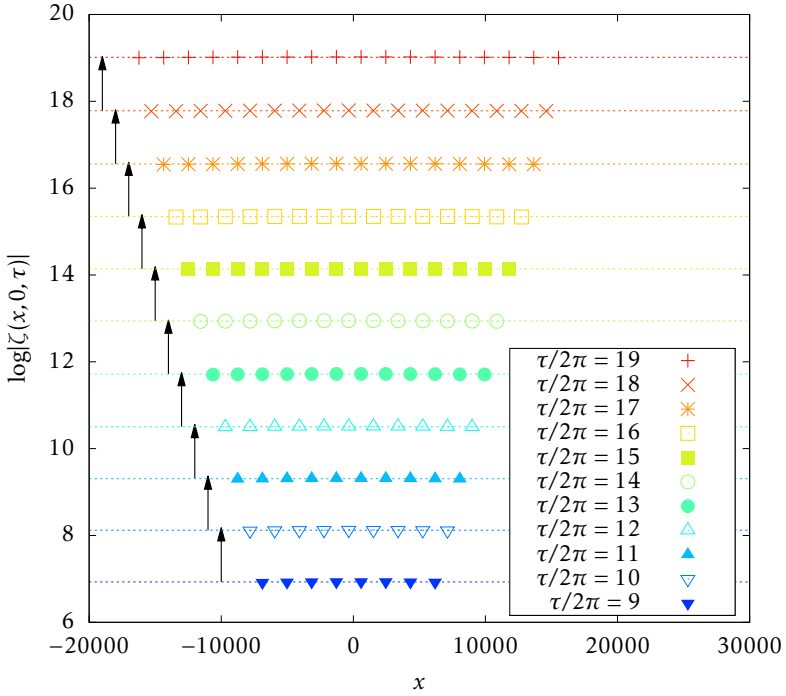

Figure 3.13: The growth of wavepackets with each period of wall motion can be illustrated by plotting the logarithm of the local maxima (corresponding to different wavepackets) at the start of different periods of wall motion ($\tau/2\pi = 9, 10, 11, ..., 19$), indicated by the symbols. The subharmonic temporal structure manifests as the staggering of the locations of these local maxima, and the convected disturbance maximum has been removed. The local maxima at a given time lie approximately on a straight line so the average was taken to indicate the size of the disturbance at this time, denoted by the dashed lines. It is anticipated that for absolute instability, the increase in magnitude over each period will be approximately constant. The arrows in the image are all of equal length, illustrating that this is the case.

the clear favouring of one direction noted earlier. However, the manner in which the family-tree structure evolves means that each new wavepacket is a superposition of the stronger daughter of a weaker mother and the weaker daughter of a stronger mother. This can be seen occurring at the top of Figure 3.4.

A contour plot was also produced for twenty periods of wall oscillation. This plot provided no further insight (the dispersion of the staggered wavepackets continues in the same manner) so is not shown.

The manner in which the staggered wavepackets grow over each period is illustrated in Figure 3.13, where the global maximum (convected downstream) has been removed and the locations of the remaining maxima have been plotted at the beginning of each period. At each time shown, all remaining maxima are of approximately the same magnitude and evenly spaced in x. Furthermore, the growth experienced over each period of

wall motion is approximately equal. This is demonstrated by the arrows of equal length, indicating the same level of growth each period. The arrow length was chosen by observing in Figure 3.11b that the temporal growth-rate for each spatial location is very close to the temporal growth-rate of the disturbance maximum. Each arrow is therefore of length $2\pi\mu_r^{max}$, where $\mu_r^{max} = \max_\alpha \mu_r$ is the maximum growth-rate associated with the flow at this Re. In this case, $\mu_r^{max} = 0.2009$. This provides clear graphical evidence of the subharmonic temporal variation of each wavepacket and also of the growth associated with each streamwise location.

Notice that the points indicating the locations of local maxima at a given time in Figure 3.13 display a spacing twice that presented in Figure 3.6. This is because the wavepacket spacing Λ, as defined for Figure 3.6, is the distance between all wavepackets, regardless of when they occur in the staggered structure.

To be more precise, there are in fact wavepackets located at every marked location in Figure 3.13 (that lie within the extent of the disturbance) at any given time and the staggering corresponds to the strengthening and weakening of each of these wavepackets with respect to one another. This can be seen in Figure 3.12 where none of the wavepackets have completely decayed when those in the staggered location become dominant. The weaker wavepackets are not included in Figure 3.13 for graphical clarity.

To a certain extent, this problem is analogous to that of the secondary instability of Tollmien–Schlichting (TS) waves in the Blasius boundary layer (Herbert, 1988). In this problem, a linear stability analysis of the Blasius boundary layer is performed and the basic state is then modified to include the resulting two-dimensional TS wave at some finite amplitude. A linear stability analysis can then be performed on the now periodic flow utilising Floquet theory. This results in 3D disturbances superimposed over the TS wave that are termed Λ-vortices due to their shape.

If the secondary instability has the same periodicity as the TS wave, the Λ-vortices are aligned. That is, at each crest of the TS wave the vortices appear in the same location. This behaviour is termed ‘fundamental’ or ‘harmonic’. If the secondary instability has half the periodicity of the TS wave, the Λ-vortices are staggered. That is, at each subsequent crest the vortices have changed location, only to return to the previous location at the next crest. This behaviour is termed ‘subharmonic’. A third regime can also be identified in which there is a detuning (i.e. the period of the secondary instability is somewhere

between one and two periods of the TS wave).

The case of staggered Λ-vortices is comparable with the temporal evolution of the wavepackets displayed in Figure 3.12 in that the solution has a quasi-period that is twice the period of the basic state.

3.4.1 Convective instability

It may be anticipated for flows which are subject to absolute instability that as Re is increased the disturbance passes from a stable region into a convectively unstable region and finally into an absolutely unstable region (Lingwood, 1997). Having presented results which suggest that $Re = 700$ yields a stable solution and $Re = 750$ yields an absolutely unstable solution, it would be logical to now attempt to locate convective instability.

To explore this possibility consider the near-critical values of $Re = 708, 709$. These cases are both expected to be marginally unstable due to their proximity to the critical Reynolds number $Re_c \sim 707.8$. Remember that for $Re = 708$ the only unstable modes correspond to the tips of fingers and this is expected to correspond to a disturbance that, to the accuracy of these plots, appears neutrally stable.

In general, the temporal growth of an absolutely unstable disturbance at each spatial location must be less than or equal to the temporal growth of the disturbance maximum. However, Figure 3.7b and Figure 3.11b suggest that the temporal growth-rates associated with any spatial location and the disturbance maximum are equal or at least similar.

Figure 3.14 compares these temporal growth-rates for $Re = 708$ and $Re = 709$ showing that even this close to Re_c these values are very close. Little more can be concluded from the simulations since the precise asymptotic value will never be reached in finite time, making it impossible to deduce whether these growth-rates are in fact equal or not. It can, however, be safely concluded that if this flow is subject to convective instability there will be a very small range of Re for which this is the case. This issue will be revisited later using the cusp map method to predict the asymptotic value of the temporal growth-rate at any streamwise location.

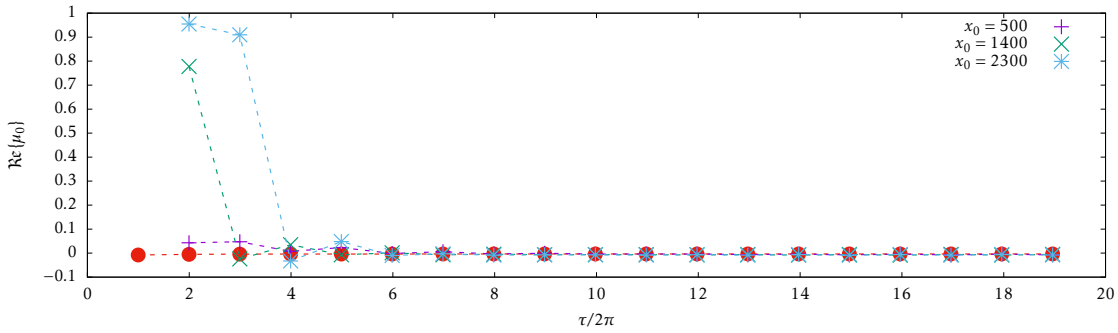

(a)

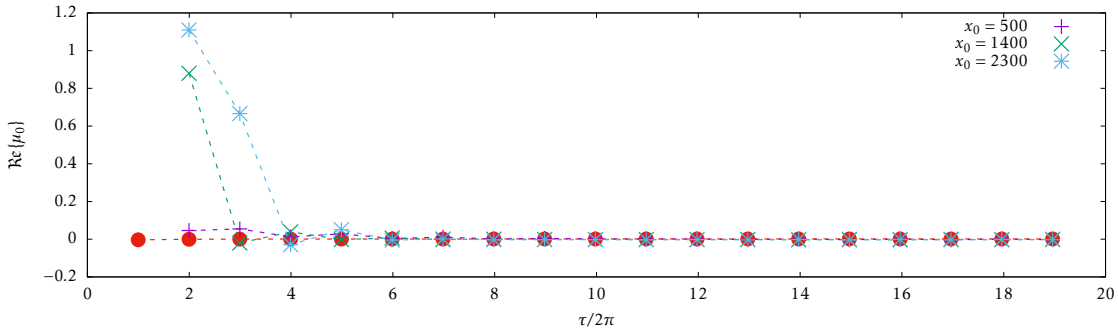

(b)

Figure 3.14: The temporal growth-rate of the disturbance maximum is calculated at the beginning of each period using (3.2.1) (•) *for* $Re = 708$ *(a) and* $Re = 709$ *(b). The temporal growth-rates associated with fixed spatial locations are calculated in each case using* (3.4.1) *for* $x_0 = 500$ *(+),* $x_0 = 1400$ *(×) and* $x_0 = 2300$ *(∗). At each location there is convergence to a single value very close to* 0.

3.5 Comparison with the finite-difference method

Consider now the finite-difference formulation described in Section 2.4. This is a method by which the impulse response of the system can be simulated and should produce identical results to those presented for the spectral method. One of the main drawbacks of this approach compared with the spectral method is the much greater computational time required to run the simulation for the same number of periods of wall motion. Results will therefore only be compared up to three periods of wall oscillation.

A further issue is that the sometimes delicate streamwise boundary conditions were found to cause unphysical effects that would gradually infiltrate the region of interest. Though this problem is not intrinsic to the finite-difference formulation, it would have taken a significant amount of time to properly address this issue and even then the comparatively slow computational speed of this method meant that this was less practical than the spectral method. This is why the finite-difference method is presented below as

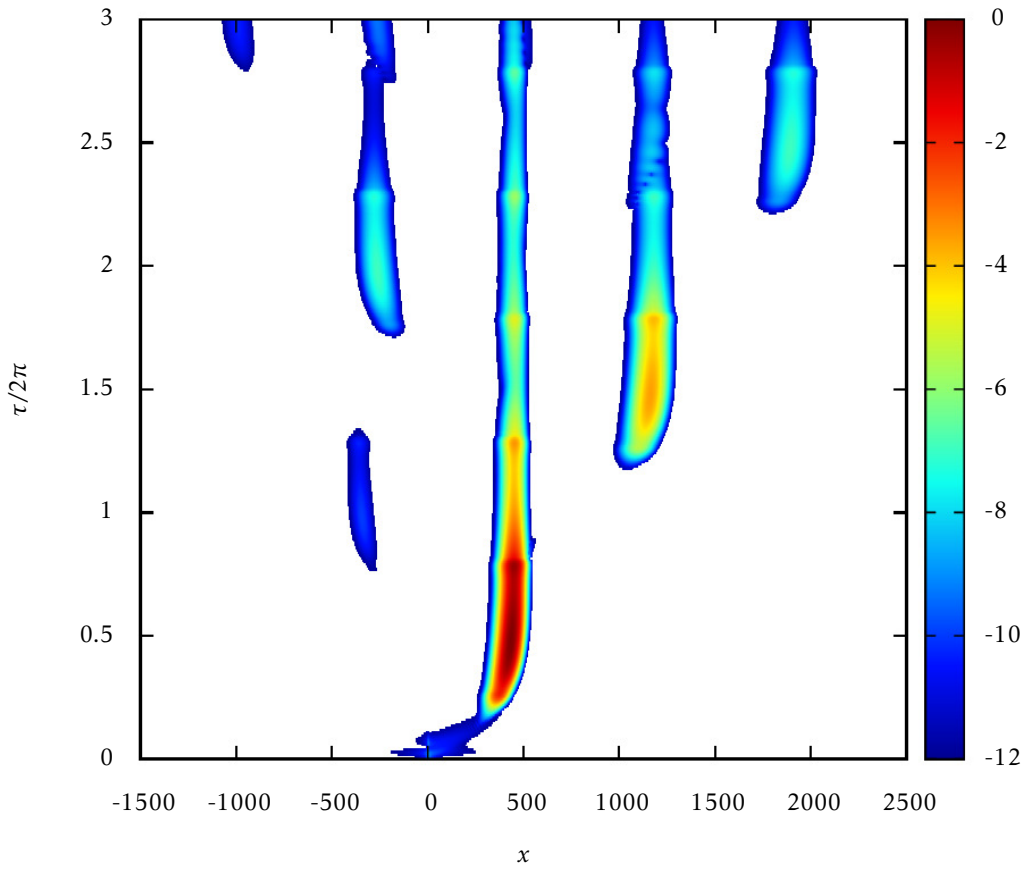

Figure 3.15: Space/time contour plot of $\log|\zeta|$ *for* $Re = 600$ *using finite-difference formulation, for comparison with Figure 3.1. The contour map is constructed in the same way as for Figure 3.1 and the agreement is excellent.*

a tool of validation rather than as a viable alternative method.

Presented in Figure 3.15 and Figure 3.16 are contour plots from the finite-difference formulation corresponding to the stable cases of $Re = 600$ and $Re = 700$ for comparison with Figure 3.1 and Figure 3.2, respectively. There is relatively good agreement. These figures can also be compared with Figure 1 and Figure 2 in Thomas *et al.* (2014) and the agreement is clear.

An unphysical feature can be seen on the right-hand side of Figure 3.16 which is caused by the edge effects propagating into the region of interest. For this plot the low-

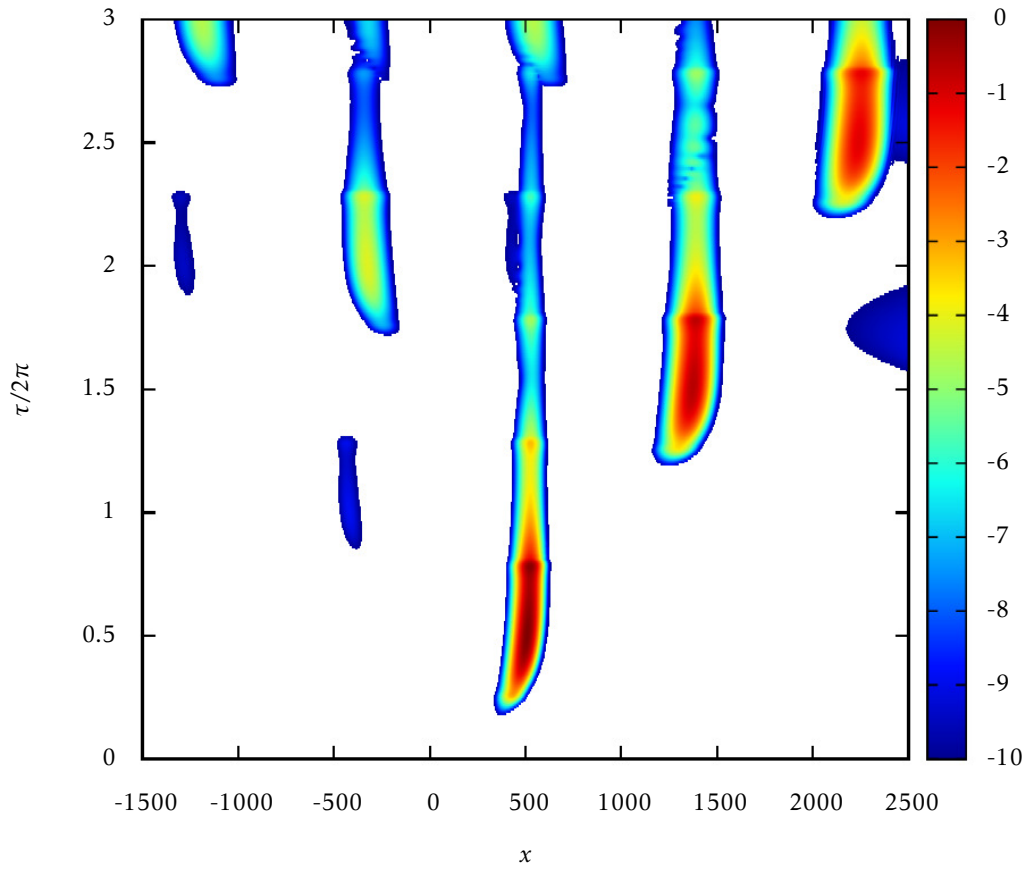

Figure 3.16: Space/time contour plot of $\log|\zeta|$ *for* $Re = 700$ *using finite-difference formulation, for comparison with Figure 3.2. The contour map is constructed in the same manner as Figure 3.1 and the agreement is good. There are some unphysical effects on the right-hand side encroaching on the region of interest.*

amplitude threshold was chosen to be higher than in Figure 3.2 (-10 rather than -12) so as to disguise some edge effects that had encroached further into the domain.

Attempts were made to reduce the impact of this unphysical behaviour but, as can be seen in Figure 3.16, the issues were never fully resolved. Efforts involved increasing the order of the temporal and spatial schemes. At the inlet and outlet, the order of the closure was reduced to improve the overall numerical stability of the scheme and several combinations of boundary conditions were implemented. A higher order predictor

for the explicit terms and integral constraint was also explored and the iteration of the corrector step used in Togneri (2011) was reintroduced to little effect.

The work of Thomas *et al.* (2014) is based on a very similar formulation and was capable of producing a contour plot for $Re = 700$ with no unphysical growth at the domain edges. However, having developed the spectral method to perform the same simulations faster allows for larger Reynolds numbers and later times to be explored and so, while these boundary issues could realistically have been resolved, the existence of an alternative, more efficient method renders this moot. All simulation results in the subsequent chapters will have been attained by the spectral method.

Summary

The comparison of the simulation results with the behaviour predicted by the Floquet eigenvalue problem has served to validate each method against the other. A qualitative assessment of the spatial/temporal structures in Section 3.1 provided some insight into the evolution of wavepackets in a Stokes layer, and a quantitative comparison with the eigenvalue problem in Section 3.2 and Section 3.3 revealed that the temporal growth-rate of the disturbance maximum appears to approach the predicted value. Also, it was shown in Section 3.4 that in the one unstable case documented in this chapter ($Re = 750$) the temporal evolution of each wavepacket suggests that this instability is absolute.

It is noted for all cases considered that the temporal growth-rate at each spatial location is very close to the temporal growth-rate of the disturbance maximum. This suggests that the transition from Floquet stability to Floquet instability appears to coincide with the onset of absolute instability. From the cases considered, there does not appear to be an intermediate region where the flow is convectively unstable before absolute instability sets in. For other flows, such as the rotating disc boundary layer (Lingwood, 1997), the transition from stability to instability coincides first with convective instability and a further increase in Re corresponds to the onset of absolute instability.

Having validated the simulation (spectral method) against the linear stability analysis (Floquet method), a final comparison was made between the spectral and finite-difference schemes for streamwise discretisation in Section 3.5. The problems arising from the streamwise boundary conditions and the comparatively long running-time of the finite-difference simulations only allowed for comparison of the space/time contour

plots for three periods of wall oscillation. However, given the agreement between the other methods and the close agreement with the work of Thomas *et al.* (2014), this was deemed sufficient validation.

Chapter 4

Absolute and convective instability in periodic flows

Introduction

The leading-order behaviour of a perturbation to a temporally periodic flow can be investigated through the asymptotic evaluation of the exact integral solution to the disturbance equation. Such an analysis serves to highlight the deeper connection between the eigenvalue problem discussed in Chapter 1 and the simulation of disturbance evolution as discussed in Chapter 2 so that these approaches can be compared in more depth than has been seen in Chapter 3. Additionally, this approach provides a framework for the definitions of absolute and convective forms of instability, terms that have thus far been used descriptively rather than rigorously.

The work described herein explores two different approaches to evaluating the solution integral: the method of steepest-descent and the eponymous method first developed by Briggs (1964) in the field of plasma physics. Both approaches are equivalent but, due to the different processes involved, more insight is provided by the consideration of both.

The extension of these methods to periodic media was first developed for the spatially periodic case by Brevdo & Bridges (1996). This approach was then adapted to the time-periodic regime in Brevdo & Bridges (1997) and the present work is based upon this approach. In particular, the solution integral is derived following Brevdo & Bridges (1997) as closely as possible, while the asymptotic evaluation is developed from the steady cases (Briggs, 1964; Bers, 1983; Lingwood, 1997; Huerre, 2002) to provide the level of detail

that was deemed necessary to contextualise and inform the subsequent work.

The approach detailed here is revisited in Appendix A for the case of the Ginzburg–Landau equation with periodic coefficients. For this equation, it is possible to write down the exact solution to the differential equation. This provides a means of comparing the leading-order analysis against the exact solution and is directly comparable with Brevdo & Bridges (1997).

In Section 4.1 the solution is derived following Brevdo & Bridges (1997). The leading-order behaviour of this integral is found in Section 4.2 by the method of steepest-descent (Huerre, 2002) and Briggs' method (Briggs, 1964), each adapted for the time-periodic case. Additionally, the results of these sections provide a means of interpretation of the numerical simulation results in terms of convective and absolute instability (which are rigorously defined in this chapter) and through the derivation of the growth-rate measures already used.

The methods discussed in this chapter are then applied to the semi-infinite Stokes layer in Chapter 5.

4.1 Integral solution to the periodic problem

This section is concerned with finding an integral expression for the disturbance in a periodic flow that is generated by some external forcing. Since Squire's theorem (Squire, 1933) has been shown to hold for temporally periodic flows (Section 1.1), only the two-dimensional problem will be considered in this section.

A 2D periodic solution to the nondimensional Navier–Stokes equations, $U(y,\tau)$, is perturbed and the resulting equations are linearised and combined into a single partial differential equation (PDE). This process is similar to the derivation of the disturbance equations in Section 1.1 except that the x-dependence is retained. For this chapter, the problem will be kept as general as possible so that the work is appropriate for any periodic flow.

The independent variables of the resulting PDE are: $\tau > 0$, the nondimensional time; $x \in (-\infty, \infty)$, the streamwise co-ordinate; and y, the wall-normal co-ordinate which may be finite or semi-infinite. The equation describing the evolution of a perturbation to the

basic state U is

$$\left[\frac{\partial}{\partial\tau}\nabla^2 + ReU(y,\tau)\nabla^2\frac{\partial}{\partial x} - ReU''\frac{\partial}{\partial x} - \frac{1}{2}\nabla^4\right]v(x,y,\tau) = 0. \tag{4.1.1}$$

This is not an equation one would generally expect to solve analytically, which is why numerical methods are usually deployed. It is, however, possible to ascertain the leading-order behaviour.

First, the problem is simplified by discretisation in y. This results in the y-derivatives being replaced with matrix approximations and reduces the number of independent variables by converting the solution $\psi(x,y,\tau)$ to a vector $\boldsymbol{\psi}(x,\tau)$ of size N. Though no particular discretisation need be committed to for this section, it is suggested that the reader bear in mind the Chebyshev discretisation of Section 1.2.

The differential equation can then be written as the differential matrix problem,

$$\left[\frac{\partial}{\partial\tau}\left(\frac{\partial^2}{\partial x^2}\boldsymbol{I} + \boldsymbol{\mathcal{D}}^2\right) + Re\boldsymbol{U}(\tau)\left(\frac{\partial^2}{\partial x^2}\boldsymbol{I} + \boldsymbol{\mathcal{D}}^2\right) - Re\boldsymbol{U}''(\tau)\frac{\partial}{\partial x}\boldsymbol{I} - \frac{1}{2}\left(\frac{\partial^2}{\partial x^2}\boldsymbol{I} + \boldsymbol{\mathcal{D}}^2\right)^2\right]\boldsymbol{v}(x,\tau) = 0, \tag{4.1.2}$$

where $\boldsymbol{I}$ denotes the identity matrix of size N. The basic state is incorporated in $\boldsymbol{U}(\tau)$ and $\boldsymbol{U}''(\tau)$ which contain the discrete vector expressions of $U(y,\tau)$ and $U''(y,\tau)$ along the diagonal and $\boldsymbol{\mathcal{D}}^j$ is the matrix approximation to the j^{th} y-derivative. This differential equation will be subject to some initial condition

$$\boldsymbol{v}(x,0) = \boldsymbol{v}_0(x), \tag{4.1.3}$$

with $\boldsymbol{v}_0(x) \to 0$ as $x \to \pm\infty$. Furthermore, it will be assumed that

$$\boldsymbol{v}(x,\tau) \to 0 \quad \text{as} \quad x \to \pm\infty \quad \forall\tau. \tag{4.1.4}$$

4.1.1 Fourier transform

The work of Brevdo & Bridges (1997) assumes a differential equation with time-periodic coefficients, but of a slightly different form to (4.1.1). This required some minor adaptation for the present work, though in essence the approach is the same.

Consider now the problem under some external forcing. This forcing can be used

to generate the initial disturbance and some such forcing was described in (2.3.1). The equation governing the response of the system to such forcing is

$$\left[\frac{\partial}{\partial\tau}\left(\frac{\partial^2}{\partial x^2}\boldsymbol{I}+\boldsymbol{\mathcal{D}}^2\right)+Re\boldsymbol{U}(\tau)\left(\frac{\partial^2}{\partial x^2}\boldsymbol{I}+\boldsymbol{\mathcal{D}}^2\right)-Re\boldsymbol{U}''(\tau)\frac{\partial}{\partial x}\boldsymbol{I}-\frac{1}{2}\left(\frac{\partial^2}{\partial x^2}\boldsymbol{I}+\boldsymbol{\mathcal{D}}^2\right)^2\right]\boldsymbol{v}(x,\tau) = \bar{\boldsymbol{g}}(x,\tau), \quad (4.1.5)$$

with initial condition (4.1.3). The following Fourier transform can then be applied

$$\boldsymbol{w}(\alpha)=\int_{-\infty}^{\infty}\boldsymbol{w}(x)\mathrm{e}^{-i\alpha x}\,\mathrm{d}x, \quad (4.1.6a)$$

$$\boldsymbol{w}(x)=\frac{1}{2\pi}\int_{-\infty}^{\infty}\boldsymbol{w}(\alpha)\mathrm{e}^{i\alpha x}\,\mathrm{d}\alpha, \quad (4.1.6b)$$

where α can still be interpreted as a streamwise wavenumber but is now, in general, complex. Note that a function is distinguishable from its transform by the choice of independent variable.

Applying this transform to (4.1.5) gives

$$\left[\frac{\partial}{\partial\tau}\left(\boldsymbol{\mathcal{D}}^2-\alpha^2\boldsymbol{I}\right)+i\alpha Re\boldsymbol{U}(\tau)\left(\boldsymbol{\mathcal{D}}^2-\alpha^2\boldsymbol{I}\right)-i\alpha Re\boldsymbol{U}''(\tau)-\frac{1}{2}\left(\boldsymbol{\mathcal{D}}^2-\alpha^2\boldsymbol{I}\right)^2\right]\boldsymbol{v}(\alpha,\tau) = \bar{\boldsymbol{g}}(\alpha,\tau). \quad (4.1.7)$$

Defining the operator $\boldsymbol{K}(\alpha)=\boldsymbol{\mathcal{D}}^2-\alpha^2\boldsymbol{I}$, multiplying through by $\boldsymbol{K}^{-1}(\alpha)$ and rearranging gives

$$\frac{\partial}{\partial\tau}\boldsymbol{v}(\alpha,\tau)=\left[\frac{1}{2}\boldsymbol{K}(\alpha)+i\alpha Re\left(\boldsymbol{U}''(\tau)\boldsymbol{K}^{-1}(\alpha)-\boldsymbol{U}(\tau)\right)\right]\boldsymbol{v}(\alpha,\tau)+\boldsymbol{g}(\alpha,\tau), \quad (4.1.8)$$

where $\boldsymbol{g}(\alpha,\tau)=\boldsymbol{K}^{-1}(\alpha)\bar{\boldsymbol{g}}(\alpha,\tau)$. The operator $\boldsymbol{K}$ is invertible since it only acts on vectors in a space where the boundary conditions holds.

The operator

$$\boldsymbol{L}(\alpha,\tau)=\frac{1}{2}\boldsymbol{K}(\alpha)+i\alpha Re\left(\boldsymbol{U}''(\tau)\boldsymbol{K}^{-1}(\alpha)-\boldsymbol{U}(\tau)\right) \quad (4.1.9)$$

only has τ dependence through the basic state U, so $\boldsymbol{L}(\alpha,\tau)$ is 2π-periodic in τ. The definition of this operator allows the problem to be written in the much more compact

form

$$\frac{\partial}{\partial\tau}\boldsymbol{v}(\alpha,\tau)=\boldsymbol{L}(\alpha,\tau)\boldsymbol{v}(\alpha,\tau)+\boldsymbol{g}(\alpha,\tau), \tag{4.1.10}$$

with initial condition

$$\boldsymbol{v}(\alpha,0)=\boldsymbol{v}_0(\alpha), \tag{4.1.11}$$

where $\boldsymbol{v}_0(\alpha)$ is the Fourier transform of $\boldsymbol{v}_0(x)$. This is a similar expression to that derived in Brevdo & Bridges (1997).

4.1.2 Fundamental matrix and Floquet theory

Consider now the matrix initial-value problem formulated for the associated homogeneous system,

$$\frac{\partial}{\partial\tau}\boldsymbol{\Phi}(\alpha,\tau)=\boldsymbol{L}(\alpha,\tau)\boldsymbol{\Phi}(\alpha,\tau), \tag{4.1.12}$$

with initial condition

$$\boldsymbol{\Phi}(\alpha,0)=\boldsymbol{I}. \tag{4.1.13}$$

The matrix $\boldsymbol{\Phi}$ is the fundamental matrix of the problem and so the columns are linearly independent vectors from which any solution can be constructed. The periodicity of $\boldsymbol{L}$ suggests the application of Floquet theory to solve the differential equation, so the solution is decomposed as

$$\boldsymbol{\Phi}(\alpha,\tau)=\boldsymbol{Q}(\alpha,\tau)\mathrm{e}^{\boldsymbol{A}(\alpha)\tau}, \tag{4.1.14}$$

where $\boldsymbol{Q}(\alpha,\tau)$ is a non-singular, smooth, 2π-periodic matrix function of τ. Taking this expression at $\tau=0$, the initial condition reveals that $\boldsymbol{Q}(\alpha,0)=\boldsymbol{I}$. From periodicity we must therefore have $\boldsymbol{Q}(\alpha,2\pi)=\boldsymbol{I}$. Thus,

$$\boldsymbol{A}(\alpha)=\frac{1}{2\pi}\log\Big(\boldsymbol{\Phi}(\alpha,2\pi)\Big), \tag{4.1.15}$$

It will be assumed here that $\boldsymbol{A}(\alpha)$ is analytic for all $\alpha\in\mathbb{C}$. This conjecture is justified in some detail in Brevdo & Bridges (1996) for the spatially periodic case.

It follows from this assumption that

$$\boldsymbol{Q}(\alpha,\tau)=\boldsymbol{\Phi}(\alpha,\tau)\mathrm{e}^{-\boldsymbol{A}(\alpha)\tau} \tag{4.1.16}$$

is an entire function in α.

4.1.3 Laplace transform

The Floquet decomposition can be used to transform the forced problem to a problem with constant coefficients by making the substitution

$$\boldsymbol{v}(\alpha,\tau) = \boldsymbol{Q}(\alpha,\tau)\boldsymbol{f}(\alpha,\tau), \tag{4.1.17}$$

where $\boldsymbol{f}$ is a vector function. Since $\boldsymbol{v}$ satisfies (4.1.10), differentiation with respect to τ gives,

$$\frac{\partial \boldsymbol{Q}}{\partial \tau}\boldsymbol{f} + \boldsymbol{Q}\frac{\partial \boldsymbol{f}}{\partial \tau} = \boldsymbol{L}\boldsymbol{v} + \boldsymbol{g} = \boldsymbol{L}\boldsymbol{Q}\boldsymbol{f} + \boldsymbol{g}, \tag{4.1.18}$$

where the independent variables have been ignored. It follows from the above consideration of (4.1.12) that

$$\begin{aligned}
\frac{\partial \boldsymbol{Q}}{\partial \tau}\boldsymbol{f} + \boldsymbol{Q}\frac{\partial \boldsymbol{f}}{\partial \tau} &= \boldsymbol{L}\boldsymbol{\Phi}\mathrm{e}^{-\boldsymbol{A}\tau}\boldsymbol{f} + \boldsymbol{g}, \\
&= \frac{\partial \boldsymbol{\Phi}}{\partial \tau}\mathrm{e}^{-\boldsymbol{A}\tau}\boldsymbol{f} + \boldsymbol{g}, \\
&= \frac{\partial}{\partial \tau}\left[\boldsymbol{Q}\mathrm{e}^{\boldsymbol{A}\tau}\right]\mathrm{e}^{-\boldsymbol{A}\tau}\boldsymbol{f} + \boldsymbol{g}, \\
&= \left(\frac{\partial \boldsymbol{Q}}{\partial \tau} + \boldsymbol{Q}\boldsymbol{A}\right)\boldsymbol{f} + \boldsymbol{g}.
\end{aligned}$$

Cancellation of the $(\partial \boldsymbol{Q}/\partial\tau)\boldsymbol{f}$ terms results in a differential equation in $\boldsymbol{f}$ with constant coefficients and a periodic forcing,

$$\frac{\partial}{\partial \tau}\boldsymbol{f}(\alpha,\tau) - \boldsymbol{A}(\alpha)\boldsymbol{f}(\alpha,\tau) = \boldsymbol{Q}^{-1}(\alpha,\tau)\boldsymbol{g}(\alpha,\tau). \tag{4.1.20}$$

The initial value is found from $\boldsymbol{v} = \boldsymbol{Q}\boldsymbol{f}$ by recalling that $\boldsymbol{Q}(\alpha,0) = \boldsymbol{I}$ and $\boldsymbol{v}(\alpha,0) = \boldsymbol{v_0}(\alpha)$, giving

$$\boldsymbol{f}(\alpha,0) = \boldsymbol{v}_0(\alpha). \tag{4.1.21}$$

The following Laplace transform can be applied to this problem (a function and its transform are again distinguished by their independent variables):

$$\boldsymbol{w}(\mu) = \int_0^\infty \boldsymbol{w}(\tau)\mathrm{e}^{-\mu\tau}\,\mathrm{d}\tau, \tag{4.1.22a}$$

$$\boldsymbol{w}(\tau) = \frac{1}{2\pi}\int_{\sigma-i\infty}^{\sigma+i\infty} \boldsymbol{w}(\mu)\mathrm{e}^{\mu\tau}\,\mathrm{d}\mu. \tag{4.1.22b}$$

The appropriate choice of σ is made below.

The resulting equation is

$$[\boldsymbol{A}(\alpha) - \mu \boldsymbol{I}]\, \boldsymbol{f}(\alpha, \mu) = \boldsymbol{s}(\alpha, \mu), \tag{4.1.23}$$

where

$$\boldsymbol{s}(\alpha, \mu) = -\int_0^\infty \boldsymbol{Q}^{-1}(\alpha, \tau) \boldsymbol{g}(\alpha, \tau) \mathrm{e}^{-\mu\tau}\, \mathrm{d}\tau - \boldsymbol{v}_0(\alpha). \tag{4.1.24}$$

The solution to (4.1.20) in Laplace space can then be written as

$$\boldsymbol{f}(\alpha, \mu) = [\boldsymbol{A}(\alpha) - \mu \boldsymbol{I}]^{-1}\, \boldsymbol{s}(\alpha, \mu). \tag{4.1.25}$$

The notation used here differs from that implemented in Brevdo & Bridges (1997), where the Laplace transform was introduced based on some frequency ω that is related to the Floquet exponent used here by $\omega = i\mu$. The symbol μ is then used to denote that Floquet multiplier in Brevdo & Bridges (1997). The decision to diverge from this notation was made for consistency with the rest of the current work. Note also that it could be considered misleading to refer to the 'frequency' of the disturbance without taking into account the periodic component in the Floquet normal-mode form.

4.1.4 Fourier and Laplace inversion

To transform back into physical space, first apply the inverse Laplace transform (4.1.22b) to (4.1.25) to get $\boldsymbol{f}(\alpha, \tau)$. This then gives

$$\boldsymbol{v}(\alpha, \tau) = \frac{\boldsymbol{Q}(\alpha, \tau)}{2\pi} \int_{\sigma - i\infty}^{\sigma + i\infty} [\boldsymbol{A}(\alpha) - \mu \boldsymbol{I}]^{-1}\, \boldsymbol{s}(\alpha, \mu) \mathrm{e}^{\mu\tau}\, \mathrm{d}\mu, \tag{4.1.26}$$

where

$$\sigma > \max\left\{ \mu_r \mid \det[\boldsymbol{A}(\alpha) - \mu \boldsymbol{I}] = 0,\ \alpha \in \mathbb{R} \right\}. \tag{4.1.27}$$

It will be seen below that this choice of σ ensures that causality is satisfied.

The inverse Fourier transform (4.1.6b) is then applied, giving the integral solution to the forced problem (4.1.5) as

$$\boldsymbol{v}(x, \tau) = \frac{1}{4\pi^2} \int_{-\infty}^{\infty} \boldsymbol{Q}(\alpha, \tau) \int_{\sigma - i\infty}^{\sigma + i\infty} [\boldsymbol{A}(\alpha) - \mu \boldsymbol{I}]^{-1}\, \boldsymbol{s}(\alpha, \mu) \mathrm{e}^{\mu\tau + i\alpha x}\, \mathrm{d}\mu\, \mathrm{d}\alpha. \tag{4.1.28}$$

4.1.5 Dispersion relation

When performing the integration in (4.1.28), the existence of poles in the complex plane are important. We can see from (4.1.28) that the integrand is not defined when the matrix $[\boldsymbol{A}(\alpha) - \mu \boldsymbol{I}]$ is singular, i.e. when $\det[\boldsymbol{A}(\alpha) - \mu \boldsymbol{I}] = 0$. In other words, the integrand is not well defined at the eigenvalues of the matrix $\boldsymbol{A}$. The dispersion relation will be defined to be the characteristic polynomial of this matrix

$$D(\alpha, \mu) = \det[\boldsymbol{A}(\alpha) - \mu \boldsymbol{I}]. \tag{4.1.29}$$

Roots of D (being singularities of the integrand) are responsible for non-trivial solutions to the problem. In other words, the dispersion relation is a relationship between α and μ for which the roots indicate that the system allows for normal mode solutions with this wavenumber and Floquet exponent. This means that solving $D(\alpha, \mu) = 0$ is equivalent to solving the eigenvalue problem described in Chapter 1, except that now $\alpha \in \mathbb{C}$ in general.

The integral solution (4.1.28) can be rewritten to show explicitly that roots to the dispersion relation generate poles in the integrand. This is achieved by introducing the adjugate matrix of $[\boldsymbol{A}(\alpha) - \mu \boldsymbol{I}]$. The adjugate of a matrix is the transpose of the cofactor matrix and is defined in this way so that the identity

$$[\boldsymbol{A}(\alpha) - \mu \boldsymbol{I}]^{-1} = \frac{1}{\det[\boldsymbol{A}(\alpha) - \mu \boldsymbol{I}]} \operatorname{adj}[\boldsymbol{A}(\alpha) - \mu \boldsymbol{I}] \tag{4.1.30}$$

holds. Here, adj denotes the adjugate which is not to be confused with the adjoint of the matrix. Due to the manner in which it is constructed, $\operatorname{adj}[\boldsymbol{A}(\alpha) - \mu \boldsymbol{I}]$ is well-defined for any choice of α and μ since every entry of $\boldsymbol{A}$ is well-defined. This allows for (4.1.28) to be rewritten as

$$\boldsymbol{v}(x, \tau) = \frac{1}{4\pi^2} \int_F \boldsymbol{Q}(\alpha, \tau) \int_L \frac{\boldsymbol{G}(\alpha, \mu)}{D(\alpha, \mu)} \mathrm{e}^{\mu\tau + i\alpha x} \, \mathrm{d}\mu \, \mathrm{d}\alpha, \tag{4.1.31}$$

where

$$\boldsymbol{G}(\alpha, \mu) = \operatorname{adj}[\boldsymbol{A}(\alpha) - \mu \boldsymbol{I}] \boldsymbol{s}(\alpha, \mu),$$

and the contours F and L are the inversion contours for the Fourier and Laplace transforms. That is, the real line and the straight line $(\sigma - i\infty, \sigma + i\infty)$, respectively. This shows explicitly that the integrand has poles when $D(\alpha, \mu) = 0$.

The roots of the dispersion relation are of interest so define the μ-roots of D to be the values of μ satisfying $D(\alpha, \mu) = 0$ for some given α and let the α-roots be the values of α satisfying $D(\alpha, \mu) = 0$ for some given μ. Note that (as shown for $\alpha \in \mathbb{R}$ in Chapter 1) for any given α there are an infinite number of μ-roots (and vice versa). For this reason, it is sometimes considered necessary to introduce a subscript to indicate that this is one value of many, i.e. $\mu_j(\alpha)$ for $j = 0, 1, 2, ...$ describes all μ-roots of D and $\alpha_k^{\pm}(\mu)$ for $k = 0, 1, 2, ...$ describes all α-roots, with the superscript indicating the sign of the imaginary part (the significance of this will be discussed later). In most cases only the most dominant roots are of interest and these may be indicated by dropping the subscript.

4.2 Leading-order asymptotic behaviour

The leading-order behaviour of the solution integral (4.1.31) will now be considered in the case of an impulsive forcing $\bar{\boldsymbol{g}}(x, \tau) = \delta(x)\delta(\tau)$ where δ is the Dirac-delta function. It is important to consider a forcing localised in both space and time so that after the initial excitation the asymptotic behaviour is dictated by the properties of the flow. For instance, it would be misleading to refer to a disturbance as absolutely unstable when the flow is subjected to forcing at regular time intervals. In particular, an impulsive excitation is used since this will excite all wavenumbers and frequencies equally.

There are two approaches to deducing the asymptotic behaviour of this integral: the method of steepest-descent (Huerre, 2002; Lingwood, 1997) in which the μ-integral is performed first, and Briggs' method (Briggs, 1964; Bers, 1983; Lingwood, 1997) in which the α-integral is performed first. An excellent comparison of these methods is presented by Lingwood (1997) for the rotating disc boundary layer in which the local velocities are dependent on the radial direction. This review has greatly informed the current work and differs from the present analysis through the steady, spatially inhomogeneous basic state.

It will be shown that the leading-order behaviour deduced is independent of the approach taken, but a naïve application of the steepest-descent method results in only a necessary condition for absolute instability. Briggs' method provides the framework for a sufficient condition via the collision criteria.

For the entirety of this section a variable, its Fourier transform, and its Laplace transform are all denoted by the same symbol with the distinction being in the independent

variable. For instance, $f(x,\tau)$ is a spatial function, $f(\alpha,\tau)$ denotes the Fourier transform and $f(x,\mu)$ denotes the Laplace transform while $f(\alpha,\mu)$ has been acted on by both transforms. This convention was used in Brevdo & Bridges (1996, 1997).

4.2.1 Integration contours

Consider the integral solution (4.1.31). In order to perform the integration along the F and L contours, they will be closed by semi-circles of infinite radius such that the integrand converges to zero along the semi-circular path, hence making no contribution to the integral.

First, consider the contour F and assume that $x > 0$. In this case the contour can be closed in the top half of the complex α-plane since

$$e^{i\alpha x} \to 0 \quad \text{as} \quad \alpha_i \to +\infty,$$

so the integrand vanishes in this limit. In the case $x < 0$ the contour must be closed in the bottom half-plane to ensure the same convergence. Hence, poles in the integrand for $\alpha_i > 0$ contribute to the downstream ($x > 0$) evolution of a disturbance and poles with $\alpha_i < 0$ contribute to the upstream ($x < 0$) evolution. This is illustrated in Figure 4.1b.

Consider now the contour L when $\tau > 0$. In this case the contour will be closed in the left half-plane since

$$e^{\mu\tau} \to 0 \quad \text{as} \quad \mu_r \to -\infty,$$

so the integrand vanishes in this limit. This is illustrated in Figure 4.1a. Notice that choosing σ such that all poles are on the left-hand side of L has ensured causality since for $\tau < 0$ the integrand converges to zero in the right half-plane. The integral is therefore zero for $\tau < 0$ since there are no poles contained within this contour. In other words, the choice of σ has ensured that the disturbance cannot develop for any times prior to the forcing.

In addition to the contours, Figure 4.1 shows the curves $\mu(F)$ and $\alpha^{\pm}(L)$. These curves are the poles of the integrand generated along the contours of integration. The curve $\mu(F)$ represents the μ-roots of D for $\alpha \in F$ and $\alpha^{\pm}(L)$ represent the α-roots of D for $\mu \in L$ (with the superscript indicating upstream or downstream contribution). It was previously noted that for a given α or μ an infinite number of poles exist, but in the figure

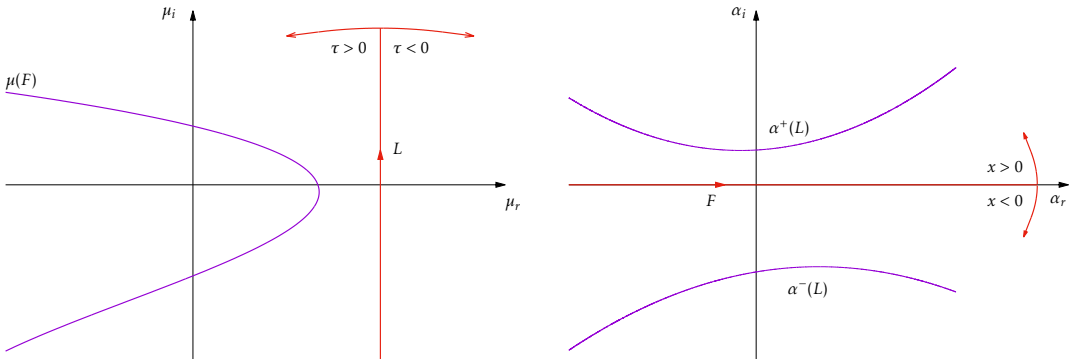

(a) (b)

Figure 4.1: Sketch of the integration contours and the corresponding poles in the complex μ-plane (a) and complex α-plane (b). The closure of the Fourier contour F above the real line corresponds to $x > 0$ to ensure that the integrand vanishes on this infinite-radius semi-circle. The closure below the real line corresponds to $x < 0$. The closure of the Laplace contour L to the left of the imaginary axis corresponds to $\tau > 0$ as the integrand vanishes on this infinite-radius semi-circle. Closure to the right corresponds to $\tau < 0$. The poles contained in these closed contours therefore contribute to the asymptotic evaluation of the solution integral and only the poles corresponding to the leading-order are shown. The poles correspond to the roots of the dispersion relation D. The curve $\mu(F)$ denotes the dominant μ-root for $\alpha \in F$ and $\alpha^{\pm}(L)$ denotes the dominant α-roots for $\mu \in L$ with the superscript indicating whether the poles correspond to $x > 0$ or $x < 0$. Since σ was chosen to ensure that all poles occur to the left of L, when $\tau < 0$ there is no contribution to the asymptotics, enforcing causality.

only the poles with the greatest contribution are shown. For the μ-roots this means that

$$\Re\mathrm{e}\{\mu(\alpha)\} \geq \Re\mathrm{e}\{\mu_j(\alpha)\} \quad \forall j. \tag{4.2.1}$$

Similarly,

$$\Im\mathrm{m}\{\alpha^+(\mu)\} \leq \Im\mathrm{m}\{\alpha_k^+(\mu)\} \quad \text{and}$$
$$\Im\mathrm{m}\{\alpha^-(\mu)\} \geq \Im\mathrm{m}\{\alpha_k^-(\mu)\} \quad \forall k.$$

It should become clear as the analysis progresses exactly why these choices are considered dominant.

4.2.2 Method of steepest-descent

The process described herein is adapted for a temporally periodic flow from Lingwood (1997) and Huerre (2002).

Laplace integration

Consider first the Laplace integral,

$$\boldsymbol{v}(\alpha,\tau) = \frac{1}{2\pi}\oint_{C_L} \frac{\boldsymbol{G}(\alpha,\mu)}{D(\alpha,\mu)} \mathrm{e}^{\mu\tau}\,\mathrm{d}\mu, \tag{4.2.3}$$

for some given α where C_L is the closed contour described above: the line L with semi-circular closure to the left. This is then related to $\boldsymbol{v}(x,\tau)$ by

$$\boldsymbol{v}(x,\tau) = \frac{1}{2\pi}\int_F \boldsymbol{Q}(\alpha,\tau)\boldsymbol{v}(\alpha,\tau)\mathrm{e}^{i\alpha x}\,\mathrm{d}\alpha. \tag{4.2.4}$$

Notice that $\boldsymbol{v}(\alpha,\tau)$ is not exactly the Fourier transform of $\boldsymbol{v}(x,\tau)$ due to the appearance of $\boldsymbol{Q}(\alpha,\tau)$ but this is a practical definition that incorporates the periodicity of the problem and keeps notation compact and efficient.

The integral (4.2.3) can be evaluated by appealing to Cauchy's residue theorem which states that for a complex function f being integrated along a closed contour C with poles c_j $(j = 1,\ldots,J)$ inside C,

$$\oint_C f(z)\,\mathrm{d}z = 2\pi i \sum_{j=1}^{J} \mathrm{Res}(f,c_j), \tag{4.2.5}$$

where $\mathrm{Res}(f,c_j)$ is the Residue of the integrand f at the pole c_j.

For integrands that can be written in the form $f(z) = g(z)/h(z)$ where g and h are holomorphic and $h(c_j) = 0$, such as (4.2.3), the residue can be calculated by

$$\mathrm{Res}(f,c_j) = \frac{g(c_j)}{h'(c_j)} \tag{4.2.6}$$

provided $h'(c_j) \neq 0$ (this means that c_j is a simple pole). Here, $'$ denotes differentiation with respect to the variable of integration (in this case z). Applying this method to (4.2.3) gives

$$\mathrm{Res}\left(\frac{\boldsymbol{G}(\alpha,\mu)}{D(\alpha,\mu)}\mathrm{e}^{\mu\tau},\mu_j(\alpha)\right) = \frac{\boldsymbol{G}\Big(\alpha,\mu_j(\alpha)\Big)}{\frac{\partial D}{\partial\mu}\Big(\alpha,\mu_j(\alpha)\Big)}\mathrm{e}^{\mu_j(\alpha)\tau}, \tag{4.2.7}$$

with $\mu_j(\alpha)$ being any μ-root of D for the given α. This gives,

$$\boldsymbol{v}(\alpha,\tau) = i\sum_{j=1}^{\infty} \frac{\boldsymbol{G}\Big(\alpha,\mu_j(\alpha)\Big)}{\frac{\partial D}{\partial\mu}\Big(\alpha,\mu_j(\alpha)\Big)}\mathrm{e}^{\mu_j(\alpha)\tau}. \tag{4.2.8}$$

Since the leading-order behaviour as $\tau \to \infty$ is of interest, denote by $\mu(\alpha)$ the $\mu_j(\alpha)$ with largest real part as in (4.2.1). It is clear from (4.2.8) that this is the most dominant term as $\tau \to \infty$. Note that $\alpha \in F$, $\mu(\alpha)$ lies on the curve $\mu(F)$ shown in Figure 4.1a.

Performing the Laplace integration in this way has resulted in

$$\boldsymbol{v}(\alpha,\tau) \sim i\frac{\boldsymbol{G}\Big(\alpha,\mu(\alpha)\Big)}{\frac{\partial D}{\partial \mu}\Big(\alpha,\mu(\alpha)\Big)}\mathrm{e}^{\mu(\alpha)\tau} \tag{4.2.9}$$

to leading order.

Fourier integration

The solution (4.1.31) can now be written as

$$\boldsymbol{v}(x,\tau) \sim \frac{i}{2\pi}\int_F \boldsymbol{Q}(\alpha,\tau)\frac{\boldsymbol{G}\Big(\alpha,\mu(\alpha)\Big)}{\frac{\partial D}{\partial \mu}\Big(\alpha,\mu(\alpha)\Big)}\mathrm{e}^{\mu(\alpha)\tau+i\alpha x}\,\mathrm{d}\alpha. \tag{4.2.10}$$

The leading-order behaviour of this integral as $\tau \to \infty$ can be found along the spatial/temporal ray $x/\tau = V$, where V is a constant, by the method of steepest-descent.

First, use $x/\tau = V$ to write the integral in the appropriate form

$$\boldsymbol{v}(\tau;V) \sim \frac{i}{2\pi}\int_F \boldsymbol{Q}(\alpha,\tau)\frac{\boldsymbol{G}\Big(\alpha,\mu(\alpha)\Big)}{\frac{\partial D}{\partial \mu}\Big(\alpha,\mu(\alpha)\Big)}\mathrm{e}^{[i\alpha V+\mu(\alpha)]\tau}\,\mathrm{d}\alpha. \tag{4.2.11}$$

By defining

$$\rho(\alpha;V) = i\alpha V + \mu(\alpha), \tag{4.2.12}$$

and setting

$$\boldsymbol{h}(\alpha,\tau) = \frac{i}{2\pi}\boldsymbol{Q}(\alpha,\tau)\frac{\boldsymbol{G}\Big(\alpha,\mu(\alpha)\Big)}{\frac{\partial D}{\partial \mu}\Big(\alpha,\mu(\alpha)\Big)}. \tag{4.2.13}$$

This integral can be written in the form

$$\boldsymbol{v}(\tau;V) \sim \int_F \boldsymbol{h}(\alpha,\tau)\mathrm{e}^{\rho(\alpha;V)\tau}\,\mathrm{d}\alpha, \tag{4.2.14}$$

where $\boldsymbol{h}$ is 2π-periodic in τ.

To perform the method of steepest-descent, a point α_* must be found such that ρ has

a saddle point at this location, i.e.

$$\frac{\partial \rho}{\partial \alpha}(\alpha_*; V) = 0. \tag{4.2.15}$$

From the definition of ρ, this is equivalent to the condition

$$\frac{\partial \mu}{\partial \alpha}(\alpha_*; V) = -iV. \tag{4.2.16}$$

It is important to note that the location of the saddle point α_* depends on the ray of interest (i.e. the choice of V). The exponent ρ can be approximated near this saddle point using the Taylor expansion

$$\rho(\alpha; V) \sim \rho(\alpha_*; V) + \frac{1}{2}\frac{\partial^2 \rho}{\partial \alpha^2}(\alpha_*; V)(\alpha - \alpha_*)^2. \tag{4.2.17}$$

The integral contour F can be deformed to the path of steepest-descent through α_*. As $\tau \to \infty$ the dominant contribution to the integral will arise in the vicinity of α_* so the deformed contour can be restricted to a small segment around α_* before being extended infinitely on either side. In evaluating the integral it is therefore appropriate to approximate $\boldsymbol{h}(\alpha, \tau)$ by $\boldsymbol{h}(\alpha_*, \tau)$ and use the Taylor expansion of ρ, giving

$$\begin{aligned}\boldsymbol{v}(\tau; V) &\sim \int_{-\infty}^{\infty} \boldsymbol{h}(\alpha_*, \tau) \mathrm{e}^{\left[\rho(\alpha_*;V) + \frac{1}{2}(\alpha-\alpha_*)^2 \frac{\partial^2 \rho}{\partial \alpha^2}(\alpha_*;V)\right]\tau} \,\mathrm{d}\alpha, \\ &= \boldsymbol{h}(\alpha_*, \tau) \mathrm{e}^{\rho(\alpha_*;V)} \int_{-\infty}^{\infty} \mathrm{e}^{\left[\frac{1}{2}\frac{\partial^2 \rho}{\partial \alpha^2}(\alpha_*;V)\tau\right]\alpha^2} \,\mathrm{d}\alpha.\end{aligned}$$

The integral is of Gaussian form, giving the solution

$$\boldsymbol{v}(\tau; V) \sim \boldsymbol{h}(\alpha_*; V) \mathrm{e}^{\rho(\alpha_*;V)\tau} \sqrt{\frac{-\pi}{\frac{1}{2}\frac{\partial^2 \rho}{\partial \alpha^2}(\alpha_*; V)\tau}}. \tag{4.2.19}$$

Using the definitions of $\boldsymbol{h}$ and ρ gives the following leading-order expression for the solution along ray $x/\tau = V$,

$$\boldsymbol{v}(x, \tau) \sim \frac{\boldsymbol{Q}(\alpha_*, \tau)\boldsymbol{G}(\alpha_*, \mu_*)}{\left[2\pi\tau \frac{\partial^2 \mu}{\partial \alpha^2}(\alpha_*)\right]^{\frac{1}{2}} \frac{\partial D}{\partial \mu}\left(\alpha_*, \mu_*\right)} \mathrm{e}^{\frac{3\pi i}{2} + i\alpha_* x + \mu_* \tau}, \tag{4.2.20}$$

where α_* is given by

$$\frac{\partial \mu}{\partial \alpha}(\alpha_*) = -iV \tag{4.2.21}$$

and $\mu_* = \mu(\alpha_*)$.

To an observer travelling along the ray $x/\tau = V$ the disturbance will therefore take the form of a wave with complex wavenumber α_*. Temporally the wavepacket will take the quasi-periodic form described by the product of a 2π-periodic function with $\exp(\mu_*\tau)$.

The observed growth over each period along this ray is given by the real part of the exponent in (4.2.20), that is

$$\lambda(V) = -\mathfrak{Im}\{\alpha_*\}V + \mathfrak{Re}\{\mu(\alpha_*)\} \tag{4.2.22}$$

Fixed spatial location ($V = 0$)

At face value, this suggests that absolute instability can be found by setting $V = 0$ to consider the leading-order temporal behaviour at any spatial location since

$$x/\tau = 0 \Rightarrow x = x_0 = constant.$$

In this case α_* is the point satisfying

$$\frac{\partial \mu}{\partial \alpha}(\alpha_*) = 0. \tag{4.2.23}$$

Relating this derivative to derivatives of the dispersion relation D gives

$$\frac{\partial D}{\partial \alpha} = \frac{\partial D}{\partial \mu}\frac{\partial \mu}{\partial \alpha} \tag{4.2.24}$$

so, for $\mu_* = \mu(\alpha_*)$, the condition (4.2.23) is equivalent to

$$\frac{\partial D}{\partial \alpha}\Big(\alpha_*, \mu_*\Big) = 0, \tag{4.2.25}$$

meaning that there is a saddle point of the dispersion relation at α_*. Using this fact gives

$$\frac{\partial^2 \mu}{\partial \alpha^2} = \frac{\partial^2 D}{\partial \alpha^2}\left[\frac{\partial D}{\partial \mu}\right]^{-1}, \tag{4.2.26}$$

and so the leading-order response (4.2.20) can be written as

$$\boldsymbol{v}(x,\tau) \sim \frac{\boldsymbol{Q}(\alpha_*,\tau)\boldsymbol{G}(\alpha_*,\mu_*)}{\sqrt{2\pi\tau\frac{\partial^2 D}{\partial\alpha^2}\left(\alpha_*,\mu_*\right)\frac{\partial D}{\partial\mu}\left(\alpha_*,\mu_*\right)}}\mathrm{e}^{\frac{3\pi i}{2}+i\alpha_* x+\mu_*\tau}. \tag{4.2.27}$$

In general, the condition (4.2.25) is interpreted as a saddle point which manifests when mapping from the μ-plane to the α-plane. This is a computationally demanding problem since α appears to the fourth power in the eigenvalue problem whereas μ only appears linearly. Instead, an equivalent condition will be used. Namely, this is the existence of a cusp at this location (Kupfer *et al.* , 1987) when mapping from the α-plane to the μ-plane. The relationship between saddle points and cusps becomes apparent by observing that

$$\frac{\partial\alpha}{\partial\mu} \to \infty \quad \text{as} \quad \mu \to \mu_* \tag{4.2.28}$$

is a direct consequence of (4.2.23). The location of such a cusp would then dictate temporal growth along any ray $x/\tau = 0$ when $\mathfrak{Re}\{\mu_*\} > 0$ and decay when $\mathfrak{Re}\{\mu_*\} < 0$ according to (4.2.22).

Necessary but not sufficient condition

Implicit in the above analysis is the assumption that the multiple Riemann sheets of $\mu(\alpha)$ can be considered separately. However, this is not always the case. The evaluation of the Fourier integral is only valid if there is no singularity of the integrand near enough to the saddle point that the deformation to the path of steepest-descent is impossible (Lingwood, 1997). Such a singularity exists when $\partial D/\partial\mu = 0$ and the location of this pole is a branch point of $\mu(\alpha)$ and so the Riemann sheets cannot all be considered separately near such a singularity.

This highlights the possibility of this approach being invalid in some cases, but ensuring validity requires a careful consideration of the geometry of $\mu(\alpha)$ in the neighbourhood of the steepest-descent path (Lingwood, 1997).

Without this additional consideration, the method of steepest-descent does not provide a sufficient condition for absolute instability as not all saddle points satisfy the *collision criteria* (Brevdo & Bridges, 1997). In terms of the saddle point in the α-plane, this criteria requires that the branches of the saddle point originate in different half-planes. This can be interpreted as the saddle point representing the coalescence of a downstream

mode and an upstream mode. It will be shown that for a saddle point that does not satisfy this criteria, there is no asymptotic contribution.

The method of steepest-descent provides a necessary condition for absolute instability, namely that the dispersion relation D has a saddle point in the complex α-plane at α_* satisfying $\mathfrak{Re}\{\mu(\alpha_*)\} > 0$. The location of saddle points can be found by adapting the eigenvalue solver developed in Chapter 1. This will be detailed later. In order to provide insight into the origin of the collision criteria, Briggs' method will now be described.

4.2.3 Briggs' Method

The process described herein is adapted from Briggs (1964) and Lingwood (1997). It is also informed by the review of this method carried out by Bers (1983). Since the classification of absolute and convective instabilities is of primary interest here, only the behaviour along the ray $x/\tau = 0$ will be considered for this method. It is straightforward to explore any other ray in the same manner as for the method of steepest-descent (Lingwood, 1997).

Fourier integration

The derivation of Briggs' method requires the Fourier integral to be performed first. The contour along which this integral is performed depends on whether considering $x > 0$ (downstream) or $x < 0$ (upstream). Let C_F^+ be the contour consisting of F closed by a semi-circle in the upper half-plane and C_F^- be closed in the lower half-plane. In the following analysis the upstream and downstream cases will involve very similar expressions so let x^+ denote $x > 0$ and x^- denote $x < 0$. It then becomes possible to write the separate expressions for upstream and downstream evolution in a single line. Utilising this compact notation, the Fourier integral can be written as

$$\boldsymbol{v}(x^\pm, \mu) = \frac{1}{2\pi} \oint_{C_F^\pm} \boldsymbol{Q}(\alpha, \tau) \frac{\boldsymbol{G}(\alpha, \mu)}{D(\alpha, \mu)} \mathrm{e}^{i\alpha x^\pm} \, \mathrm{d}\alpha, \tag{4.2.29}$$

which can be related to $\boldsymbol{v}(x^\pm, \tau)$ by performing the Laplace integral,

$$\boldsymbol{v}(x^\pm, \tau) = \frac{1}{2\pi} \int_L \boldsymbol{v}(x^\pm, \mu) \mathrm{e}^{\mu\tau} \, \mathrm{d}\mu. \tag{4.2.30}$$

Letting $H(x)$ denote the heavyside function,

$$H(x) = \begin{cases} 1 & x > 0, \\ 0 & \text{otherwise} \end{cases}$$

provides a means of writing (4.2.29) for all x,

$$\boldsymbol{v}(x,\mu) = H(x)\boldsymbol{v}(x^+,\mu) + H(-x)\boldsymbol{v}(x^-,\mu), \tag{4.2.31}$$

and a similar expression holds for $\boldsymbol{v}(x,\tau)$. It is straightforward to apply Cauchy's residue theorem in this case, noting that the poles in each half-plane only contribute to the relevant choice of $x^\pm$. Remembering that $\alpha_k^\pm(\mu)$ denotes the α-roots of D with upstream $(-)$ or downstream $(+)$ contributions, we can write

$$\operatorname{Res}\left(\boldsymbol{Q}(\alpha,\tau)\frac{\boldsymbol{G}(\alpha,\mu)}{D(\alpha,\mu)}\mathrm{e}^{i\alpha x^\pm}, \alpha_k^\pm(\mu)\right) = \boldsymbol{Q}(\alpha_k^\pm(\mu),\tau)\frac{\boldsymbol{G}\left(\alpha_k^\pm(\mu),\mu\right)}{\frac{\partial D}{\partial\alpha}\left(\alpha_k^\pm(\mu),\mu\right)}\mathrm{e}^{i\alpha_k^\pm(\mu)x^\pm}, \tag{4.2.32}$$

having used the g/h rule described above. This gives the two expressions

$$\boldsymbol{v}(x^\pm,\mu) = \pm i\sum_{k=1}^{\infty}\boldsymbol{Q}(\alpha_k^\pm(\mu),\tau)\frac{\boldsymbol{G}\left(\alpha_k^\pm(\mu),\mu\right)}{\frac{\partial D}{\partial\alpha}\left(\alpha_k^\pm(\mu),\mu\right)}\mathrm{e}^{i\alpha_k^\pm(\mu)x^\pm}, \tag{4.2.33}$$

where the $\pm$ at the start of this expression arises since the two contours are oriented in opposite directions. Take the positive value for $x > 0$ and the negative value for $x < 0$. For the downstream expression, take all the $\pm$ signs to be '+', and take them all to be '−' for the upstream behaviour.

Observing the sign of the imaginary parts in the exponential terms reveals that the upstream (downstream) expression consists of a superposition of modes that decay in the upstream (downstream) direction. Inspection of these terms also justifies the selection of dominant modes according to (4.2.2).

Taking this expression and performing the Laplace transform can, in principle, reveal the detailed impulsive response. However, to deduce the asymptotic behaviour of $\boldsymbol{v}(\alpha,\mu)$ as $\tau\to\infty$ it is convenient to deform the Laplace contour L as far to the left as possible. In order to explore this deformation consider a given μ and, fixing the imaginary part, decrease the real part as far as possible. This process needs to be performed for all initial μ on L, i.e. for all values of the imaginary part.

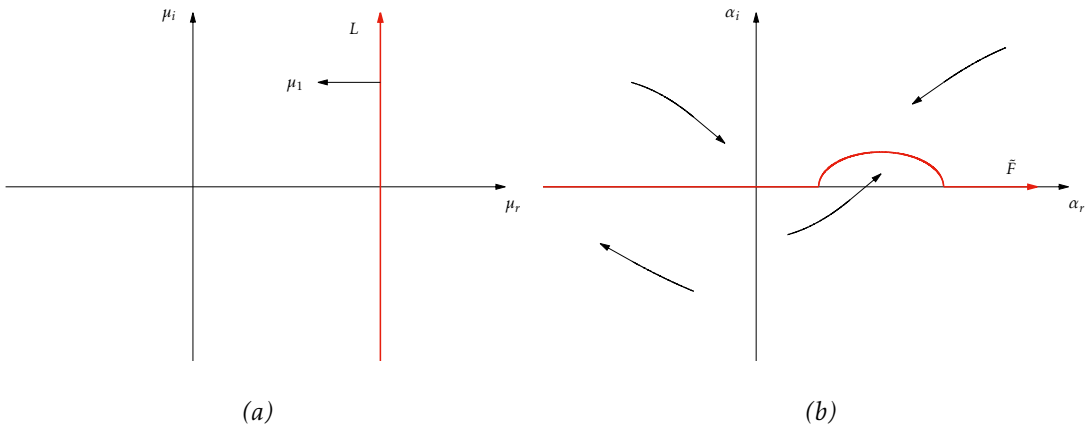

Figure 4.2: A sketch showing that as μ is moved horizontally (a), the poles corresponding to α-roots of D also move (b). When μ_1 is reached, a pole that originated in the lower half-plane is now in the upper half-plane and so the contour F has been deformed to $\tilde{F}$ to ensure that both the upstream and downstream expressions are continuous during the movement of μ.

If this horizontal movement can be continued into the stable region ($\mu_r < 0$) for all choices of the imaginary part then the largest term will decay as $\tau \to \infty$, but if there exists a μ_0 in the right half-plane beyond which this movement becomes invalid, then this results in asymptotic temporal growth at every spatial location (as $\tau \to \infty$).

Branch points and analytic continuation

As μ is moved left, the corresponding α-roots move around the complex plane and it is possible for these poles to cross the real axis. For demonstrative purposes, let μ_1 denote a point along the horizontal path of μ such that a pole in the lower half of the α-plane has crossed into the upper half-plane. An illustration of this is given in Figure 4.2.

This results in a discontinuous jump in the value of $\boldsymbol{v}(x^+, \mu)$ since there is now an additional pole contained within the contour C_F^+ (so the jump is the size of the residue at this pole). Hence, the μ at which this mode first touches the real axis is a branch point of $\boldsymbol{v}(x^+, \mu)$. There is also a discontinuity in $\boldsymbol{v}(x^-, \mu)$ from the removal of a pole from within the contour C_F^-. These same arguments hold in reverse for a pole moving from the upper half-plane to the lower half-plane.

Branch points can be found for all possible imaginary parts of μ and branch curves can be drawn as the locus of these branch points. The branch curve will be equivalent to the curve $\mu(F)$ in Figure 4.1 since the branch points form just as a pole crosses into a different half-plane, i.e. when $\alpha \in \mathbb{R}$.

To deal with these branch curves, analytic continuations of $\boldsymbol{v}(x^{\pm},\mu)$ can be defined by deforming the F contour around these problem points to $\tilde{F}$ (see Figure 4.2) and then closing the contour in the same manner as above. Letting $\tilde{C}_{\tilde{F}}^{\pm}$ denote the deformed, closed contours, the analytic continuations of $\boldsymbol{v}(x^{\pm},\mu)$ can be written as

$$\tilde{\boldsymbol{v}}(x^{\pm},\mu) = \frac{1}{2\pi}\oint_{\tilde{C}_{\tilde{F}}^{\pm}} \boldsymbol{Q}(\alpha,\tau)\frac{\boldsymbol{G}(\alpha,\mu)}{D(\alpha,\mu)}\mathrm{e}^{i\alpha x^{\pm}}\,\mathrm{d}\alpha. \tag{4.2.34}$$

It is readily confirmed that that these are analytic continuations of $\boldsymbol{v}(x^{+},\mu)$ and $\boldsymbol{v}(x^{-},\mu)$ since they are identically zero on the right-hand side of L and $\tilde{\boldsymbol{v}}(x^{\pm},\mu)$ are well defined at any branch point. Cauchy's residue theorem can then be used to write

$$\tilde{\boldsymbol{v}}(x^{\pm},\mu) = \pm i\sum_{k=1}^{\infty} \boldsymbol{Q}(\alpha_k^{\pm}(\mu),\tau)\frac{\boldsymbol{G}\left(\alpha_k^{\pm}(\mu),\mu\right)}{\frac{\partial D}{\partial\alpha}\left(\alpha_k^{\pm}(\mu),\mu\right)}\mathrm{e}^{i\alpha_k^{\pm}(\mu)x^{\pm}}, \tag{4.2.35}$$

which differs from (4.2.33) in the definition of $\alpha_k^{\pm}(\mu)$. The superscript now refers to the origin of the pole when $\mu \in L$. If a pole crosses the real α-axis from above it remains in the expression for $\tilde{\boldsymbol{v}}(x^{+},\mu)$ and if it crosses the real axis from below it remains in the expression for $\tilde{\boldsymbol{v}}(x^{-},\mu)$. This allows for the possibility of $\tilde{\boldsymbol{v}}(x,\mu)$ growing with respect to one or both spatial directions.

As for $\boldsymbol{v}(x,\mu)$, the analytic continuation can be written for all x in terms of the heavyside function,

$$\tilde{\boldsymbol{v}}(x,\mu) = H(x)\tilde{\boldsymbol{v}}(x^{+},\mu) + H(-x)\tilde{\boldsymbol{v}}(x^{-},\mu). \tag{4.2.36}$$

Second-order poles (saddle points)

As μ is continually moved to the left, it is possible to define analytic continuations of $\boldsymbol{v}(x^{+},\mu)$ and $\boldsymbol{v}(x^{-},\mu)$ until there is no further deformation of the F contour that is valid. Let μ_0 denote the point along the horizontal movement at which two poles originating in opposite half-planes coalesce at α_0. That is, as $\mu \to \mu_0$ there exist k_1 and k_2 such that $\alpha_{k_1}^{+}(\mu) \to \alpha_0$ and $\alpha_{k_2}^{-}(\mu) \to \alpha_0$, see Figure 4.3. The deformed F contour is then pinched, meaning it must pass through the pole at α_0.

Being the point of coalescence of two simple poles, α_0 is a double pole of the integrand and therefore must satisfy

$$\frac{\partial D}{\partial\alpha}(\alpha_0,\mu_0) = 0. \tag{4.2.37}$$

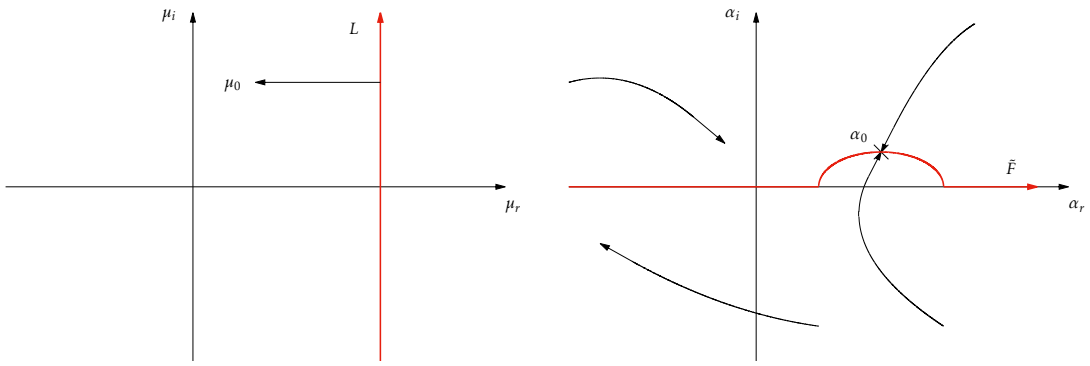

(a) *(b)*

Figure 4.3: A sketch showing the pinching of the Fourier contour. As μ is moved horizontally to μ_0 (a), poles originating in each half-plane collide at α_0 (b). This constrains the deformed Fourier contour $\tilde{F}$ to pass through this point. This double pole now contributes equally to both the upstream and downstream expressions. Notice that if this collision was between two modes originating in the same half-plane, the contour would not be constrained in this way, indicating the need for the collision criteria.

This results in an infinite contribution to both $\tilde{\boldsymbol{v}}(x^+, \mu)$ and $\tilde{\boldsymbol{v}}(x^-, \mu)$.

It is important to note that there is only a pinching of the deformed F contour if this double pole corresponds to the collision of poles that originated in opposite half-planes. The collision of poles that originate in the same half-plane produces a finite contribution to $\tilde{\boldsymbol{v}}(x^\pm, \mu)$.

It will now be shown that while it is informative to find a pair (α_0, μ_0) satisfying

$$D(\alpha_0, \mu_0) = 0, \tag{4.2.38a}$$

$$\frac{\partial D}{\partial \alpha}\Big(\alpha_0, \mu_0\Big) = 0, \tag{4.2.38b}$$

which describes a saddle point of the dispersion relation, it is also necessary for this saddle point to be of pinch-type, meaning that this collision is between two poles originating in opposite half-planes. Only pinch-type saddle points contribute to the asymptotic behaviour as $\tau \to \infty$. This condition is referred to as the collision criteria in Brevdo & Bridges (1997) and this term is also used for the current work.

To illustrate the behaviour around some double root α_0 the dispersion relation can be

expressed in some vicinity of α_0 by the Taylor expansion,

$$\begin{aligned} D(\alpha,\mu) = D(\alpha_0,\mu_0) + \frac{\partial D}{\partial \alpha}\Big(\alpha_0,\mu_0\Big)(\alpha-\alpha_0) + \\ \frac{\partial D}{\partial \mu}\Big(\alpha_0,\mu_0\Big)(\mu-\mu_0) + \frac{1}{2}\frac{\partial^2 D}{\partial \alpha^2}\Big(\alpha_0,\mu_0\Big)(\alpha-\alpha_0)^2 + \\ \frac{1}{2}\frac{\partial^2 D}{\partial \mu^2}\Big(\alpha_0,\mu_0\Big)(\mu-\mu_0)^2 + \frac{1}{2}\frac{\partial^2 D}{\partial \alpha \partial \mu}\Big(\alpha_0,\mu_0\Big)(\alpha-\alpha_0)(\mu-\mu_0) + \ldots \end{aligned} \tag{4.2.39}$$

Using (4.2.38) and the fact that $|\alpha-\alpha_0| = \mathcal{O}(|\mu-\mu_0|^{\frac{1}{2}})$ (a result carried across from the steady case), retaining only the two largest terms gives

$$D(\alpha,\mu) \sim \frac{\partial D}{\partial \mu}\Big(\alpha_0,\mu_0\Big)(\mu-\mu_0) + \frac{1}{2}\frac{\partial^2 D}{\partial \alpha^2}\Big(\alpha_0,\mu_0\Big)(\alpha-\alpha_0)^2. \tag{4.2.40}$$

This is an approximation to the dispersion relation in the neighbourhood of the double pole. Set $D(\alpha,\mu) = 0$ to find a leading-order expression for the poles that collide at this location. This gives

$$\alpha \sim \alpha_0 \pm i\left[2\frac{\partial D}{\partial \mu}\Big(\alpha_0,\mu_0\Big)\right]^{\frac{1}{2}}\left[\frac{\partial^2 D}{\partial \alpha^2}\Big(\alpha_0,\mu_0\Big)\right]^{-\frac{1}{2}}(\mu-\mu_0)^2. \tag{4.2.41}$$

Note that, by design, $\alpha \to \alpha_0$ as $\mu \to \mu_0$.

Differentiating (4.2.40) with respect to α gives

$$\frac{\partial D}{\partial \alpha}\Big(\alpha,\mu\Big) \sim 2\frac{\partial \mu}{\partial \alpha}(\alpha_0)\frac{\partial D}{\partial \mu}\Big(\alpha_0,\mu_0\Big) + \frac{\partial^2 D}{\partial \alpha^2}\Big(\alpha_0,\mu_0\Big)(\alpha-\alpha_0), \tag{4.2.42}$$

and since $\partial D/\partial\alpha = 0$ it is also known that $\partial\mu/\partial\alpha = 0$. This equation can then be written as

$$\frac{\partial D}{\partial \alpha}\Big(\alpha,\mu\Big) \sim \pm i\left[2\frac{\partial D}{\partial \mu}\Big(\alpha_0,\mu_0\Big)\frac{\partial^2 D}{\partial \alpha^2}\Big(\alpha_0,\mu_0\Big)\right]^{\frac{1}{2}}(\mu-\mu_0)^{\frac{1}{2}}. \tag{4.2.43}$$

This reveals that, in a neighbourhood of α_0, there are two poles moving towards one another in opposite directions. Hence, if α_0 denotes the collision point of two modes originating in the same half-plane, then as $\alpha \to \alpha_0$ the terms in the expression (4.2.35) cancel out since $\partial D/\partial\alpha$ has opposite sign for each of the colliding modes.

Returning to the case in which α_0 denotes a pinching point (collision between two poles originating in opposite half-planes), both the contours $C_F^{\pm}$ pass through α_0. Here,

$\tilde{\boldsymbol{v}}(x^{\pm},\mu)$ are given to leading order by

$$\tilde{\boldsymbol{v}}(x^{\pm},\mu) \sim \pm i\boldsymbol{Q}(\alpha_0,\mu_0)\frac{\boldsymbol{G}(\alpha_0,\mu_0)}{\frac{\partial D}{\partial \alpha}\left(\alpha_0,\mu_0\right)}\mathrm{e}^{i\alpha_0 x^{\pm}}, \tag{4.2.44}$$

with the ± sign arising from the different orientations of the closed contours $C_F^{\pm}$. From (4.2.43) it is clear that $\partial D/\partial\alpha$ will have opposite signs for $\tilde{\boldsymbol{v}}(x^{+},\mu)$ and $\tilde{\boldsymbol{v}}(x^{-},\mu)$. Considering this sign difference along with that due to the contour orientation means that $\tilde{\boldsymbol{v}}(x^{+},\mu) = \tilde{\boldsymbol{v}}(x^{-},\mu)$. Thus, using (4.2.36) and the fact that $H(-x) = 1 - H(x)$ gives

$$\tilde{\boldsymbol{v}}(x,\mu) \sim \frac{\pm i\boldsymbol{Q}(\alpha_0,\mu_0)\boldsymbol{G}(\alpha_0,\mu_0)}{\left[2\frac{\partial D}{\partial \mu}\left(\alpha_0,\mu_0\right)\frac{\partial^2 D}{\partial \alpha^2}\left(\alpha_0,\mu_0\right)\right]^{\frac{1}{2}}}\mathrm{e}^{i\alpha_0\tau}\frac{\mathrm{e}^{i\alpha_0\tau}}{\sqrt{\mu-\mu_0}}, \tag{4.2.45}$$

for all x. The ± depends on which of $\tilde{\boldsymbol{v}}(x^{+},\mu)$ and $\tilde{\boldsymbol{v}}(x^{-},\mu)$ are assigned the positive and negative value from (4.2.43), remembering that the poles could have crossed the axis several times before colliding so this must be found for any specific case of interest.

Laplace integration

The pole at μ_0 is a branch pole arising from the square root singularity in (4.2.45) and thus there is a horizontal branch cut to the left of μ_0. Note that the method allows for an infinite number of such μ_0 for the continuous choice of imaginary part.

The Laplace integration can be performed over a contour $\tilde{L}$ that does not pass through any of these branch cuts, i.e. it must lie to the right of the branch pole that appears furthest to the right as shown in Figure 4.4.

Ignoring the ±, this gives

$$\boldsymbol{v}(x,\tau) \sim \frac{\boldsymbol{Q}(\alpha_0,\tau)\boldsymbol{G}(\alpha_0,\mu_0)}{\left[2\frac{\partial D}{\partial \mu}\left(\alpha_0,\mu_0\right)\frac{\partial^2 D}{\partial \alpha^2}\left(\alpha_0,\mu_0\right)\right]^{\frac{1}{2}}}\frac{\mathrm{e}^{i\alpha_0 x}}{2\pi}\int_{\tilde{L}}\frac{\mathrm{e}^{\mu\tau}}{\sqrt{\mu-\mu_0}}\,\mathrm{d}\mu, \tag{4.2.46}$$

where $\tilde{L}$ can be defined so that its end points are $\pm i\infty$. The integration is performed by making the substitution

$$\mu' = -i\sqrt{\tau(\mu-\mu_0)} \Rightarrow \frac{\mathrm{d}\mu'}{\mathrm{d}\mu} = -\frac{i}{2}\sqrt{\frac{\tau}{\mu-\mu_0}} \tag{4.2.47}$$

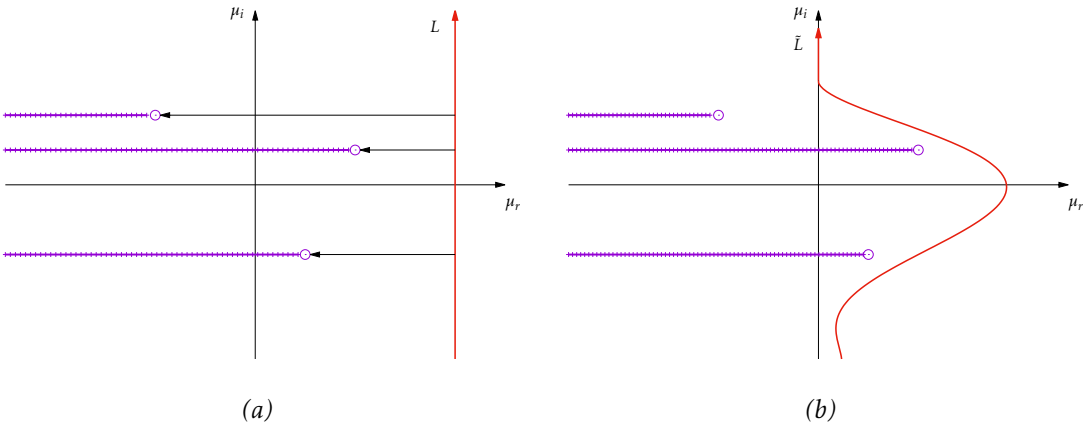

(a) *(b)*

Figure 4.4: A sketch showing how $\tilde{L}$ can be defined. In (a), the movement of μ to the left of the L contour reveals three singularities with horizontal branch cuts (from the square root in the Taylor expansion). In (b), L has been deformed to $\tilde{L}$ so that all branch cuts continue to lie on the left of this contour. In reality, since this process is performed for all possible values of μ_i, the locus of all branch cuts will form a curve. Provided this curve lies to the left of $\tilde{L}$, the exact position of the contour is unimportant but it is straightforward to ensure that the endpoints of $\tilde{L}$ are $\pm i\infty$.

so that $\mu' \to \pm\infty$ as $\mu \to \pm i\infty$ and thus

$$\begin{aligned}\int_{\tilde{L}} \frac{\mathrm{e}^{\mu\tau}}{\sqrt{\mu-\mu_0}}\,\mathrm{d}\mu &= \frac{2i}{\sqrt{\tau}}\int_{-\infty}^{\infty} \mathrm{e}^{\mu_0\tau-(\mu')^2}\frac{\mathrm{d}\mu'}{\mathrm{d}\mu}\,\mathrm{d}\mu \\ &= \frac{2i\mathrm{e}^{\mu_0\tau}}{\sqrt{\tau}}\int_{-\infty}^{\infty}\mathrm{e}^{-(\mu')^2}\,\mathrm{d}\mu' \\ &= 2i\sqrt{\frac{\pi}{\tau}}\mathrm{e}^{\mu_0\tau}.\end{aligned}$$

This gives the leading-order behaviour as

$$\boldsymbol{v}(x,\tau) \sim \frac{\boldsymbol{Q}(\alpha_0,\tau)\boldsymbol{G}(\alpha_0,\mu_0)}{\sqrt{2\pi\tau\frac{\partial D}{\partial\mu}\left(\alpha_0,\mu_0\right)\frac{\partial^2 D}{\partial\alpha^2}\left(\alpha_0,\mu_0\right)}}\mathrm{e}^{\frac{3\pi i}{2}+i\alpha_0 x+\mu_0\tau}, \tag{4.2.49}$$

where α_0 is the location of the pinch-type saddle point with $\mu_0 = \mu(\alpha_0)$ furthest right in the μ-plane.

Notice that (4.2.49) is the same as (4.2.27) in the case that α_* is a saddle point of pinch-type. Both α_* and α_0 have been defined as saddle points of the dispersion relation, but through Briggs' method it is ensured that α_0 satisfies the collision criteria.

Spatially amplifying waves

Consider the possibility that the branch cut that is furthest to the right is to the left of the imaginary axis. In this case the contour $\tilde{L}$ can be chosen to be the imaginary axis in the μ-plane. Such a flow is not subject to absolute instability since all contributions along the ray $x/\tau = 0$ decay as $\tau \to \infty$. In this case it is convenient to formulate the eigenvalue problem to find a complex α for a prescribed, purely imaginary μ (instead of finding a complex μ for a prescribed, real α).

When this approach is appropriate (i.e. in absolutely stable systems) the resulting disturbance exhibits exponential behaviour in the streamwise x direction. For instance, if $\alpha_i > 0$ the disturbance displays exponential growth for $x > 0$ and decay for $x < 0$. This approach is often referred to in steady stability analysis as the spatial problem whereas the temporal problem is that with the prescribed, real wavenumber.

4.3 Interpretation of results

Assume for this section that it is implicit in any reference to a saddle point that the collision criteria is satisfied. A framework will be now be provided to distinguish between convective and absolute instabilities when presented with the evolution of a disturbance such as those discussed in Chapter 3. Consider the case in which the external forcing is an approximation to the impulse $g(x,\tau) = \delta(x)\delta(\tau)$ so that all wavenumbers and frequencies are seeded approximately equally.

4.3.1 Definitions of absolute and convective instability

A stable solution will be defined for the present work as a solution $\boldsymbol{v}$ satisfying

$$\max_x\{\boldsymbol{v}(x,\tau)\} \to 0 \quad \text{as} \quad \tau \to \infty. \tag{4.3.1}$$

A solution is considered unstable if the condition

$$\max_x\{\boldsymbol{v}(x,\tau)\} \to \infty \quad \text{as} \quad \tau \to \infty \tag{4.3.2}$$

holds. Notice that the possibility of a finite limit is not accounted for in either of these definitions. This is because the linear stability characteristics are explored only through

roots of the dispersion relation, which only allows for disturbances with exponential growth/decay. In other settings, it may be necessary to define instability as any disturbance that is not stable according to (4.3.1).

The category of unstable solutions can be further decomposed into two forms of instability depending on the behaviour of the solution at a fixed spatial location. In addition to satisfying (4.3.2), a convective instability exhibits temporal decay at every spatial location,

$$\boldsymbol{v}(x_0, \tau) \to 0 \quad \text{as} \quad \tau \to \infty \quad \forall -\infty < x_0 < \infty. \tag{4.3.3}$$

An absolute instability is one that grows with time at every location so will here be defined as a disturbance that, in addition to satisfying (4.3.2), also satisfies

$$\boldsymbol{v}(x_0, \tau) \to \infty \quad \text{as} \quad \tau \to \infty \quad \forall -\infty < x_0 < \infty. \tag{4.3.4}$$

Again, the possibility of a finite limit is not considered in this framework.

An alternative means of describing these definitions is by considering the disturbance evolution along spatial/temporal rays. A disturbance is categorised as unstable if there exists some ray $x/\tau = V$ along which the disturbance grows with time and stable if no such ray exists. If unstable, the instability is categorised as convective if temporal decay is observed along the ray $x/\tau = 0$ and absolute if this ray displays temporal growth. Recasting the above definitions in terms of rays results in essentially the same definitions as used in Schmid & Henningson (2001).

4.3.2 Disturbance maximum

Consider the evolution of the disturbance maximum. Whether this is associated with temporal growth or decay leads to the classification of the disturbance as stable or unstable.

Leading-order temporal behaviour

The expression for the growth along a given ray (4.2.22) can be differentiated with respect to V,

$$\lambda = -\alpha_i V + \mu_r \quad \Rightarrow \quad \frac{\mathrm{d}\lambda}{\mathrm{d}V} = -\alpha_i.$$

Setting this derivative to zero reveals that maximum growth is observed when $\alpha_i = 0$.

Consider $\alpha \in \mathbb{R}$ (since the maximum growth should correspond to such a value). Let $\mu(\alpha)$ denote the corresponding Floquet exponent so that this pair satisfy $D(\alpha, \mu(\alpha)) = 0$. Now let α_{max} be the real wavenumber that corresponds to the maximum growth-rate,

$$\frac{\partial \mu_r}{\partial \alpha}(\alpha_{max}) = 0. \tag{4.3.5}$$

It follows that $\partial\mu/\partial\alpha$ is purely imaginary at this α. This is consistent with the saddle point condition (4.2.21) since V must be real. It is now possible to select V so that an observer moving along the ray observes a complex wavenumber α_{max} and Floquet exponent $\mu(\alpha_{max})$. Hence, define V_{max} such that

$$\frac{\partial \mu}{\partial \alpha}(\alpha_{max}) = -i V_{max}. \tag{4.3.6}$$

An observer travelling along the ray $x/\tau = V_{max}$ will then observe a growth of

$$\lambda(V_{max}) = \mu_r(\alpha_{max}), \tag{4.3.7}$$

since $\alpha \in \mathbb{R}$. This means there must exist some ray V_{max} which displays the growth-rate of the least stable mode for $\alpha \in \mathbb{R}$. Along this ray the asymptotic behaviour of the disturbance for large times is given by

$$\boldsymbol{v}(x_0 + V_{max}\tau, \tau) \sim \boldsymbol{B}_{max}(\tau)\frac{1}{\sqrt{\tau}} e^{\mu(\alpha_{max})\tau}, \tag{4.3.8}$$

where $\boldsymbol{B}_{max}$ is a matrix function that is 2π-periodic and includes all of the constants in (4.2.20). Since it was observed from differentiating (4.2.22) that the ray corresponding to greatest growth corresponds to $\alpha_i = 0$, the growth of the disturbance along the ray $x/\tau = V_{max}$ is greater than along any other ray. It follows from (4.3.8) that the disturbance maximum should, in general, asymptotically behave like the least stable mode for $\alpha \in \mathbb{R}$.

The wavenumber α_{max} and Floquet exponent $\mu(\alpha_{max})$ can be found by solving the eigenvalue problem for an appropriate selection of $\alpha \in \mathbb{R}$ and selecting the α corresponding to largest μ_r, as seen in Section 3.2. If $\mu_r(\alpha_{max}) < 0$ the disturbance is stable, and if $\mu_r(\alpha_{max}) > 0$ the disturbance is unstable.

Note that no real value of V_{max} can be chosen unless (4.3.5) is satisfied. This means that if the least stable mode does not correspond to a local maximum, there is no valid

ray along which this mode will manifest. This additional condition is used to justify the selection of the predicted dominant mode when $Re = 700$ in Section 3.2. In this case, the local maximum at $\alpha = 0.3727$ was selected rather than the least stable mode at $\alpha = 0$. The maximum at $\alpha = 0$ is not a turning point so (4.3.5) is not satisfied here. This argument only holds for $\alpha \in \mathbb{R}$ which allows the real and imaginary parts of the saddle point condition to be considered separately.

Measuring the temporal growth-rate

Unlike in the single wavenumber case, the leading-order behaviour also incorporates a $1/\sqrt{\tau}$ term multiplied by the expected normal mode solution as can be seen in (4.3.8). It is expected that the disturbance maximum will display a superposition of each mode with its complex conjugate (as for the single wavenumber case) so, taking the wall vorticity as being representative of the disturbance evolution, the disturbance maximum is expected to have the form

$$\max_x\{\zeta(x,0,\tau)\} \approx \frac{1}{\sqrt{\tau}}\left(p_1(\tau)\mathrm{e}^{\mu\tau} + p_2(\tau)\mathrm{e}^{\bar{\mu}\tau}\right), \tag{4.3.9}$$

for large τ. The 2π-periodic functions p_1 and p_2 are related through a half-period time-shift, complex conjugation and multiplication by a constant, but only the periodicity is necessary for this method.

An alternative to simply using the wall values would be to take the integral over the wall-normal domain to account for the variation of ζ with y, but there is little practical difference between these two approaches so measuring only the wall vorticity is well justified for its simplicity.

Using this approach to measure the temporal growth associated with the disturbance maximum has several drawbacks. First, the leading-order behaviour is deduced for the ray $x/\tau = V_{max}$ that exhibits greater growth than any other ray, but the choice of ray along which this growth can be measured is not immediately apparent.

The location of this ray can be approximated by considering the wavepacket spacing, but a small error in the choice of V_{max} would mean that the measured growth-rate becomes less accurate with time as the spatial location associated with this ray at a given time ($x = \tau V_{max}$) diverges from the actual value.

For this reason, the global maximum is taken at each time which causes some discontinuities in the time-history when subsequent maxima correspond to different spatial

locations. This produces spurious results. Instead, the envelope of the wall vorticity will be taken using a Hilbert transform and the time-history of this real-valued, positive function will be used instead. Some information is lost through this approach, namely the value of μ_i, but the temporal growth-rate μ_r can be calculated for each time step by assuming the wall-vorticity to be of the form

$$\max_x |\zeta(x,0,\tau)| = \frac{1}{\sqrt{\tau}} p(\tau) \mathrm{e}^{\mu_r \tau}, \tag{4.3.10}$$

for large τ, where $|f|$ is shorthand to denote the envelope of a function f, calculated by the Hilbert transform.

Utilising the periodicity of p allows for the construction of the system

$$f_0 = A, \tag{4.3.11a}$$

$$f_1 = A\lambda, \tag{4.3.11b}$$

where

$$f_0 = \sqrt{\tau_0}\max_x|\zeta(x,0,\tau_0)|, \tag{4.3.12a}$$

$$f_1 = \sqrt{\tau_0+2\pi}\max_x|\zeta(x,0,\tau_0+2\pi)|, \tag{4.3.12b}$$

$$A = p(\tau_0)\mathrm{e}^{\mu_r\tau_0}, \tag{4.3.12c}$$

$$\lambda = \mathrm{e}^{2\pi\mu_r}. \tag{4.3.12d}$$

It can then be deduced that

$$\mu_r = \frac{1}{2\pi}\log(f_1/f_0), \tag{4.3.13}$$

or, substituting the original known values back in,

$$\mu_r(\tau_0) = \frac{1}{2\pi}\log\left(\sqrt{1+\frac{2\pi}{\tau_0}}\frac{\max_x|\zeta(x,0,\tau_0+2\pi)|}{\max_x|\zeta(x,0,\tau_0)|}\right). \tag{4.3.14}$$

This measure can be used to approximate the temporal growth-rate of the disturbance maximum at a given time. This can then be compared with the expected growth-rate found from the Floquet eigenvalue problem. This comparison was made in Section 3.2 using the identical expression (3.2.1). If $\mu_r > 0$ the disturbance is unstable and if $\mu_r < 0$ the disturbance is stable.

4.3.3 Fixed spatial locations

By considering the temporal evolution of the disturbance at fixed spatial locations, unstable disturbances can be categorised as convective or absolute. Unstable disturbances that exhibit temporal decay at every spatial location are convectively unstable and disturbances that growth at every spatial location are absolutely unstable.

Leading-order temporal behaviour

Now consider the ray $x/\tau = 0$, i.e. the laboratory frame. If temporal growth is observed in this frame, the solution is absolutely unstable. For this frame of reference, the saddle point condition becomes

$$\frac{\partial \mu}{\partial \alpha}(\alpha_*) = 0. \tag{4.3.15}$$

In addition to this condition, it is also necessary that the saddle point is of pinch-type. when this is the case, the asymptotic temporal behaviour of the disturbance at some spatial location x_0 for large τ is given by

$$\boldsymbol{v}(x_0, \tau) \sim \boldsymbol{B}_0(\tau) \frac{1}{\sqrt{\tau}} \mathrm{e}^{\mu(\alpha_*)\tau}, \tag{4.3.16}$$

where $\boldsymbol{B}_0$ is a matrix function that is 2π-periodic and incorporates all the constants in the full expression (4.2.27). If the growth-rate $\lambda(0) = \mathfrak{Re}\{\mu(\alpha_*)\}$ is positive, then the disturbance is absolutely unstable.

Measuring temporal growth-rates

When considering the temporal evolution of a disturbance at a fixed streamwise location it can be seen from (4.3.16) that, once the complex conjugate is incorporated, the wall-vorticity will approach

$$\zeta_0(\tau) = \zeta(x_0, 0, \tau) \approx \frac{1}{\sqrt{\tau}} \left(p_1(\tau) \mathrm{e}^{\mu_0 \tau} + p_2(\tau) \mathrm{e}^{\bar{\mu}_0 \tau} \right) \tag{4.3.17}$$

for large τ, where x_0 is some fixed streamwise position, μ_0 is the Floquet exponent associated with the evolution at a fixed spatial location and p_1, p_2 are 2π-periodic in τ. Unlike the ray of maximum growth, it is trivial to ascertain the ray $x/\tau = 0$ simply by fixing x_0. Furthermore, since the time-history at a fixed spatial location will have none

of the problems associated with that of the disturbance maximum, the complex values of the vorticity can be retained. Making use of the periodicity of p_1 and p_2 the following system of equations can be derived

$$\zeta_0(\tau_0) = \frac{1}{\sqrt{\tau_0}}\left(p_1(\tau_0)\mathrm{e}^{\mu_0\tau_0} + p_2(\tau_0)\mathrm{e}^{\mu_0^*\tau_0}\right), \tag{4.3.18a}$$

$$\zeta_0(\tau_0 + 2\pi) = \frac{1}{\sqrt{\tau_0 + 2\pi}}\left(p_1(\tau_0)\mathrm{e}^{\mu_0\tau_0}\mathrm{e}^{2\pi\mu_0} + p_2(\tau_0)\mathrm{e}^{\mu_0^*\tau_0}\mathrm{e}^{2\pi\mu_0}\right), \tag{4.3.18b}$$

$$\zeta_0(\tau_0 + 4\pi) = \frac{1}{\sqrt{\tau_0 + 4\pi}}\left(p_1(\tau_0)\mathrm{e}^{\mu_0\tau_0}\mathrm{e}^{4\pi\mu_0} + p_2(\tau_0)\mathrm{e}^{\mu_0^*\tau_0}\mathrm{e}^{4\pi\mu_0}\right). \tag{4.3.18c}$$

Then define

$$f_0 = \sqrt{\tau_0}\,\zeta_0(\tau_0), \tag{4.3.19a}$$

$$f_1 = \sqrt{\tau_0 + 2\pi}\,\zeta_0(\tau_0 + 2\pi), \tag{4.3.19b}$$

$$f_2 = \sqrt{\tau_0 + 4\pi}\,\zeta_0(\tau_0 + 4\pi), \tag{4.3.19c}$$

$$B_1 = p_1(\tau_0)\mathrm{e}^{\mu_0\tau_0}, \tag{4.3.19d}$$

$$B_2 = p_2(\tau_0)\mathrm{e}^{\mu_0^*\tau_0}, \tag{4.3.19e}$$

$$\lambda = \mathrm{e}^{2\pi\mu_0}, \tag{4.3.19f}$$

which results in the system of equations

$$f_0 = B_1 + B_2, \tag{4.3.20a}$$

$$f_1 = B_1\lambda + B_2\lambda^*, \tag{4.3.20b}$$

$$f_2 = B_1\lambda^2 + B_2\lambda^{*2}. \tag{4.3.20c}$$

This is an identical system of equations as for the single wavenumber case and can be solved in the same way to give

$$\lambda_r = \frac{\mathrm{Im}\{f_2/f_0\}}{2\mathrm{Im}\{f_1/f_0\}}, \tag{4.3.21a}$$

$$|\lambda| = \sqrt{-\frac{\mathrm{Im}\{f_2/f_1\}}{\mathrm{Im}\{f_0/f_1\}}}, \tag{4.3.21b}$$

and thus

$$\mathfrak{Re}\{\mu_0\} = \frac{1}{2\pi}\ln(|\lambda|), \tag{4.3.22a}$$

$$\mathfrak{Im}\{\mu_0\} = \frac{1}{2\pi}\cos^{-}1\left(\frac{\lambda_r}{|\lambda|}\right). \tag{4.3.22b}$$

Reintroducing the original variables gives the following expression for $\mathfrak{Re}\{\mu_0\}$ at each time,

$$\mathfrak{Re}\{\mu_0(\tau_0)\} = \frac{1}{2\pi}\ln\left[-\sqrt{1+\frac{4\pi}{\tau_0}}\frac{\mathfrak{Im}\{\zeta(x_0,0,\tau_0+4\pi)/\zeta(x_0,0,\tau_0+2\pi)\}}{\mathfrak{Im}\{\zeta(x_0,0,\tau_0)/\zeta(x_0,0,\tau_0+2\pi)\}}\right]. \tag{4.3.23}$$

This measurement can be used to deduce the nature of an unstable solution: convective or absolute. The disturbance can be shown to be unstable using (4.3.14), and then if the instability is absolute $\mathfrak{Re}\{\mu_0\} > 0$ and if the instability is convective $\mathfrak{Re}\{\mu_0\} < 0$. Use was made of (4.3.23) in Section 3.4 with the identical expression (3.4.1).

Summary

In this chapter, it was shown that the response of a temporally periodic flow to an impulsive excitation can be described by a solution integral (Section 4.1). Two methods were then implemented in Section 4.2 to deduce the leading-order behaviour of this integral as $\tau \to \infty$. Both the method of steepest-descent and Briggs' method were adapted from the approaches well documented for the steady problem (Briggs, 1964; Bers, 1983; Lingwood, 1997; Huerre, 2002).

Both methods were in agreement with regards to the expression for the leading-order behaviour of the disturbance at fixed spatial locations. This behaviour is dictated by the locations of saddle points in the dispersion relation in the complex α-plane (or the corresponding cusps in the complex μ-plane). It was shown through Briggs' method that an additional condition is that the saddle point is of pinch-type. That is, it satisfies the collision criteria that the branches of the saddle point originate in opposite halves of the complex α-plane. A brief discussion touched on why a naïve application of the method of steepest-descent can overlook this condition.

The concepts of absolute and convective instability were properly defined in Section 4.3. By appealing to the expected form of the leading-order behaviour, a means of

measuring both the temporal growth of the disturbance maximum and the growth at any fixed streamwise location was derived, as used in Chapter 3.

The necessary and sufficient conditions described in this chapter will be applied to the semi-infinite Stokes layer in Chapter 5. This will provide further insight into the evolution of disturbances in this flow and allow for a more detailed comparison of the two methods than was possible in Chapter 3.

Chapter 5

The cusp map method for the semi-infinite Stokes layer

Introduction

In Chapter 4, the leading-order behaviour of an impulse response to a general periodic flow was found. The necessary and sufficient conditions for absolute instability in this regime, as reported in Brevdo & Bridges (1997), were then deduced in analogy with the steady case. In this chapter, these conditions will be applied to the semi-infinite Stokes layer in support of the interpretation of the simulations results presented in Chapter 3: that this flow is subject to absolute instability.

First it is noted that, in addition to being temporally periodic, the velocity profile of the Stokes layer is completely reversed by a time shift of half a period (antiperiodicity). It was already noted in Chapter 1 that this feature constrains the locations of eigenvalues (which must appear in complex conjugate pairs). This and other symmetries will be explored in this chapter and the manner in which these symmetries constrain the conditions for absolute instability will be discussed.

The temporal variation of the impulse response to the Stokes layer at $Re = 750$ will be explored through the locating of cusps with certain characteristics. This will provide further insight into some of the features discussed in Chapter 3 and it will be confirmed that the behaviour predicted by these cusps is consistent with the numerical simulations.

5.1 Symmetries in antiperiodic flows

It was shown in Chapter 4 that a disturbance in a temporally periodic flow displays temporal growth at all spatial locations if there is a saddle point of the dispersion relation that corresponds to the collision of an upstream developing mode with a downstream developing mode. In addition to having a period of 2π, the Stokes layer is also antiperiodic with an antiperiod of π. That is, the velocity profile is exactly reversed by a time shift of π (half a period). This results in a blurring of the definitions of upstream and downstream (as was discussed in Section 3.1) and so it may be expected that the antiperiodicity would influence the collision criteria. In this section, the manner in which the antiperiodicity of a flow can constrain the dispersion relation is explored.

Consider the eigenvalue problem (1.2.7) as derived in Chapter 1,

$$\frac{\partial}{\partial\tau}\mathcal{L}\psi(y,\tau)=\left[\frac{1}{2}\mathcal{L}-\mu-i\alpha ReU\right]\mathcal{L}\psi(y,\tau)+i\alpha ReU''\psi(y,\tau), \tag{5.1.1}$$

where $\psi(y,\tau)$ is 2π-periodic in τ and

$$\mathcal{L}=\frac{\partial^2}{\partial y^2}-\alpha^2.$$

This describes a disturbance with wavenumber α, Floquet exponent μ, and periodic eigenfunction ψ. That is, the solution is characterised by

$$\Big[\alpha,\mu,\psi(y,\tau)\Big], \tag{5.1.2}$$

which is equivalent to $D(\alpha,\mu)=0$.

There are a series of actions that can be performed that preserve the characteristic of solving the disturbance equation (5.1.1). First, taking the complex conjugate yields

$$\frac{\partial}{\partial\tau}\mathcal{L}\bar{\psi}(y,\tau)=\left[\frac{1}{2}\mathcal{L}-\bar{\mu}+i\bar{\alpha}ReU\right]\mathcal{L}\bar{\psi}(y,\tau)-i\bar{\alpha}ReU''\bar{\psi}(y,\tau).$$

Comparison with the original equation gives a solution characterised by

$$\Big[-\bar{\alpha},\bar{\mu},\bar{\psi}(y,\tau)\Big]. \tag{5.1.3}$$

This shows that if $D(\alpha,\mu)=0$ then $D(-\bar{\alpha},\bar{\mu})=0$ and will be referred to as the *complex con-*

jugate symmetry. This symmetry holds for all flows since the periodicity/antiperiodicity has not been used.

A time shift of $\tau \to \tau + \pi$ is equivalent to taking $U \to -U$. This should not alter the asymptotic dynamics since these are only meaningful for $\tau \to \infty$. The antiperiodicity may be used to deduce more solutions from (5.1.2). Taking the original equation (5.1.1) this time shift can be applied, giving

$$\frac{\partial}{\partial \tau}\mathcal{L}\psi(y,\tau+\pi) = \left[\frac{1}{2}\mathcal{L} - \mu + i\alpha ReU\right]\mathcal{L}\psi(y,\tau+\pi) - i\alpha ReU''\psi(y,\tau+\pi).$$

This yields the *time-shift symmetry*,

$$\Big[-\alpha, \mu, \psi(y,\tau+\pi)\Big], \tag{5.1.4}$$

so if $D(\alpha,\mu) = 0$ then $D(-\alpha,\mu) = 0$.

Finally, performing both this time shift and complex conjugation yields

$$\frac{\partial}{\partial \tau}\mathcal{L}\bar{\psi}(y,\tau+\pi) = \left[\frac{1}{2}\mathcal{L} - \bar{\mu} - i\bar{\alpha} ReU\right]\mathcal{L}\bar{\psi}(y,\tau+\pi) + i\bar{\alpha} ReU''\bar{\psi}(y,\tau+\pi),$$

giving the *complex conjugate & time-shift symmetry*,

$$\Big[\bar{\alpha}, \bar{\mu}, \bar{\psi}(y,\tau+\pi)\Big]. \tag{5.1.5}$$

Therefore, if $D(\alpha,\mu) = 0$, then $D(\bar{\alpha},\bar{\mu}) = 0$.

Gathering all of these equivalences together reveals that if $[\alpha,\mu,\psi(y,\tau)]$ solves the eigenvalue problem then so must $[-\alpha,\mu,\psi(y,\tau+\pi)]$, $[\bar{\alpha},\bar{\mu},\bar{\psi}(y,\tau+\pi)]$ and $[-\bar{\alpha},\bar{\mu},\bar{\psi}(y,\tau)]$.

In terms of the dispersion relation, for which the eigenfunction ψ is not important, this means that if $D(\alpha,\mu) = 0$ then it must also hold that $D(-\alpha,\mu) = D(\bar{\alpha},\bar{\mu}) = D(-\bar{\alpha},\bar{\mu}) = 0$.

5.1.1 Special cases

Consider the special case $\alpha \in \mathbb{R}$. In this case conjugation has no effect, i.e. $\bar{\alpha} = \alpha$. Hence, the complex conjugate symmetry becomes

$$\Big[-\alpha, \bar{\mu}, \bar{\psi}(y,\tau)\Big], \tag{5.1.6}$$

and the complex conjugate & time-shift symmetry becomes

$$\left[\alpha, \bar{\mu}, \bar{\psi}(y, \tau + \pi)\right]. \tag{5.1.7}$$

Comparing (5.1.7) with (5.1.2) shows that for a given $\alpha \in \mathbb{R}$, if μ is an eigenvalue, then $\bar{\mu}$ must also be an eigenvalue. This was already discussed in Chapter 1, though it is interesting to note that this symmetry no longer holds for complex α. Comparison of (5.1.6) with the time-shift symmetry (5.1.4) gives the same result for $-\alpha$.

Hence, if $D(\alpha, \mu) = 0$ and $\alpha \in \mathbb{R}$, then it must also hold that $D(\alpha, \bar{\mu}) = 0$.

Another special case of interest is when $\bar{\mu} = \mu$. This is clearly the case when $\mu \in \mathbb{R}$ but the harmonic decomposition allows for further instances where this essentially holds. Remember that the periodic function ψ is decomposed into harmonics in (1.2.8),

$$\psi(y, \tau) = \sum_{n=-\infty}^{\infty} \psi_n(y) \mathrm{e}^{in\tau}. \tag{5.1.8}$$

as discussed earlier. This means that if μ is an eigenvalue then $\mu \pm ki$ must also be an eigenvalue for $k \in \mathbb{N}$. This is because k can simply be absorbed into the infinite sum as a relabelling.

If $\mu_i = 1/2$, taking the complex conjugate of μ is equivalent to taking $\mu \to \mu - i$ so, for μ of the form

$$\mu = \mu_r + \frac{ik}{2}, \quad \text{for} \quad k \in \mathbb{Z}, \tag{5.1.9}$$

it follows that if μ is an eigenvalue then $\bar{\mu}$ must necessarily be an eigenvalue (regardless of the value of α) since conjugation is equivalent to an integer shift in the imaginary part of μ.

In this special case, the complex conjugate symmetry becomes

$$\left[-\bar{\alpha}, \mu, \bar{\psi}(y, \tau)\right], \tag{5.1.10}$$

and the complex conjugate & time-shift symmetry becomes

$$\left[\bar{\alpha}, \mu, \bar{\psi}(y, \tau + \pi)\right]. \tag{5.1.11}$$

Comparison of (5.1.11) with (5.1.2) reveals that for a given μ of this form, if α is an

eigenvalue then $\bar{\alpha}$ must also be an eigenvalue. The same must hold for $-\alpha$ and $-\bar{\alpha}$.

Hence, if $D(\alpha, \mu) = 0$ with $\mu = \mu_r + ik/2$, then it must also hold that $D(\bar{\alpha}, \mu) = 0$.

5.1.2 Demonstration of symmetries and modal coalescence

The symmetry of the dispersion relation will now be demonstrated through solution of the eigenvalue problem. First, the eigenvectors associated with two complex conjugate μ-roots of the dispersion relation for a fixed, real α will be considered. It will be shown that, as predicted above, these eigenvectors are time-shifted, complex conjugates of one another. Following this, the special case in which two μ-roots have coalesced on the real line will be considered and it will be shown that in this case the eigenvector displays the same symmetry with itself.

Below, it will be assumed that each eigenvalue μ has a single corresponding eigenfunction $\boldsymbol{\psi}$. This is not necessarily always the case since repeated eigenvalues can be associated with two or more linearly independent eigenfunctions. When multiple eigenfunctions are associated with a single eigenvalue, these functions span a subspace. This is called the eigenspace and is of the same dimension as the number of linearly independent eigenfunctions.

For the following two examples, there are no repeated eigenvalues so the eigenspace is of dimension one. This is consistent with all of the examples explored in the present work so higher dimension eigenspaces are not considered in any detail. However, the possibility of repeated eigenvalues should not be ignored. Where appropriate, the issues arising when the eigenspace is of a higher dimension are alluded to.

Real α, complex conjugate μ

Consider $\alpha \in \mathbb{R}$. Let μ be one possible μ-root of the dispersion relation corresponding to this α. Letting $\boldsymbol{\psi}$ denote the eigenfunction associated with μ, we can characterise this solution by

$$\Big[\alpha, \mu, \psi(y, \tau)\Big].$$

Furthermore, it has already been shown that (for real α) there must also be a solution

$$\Big[\alpha, \bar{\mu}, \bar{\psi}(y, \tau + \pi)\Big],$$

due to the symmetries of the problem. The problem explored here is linear, meaning that if any function is a solution to the problem, then so too is any constant multiple of this function. This means that, when μ is not real (i.e. μ and $\bar{\mu}$ are distinct), the eigenfunctions associated with μ and $\bar{\mu}$ are expected be related by

$$\psi(y,\tau;\mu) = C\bar{\psi}(y,\tau+\pi;\bar{\mu}), \tag{5.1.12}$$

where C is some complex constant that arises due to the linearity of the problem. For this α, the eigenfunctions associated with these two values of μ should be time-shifted, complex conjugated versions of the same function up to this multiplicative constant.

This assertion is made under the stated assumption that the eigenspace has a dimension of one. In the case of repeated eigenvalues, the symmetry arguments only suggest that the linearly independent eigenfunctions span the same subspace. The equivalence of eigenfunctions thus becomes more difficult to show.

In order to demonstrate whether (5.1.12) holds, the eigenvectors are found by the method described in Section 1.4. Here, the term eigenvector refers to the discrete approximation to the eigenfunction (rather than the concatenated vector found directly by the numerical approach). Let μ denote the eigenvalue with positive imaginary part so that $\bar{\mu}$ has negative imaginary part and introduce the notation,

$$\psi_1(y,\tau) = \psi(y,\tau;\mu), \tag{5.1.13a}$$

$$\psi_2(y,\tau) = \psi(y,\tau;\bar{\mu}). \tag{5.1.13b}$$

Now, as an example fix $\alpha = 0.374$. Solving the eigenvalue problem results in the unstable Floquet exponents $\mu = 0.198063 \pm 0.108927$ and no repeated eigenvalues. The eigenvectors corresponding to these eigenvalues should be linearly related by (5.1.12). This equivalence is illustrated in Figure 5.1a. The appropriate eigenvectors can be extracted and are shown at a fixed y location over a period of oscillation in Figure 5.1b and Figure 5.1c.

To demonstrate that these eigenvectors are indeed equal under complex conjugation and a time shift of half a period, note that it follows from (5.1.12) that the ratio

$$\frac{\psi_1(y,\tau)}{\bar{\psi}_2(y,\tau+\pi)}, \tag{5.1.14}$$

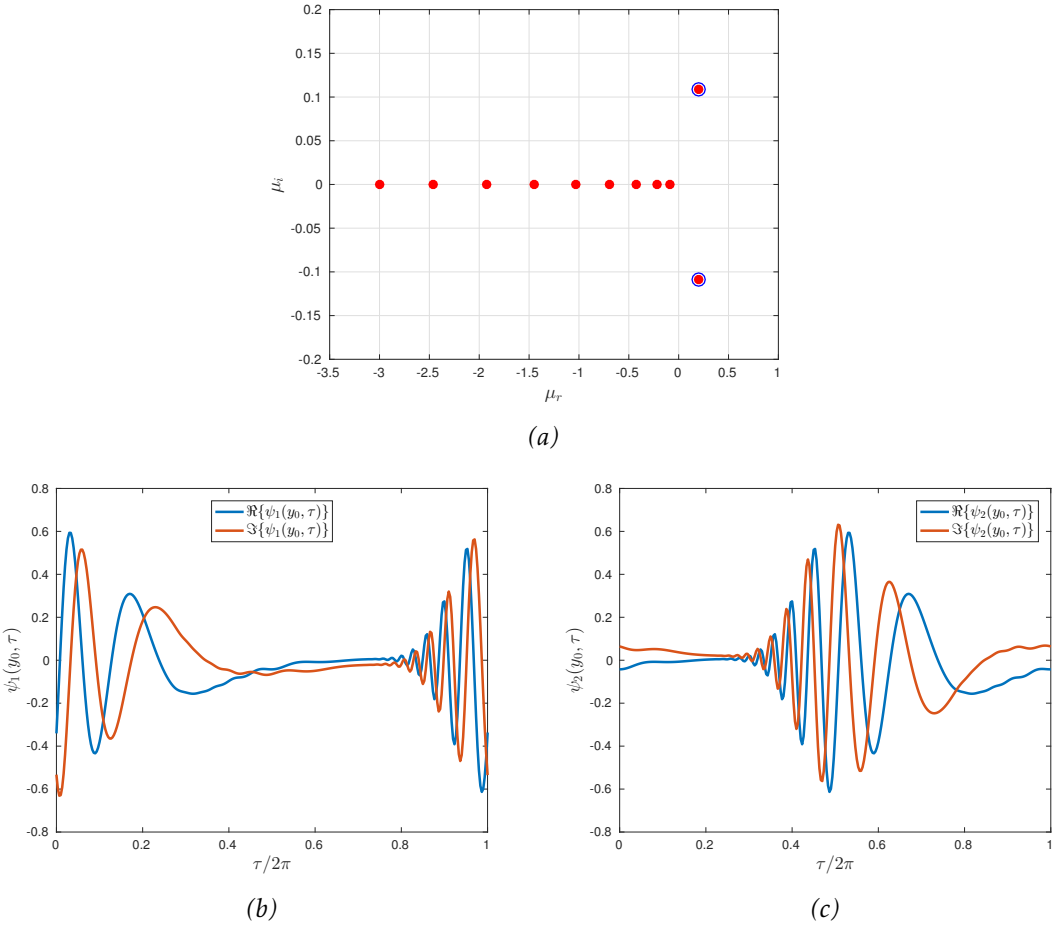

Figure 5.1: The eigenvalue problem has been solved for $\alpha = 0.374$ and the resulting eigenvalues have been plotted in (a). In (b) and (c), the real and imaginary parts of the 2π-periodic eigenvectors have been plotted for the complex conjugate pair of eigenvalues in the unstable region of the μ-plane (indicated with circles) for a fixed y location corresponding to the maximum absolute value when $\tau = 0$. Choosing a different y location makes little difference to the qualitative features.

is independent of y and τ and can be determined using a single choice of these parameters. Here, the constant C will be defined as

$$C = \frac{\psi_1(y = y_0, \tau = 0)}{\bar{\psi}_2(y = y_0, \tau = \pi)}, \tag{5.1.15}$$

where y_0 is the location of the absolute value of ψ_1 when $\tau = 0$. The eigenvector $\boldsymbol{\psi}_2$ was then rescaled by dividing by C and compared against an unchanged $\boldsymbol{\psi}_1$. In Figure 5.2, the real and imaginary parts are compared separately and the agreement is excellent. For this example it has thus been demonstrated that the eigenfunctions exhibit the anticipated symmetries.

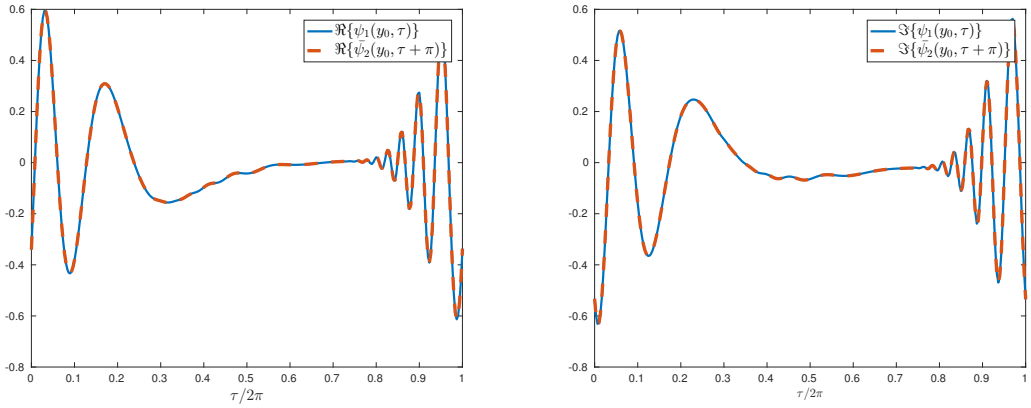

(a) *(b)*

Figure 5.2: Comparison of ψ_1 at the fixed y location with the complex conjugate of ψ_2 shifted by half a period. In (a) the real parts are compared and in (b) the imaginary parts are compared. The agreement is clear. A marginally thicker, dashed line was necessary to indicate the two different curves.

To check consistency, the ratio (5.1.14) was calculated for several choices of y and τ. For all cases tested this ratio was equal to C as defined in (5.1.15).

Real α, real μ

Consider now a case in which the two complex conjugate eigenvalues have coalesced on the real line. In this case the eigenvalue is its own complex conjugate, and thus the corresponding eigenfunction should display the same symmetry with itself (again, assuming that each eigenvalue has only a single corresponding eigenfunction). In other words, taking a time shift of half a period and conjugating the eigenvector is expected to produce an identical periodic function up to a multiplicative constant.

Since there is only one eigenvalue/eigenvector pair of interest, denote by $\boldsymbol{\psi}(\tau)$ the eigenvector corresponding to this value of μ for a given α. Since an eigenvector is only given up to a multiplicative constant, the symmetry of the periodic eigenvector with itself can only be defined up to this constant. This means that the time-shifted, complex conjugate of the eigenvector is a constant multiple of the original eigenvector. Thus, the constant C can be defined as in (5.1.15) with $\boldsymbol{\psi}_1(\tau) = \boldsymbol{\psi}_2(\tau) = \boldsymbol{\psi}(\tau)$ and is used to rescale the eigenvector for comparison with the original $\boldsymbol{\psi}$.

For demonstrative purposes take $\alpha = 0.374732$. The eigenvalues for this α are plotted in Figure 5.3a with the eigenvalue of interest being the only one in the unstable region of

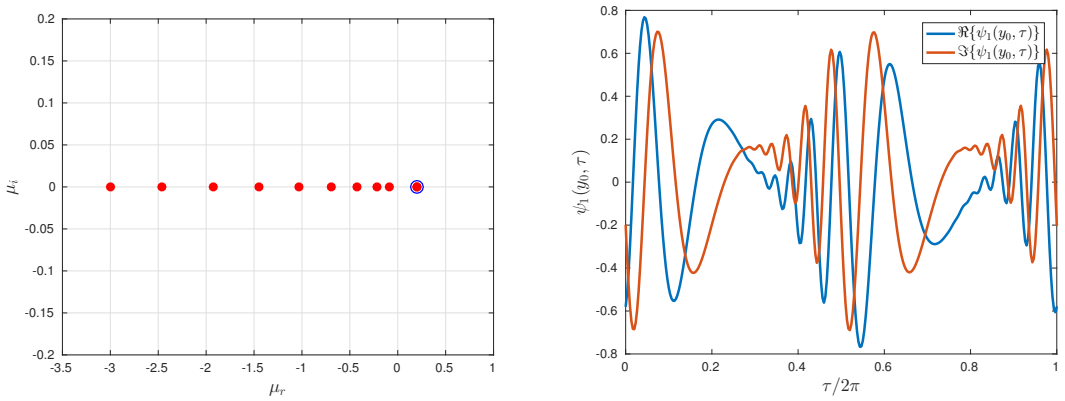

(a) (b)

Figure 5.3: The eigenvalue problem has been solved for $\alpha = 0.374732$ and the resulting eigenvalues are plotted in (a). The real and imaginary parts of the 2π-periodic eigenvector are plotted in (b) for the only eigenvalue in the unstable region of the μ-plane (indicated with a circle) for a fixed y location corresponding to the maximum absolute value when $\tau = 0$. Choosing a different y location makes little difference to the qualitative features.

the complex μ-plane. In this example there is again no evidence of repeated eigenvalues so the linear comparison (5.1.12) is appropriate. The (single) corresponding periodic eigenvector is plotted in Figure 5.3b at a fixed y location.

When comparing the eigenvector in Figure 5.3 with those in Figure 5.1, the most striking feature is that in the current case the disturbance reaches a high-amplitude twice in a period rather than once. This is to be expected since a second peak is required for the periodic eigenvector to exhibit the required symmetry. It is interesting to note that this eigenvector is not dissimilar to what would be observed if the eigenvectors corresponding to μ and $\bar{\mu}$ in Figure 5.1 were summed. This consistent with the interpretation of the μ in Figure 5.3a being a coalescence of the complex conjugate pairs seen in Figure 5.1a.

In order to ensure that the eigenvector ψ satisfies the anticipated symmetry, the real and imaginary parts are compared with the time-shifted, complex conjugated, rescaled ψ. These plots are shown in Figure 5.4 and again the agreement is excellent. It is worth noting that in this case the multiplicative constant satisfies $|C| = 1$. This means that there is no amplification of the eigenvector within a single period of wall motion. This could have been anticipated since the growth or decay of the eigenfunction is dictated by the real part of the eigenvalue μ.

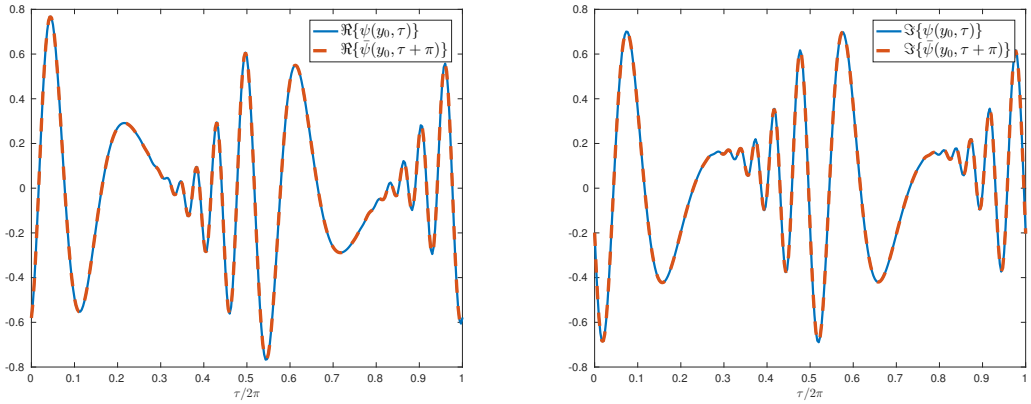

(a) *(b)*

Figure 5.4: Comparison of ψ at the fixed y location with its complex conjugate shifted by half a period. In (a) the real parts are compared and in (b) the imaginary parts are compared. The agreement is clear. Again, a marginally thicker, dashed line was necessary to indicate the two different curves.

5.2 Collision criteria for antiperiodic flows

It has now been shown that the dispersion relation corresponding to a flow that is temporally antiperiodic is constrained by the symmetries associated with this antiperiodicity. It is expected that these symmetries will in turn constrain the existence of saddle points of the dispersion relation. To explore this possibility, Briggs' method will now be revisited for flows displaying the symmetries discussed in Section 5.1. The steepest-descent method will not be revisited since it is more difficult to show that the collision criteria is satisfied whereas in Briggs' method this condition is clear and explicit.

First note that due to the time-shift symmetry, it must always hold that

$$D(\alpha,\mu)=0 \iff D(-\alpha,\mu)=0.$$

This means that if there is a downstream growing mode there must also be an upstream mode growing with the same growth-rate and vice versa. Therefore, if α_0 denotes a pinch-point of the dispersion relation, then there must be another pinch-point at $-\alpha_0$. This dos not significantly impact the existence of collisions but is important to consider when visualising the movement of α-roots in the complex plane.

Consider now the initial set-up as sketched in Figure 4.1. The contour F lies on the real line. This means that for any $\mu \in \mu(F)$ it must also hold that $\bar{\mu} \in \mu(F)$ since it has been

shown that, for real α,

$$D(\alpha, \mu) = 0 \iff D(\alpha, \bar{\mu}) = 0,$$

from the complex conjugate & time-shift symmetry when $\alpha \in \mathbb{R}$. The curve $\mu(F)$ must therefore be symmetric in the real axis.

The process, as before, is to select some μ on L and, fixing the imaginary part, move to the left. It is not possible for a collision to occur that satisfies the collision criteria until at least one α-root of the dispersion relation reaches the real axis. Thus, there is no behaviour of interest until the leftward path of μ touches the curve $\mu(F)$ (at such a point the corresponding α-root lies on F, i.e. the real axis). Notice that this demonstrates through the framework of Briggs' method what has already been shown through the method of steepest-descent: that the temporal growth-rate of a disturbance at all spatial locations is bounded from above by the temporal growth-rate of the disturbance maximum, which corresponds to $\alpha \in \mathbb{R}$. It also suggests that any collisions with μ to the right of $\mu(F)$ do not satisfy the collision criteria.

In order to provide an illustration of how the symmetries of the flow may constrain the existence of absolute instability, we focus on the case where the imaginary part of μ is selected to take the value $k/2$ for some $k \in \mathbb{Z}$. This value is fixed throughout the whole process, so for any μ along the horizontal path from L to $\mu(F)$ it must hold that

$$D(\alpha, \mu) = 0 \iff D(\bar{\alpha}, \mu) = 0$$

from the complex conjugate & time-shift symmetry in this special case. That is, for any μ along this path, the corresponding α-roots appear in complex conjugate pairs. As μ is moved to the left, the corresponding movement of all α-roots is therefore symmetric in the real axis.

When μ reaches the curve $\mu(F)$, at least one α-root touches the real axis. According to the complex conjugate & time-shift symmetry there must be another α-root that touches the real axis in the same location due to the symmetric motion of α-roots. In Figure 5.5 the symmetric movement of the α-roots and the subsequent collision of complex conjugate modes on the real line is demonstrated.

This shows that the symmetries of the problem ensure that there is a collision of α-roots on the real line for all $\mu_i = k/2$. Moreover, this collision must satisfy the colli-

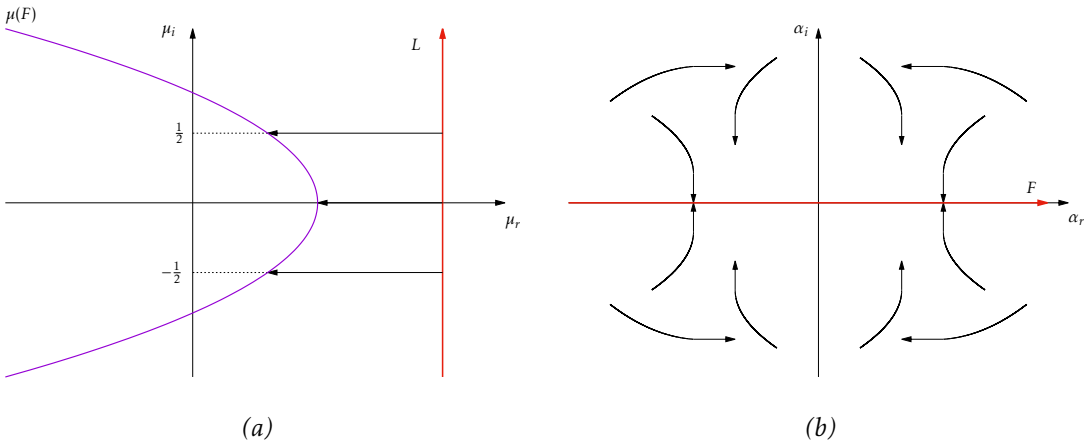

Figure 5.5: A sketch illustrating a collision that is constrained by the flow symmetries. In (a) three paths are chosen between L and $\mu(F)$ along which the movement of the corresponding α-roots of D must be symmetric in the real axis since $\mu_i = k/2$ for all μ on each path. In (b) the movement of several α-roots is demonstrated for any one of these paths. The complex conjugate symmetry means that when one α-root touches F from one side, there must be another α-root that touches F from the other side. Thus F is pinched on the real line. In addition to the complex conjugate symmetry there is a $\alpha \to -\alpha$ symmetry. Hence, for any collision that causes a pinching of the F contour at α_0, there must be another collision that causes a pinching of F at $-\alpha_0$.

sion criteria since it is a coalescence of a complex conjugate pair. The F contour is thus pinched on the real line.

Implicit in this work is the assumption that each eigenvalue has only one associated eigenfunction. If this is not the case, the apparent collision of α-roots does not necessarily correspond to a coalescence of eigenfunctions in the manner demonstrated in Figure 5.3. That is, if the α-roots pass over one another but the eigenfunctions remain distinct, this would not necessarily manifest as a collision. This consideration is not explored here since every case that has been inspected satisfies the assumption of a one-dimensional eigenspace, however this logical possibility should not be overlooked.

In Figure 5.5, the coalescence of two simple poles of the integrand into a second order pole is considered. There is no reason that higher order collisions cannot occur but it should be noted that, for the special cases ($\mu_i = k/2$ and $\alpha_i = 0$), the symmetry of the poles in the real axis of the α-plane means that only poles of an even order are possible. This is because collisions on the real axis occur between complex conjugate pairs.

For instance, if there is a collision of two α-roots at some α_0 and a third root was to collide at the same location then so must the complex conjugate of this third root, resulting in a fourth-order pole of the integrand at α_0.

Note also that in this case the collision on the real axis of two poles originating in the same half-plane must be accompanied by a collision of their complex conjugates at the same location. This suggests that it is not possible for a collision with $\mu_i = k/2$ and $\alpha_i = 0$ to occur that does not satisfy the collision criteria.

5.2.1 Other Collisions

It has been shown that the antiperiodicity of the Stokes layer has constrained the problem in such a way that there must be saddle points of pinch-type. However, it has not been possible to draw conclusions about collisions not caused by the flow symmetry. For instance, it is possible that there is a collision on the real line as μ undergoes the described movement from L to $\mu(F)$ even if the imaginary part is not prescribed the special value discussed above. If this is the case, it is not possible to discern from symmetry arguments whether such a collision is of pinch-type or whether the F contour can be deformed around this point.

Furthermore, there has been no discussion of collisions that occur at complex α. However, such collisions require μ to be moved past the curve $\mu(F)$ and so even those satisfying the collision criteria will contribute a growth-rate at each spatial location lower than that observed for $\alpha \in \mathbb{R}$. These collisions would therefore be of less consequence in deducing the leading-order asymptotic behaviour of the disturbance.

5.2.2 Harmonic and subharmonic temporal evolution

The saddle points that arise in the argument above must have $\mathrm{Im}\{\mu_*\} = k/2$ for any $k \in \mathbb{Z}$. It will now be shown that these cusps can be categorised as either harmonic or subharmonic based on the temporal variation they describe.

Consider even $k = 2m$ so that $\mathrm{Im}\{\mu_*\} = m \in \mathbb{Z}$. Due to the harmonic decomposition of the disturbance, any such case is equivalent to $\mathrm{Im}\{\mu_*\} = 0$ so we can write $\mu_* = \mu_r \in \mathbb{R}$. Using the expression for the leading-order behaviour at a fixed spatial location (4.3.16),

$$\psi(x_0, y, \tau) \sim \frac{1}{\sqrt{\tau}} p(y, \tau) \mathrm{e}^{\mu_r \tau}, \tag{5.2.1}$$

where p is 2π-periodic in τ. It is clear that this expression (ignoring the $1/\sqrt{\tau}$ term) describes a quasi-periodic function in τ with quasi-period 2π (according to the specific definition of quasi-periodicity used in this work). The quasi-period is equal to the period

of the underlying wall motion so, in consistency with the terms used in Chapter 3, this behaviour is termed *harmonic*.

Now consider odd $k = 2m+1$, meaning $\mathrm{Im}\{\mu_*\} = 1/2 + m$ for any $m \in \mathbb{Z}$. This problem can be reduced to $\mathrm{Im}\{\mu_*\} = 1/2$ so we can write $\mu_* = \mu_r + i/2$ with $\mu_r \in \mathbb{R}$. Appealing again to (4.3.16) gives

$$\psi(x_0, y, \tau) \sim \frac{1}{\sqrt{\tau}} p(y,\tau) e^{\mu_r \tau + \frac{i}{2}\tau} = \frac{1}{\sqrt{\tau}} p(y,\tau)\left[\cos\left(\frac{\tau}{2}\right) + i\sin\left(\frac{\tau}{2}\right)\right] e^{\mu_r \tau}. \tag{5.2.2}$$

The function in square brackets is periodic in τ with period 4π and so the function

$$p(y,\tau)\left[\cos\left(\frac{\tau}{2}\right) + i\sin\left(\frac{\tau}{2}\right)\right]$$

also has a period of 4π. Such a disturbance has a quasi-period of twice that of the underlying wall motion and is thus termed *subharmonic*.

The terms harmonic and subharmonic were used descriptively in Chapter 3, and it has now been shown how this distinction can be rigorously defined by considering the imaginary part of the Floquet exponent.

5.3 The cusp map method

The leading-order evaluation of the solution integral via the method of steepest-descent provides a necessary condition for absolute instability: that the dispersion relation D has a saddle point in the complex α-plane at some α_* (and a corresponding cusp in the complex μ-plane at some μ_*) such that $\mathfrak{Re}\{\mu_*\} > 0$. It was then shown that in addition to this condition, the double root of the dispersion relation must be caused by the collision of modes originating in opposite half-planes. It has also been shown, by appealing to the symmetries of the flow, that collisions of this type should occur in the Stokes layer when $\alpha \in \mathbb{R}$ and $\mu_i = k/2$ for $k \in \mathbb{Z}$.

The method that will now be implemented, based on these results, is that a straight grid in the complex α-plane, located around the real line, will be mapped through roots of the dispersion relation to the complex μ-plane using the eigenvalue solver developed in Chapter 1. Cusps in the complex plane can then be found, indicating the existence of a corresponding saddle point (Kupfer *et al.* , 1987). It will be assumed that the collision criteria is satisfied if these cusps display the anticipated properties of collisions that are

constrained by the antiperiodicity of the flow.

5.3.1 Cusp maps in the pure Stokes layer

In Chapter 3, the impulse response of the semi-infinite Stokes layer was explored. The results presented for $Re = 750$ appeared to suggest that there is absolute instability since the impulse response undergoes temporal growth at each spatial (streamwise) location. Furthermore, at each spatial location considered the disturbance was found to display a subharmonic form of temporal variation.

The case of the semi-infinite Stokes layer at $Re = 750$ will now be revisited in the context of the cusp map method outlined above. A search for cusps will be conducted in a neighbourhood of the real line since the symmetry arguments presented above anticipate the existence of cusps with $\alpha_* \in \mathbb{R}$ and that these will correspond to $\mathfrak{Im}\{\mu_*\} = k/2$ ($k \in \mathbb{Z}$).

It may be recalled that an intriguing feature of the variation in μ as α is moved along the real line is the existence of the small finger-like protrusions. The fingers are formed when the complex conjugate pairs of μ coalesce on the real axis, move along the real axis, then leave the real axis once more. This behaviour is described and documented in Blennerhassett & Bassom (2002) and in Section 1.4. The generic nature of this behaviour is explored in a simplified setting in Appendix B.

The significance of these features in finding absolute instability is that along such fingers the imaginary part of μ is fixed while the real part increases and decrease. When plotted in the complex plane, this suggests that these features may display characteristics associated with cusps. Furthermore, these protrusions occur when $\mu_i = 0$ which means that the symmetry of the flow should ensure that there are cusps in these locations.

Presented in Figure 5.6 are three unstable cusps found at the locations of these protrusions. These cusps all correspond to real α_* and have $\mathfrak{Im}\{\mu_*\} = 0$ so describe harmonic temporal evolution. These cusps should contribute to the asymptotic evolution of the disturbance at every streamwise location since cusps with $\mathfrak{Im}\{\alpha_*\} = \mathfrak{Im}\{\mu_*\} = 0$ are expected to satisfy the collision criteria, based on the symmetry arguments implemented in Section 5.1. Furthermore, they contribute temporal growth at each streamwise location since $\mathfrak{Re}\{\mu_*\} > 0$ in all three cases. Cusps that contribute harmonic temporal variation will sometimes be referred to as *harmonic cusps* for brevity.

The dispersion relation was explored further to locate the anticipated cusps with

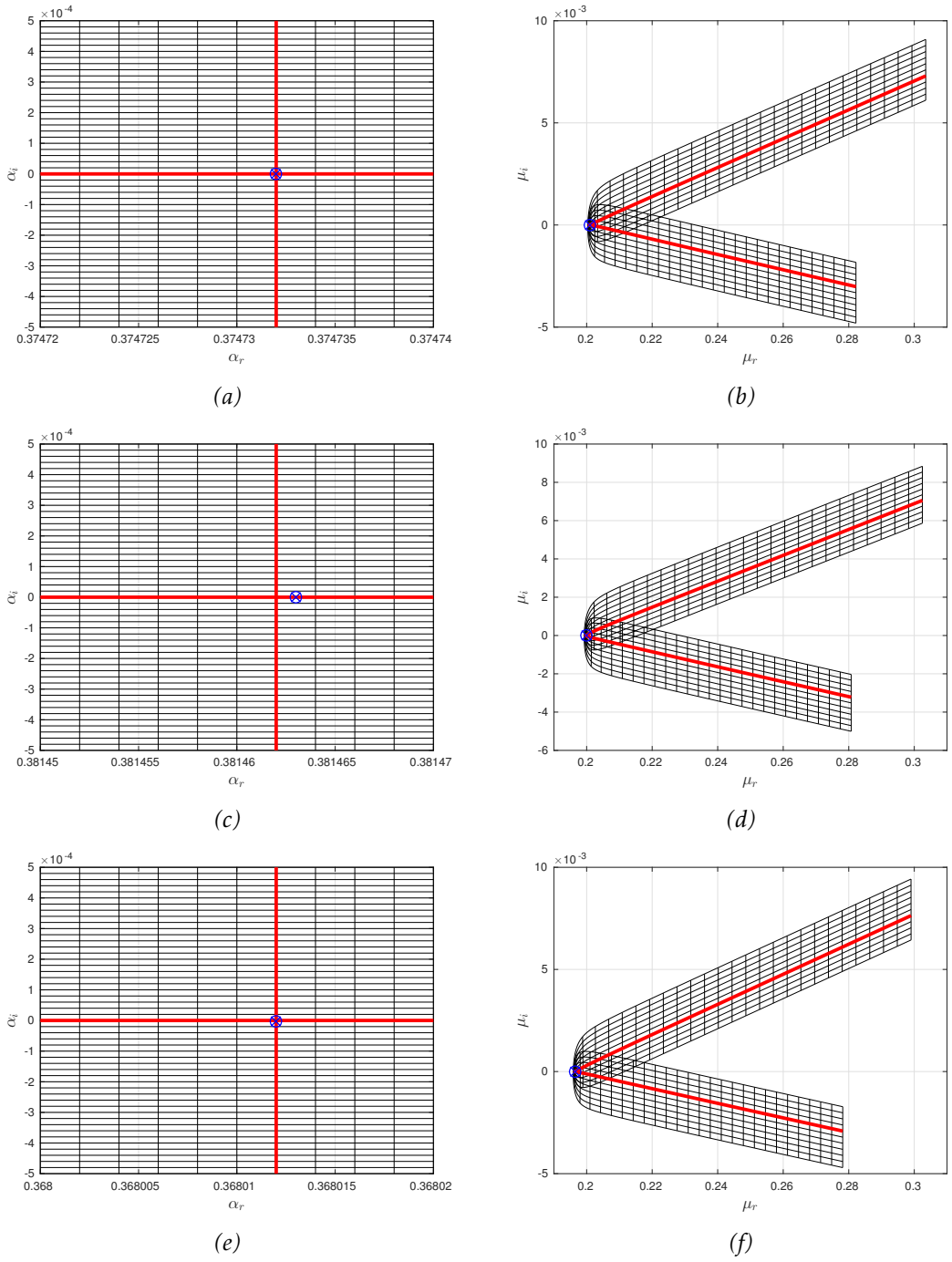

Figure 5.6: Three cusps found in the pure Stokes layer at Re = 750. The straight grids in the α-plane are shown in (a), (c), (e) and have been mapped via $D(\alpha, \mu) = 0$ to the complex μ-plane in (b), (d), (f), respectively. The circled crosses indicate the location of μ_* and α_* in each case, with the nearest grid lines indicated by greater thickness to better demonstrate the cusp characteristics in the μ-plane. All 3 cusps have $\mathfrak{Re}\{\mu_*\} > 0$ and $\mathfrak{Im}\{\mu_*\} = 0$ and correspond to the fingers described earlier.

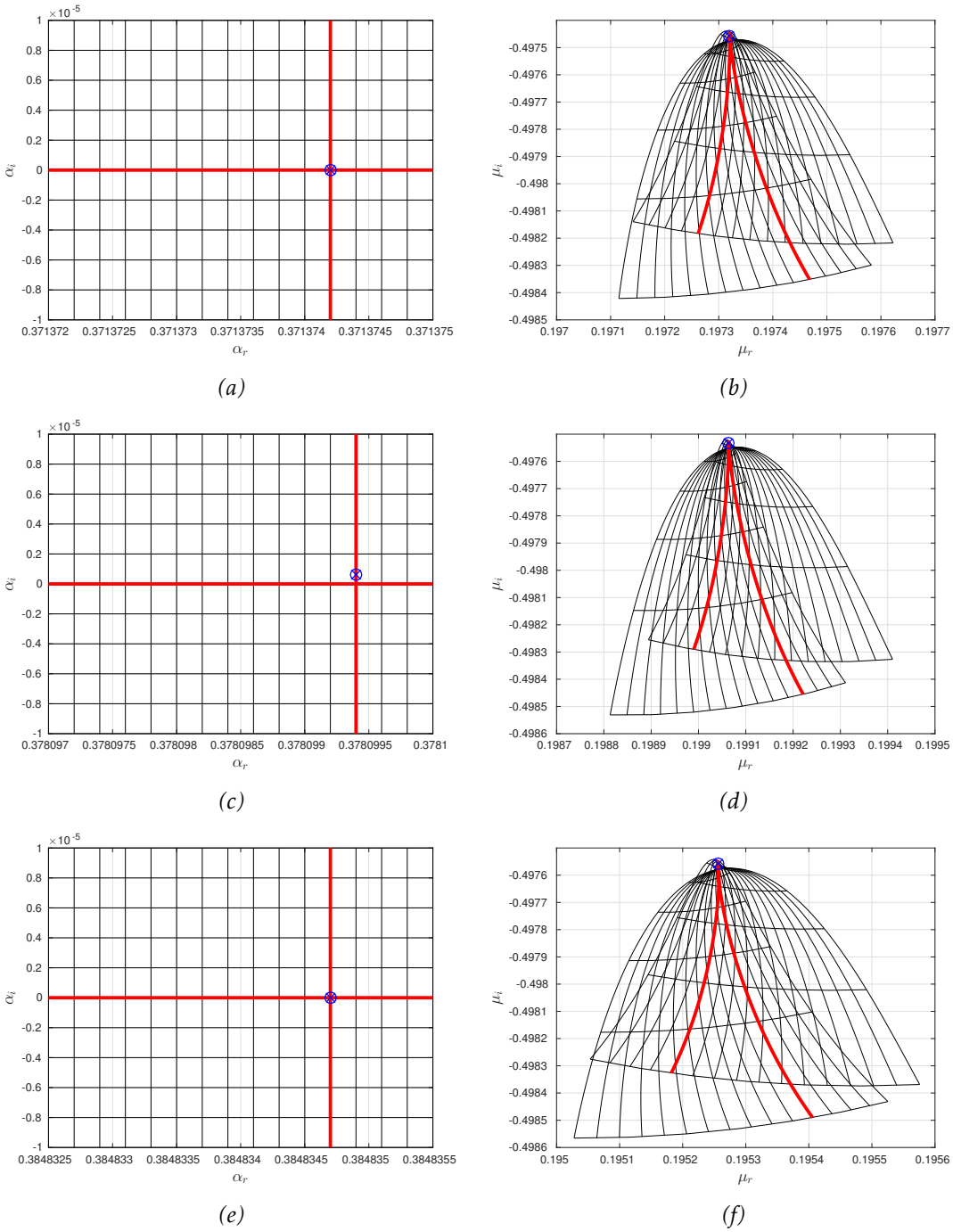

Figure 5.7: Three more cusps found in the pure Stokes layer at $Re = 750$. The straight grids in the α-plane are shown in (a), (c), (e) and have been mapped via $D(\alpha, \mu) = 0$ to the complex μ-plane in (b), (d), (f), respectively. The circled crosses indicate the location of μ_* and α_* in each case, with the nearest grid lines indicated by greater thickness to better demonstrate the cusp characteristics in the μ-plane. All 3 cusps have $\mathfrak{Re}\{\mu_*\} > 0$ and $\mathfrak{Im}\{\mu_*\} \sim -1/2$.

$\mathfrak{Im}\{\mu_*\} = 1/2$. Such cusps do not correspond to the finger-like protrusions. Presented in Figure 5.7 are three such unstable cusps located between each of the harmonic cusps shown in Figure 5.7. Since these cusps also satisfy the collision criteria and $\mathfrak{Re}\{\mu_*\} > 0$ for each, they describe subharmonic temporal variation at every spatial location and will thus be referred to as *subharmonic cusps*.

Note the very small scales required to properly observe these cusps, which have similar growth-rates to one another and the harmonic cusps already seen. Since it is difficult to ascertain the growth-rates from these figure, Table 5.1 shows the locations of α_* and μ_*.

Figure	$\mathfrak{Re}\{\alpha_*\}$	$\mathfrak{Im}\{\alpha_*\}$	$\mathfrak{Re}\{\mu_*\}$	$\mathfrak{Im}\{\mu_*\}$
5.6a,5.6b	0.374732	0	0.200921	0
5.6c,5.6d	0.381463	0	0.199897	-5×10^{-13}
5.6e,5.6f	0.368012	-2×10^{-6}	0.196484	-5×10^{-6}
5.7a,5.7b	0.3713742	2×10^{-21}	0.1973202	-0.4974585
5.7c,5.7d	0.3780994	7×10^{-7}	0.1990632	-0.4975318
5.7e,5.7f	0.3848347	0	0.1952561	-0.4975586

Table 5.1: The values of α_* and μ_* corresponding to Figure 5.6 and Figure 5.7. Notice that for the cusps that contribute subharmonic temporal variation ($\mathfrak{Im}\{\mu_*\} = 1/2$), the values are given to an extra decimal place due to the finer grids used.

A drawback of this method is that the locations of the cusps can only be approximated by the nearest grid-line. If the plots of Figure 5.6 and Figure 5.7 were observed at smaller scales it would reveal that these values of (α_*, μ_*) do not correspond to the exact locations of cusps. This combined with the limited precision of numerical methods offers a plausible explanation for why the subharmonic cusps have $\mathfrak{Im}\{\mu_*\} \sim 0.497$ rather than $= 1/2$.

Since all α_* lie on the real axis, these cusps can be compared against the growth-rate curve for real α (Figure 3.7a) by plotting the values of $\mathfrak{Re}\{\mu_*\}$ against α_*. This confirms, in Figure 5.8, that the harmonic cusps shown in Figure 5.6 do in fact all lie on the fingers protruding from the growth-rate curves. The subharmonic cusps of Figure 5.7 lie between these fingers. It is interesting to note that the fingers are evenly spaced in α, and so too are the cusps that lie halfway between them.

Some of the ideas discussed in Chapter 3 will now be revisited since the cusp map method provides further insight into the evolution of these disturbances. Consider the pure (semi-infinite) Stokes layer at $Re = 750$.

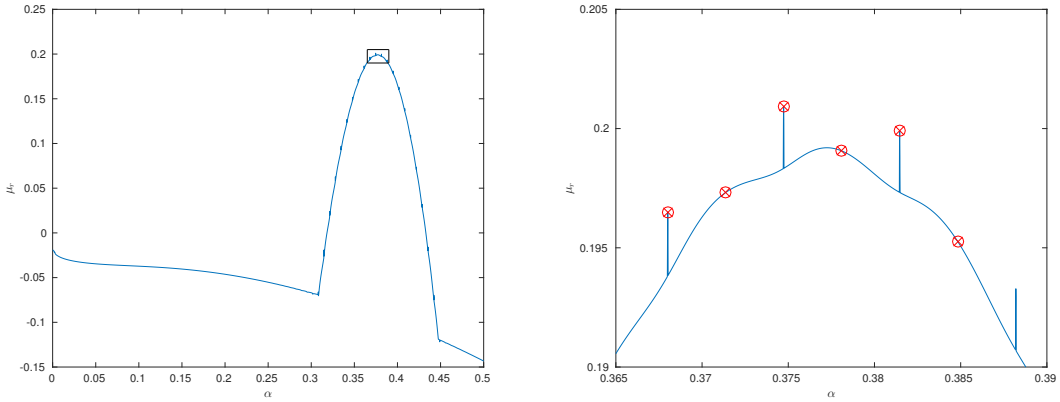

(a) *(b)*

Figure 5.8: The growth-rate μ_r is plotted against real α for the pure Stokes layer with $Re = 750$ (a). A small portion at the tip of this curve is shown in (b) and the locations of the cusps are indicated by circled crosses. The cusps are roughly evenly spaced in α and occur either at the tip of the finger or halfway between them. Only the six cases of Figure 5.6 and Figure 5.7 are indicated but it is assumed that this pattern would hold for all cusps.

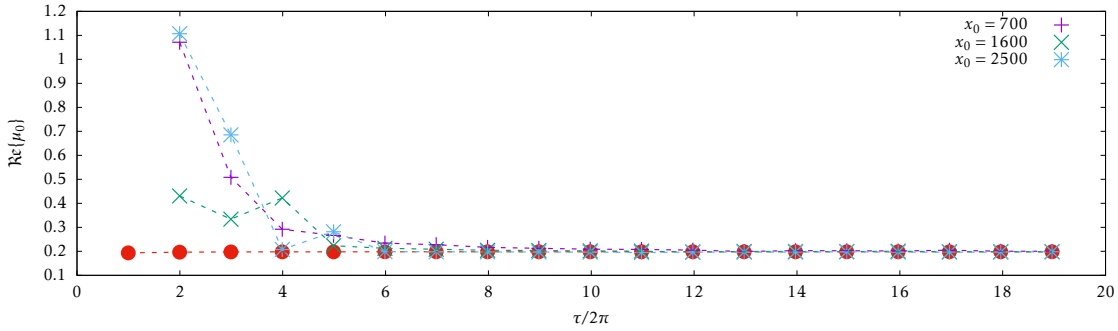

Figure 5.9: The temporal growth-rates corresponding to the disturbance maximum and the temporal evolution at three different locations in the pure Stokes layer at $Re = 750$. This plot is the same as Figure 3.11 except the measured growth-rate of the disturbance maximum is included (•), as seen in Figure 3.7b for the first ten periods of wall motion.

5.3.2 Growth and staggering of wavepackets

It was shown in Figure 3.11b (and reproduced in Figure 5.9) that when $Re = 750$ the temporal growth-rate associated with a selection of streamwise location and the temporal growth-rate associated with the disturbance maximum converge to very similar values in twenty periods of wall oscillation. The subsequent discussion was cautious since the asymptotic values of the growth-rate will not be reach in finite time.

It has since been seen in some detail that the temporal growth of the disturbance maximum is dictated by the most unstable mode for real α (Section 4.3). Furthermore,

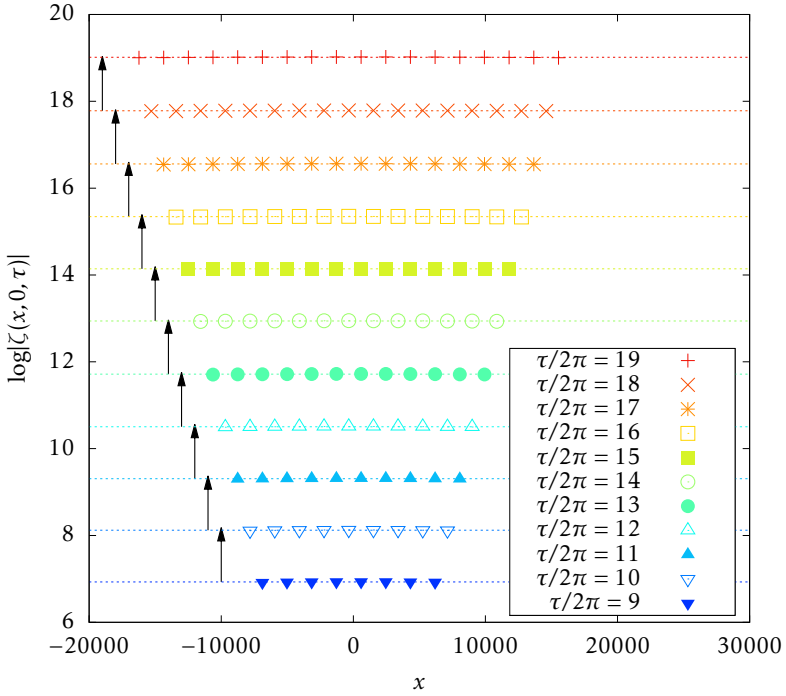

Figure 5.10: The logarithm of local maxima plotted at the start of several periods shows that at every time all wavepackets are of the same magnitude and that this magnitude increases at a constant growth-rate (see Figure 3.13 for full description).

the temporal growth at any fixed point in space is dictated by the locations of cusps, which have now been seen that correspond to real α. Moreover, the maximum growth-rate over all $\alpha \in \mathbb{R}$ is found at the tip of a finger which is also the location of the cusp with maximum growth-rate. This suggests that the temporal growth at each spatial location is indeed equal to that of the disturbance maximum.

While the cusp map method of Figure 5.6 and Figure 5.7 has only been employed for $Re = 750$, the existence of the cusps was predicted by appealing to the symmetries of the problem. These symmetries apply for all Re which suggests that similar cusps exist in all cases. This suggests that there is no region of convective instability in the Stokes layer between the regions of stability and absolute instability.

In Section 3.4, a subharmonic temporal variation was observed in which the wavepackets are staggered periodically. Figure 3.13 (reproduced in Figure 5.10) illustrates that each disturbance wavepacket (at a fixed location) undergoes the same growth each period even though the location of each wavepacket changes each period.

The size of the arrows in Figure 3.13 and Figure 5.10 was not fully justified at the

time, but the temporal growth-rate associated with each streamwise location has now been found by the cusp map method. The cusp displaying maximum temporal growth has a growth-rate of $\mu_r = 0.200921$ and so, to account for the rescaling of time in these plots the arrows are all of length $2\pi\mu_r = 1.2624$. Not only is the agreement clear, but the agreement seems to improve for later times. This is to be expected from a comparison of finite-time simulations against the asymptotically predicted behaviour. The differences in the growth-rates for the 6 cusps shown in Figure 5.8 would not be visible on this plot.

5.3.3 Periodic orbits and subharmonic temporal variation

To some extent, it is surprising that at each streamwise location the temporal variation of this disturbance is subharmonic since the most unstable cusp has imaginary part 0. However, it has already been noted that the growth-rates of the 6 cusps discussed above are incredibly close to one another so it is anticipated that no single cusp would become sufficiently dominant for the others to be disregarded within the twenty periods of oscillation investigated. The behaviour at any given streamwise location is characterised by a summation of several modes showing harmonic temporal growth and several showing subharmonic temporal growth so the superposition would be expected to be subharmonic.

Superposition of harmonic and subharmonic modes

Having shown that the temporal growth-rate experienced by the disturbance at every spatial location is consistent with the cusp map method, the temporal periodicity of the disturbance in these locations can be investigated by normalising the value of the wall vorticity at some initial time (so that it lies on the unit circle in the complex plane) and comparing this with the normalised wall vorticity at the same phase of subsequent periods of wall oscillation in the same location.

For illustrative purposes, the superposition of multiple cusps with both harmonic and subharmonic temporal characteristics (which will be referred to as harmonic modes and subharmonic modes, respectively) will be simplified to just considering one of each type (noting that subharmonic modes appear in complex-conjugate pairs).

The problem will be further simplified by assuming that these modes have equal growth-rates, although it is known that the harmonic mode corresponds to marginally

larger temporal growth.

It will be assumed that the wall vorticity at a fixed location $\zeta_0(\tau) = \zeta(x_0, 0, \tau)$ has the form

$$\zeta_0(\tau) = p_1(\tau)e^{(\mu_r + \frac{i}{2})\tau} + p_2(\tau)e^{(\mu_r - \frac{i}{2})\tau} + p_3(\tau)e^{\mu_r \tau}, \tag{5.3.1}$$

where p_1, p_2 and p_3 are complex valued, 2π-periodic functions.

Fix an initial time τ_0 and define the following constants

$$A = p_1(\tau_0)e^{(\mu_r + \frac{i}{2})\tau_0}, \tag{5.3.2a}$$

$$B = p_2(\tau_0)e^{(\mu_r - \frac{i}{2})\tau_0}, \tag{5.3.2b}$$

$$C = p_3(\tau_0)e^{\mu_r \tau_0}. \tag{5.3.2c}$$

It is then possible to express ζ_0 at the same phase of subsequent periods in terms of these constants,

$$\zeta_0(\tau_0) = A + B + C, \tag{5.3.3a}$$

$$\zeta_0(\tau_0 + 2\pi) = Ae^{2\pi\mu_r}e^{i\pi} + Be^{2\pi\mu_r}e^{-i\pi} + Ce^{2\pi\mu_r} = (-A - B + C)e^{2\pi\mu_r}, \tag{5.3.3b}$$

$$\zeta_0(\tau_0 + 4\pi) = Ae^{4\pi\mu_r}e^{i2\pi} + Be^{4\pi\mu_r}e^{-i2\pi} + Ce^{4\pi\mu_r} = (A + B + C)e^{4\pi\mu_r}. \tag{5.3.3c}$$

Observing the pattern, it can be stated that

$$\zeta_0(\tau_0 + 2k\pi) = \Big((-1)^k(A + B) + C\Big)e^{2k\pi\mu_r}, \tag{5.3.4}$$

for $k = 0, 1, 2, \ldots$.

Without loss of generality, assume that $\zeta_0(\tau_0)$ lies in the top right quadrant of the complex plane, i.e. $\mathfrak{Re}\{\zeta_0(\tau_0)\}, \mathfrak{Im}\{\zeta_0(\tau_0\} > 0$. If this is not the case, the problem can be adjusted by dividing all expressions by some complex number which ensures that this is the case.

Consider the wall vorticity at some given time τ_0,

$$\zeta_0(\tau_0) = A + B + C$$

and call the complex argument of this value θ_0. This is given by

$$\theta_0 = \mathrm{Arg}[\zeta_0(\tau_0)] = \arctan\left(\frac{\mathfrak{Im}\{\zeta_0(\tau_0)\}}{\mathfrak{Re}\{\zeta_0(\tau_0\}}\right) = \arctan\left(\frac{A_i + B_i + C_i}{A_r + B_r + C_r}\right). \tag{5.3.5}$$

Now consider the wall vorticity after a period of wall motion has passed,

$$\zeta_0(\tau_0 + 2\pi) = (-A - B + C)\mathrm{e}^{2\pi\mu_r}. \tag{5.3.6}$$

Denote the complex argument of this value by θ_1. For demonstrative purposes, assume that $\zeta_0(\tau_0 + 2\pi)$ also lies in the top right quadrant. Then

$$\theta_1 = \mathrm{Arg}[\zeta_0(\tau_0 + 2\pi)] = \arctan\left(\frac{\mathrm{e}^{2\pi\mu_r}(-A_i - B_i + C_i)}{\mathrm{e}^{2\pi\mu_r}(-A_r - B_r + C_r)}\right) = \arctan\left(\frac{-A_i - B_i + C_i}{-A_r - B_r + C_r}\right). \tag{5.3.7}$$

Note the cancellation of the exponential amplification within the arctan. The expression for θ_1 varies depending on which quadrant $\zeta_0(\tau_0 + 2\pi)$ lies in so a full expression is given by

$$\theta_1 = \mathrm{Arg}[\zeta_0(\tau_0 + 2\pi)] = \begin{cases} \arctan\left(\frac{-A_i - B_i + C_i}{-A_r - B_r + C_r}\right) & \text{if} \quad (-A_r - B_r + C_r) > 0, \\ \frac{\pi}{2} - \arctan\left(\frac{-A_r - B_r + C_r}{-A_i - B_i + C_i}\right) & \text{if} \quad (-A_i - B_i + C_i) > 0, \\ -\frac{\pi}{2} - \arctan\left(\frac{-A_r - B_r + C_r}{-A_i - B_i + C_i}\right) & \text{if} \quad (-A_i - B_i + C_i) < 0, \\ \arctan\left(\frac{-A_i - B_i + C_i}{-A_r - B_r + C_r}\right) \pm \pi & \text{if} \quad (-A_r - B_r + C_r) < 0. \end{cases} \tag{5.3.8}$$

Again, the exponential amplification cancels so the value of θ_1 is dependent only on the ratio of the real and imaginary parts of $(-A - B + C)$.

The subsequent expressions of $\zeta_0(\tau_0 + 2k\pi)$ for even k differ from the $k = 0$ case above through multiplication by a real number (exponential amplification) and the expressions for odd k are similarly related to the case $k = 1$. These real numbers cancel in the quotient within the argument of arctan. Thus,

$$\mathrm{Arg}[\zeta_0(\tau_0 + 2k\pi)] = \begin{cases} \theta_0 & k = 0, 2, 4, \ldots \\ \theta_1 & k = 1, 3, 5, \ldots \end{cases}, \tag{5.3.9}$$

which shows that if $\zeta_0(\tau_0 + 2k\pi)$ is divided by its magnitude (normalised) and the resulting complex values are plotted for $k = 0, 1, 2, \ldots$ then for every even k these points will lie in the same location on the unit circle (characterised by the angle θ_0) and for every

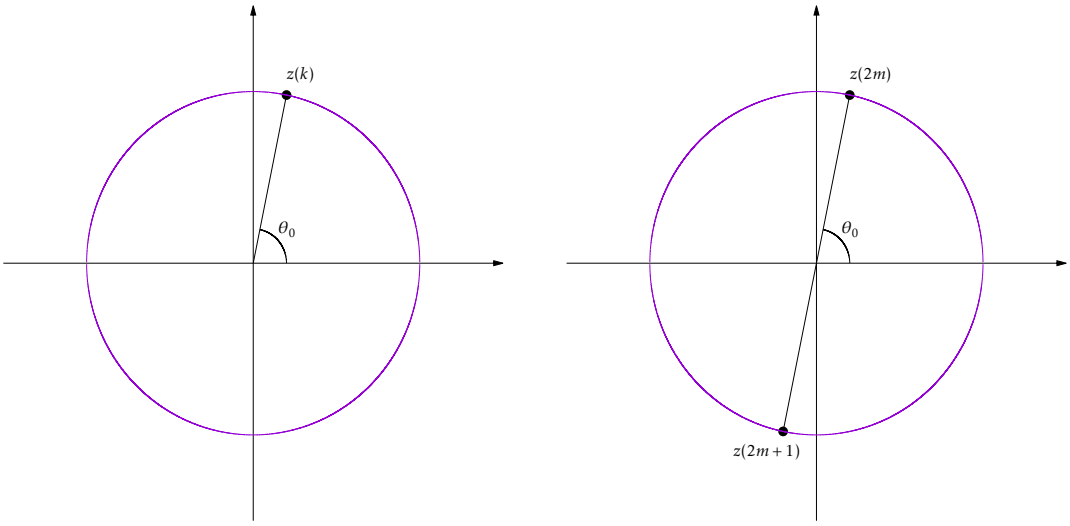

Figure 5.11: Examples of the expected behaviour of $z(k)$ for the purely harmonic (a) and purely subharmonic (b) cases. In (a), the value of z is independent of the choice of k. In (b) the value of z depends on whether k is even or odd. Note that the line passing from $z(2m+1)$ to $z(2m)$ is a straight line passing through the origin since $\theta_1 = \theta_0 - \pi$.

odd k the points will lie in a second location (characterised by the angle θ_1). In order to demonstrate this clearly, let

$$z(k) = \frac{\zeta_0(\tau_0 + 2k\pi)}{|\zeta_0(\tau_0 + 2k\pi)|}, \tag{5.3.10}$$

so that it is anticipated that for $k = 0, 1, 2, 3...$, the location of z on the unit circle will alternate between two locations, with complex arguments of θ_0 and θ_1. It is therefore convenient to introduce another number m so that $z(2m)$ denotes the value of z for even k and $z(2m+1)$ represents odd k.

Consider the special case of a purely harmonic mode. In this case A and B are zero, and so $\theta_1 = \theta_0$. Hence, $z(k)$ all appear in the same location for all k. Considering the case of a purely subharmonic mode, $C = 0$ so $\theta_1 = \theta_0 - \pi$. In this case, $z(k)$ alternates between two locations on opposite sides of the unit circle as k alternates between odd and even. Examples of this behaviour are given in Figure 5.11. Considering harmonic and subharmonic modes together means there is no such relationship between θ_0 and θ_1.

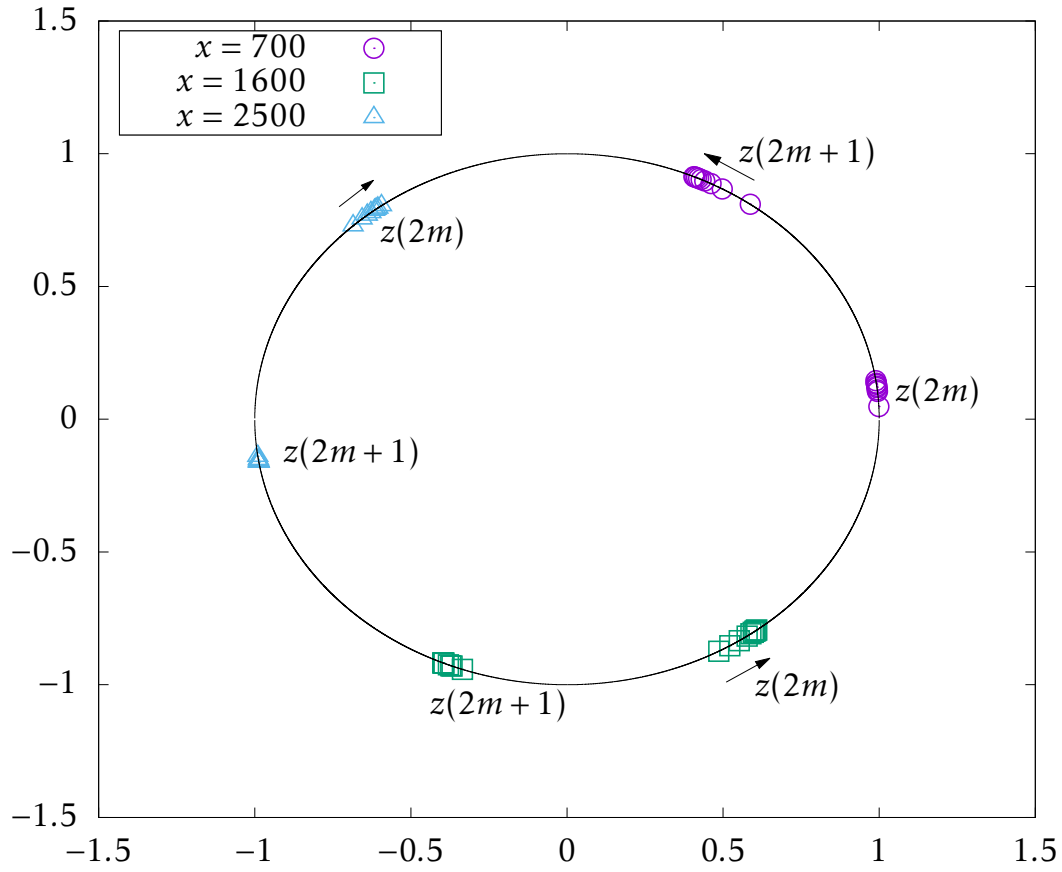

Figure 5.12: Measured behaviour of $z(k)$ at 3 different locations ($x = 700, 1600, 2500$) for the pure Stokes layer at $Re = 750$. The symbols indicate which location a point corresponds to and each is labelled as $z(2m)$ if it corresponds to even k and $z(2m+1)$ if it corresponds to odd k. If there is a general movement of values in a particular direction for increasing m, this has been indicated by an arrow in said direction. However, even in these cases there is a somewhat random distribution of points and for later times there is some evidence to suggest a reversal of direction. In all three cases $z(k)$ appear in two clusters (for even and odd k).

Comparison with simulations

It is anticipated that the temporal evolution of disturbances in the pure Stokes layer at any spatial location will behave approximately in the manner described for the superposition of both types of mode, so $z(k)$ is shown in Figure 5.12 for $Re = 750$. Considering the fact that the model is a significantly simplified means of describing the modal behaviour, the agreement is very good.

Shown in Figure 5.12 are the values of $z(k)$ at the three x locations corresponding to the wavepacket maxima and τ_0 is taken to be as close to 4π as the discrete time-step allows. For $x = 700$ the plotted points are for $1 < k < 18$ and for $x = 1600$ and $x = 2500$

this is restricted to $2 < k < 18$ and $3 < k < 18$, respectively. This removes points for times in which the wavepacket at each location is still forming and thus does not conform to the general behaviour.

Since the temporal growth-rates of the subharmonic cusps are lower than the growth-rates of the harmonic cusps it is anticipated that in the limit $\tau \to \infty$ (or $k \to \infty$), the temporal evolution at any fixed spatial location will approach that of purely harmonic growth. With this in mind it is somewhat unexpected that as k increases the clusters move further apart for all locations. However, at the later times this *drift* becomes less pronounced and there is some evidence to suggest that the direction reverses. This would allow for the possibility of this plot approaching Figure 5.11a as $\tau \to \infty$.

5.4 Wavepacket and cusp separation

The observation that, in this case, the cusps appear evenly spaced in α will now be discussed in some detail. Taking Δ_α^c to be the average distance between each of the subsequent α_* in Table 5.1 (which agree to four decimal places) gives $\Delta_\alpha^c = 0.003365$. Much in the same way as the spectral resolution parameter $\Delta\alpha$ controls the domain size in the simulations (see Section 2.3), it will be seen here that the value Δ_α^c appears to be strongly related to the streamwise wavepacket separation of the impulse response.

The size of the structures associated with Δ_α^c are given by

$$\frac{2\pi}{\Delta_\alpha^c} \approx 1867.2. \tag{5.4.1}$$

This value can be compared against the wavepacket spacing shown in Figure 3.6, for which the average value at $Re = 750$ is $\Lambda = 933.3$. It is therefore intriguing to note that $2\pi/\Delta_\alpha^c$ is remarkably close to $2\Lambda = 1866.6$. In fact, these values are equal to the nearest whole number.

The doubling of the wavepacket spacing Λ is not an arbitrary action that makes the numbers coincide, but actually has physical significance. It has already been noted in Section 3.4 that Λ is the distance between all wavepackets, regardless of when they occur in the staggered structure. The length 2Λ therefore describes the streamwise distance over which the same staggered pattern repeats itself. This is essentially the x-periodicity of the structures (if the dispersive effects are ignored), so it is not surprising that this

value is related to the resolution of cusps, Δ_α^c, in this way.

5.4.1 A simple model for the superposition of cusps

In order to assess the possibility of the value of Δ_α^c being responsible for the streamwise wavepacket separation, consider a complex function of the form

$$Z(x,\tau) = \sum_{n=0}^{N} A_n(x,\tau) \mathrm{e}^{i\alpha_n x + \mu_n \tau}. \tag{5.4.2}$$

The cusps are evenly spaced in α so let

$$\alpha_n = \alpha_0 + n\Delta_\alpha^c \tag{5.4.3}$$

where α_0 and Δ_α^c can be taken from Table 5.1. Half of the cusps have $\mathfrak{Im}\{\mu_*\} = 0$ and half have $\mathfrak{Im}\{\mu_*\} = 1/2$ so let

$$\mathfrak{Im}\{\mu_n\} = \begin{cases} 0 & n \text{ even}, \\ \frac{1}{2} & n \text{ odd}. \end{cases} \tag{5.4.4}$$

This leaves the choice of $\mathfrak{Re}\{\mu_n\}$ and $A_n(x,\tau)$ to construct models of varying complexity. The parameter N controls how many modes are considered. Here $N = 5$ will be fixed so that only the 6 cusps found above are included in the problem.

Simplest model

The simplest model that will be explored here will fix $\mathfrak{Re}\{\mu_n\} = 0.2$ for all n and $A_n(x,\tau) = 1$. It will be seen that a model this simple is capable of displaying subharmonic temporal variation at every spatial location and a fixed wavepacket spacing of 2Λ.

The staggered behaviour of the wavepacket maxima for this model is indicated in Figure 5.13. This plot shows that even though the lowest wavenumber in this model is larger than 0.3, the interaction of several modes has resulted in a periodicity of about 1800, as anticipated by the selection of Δ_α^c. The locations of the maxima alternate as each period completes in a manner analogous to the staggering of wavepackets in the Stokes layer. This staggering continues for later times, but these are not shown here.

By adjusting the parameter Δ_α^c, the distance between peaks could be increased or decreased. In Figure 5.14 the variation of $|Z|$ with x is shown at $\tau = 0$ for a selection of Δ_α^c and $\alpha_0 = 0.3$. This shows that as Δ_α^c is increased, the separation of the peaks of $|Z|$

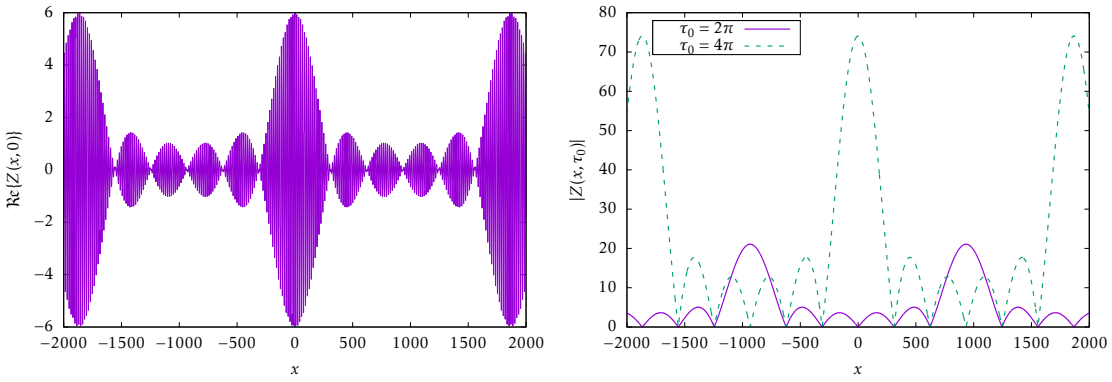

(a) (b)

Figure 5.13: Spatial variation of the model (5.4.2) *when* $\Re\mathfrak{e}\{\mu_n\} = 0.2$ *and* $A_n(x,\tau) = 1$ *for all* n. *In (a) the oscillatory nature of* $\Re\mathfrak{e}\{Z\}$ *is shown at* $\tau = 0$ *(the start of the first period) with three clear maxima. In (b),* $|Z|$ *is plotted against* x *for two choices of* $\tau = \tau_0$ *corresponding to the start of the second and third periods. It can be seen that the locations of the maxima are staggered: Every two periods the maxima return to the same location (but amplified) while they lie halfway between these locations for the intermediate period.*

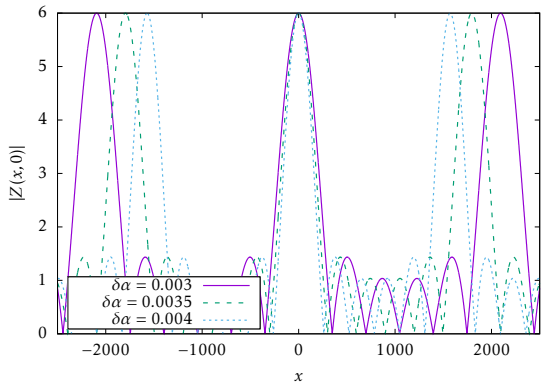

Figure 5.14: The variation of $|Z|$ *with* x *is shown at* $\tau = 0$ *for* $\Delta_\alpha^c = 0.003, 0.0035, 0.004$ *which should correspond to an imposed* x*-periodicity of* $2\pi/\Delta_\alpha^c \approx 2094, 1795, 1571$, *respectively. This corresponds with the locations of the peaks in* $|Z|$ *in each case.*

decreases. The separation of the peaks in each case appears to be $2\pi/\Delta_\alpha^c$, as expected.

Model with differing growth-rates

A slightly more realistic model is investigated by selecting the temporal growth-rates $\Re\mathfrak{e}\{\mu_n\}$ to be equal to the growth-rates associated with each cusp $\Re\mathfrak{e}\{\mu_*\}$ which can be found in Table 5.1. In this case, the fact that the cusps with $\Re\mathfrak{e}\{\mu_*\} = 0$ (subharmonic) are associated with greater growth than those with $\Re\mathfrak{e}\{\mu_*\} = 1/2$ (subharmonic) is incorporated into the model. In Figure 5.15, it can be seen that this only slightly modifies the

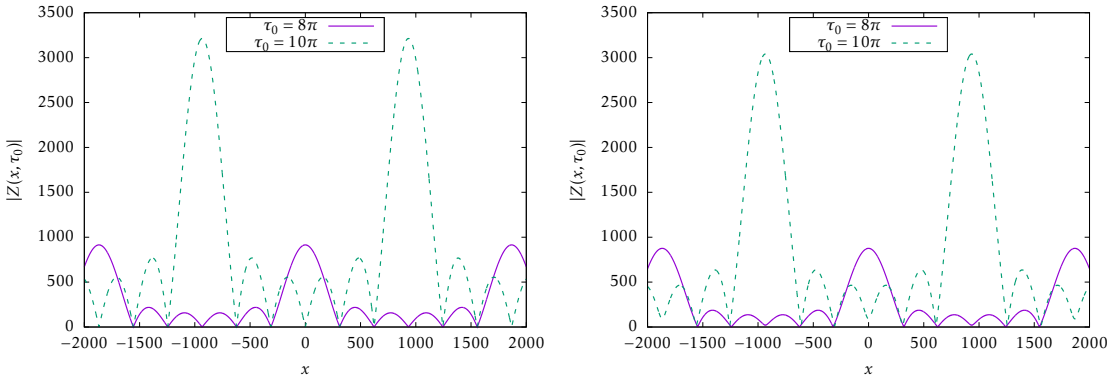

Figure 5.15: Comparison of the spatial variation of Z at two choices of τ_0 that differ by 2π. Shown in (a) is the result of the simplest model implemented here, where $\mathfrak{Re}\{\mu_n\} = 0.2$ for all n. Shown in (b) is the same result for the model in which the temporal growth-rates are extracted from Table 5.1, i.e. $\mathfrak{Re}\{\mu_n\} = \mathfrak{Re}\{\mu_*\}$. Both plots are in excellent agreement.

behaviour already seen.

The close agreement between these two models indicates that the different growth-rates of the cusps do not have a strong impact on the structure of the impulse response. In fact, the only discernible difference between these two cases in Figure 5.15 are slightly lower amplitudes of the peaks when different growth-rates are incorporated. The structure is practically identical.

Inclusion of dispersive effects

One feature of the disturbance evolution not reproduced by this model is the manner in which the family-tree structure evolves. When $A_n(x,\tau) = 1$, the model (5.4.2) has infinite spatial extent for all times. The impulse response can therefore be crudely approximated by localising A_n in space and allowing for the diffusion of the structures as time progresses. Let

$$A_n(x,\tau) = \frac{1}{\sqrt{\tau}} \mathrm{e}^{-\frac{x^2}{4\gamma\tau}}, \tag{5.4.5}$$

so that A_n takes the form of a Gaussian that widens and decays as τ increases. The value of γ is chosen so that as each period completes, the diffusive distance of Z matches the separation of the wavepackets since this is what is observed for disturbances in the Stokes layer. A value of

$$\gamma = \frac{\pi}{2(\Delta_\alpha^c)^2} \tag{5.4.6}$$

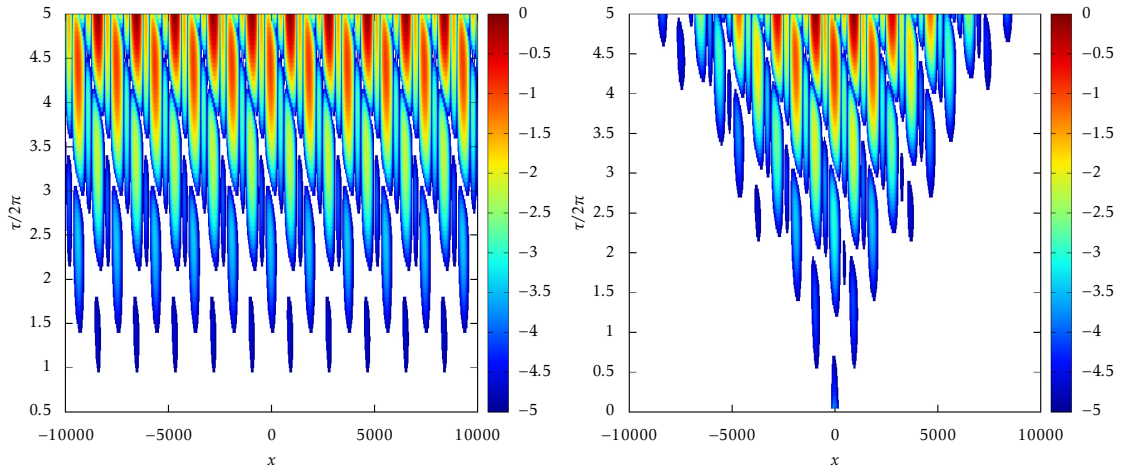

(a) *(b)*

Figure 5.16: Contour plots showing the space/time evolution of Z in two cases for which $\mathfrak{Re}\{\mu_n\}$ are taken from Table 5.1. In (a), $A_n(x,\tau) = 1$ and this imposes an exact periodicity on Z. In (b), $A_n(x,\tau)$ has the form discussed in (5.4.5)*, which localises the extent of Z in space and allows for diffusion as τ increases. The contour plots are constructed in the same way as elsewhere, and the family-tree structure is clear in (b).*

was found to be appropriate up to an $\mathcal{O}(1)$ adjustment.

The spatial/temporal evolution of Z is presented in the form of contour plots in Figure 5.16. In both cases, the growth-rates $\mathfrak{Re}\{\mu_n\}$ are taken from the cusp locations (Table 5.1). In one case $A_n = 1$ whereas in the other A_n takes the form (5.4.5). The analogy of the latter with the family-tree structure suggests that it is the spacing between cusps that is responsible for the structures observed and discussed throughout this work.

More complex models can be constructed in which A_n is given a different value for each n. Also, larger values of N can be taken. The wall-normal variation can also be included in A_n, which can also incorporate the temporal behaviour of the eigenfunction associated with each cusp. The model was kept as simple as possible here but was still found to display the family-tree structure observed in the much more complicated impulse response in the Stokes layer.

The agreement between the observed disturbance evolution and the simplified model employed here suggests that the existence of multiple cusps of harmonic and subharmonic type is significant in the generation of the complex and intriguing structures observed in this flow. This means that while the leading-order behaviour of a disturbance at a fixed spatial location is characterised by the most unstable cusp, such an approach

would not provide any insight into the structures of the impulse response.

5.4.2 Investigation for other Reynolds numbers

The relationship between the streamwise separation of wavepackets in the Stokes layer and the α separation of the cusps found for this flow has been explored for $Re = 750$. In order to demonstrate that this relationship is independent of Re, the distance between fingers protruding from the growth-rate curves will be measured for a selection of Re and compared against the wavepacket spacing Λ presented in Figure 3.6.

The location of cusps in the complex μ-plane is a computationally expensive and time consuming process. This means that it is not feasible to locate enough cusps to measure the distance between them for a selection of Re and compare this against Λ. Instead, it is recalled that the antiperiodicity of the flow ensures that cusps will exist for $\alpha \in \mathbb{R}$ when $\mu = \mu_r + ik/2$ (for any $K \in \mathbb{Z}$). It has been observed when $Re = 750$ that the tips of the fingers protruding from the growth-rate curves correspond to cusps with $\mu_* \in \mathbb{R}$. It has also been seen that there are cusps halfway between each of these with $\mathrm{Im}\,\mu_* = 1/2$.

It will now be assumed that this behaviour holds for all Re. Assuming that the tips of fingers correspond to cusps is reasonable given that no curves have been observed that display fingers for $\alpha \notin \mathbb{R}$. There is less evidence of the existence of cusps with $\mathrm{Im}\{\mu_*\} = 1/2$ between each finger but it will be assumed for efficiency that this is indeed the case.

Evidence of the assertion that the spacing of cusps with α is responsible for the streamwise separation of wavepackets is provided by comparing $2\pi/\Delta_\alpha^c$ with 2Λ. Alternatively, since the distance between fingers is assumed to be double the distance between cusps, it is anticipated that

$$\frac{2\pi}{\Delta_f^\alpha} = \Lambda \tag{5.4.7}$$

where Δ_f^α is the spacing between fingers and is expected to equal $2\Delta_\alpha^c$.

This comparison will be made for $Re = 700, 750, 800, 850$. In all of these cases it was confirmed that Δ_f^α is constant. Good agreement between this value and Λ will suggest that the difference between the wavenumbers of adjacent cusps imposes the wavepacket spacing on the problem.

In Figure 5.17, the wavepacket separation as predicted by Δ_f^α is compared against the measured values of Λ already calculated for $Re = 700, 750, 800$ and there is clear agreement. The case of $Re = 750$ is highlighted since the cusp locations have been found

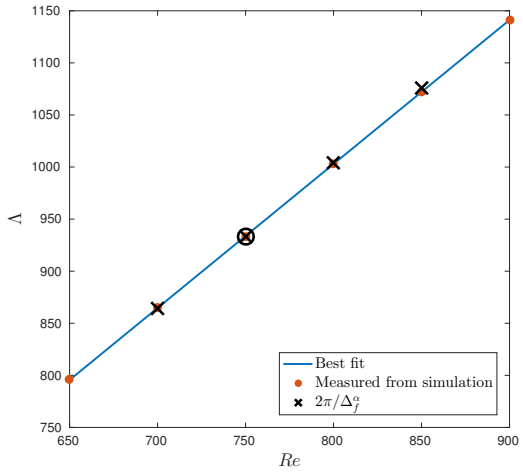

Figure 5.17: The streamwise wavepacket separation Λ, as measured from the simulations (see Figure 5.17) is compared against $2\pi/\Delta_f^\alpha$, where Δ_f^α is the distance between fingers for each Re (×). The case of $Re = 750$ is circled to indicate that this value of Δ_f^α is more accurate than in any of the other cases. There is a discrepancy between the two values when $Re = 800$ which is of size ~ 2.

to a much higher accuracy in this case.

For the case of $Re = 850$, there appears to be a discrepancy between $2\pi/\Delta_f^\alpha$ and Λ. The imprecise nature of the measurements (of both Δ_f^α and Λ) means that a discrepancy of this size is acceptable under the hypothesis that Δ_f^α and Λ are related in this manner.

During this brief investigation, it was observed that the length of the fingers seems to decrease with increasing Re, similarly for $Re < 700$ there is little evidence of these protrusions. The investigation was not extended to larger or smaller Re for this reason. Further confirmation could be provided by considering a finer resolution of Re.

It is noted that in this investigation the finger separation for $Re = 700$ was found to be $\Delta_f^\alpha \sim 0.0073$. This value will be revisited in the next chapter.

5.4.3 Cusps and the Fourier spectrum

It was noted in Section 3.3 that for $Re = 700, 750$, the Fourier spectrum of the disturbance at $\tau = 40\pi$ displays several peaks at distinct wavenumbers (see Figure 3.9). Having observed that many of the features of the disturbance evolution are shared by the evolution of the function Z, which consists of several modes at distinct wavenumbers, this behaviour will now be explored in more detail.

In Figure 5.18, the Fourier spectrum of the wall vorticity after twenty periods of wall

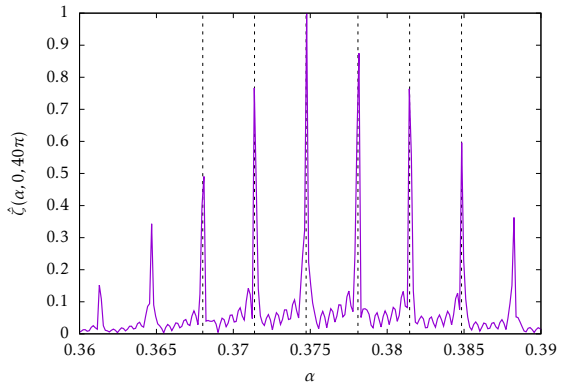

Figure 5.18: The absolute value of the normalised Fourier spectrum of the wall vorticity is plotted after twenty periods of wall motion, $|\hat{\zeta}(\alpha, 0, 40\pi)|$. The locations of the peaks closely correspond to the locations of cusps presented in Table 5.1. Hence, by the 20^{th} period of wall motion, the impulse response is behaving like a discrete set of modes with slightly different growth rates, much like the model (5.4.2).

motion, $\zeta(x, 0, 40\pi)$, is plotted again (see Figure 3.9) over a smaller range of wavenumbers so that the distinct peaks are clearer. Also shown in Figure 5.18 are the locations of the cusps presented in Table 5.1. The locations of the peaks in the spectrum appear to coincide excellently with the locations of the cusps.

The Fourier spectrum at this time is similar to how a numerical approximation to the superposition of several delta functions at distinct α might appear. This supports the findings above which indicate that the impulse response of this flow displays a structure analogous to the function Z, as defined in (5.4.2), for which the Fourier spectrum would be exactly the superposition of several delta functions at these locations.

Summary

In this chapter, the symmetries of the semi-infinite Stokes layer were explored (Section 5.1) and it was shown that the antiperiodicity of the flow constrains the existence of cusps that satisfy the collision criteria (Section 5.2).

The eigenvalue solver derived in Chapter 1 was then used as a discrete approximation to the dispersion relation in Section 5.3. Six examples of cusps were found for the pure Stokes layer at $Re = 750$ that satisfied the conditions predicted from appealing to the flow symmetries. Half of these cusps describe harmonic temporal variation and half describe subharmonic temporal variation. All six had very similar growth-rates. The behaviour predicted by the cusps was then tested against the simulation results. It was

also confirmed that at each spatial (streamwise) location, the temporal growth of the disturbance was equal to the temporal growth associated with the disturbance maximum.

In Section 5.4, it was also seen that the spatial/temporal characteristics of the impulse response are comparable to a simple model consisting of the superposition of modes with alternating harmonic and subharmonic variation. This model was found to be capable of recreating the streamwise wavepacket separation observed in Section 3.1 and the family-tree structure of these wavepackets (once diffusion was taken into account). These results suggest that the wavepacket separation is controlled by the α separation of the cusps with and it was shown that there was good agreement between the α separation of fingers and the measured wavepacket spacing for a small selection of Re.

Chapter 6

The Stokes layer modified by high-frequency noise

Introduction

Although the eigenvalue analysis (Chapter 1) and linear simulation (Chapter 2) have been shown to be in good agreement (Chapter 3 and Chapter 5), experiments report a critical Reynolds number less than half that predicted. This serious discrepancy suggests that, for whatever reason, the mathematical model is failing to be representative of the physical system.

Simplifying problems to the extent that analytical tools can be used involves stripping the system of features that can reasonably be assumed to have negligible (or at least minimal) effects. For instance: channels and pipes are generally assumed to be infinitely long which is appropriate provided the behaviour at inlets and outlets is of no interest; the Blasius boundary layer is often approximated as being parallel even though the boundary layer grows with distance from the leading edge; any boundary layer flow (such as the Blasius boundary layer or the Stokes layer) is studied under the assumption of a semi-infinite region of fluid, an assumption that is representative of flows in which a second boundary or free surface is sufficiently far away; and for wake and jet flows an infinite region is used and can be similarly justified.

In some cases it is possible to study these flows without such simplifications, especially when these effects are important, but the reason these assumptions are so prevalent in the field is that in many cases the idealised flows are representative of real life. More-

over, working in an idealised regime enables the development of tools and techniques for application to more complex models. For example, surface roughness is often absent from mathematical models (as is the case in the present work) but can, in some cases, greatly effect the dynamics of the flow. Once a solver has been constructed for a flow without surface roughness it is sometimes then possible to incorporate some approximation to this feature in the boundary conditions.

In the case of a Stokes layer, one particular feature removed from the mathematical model and not present in steady flows is the noise associated with mechanically generating the plate oscillation. Reported as approximately 1% in some experiments (Clamen & Minton, 1977; Eckmann & Grotberg, 1991; Hino *et al.* , 1976; Akhaven *et al.* , 1991) it is unsurprising that the work of Hall (1978) and Blennerhassett & Bassom (2002, 2006) do not consider its effect. As earlier studies in the field, the mathematical basis of the method needed to be established first and foremost. However, the remarkable reduction in Re_c observed by Thomas *et al.* (2015) suggests that even noise of low amplitude can have a dramatic effect on the stability of the flow.

As an early study into this modification, the noise model incorporated by Thomas *et al.* (2015) is of the simplest appropriate form. Results were relatively insensitive to parameters describing the exact form of the noise while a very small change in the magnitude could reduce Re_c significantly. This suggests that some model of noise should be incorporated into the Stokes layer in order to be representative of the real-life flow it is intended to approximate, even in the idealised environment of the linear stability analysis.

In addition to destabilisation, the introduction of noise is in some cases accompanied by qualitative changes to the disturbance evolution. In the monochromatic (single frequency) Stokes layer the disturbance maximum is convected downstream, away from the point of excitation, whereas in the nonmonochromatic (noisy) Stokes layer disturbances have been observed with the disturbance maximum confined to a region near the initial point of excitation (Thomas, 2016). In these cases, there also appears to be a change in the temporal evolution of the wavepackets from the subharmonic staggering already discussed to harmonic behaviour.

In the following discussion, only the semi-infinite case will be considered (or the flow in a channel that is wide enough to be a good approximation to the semi-infinite case). There will be no steady mean flow, so the flow will be of a purely oscillatory form, though

a mean flow could be incorporated in the same manner described in Chapter 1.

The reformulation of the problem will be performed in Section 6.1 followed by a discussion on the symmetries of this basic state. Throughout this chapter, the semi-infinite Stokes layer already discussed in detail will be described as either the pure or monochromatic Stokes layer and will be compared directly against three cases: one of low-level noise, one of significant noise, and one of high-level noise in Section 6.2. Finally, a parametric exploration will be conducted to explore the destabilising effect that noise can have on the system in Section 6.3.

6.1 Basic state and problem formulation

6.1.1 Basic state for simulation

The methods described above will now be adapted to the case of an otherwise stationary viscous fluid subjected to in-plane wall oscillation modified by high-frequency noise. The nondimensional wall velocity will be described by

$$U_w^* = U_0\Big[\cos(\omega t) + \delta\Big(a_p\cos(p\omega t) + b_p\sin(p\omega t)\Big)\Big], \tag{6.1.1}$$

where $a_p^2 + b_p^2 = 1$ so that δ is a measure of the level of noise. Note that an alternative, equivalent expression is found by writing

$$a_p\cos(p\omega t) + b_p\sin(p\omega t) = \pm\cos(p\omega t + \phi),$$

where $\phi = \arctan(b_p/a_p)$. This makes it clear that the parameter pair (a_p, b_p) controls the phase of the noise.

In order for Floquet theory to be appropriate, let p be a positive integer so that the wall motion still has the same period as the fundamental oscillation. The term *fundamental* is here used to refer to the purely sinusoidal component $U_0\cos(\omega t)$, recovered when $\delta = 0$.

The problem will be nondimensionalised in the same manner as for the monochromatic Stokes layer, using the frequency of the fundamental oscillation (ω) to define a nondimensional time (τ) and the amplitude of oscillation (U_0) as a velocity scale. Lengths will also be scaled with δ_s, the Stokes layer thickness (1.2.1) associated with the funda-

mental oscillation. The resulting nondimensional wall motion is

$$U_w = \cos(\tau) + \delta\Big(a_p\cos(p\tau) + b_p\sin(p\tau)\Big). \tag{6.1.2}$$

Under certain assumptions, this wall motion can used as a boundary condition in solving the nondimensional Navier–Stokes equations to produce the basic state

$$U_B(y,\tau;p) = \mathrm{e}^{-y}\cos(\tau - y) + \delta\mathrm{e}^{-\sqrt{p}y}\Big[a_p\cos(p\tau - \sqrt{p}y) + b_p\sin(p\tau - \sqrt{p}y)\Big] \tag{6.1.3}$$

in the semi-infinite configuration. This can easily be incorporated into the linear simulation simply by changing the basic state. This requires the derivatives

$$\begin{aligned}\frac{\partial U_B}{\partial y} &= \mathrm{e}^{-y}\left[\sin(\tau - y) - \cos(\tau - y)\right] \\ &\quad + \delta\sqrt{p}\mathrm{e}^{-\sqrt{p}y}\Big[(a_p - b_p)\sin(p\tau - \sqrt{p}y) - (a_p + b_p)\cos(p\tau - \sqrt{p}y)\Big],\end{aligned} \tag{6.1.4a}$$

$$\frac{\partial^2 U_B}{\partial y^2} = -2\mathrm{e}^{-y}\sin(\tau - y) - 2\delta p\mathrm{e}^{-\sqrt{p}y}\Big[a_p\sin(p\tau - \sqrt{p}y) - b_p\cos(p\tau - \sqrt{p}y)\Big]. \tag{6.1.4b}$$

Disturbances to this flow can now be simulated for a single fixed wavenumber and for spatially localised impulse responses using the same methods as described in Chapter 2. The linear stability analysis, however, requires further modification.

6.1.2 Floquet reformulation

Consider the flow generated in a channel of dimensional half-width l by the in-plane wall motion of both boundaries as described by (6.1.2), i.e. wall oscillation with noise. The same nondimensionalisation can be performed, introducing the nondimensional channel width $h = l/\delta_s$. The resulting flow is described by

$$U_b(y,\tau;p;h) = \mathfrak{Re}\left\{\frac{\cosh[(1+i)y]}{\cosh[(1+i)h]}\mathrm{e}^{i\tau}\right\} + \delta\mathfrak{Re}\left\{\frac{\cosh[(1+i)y\sqrt{p}]}{\cosh[(1+i)h\sqrt{p}]}(a_p - ib_p)\mathrm{e}^{ip\tau}\right\}, \tag{6.1.5}$$

which is distinguished from the semi-infinite flow (6.1.3) by the lower case subscript. It can readily be confirmed that results are virtually indistinguishable from the semi-infinite case for $h \geq 14$. The Floquet method will therefore be applied to $U_b(y,\tau;p;16)$ as an approximation to $U_B(y,\tau;p)$ since the bounded geometry is more natural for the Chebyshev collocation method.

The basic state U_b can also be written in the form

$$U_b = \Big[u_1(y)\mathrm{e}^{i\tau} + \bar{u}_1(y)\mathrm{e}^{-i\tau}\Big] + \delta\Big[u_p(y)(a_p - ib_p)\mathrm{e}^{ip\tau} + \bar{u}_p(y)(a_p + ib_p)\mathrm{e}^{-ip\tau}\Big], \tag{6.1.6}$$

where $\bar{u}_1$ and $\bar{u}_p$ are the complex conjugates of u_1 and u_p, respectively.

Stability equations

As before, this basic state will be perturbed by a 2D disturbance (expressed as a stream function) and linearised about the basic state U_b. Assuming that the disturbance has a normal-mode form in the streamwise direction, the wavenumber α will be fixed. Floquet's theorem is applied, as in (1.2.6), leaving the stability equation unchanged as

$$\frac{\partial}{\partial\tau}\mathcal{L}\psi = \Big[\frac{1}{2}\mathcal{L} - \mu - i\alpha ReU\Big]\mathcal{L}\psi + i\alpha ReU''\psi, \tag{6.1.7}$$

see (1.2.7). The harmonic decomposition of ψ (1.2.8) can again be applied,

$$\psi(y,\tau) = \sum_{n=-\infty}^{\infty} \psi_n(y)\mathrm{e}^{in\tau}. \tag{6.1.8}$$

Considering (6.1.6), it is expected that the multiplication of U_b and ψ in (6.1.7) will result in the n^{th} harmonic ψ_n interacting with the adjacent harmonics $\psi_{n\pm1}$ in the same manner that was observed for the monochromatic case (see Section 1.2). For this flow, the introduction of the frequency p means that ψ_n is also coupled with $\psi_{n\pm p}$.

This can be seen once the stability equation (6.1.7) is rewritten as an infinite system using (5.1.8) and (6.1.6). Comparing coefficients of $\exp(in\tau)$ gives, for each n,

$$\begin{aligned}(\mathcal{L} - \alpha^2 - 2\mu - 2in)\mathcal{L}\psi_n = i\alpha Re\Big[&u_1(\mathcal{L}\psi_{n-1} - 2i\psi_{n-1}) + \\ &\bar{u}_1(\mathcal{L}\psi_{n+1} + 2i\psi_{n+1}) + (a_p - ib_p)(\mathcal{L}\psi_{n-p} - 2ip\psi_{n-p}) + \\ &(a_p + ib_p)\bar{u}_p(\mathcal{L}\psi_{n+p} + 2ip\psi_{n+p})\Big].\end{aligned} \tag{6.1.9}$$

Reduction to a matrix problem

As before, y-derivatives are approximated by pseudospectral matrices with the appropriate boundary conditions taken into account in the manner discussed in Section 1.2

(Trefethen, 2000). This introduces the matrix operators

$$\mathcal{L} \to \boldsymbol{L}, \tag{6.1.10a}$$

$$\frac{1}{2}\left(\frac{\partial^4}{\partial y^4} - 2\alpha^2\frac{\partial^2}{\partial y^2} + \alpha^4\right) \to \boldsymbol{V}, \tag{6.1.10b}$$

$$\boldsymbol{M}_1 = \boldsymbol{L}^{-1}\boldsymbol{u}_1(\boldsymbol{L} - 2i\boldsymbol{I}), \tag{6.1.10c}$$

$$\boldsymbol{M}_p = \boldsymbol{L}^{-1}(a_p - ib_p)\boldsymbol{u}_p(\boldsymbol{L} - 2ip\boldsymbol{I}), \tag{6.1.10d}$$

which are similar to those for the monotonic case (1.2.12). This gives, for each n,

$$-i\alpha Re\left[\bar{\boldsymbol{M}}_1\boldsymbol{\psi}_{n+1} + \bar{\boldsymbol{M}}_p\boldsymbol{\psi}_{n+p}\right] + (\boldsymbol{L}^{-1}\boldsymbol{V} - in\boldsymbol{I})\boldsymbol{\psi}_n - i\alpha Re\left[\boldsymbol{M}_1\boldsymbol{\psi}_{n-1} + \boldsymbol{M}_p\boldsymbol{\psi}_{n-p}\right] = \mu\boldsymbol{\psi}_n. \tag{6.1.11}$$

The infinite system is then truncated by assuming $\psi_n = 0$ for all $|n| > N$ and the harmonic vectors are concatenated into the vector $\boldsymbol{\phi}$ as in (1.2.17). This again results in an eigenvalue problem $\boldsymbol{A}\boldsymbol{\phi} = \mu\boldsymbol{\phi}$ where the block tridiagonal matrix $\boldsymbol{A}$ has additional non-zero blocks on the diagonals p above and below the main diagonal, i.e.

$$\boldsymbol{A} = \begin{pmatrix}
\boldsymbol{C}_{-N} & \boldsymbol{B}_1^* & \boldsymbol{0} & \dots & \boldsymbol{B}_p^* & \boldsymbol{0} & \dots & \dots & \boldsymbol{0} \\
\boldsymbol{B}_1 & \boldsymbol{C}_{-N+1} & \boldsymbol{B}_1^* & & & \boldsymbol{B}_p^* & & & \vdots \\
\boldsymbol{0} & \boldsymbol{B}_1 & \boldsymbol{C}_{-N+2} & \boldsymbol{B}_1^* & & & -\boldsymbol{B}_p^* & & \\
\vdots & & \ddots & \ddots & \ddots & & & \ddots & \\
\boldsymbol{B}_p & & & \boldsymbol{B}_1 & \boldsymbol{C}_{-N+p} & \boldsymbol{B}_1^* & & & \boldsymbol{B}_p^* \\
\boldsymbol{0} & \ddots & & & \ddots & \ddots & \ddots & & \boldsymbol{0} \\
\vdots & & \boldsymbol{B}_p & & & \boldsymbol{B}_1 & \boldsymbol{C}_{N-2} & \boldsymbol{B}_1^* & \vdots \\
\vdots & & & \boldsymbol{B}_p & & & \boldsymbol{B}_1 & \boldsymbol{C}_{N-1} & \boldsymbol{B}_1^* \\
\boldsymbol{0} & \dots & \dots & \boldsymbol{0} & \boldsymbol{B}_p & \boldsymbol{0} & \dots & \boldsymbol{B}_1 & \boldsymbol{C}_N
\end{pmatrix},$$

where

$$\begin{aligned}
C_n &= (\boldsymbol{L}^{-1}\boldsymbol{V} - in\boldsymbol{I}), \\
\boldsymbol{B}_k &= -i\alpha Re\boldsymbol{M}_k \quad \text{for} \quad k \in \{1, p\}, \\
\boldsymbol{B}_k^* &= -i\alpha Re\bar{\boldsymbol{M}}_k \quad \text{for} \quad k \in \{1, p\}.
\end{aligned}$$

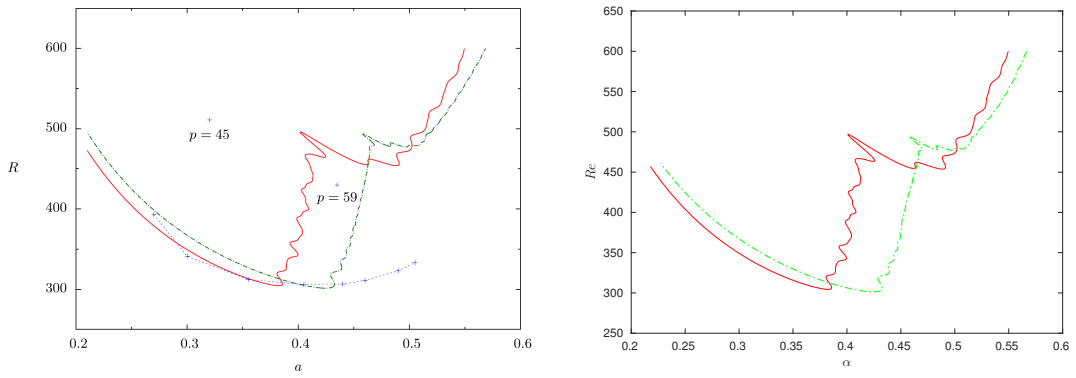

(a) (b)

Figure 6.1: Comparison of neutral curves found by Thomas et al. *(2015) (a) and those found in the present study (b). For both the curves shown* $h = 16$, $(a_p, b_p) = (1, 0)$ *and* $\delta = 0.01$. *The noise frequencies are* $p = 69$ *(solid line) and* $p = 76$ *(chained line). The crosses and dotted line in (a) show the critical Reynolds number for a selection of different values for* p *and these are not reproduced in (b). In Thomas* et al. *(2015), the Reynolds number is denoted* R *(rather than Re) and the wavenumber is denoted* a *(rather than* α*). The axes in (a) are labelled based on this notation.*

Validation

The methods described in Chapter 1 can now be used to solve this problem and thus deduce the stability of the flow for given parameters. Fixing δ, p and (a_p, b_p) allows for determination of neutral curves by pseudo-arclength continuation. This method can also be adapted to deduce the temporal growth of a disturbance at any fixed spatial location and hence deduce if an instability is convective or absolute via the cusp map method (see Chapter 5).

Comparison of neutral curves with those presented in Thomas *et al.* (2015) for the large channel ($h = 16$) are shown in Figure 6.1 confirming that the present study is capable of picking out the interesting features found by Thomas *et al.* (2015). This is a significant contribution to the study of such a flow since these curves had yet to be reproduced by an independently developed code. As yet, no attempt has been made to explain the interesting qualitative features of these curves but the reproduction of identical features suggests that this is a physical phenomenon and not a spurious numerical feature.

6.1.3 Flow symmetries

It was previously observed for the pure Stokes layer that in addition to being periodic with period 2π, the basic state is antiperiodic with antiperiod π. This symmetry was then shown to constrain the existence of cusps in the complex plane, revealing that disturbances in antiperiodic flows undergo a temporal growth at each streamwise location that is associated with $\alpha \in \mathbb{R}$, as is the temporal growth of the disturbance maximum. It will now be considered whether the modified basic state (6.1.3) is subject to the same symmetry. Consider (6.1.3),

$$U_B(y,\tau;p) = \mathrm{e}^{-y}\cos(\tau - y) + \delta \mathrm{e}^{-\sqrt{p}y}\Big[a_p\cos(p\tau - \sqrt{p}y) + b_p\sin(p\tau - \sqrt{p}y)\Big],$$

and take a time shift of half a period, $\tau \to \tau + \pi$,

$$U_B(y,\tau+\pi;p) = -\mathrm{e}^{-y}\cos(\tau - y) + \delta \mathrm{e}^{-\sqrt{p}y}\Big[a_p\cos(p\tau + p\pi - \sqrt{p}y) + b_p\sin(p\tau + p\pi - \sqrt{p}y)\Big].$$

Now, cos and sin are antiperiodic with period π so

$$\cos(\theta + p\pi) = \begin{cases} \cos(\theta) & \text{if } p \text{ even}, \\ -\cos(\theta) & \text{if } p \text{ odd} \end{cases} \tag{6.1.13}$$

and

$$\sin(\theta + p\pi) = \begin{cases} \sin(\theta) & \text{if } p \text{ even}, \\ -\sin(\theta) & \text{if } p \text{ odd} \end{cases} \tag{6.1.14}$$

for any θ. This can be shown by appealing to the appropriate trigonometric identities.

The case of odd p

Consider first the possibility that p is odd. In this case, a time shift of half a period, $\tau \to \tau + \pi$, is equivalent to a complete reversal of direction, i.e.

$$U_B(y,\tau+\pi;p) = -U_B(y,\tau;p). \tag{6.1.15}$$

It follows that all of the symmetry arguments for the pure Stokes layer (as shown in Section 5.1) must also hold in this case. Based on these arguments, collisions that satisfy the collision criteria are anticipated on the real axis of the complex α-plane corresponding

to $\mu = \mu_r + ik/2$ ($k \in \mathbb{Z}$), see Section 5.2.

Also, for $\alpha \in \mathbb{R}$ the μ-roots of the dispersion relation will appear in complex conjugate pairs.

The case of even p

Now consider p even. In this case, a time shift of half a period reverses the sign of the fundamental oscillation but returns the noise to its original value, i.e

$$U_B(y, \tau + \pi; p) = -e^{-y}\cos(\tau - y) + \delta e^{-\sqrt{p}y}\left[a_p \cos(p\tau - \sqrt{p}y) + b_p \sin(p\tau - \sqrt{p}y)\right].$$

In this case the symmetry arguments used in Section 5.1 cannot be applied. However, since p sits between two odd values it is anticipated that the behaviour would not be dissimilar to that for odd p. This hypothesis will be discussed in detail later.

Possible convective properties of absolutely unstable flows

In the case of even p, the antiperiodicity of the flow breaks down and so it cannot be assumed that there are cusps with $\alpha_* \in \mathbb{R}$.

It was seen in Section 4.3 that the temporal evolution of the disturbance along the ray with greatest temporal growth ($x/\tau = V_{max}$) is associated with $\alpha \in \mathbb{R}$. If the temporal growth along the ray $x/\tau = 0$ (fixed spatial location) is no longer associated with $\alpha \in \mathbb{R}$, then there must be some other ray that experiences greater growth, i.e. $V_{max} \neq 0$. In the simulations, it is anticipated that this will manifest as the disturbance experiencing some convection away from the point of excitation while simultaneously experiencing growth at every spatial location.

Recall the convection of the disturbance maximum away from the point of excitation in the monochromatic Stokes layer (discussed in Chapter 3). This feature would suggest that $V_{max} \neq 0$ for this flow (as is assumed when measuring the temporal growth of the disturbance maximum). However, it was shown in Section 5.3 that the temporal growth at every choice of x is equal to the growth of the maximum. It follows that the temporal growth along the ray $x/\tau = V_{max}$ is no greater than that along the ray $x/\tau = 0$.

In the case of even p it is expected that some ray $x/\tau = V \neq 0$ undergoes greater temporal growth than that seen along $x/\tau = 0$. This suggests that the whole disturbance, rather than just the disturbance maximum, will experience some form of convection along this

ray.

To clarify, this behaviour is not to be confused with convective instability. In a convectively unstable flow the entire disturbance moves away from the point of excitation and there is decay at every spatial location. Described above is the possibility of an absolutely unstable flow for which some ray exists that exhibits greater temporal growth than displayed at each spatial location. Such disturbances will have convective properties but still experience temporal growth at every spatial location. This behaviour is what might generally be expected of an absolute instability, with the pure Stokes layer (and the noisy Stokes layer with odd p) being a special case.

Near harmonic and near subharmonic modes

Having noted that the flow symmetries responsible for the significance of $\mu = \mu_r + ik/2$ (for $k \in \mathbb{Z}$) no longer apply for even p, it is no longer expected that the cusps will display purely harmonic temporal variation (associated with $\mathrm{Im}\{\mu_*\} = 0$) or purely subharmonic spatial variation (associated with $\mathrm{Im}\{\mu_*\} = 1/2$). However, when μ_i is in a neighbourhood of either of these values, the disturbance will experience temporal behaviour similar to the harmonic and subharmonic variation already discussed.

To demonstrate this, consider the general form of a Floquet mode,

$$\psi(y,\tau) = p(y,\tau)\mathrm{e}^{(\mu_r+i\mu_i)\tau}, \tag{6.1.16}$$

where p is 2π-periodic in τ. Taking a $\tau \to \tau + 2\pi$ shift yields

$$\begin{aligned}\psi(y,\tau+2\pi) &= p(y,\tau)\mathrm{e}^{(\mu_r+i\mu_i)\tau}\mathrm{e}^{(\mu_r+i\mu_i)2\pi},\\ &= \mathrm{e}^{(\mu_r+i\mu_i)2\pi}\psi(y,\tau),\\ &= \mathrm{e}^{2\pi\mu_r}\mathrm{e}^{2\pi i\mu_i}\psi(y,\tau).\end{aligned}$$

This shows that the passing of a period of wall motion results in the amplification of the disturbance through multiplication by the real number $\exp(2\pi\mu_r)$. There is also multiplication by the complex number $\exp(2\pi i\mu_i)$, which has magnitude 1.

The latter of these actions performs a phase-shift on the disturbance. In particular, if $\mu_i = 0$ this is the same as multiplying by 1 (no change in the phase) and if $\mu_i = 1/2$ this is the same as multiplying by -1 (so the passing of a second period will act as multiplication

by 1).

If μ_i is close to (but not equal to) 0, this is equivalent to multiplying by a complex number of magnitude 1 that is near to 1. This describes a small shift in the phase of the disturbance. A small enough phase-shift can have little to no impact on the disturbance envelope and when this is the case it is fairly difficult to distinguish the temporal behaviour from a purely harmonic mode. Similarly, for a value of μ_i close to (but not equal to) 1/2 the temporal variation could not easily be distinguished from a purely subharmonic mode.

In the following work, the terms *near harmonic* and *near subharmonic* will be used to describe disturbances with μ_i in the neighbourhood of 0 or 1/2, respectively. It is anticipated that the cusps found when p is even will be of such a form, at least for low levels of noise that are broadly similar to the monochromatic flow.

6.2 Case studies

The introduction of noise to the Stokes layer has several effects on the disturbance evolution in addition to the destabilisation discussed in Thomas *et al.* (2015). These features will now be explored utilising space/time contour plots and growth-rate measures for direct comparison with the pure Stokes layer (Chapter 3). Particular focus will be placed on the temporal evolution at fixed spatial locations through application of the cusp map method.

Three cases will be considered in this section and will be described as *low-level* noise, *significant* noise and *high-level* noise. These terms are used to reflect how much the qualitative features of the monochromatic flow have changed in each case. In all three cases $(a_p, b_p) = (1, 0)$ and $p = 60$ will be fixed for consistency and for each case the remaining parameters will be,

- **Low-level noise:** $\delta = 0.0002$, $Re = 750$,
- **Significant noise:** $\delta = 0.0008$, $Re = 700$,
- **High-level noise:** $\delta = 0.01$, $Re = 500$.

Notice that Re is decreased as δ is increased since larger values of δ are associated with a destabilised flow. These values of Re were chosen so that the growth-rates will be broadly similar in all three cases.

Having noted that there are anticipated differences between odd and even p, these cases will also be compared against $p = 59, 61$ to deduce how sensitive the flow is to a unit shift in this parameter. Focus is placed on the even choice of $p = 60$ since it is anticipated from the flow symmetries that there will be cusps for odd p when $\alpha \in \mathbb{R}$ and when $\mu = \mu_r + ik/2$, whereas for even p each cusp needs to be found individually.

An immediate assessment of the changes brought about by the introduction of noise will be made by observing the spatial/temporal structure of the disturbances for the first three periods of wall-motion. The temporal growth-rates associated with the disturbance maximum and a selection of spatial locations will then be measured and the former will be compared against the growth-rate curves for real α found through solving the Floquet eigenvalue problem.

Further insight into the behaviour at fixed streamwise locations will be provided by application of the cusp map method. Since p is even, it is not expected that cusps will correspond to real α and the effect this has on the disturbance evolution will be explored by comparing the results against those for $p = 59, 61$.

6.2.1 Features of early evolution

The disturbance evolution will now be explored for the first three periods of wall motion in the three cases of interest. It is shown that the presence of noise can disrupt the family-tree structure discussed for the monochromatic case in Section 3.1.

Low-level noise

Figure 6.2 shows the spatial/temporal evolution of the impulse response in the case of low-level noise ($\delta = 0.0002$, $Re = 750$) for the first three periods of wall motion. This figure is directly comparable with the monochromatic case at the same Re given in Figure 3.4. The disturbance displays a broadly similar family-tree structure: daughter wavepackets are generated at the same times and the wavepacket spacing appears to be the same. The disturbance maximum is still convected to positive x through subsequent wavepackets while each individual wavepacket decays until its grand-daughter wavepacket is superimposed over it, resulting in the subharmonic temporal growth of each wavepacket.

Unlike Figure 3.4, in Figure 6.2 the space between the wavepackets now shows a high

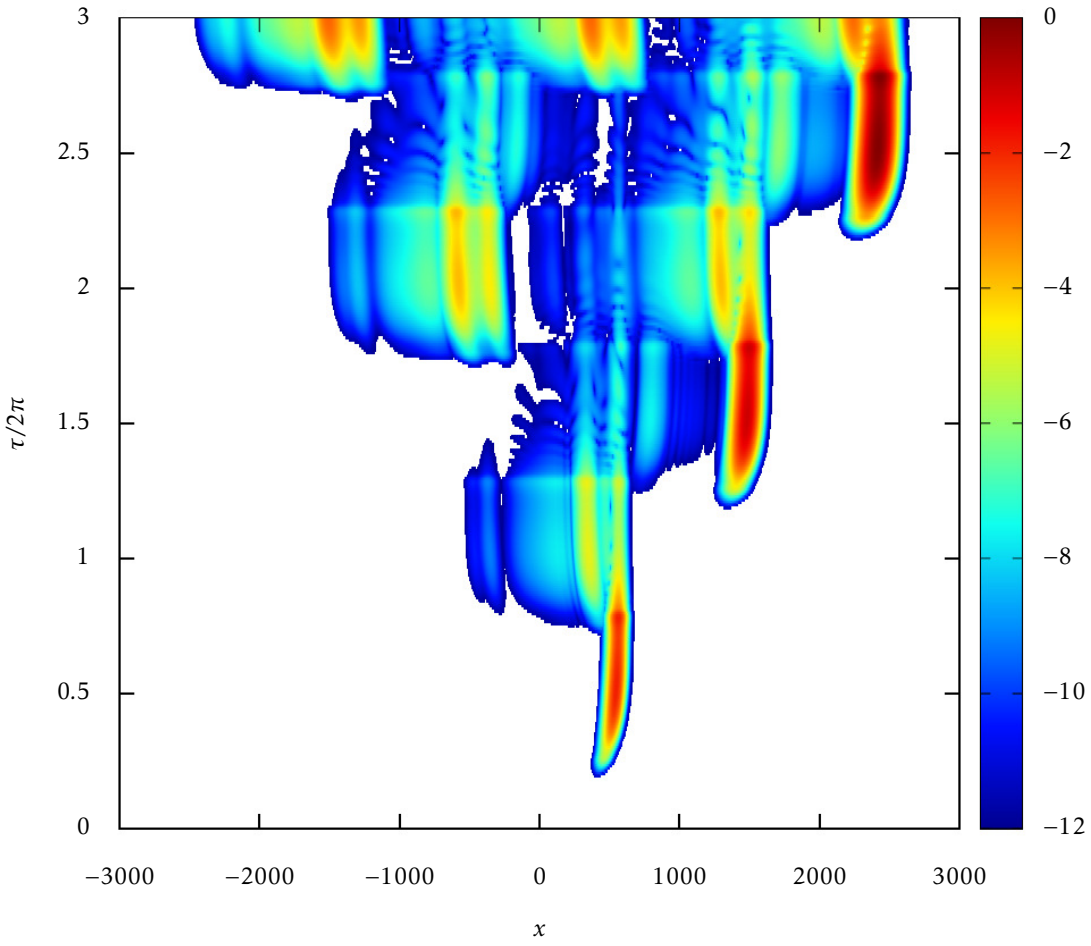

Figure 6.2: Space/time contour plot of the logarithm of the wall vorticity envelope $\log|\zeta(x,0,\tau)|$ *for* $\delta = 0.0002$, $(a_p, b_p) = (1,0)$ *and* $p = 60$ *at* $Re = 750$ *for comparison with Figure 3.4, constructed in the same way.*

enough amplitude to be visible on this plot (both contour plots employ the same low amplitude cut-off) and *secondary* wavepackets have been introduced that are generated in the same direction and at roughly the same time as the weaker of the two daughter wavepackets but are of greater amplitude and much closer to their respective mothers. There are also weaker secondary wavepackets on the opposite side of each mother (the same side as the strongest of the daughter wavepackets).

In this case these secondary wavepackets are much weaker than the dominant daughter wavepackets. It will be seen below that this feature becomes more significant for

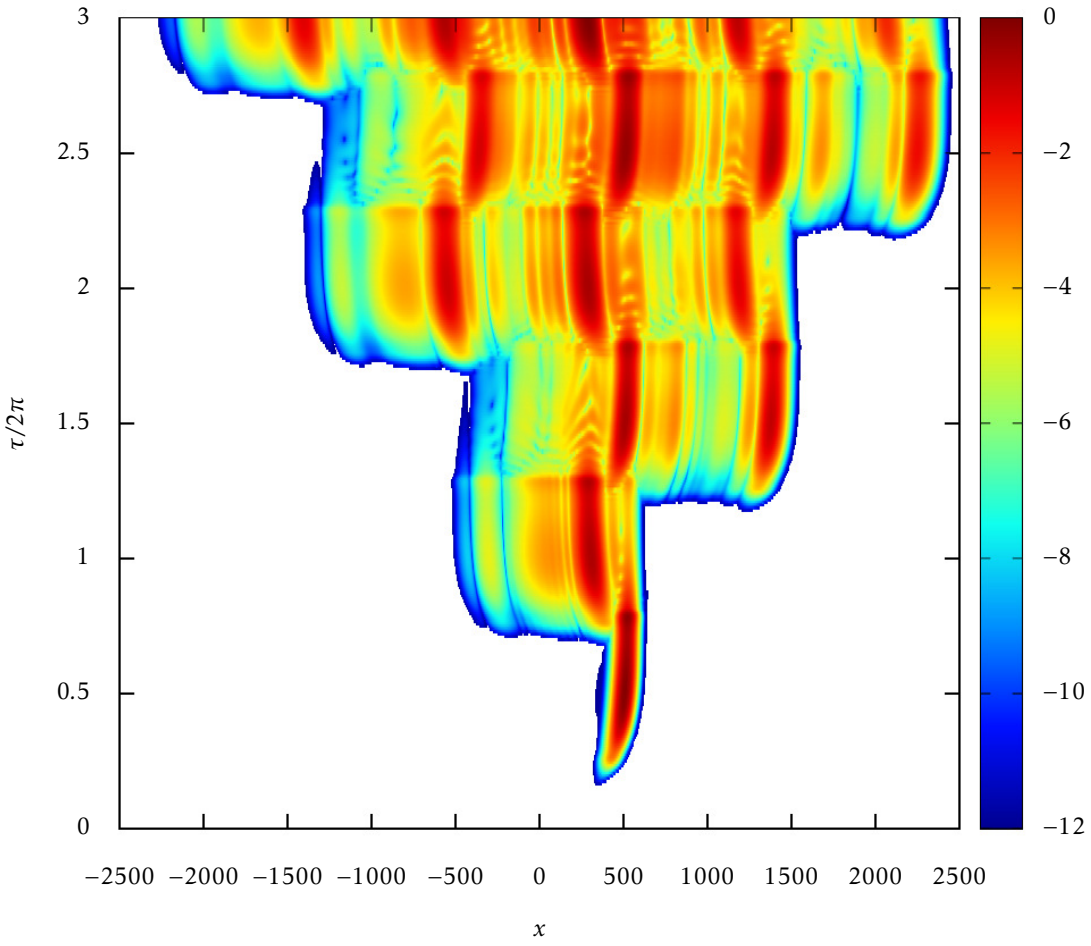

Figure 6.3: Space/time contour plot of the logarithm of the wall vorticity envelope $\log|\zeta(x,0,\tau)|$ *for* $\delta = 0.0008$, $(a_p, b_p) = (1,0)$ *and* $p = 60$ *at* $Re = 700$. *Can be compared against Figure 3.2 and is constructed in the same way.*

larger levels of noise.

Significant noise

The corresponding contour plot for the case of significant noise ($\delta = 0.0008$, $Re = 700$) is shown in Figure 6.3 which can be compared with the monochromatic case at the same Re in Figure 3.2. Not only does the disturbance now display growth at this Re but the multiple wavepackets are now connected by regions of significant amplitude.

The family-tree structure is essentially retained and the spacing between local max-

ima that will continue to be described as mother and daughter wavepackets has remained invariant. It is interesting to note that in both this case and the case of low-level noise the streamwise wavepacket separation is the same as for the monochromatic case at the same Re. It is anticipated, based on the discussion in Section 5.4, that this will correspond to the same α_r separation of cusps.

A particularly interesting development is that the secondary wavepackets that were introduced at low values of δ have become significant and are now more dominant than the daughter wavepackets, meaning that the disturbance maximum now appears confined to a corridor around the original mother wavepacket. This means that after only three periods of wall motion, temporal growth is observed at the locations of the mother/daughter wavepackets and the disturbance displays much less weighting towards positive x.

While there is no evidence in this plot of the disturbance structure undergoing convection (as was predicted for even p) it is worth noting for a later discussion that any movement of the disturbance maximum would be a good indication of the movement of the disturbance as a whole since the disturbance maximum sits within the broader structure. Later, this observation will be used to inform an investigation into the convective properties of this disturbance.

High-level noise

In Figure 6.4 the contour plot for the first three periods of wall motion is shown for the case of high-level noise ($\delta = 0.01$, $Re = 500$). The multiple wavepacket response has been replaced with a single wavepacket that undergoes growth and travels in alternating directions with the direction of travel being dictated by that of the wall motion. This figure suggests that for any fixed x the disturbance undergoes harmonic temporal growth.

Notice the increased amount of white space for earlier times seen at the bottom of Figure 6.4. This indicates that the disturbance undergoes greater temporal growth in the case of high-level noise than in either of the other cases despite taking a significantly smaller value of Re in this case (as will be confirmed later). The dramatic destabilisation associated with increasing the level of noise will be explored in Section 6.3.

Note also that in this case the noise level of $\delta = 0.01$ is comparable to that observed in experiments. This suggests that the family-tree structure may not necessarily be present

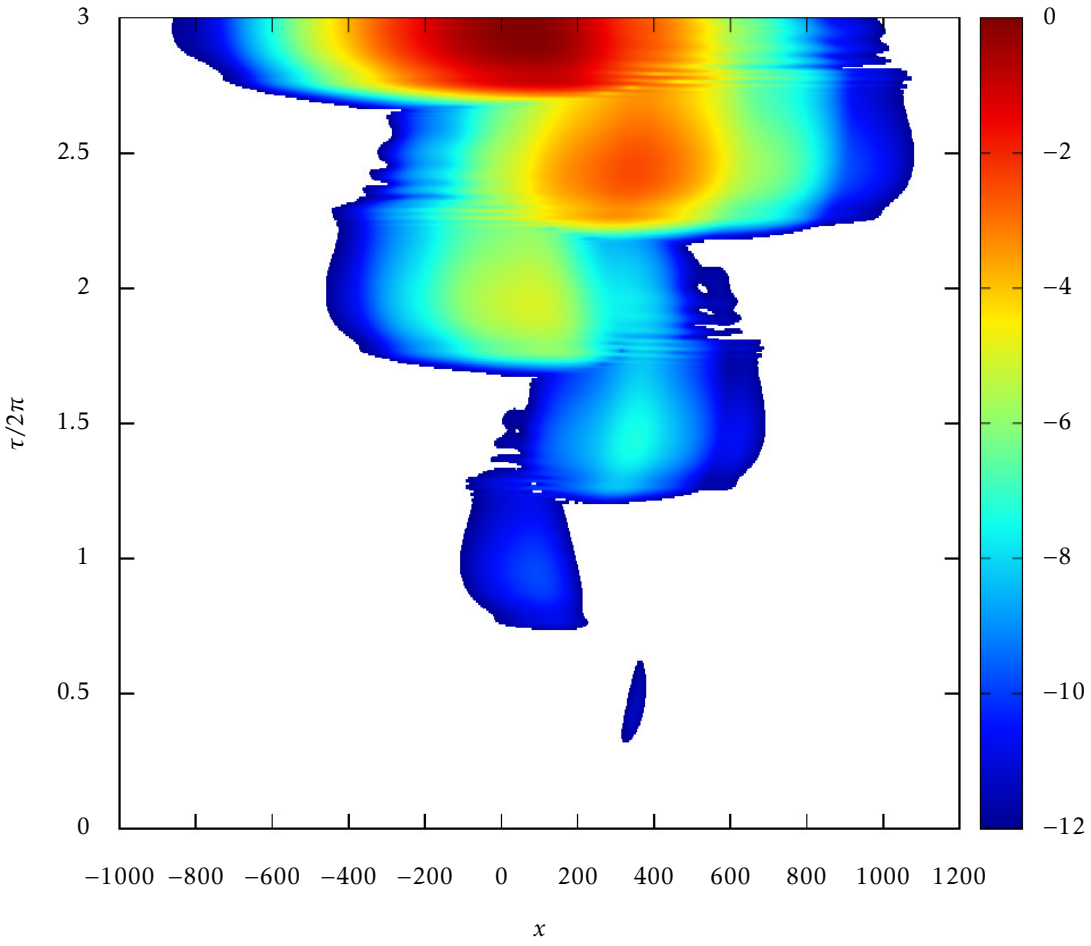

Figure 6.4: Space/time contour plots of $\log|\zeta(x,0,\tau)|$ *for* $Re = 500$, $\delta = 0.01$ *and* $p = 60$ *with* $(a_p, b_p) = (1,0)$. *There is little evidence of the family-tree structure for this level of noise.*

in experimental observations.

This contour plot shows that beyond a certain level of noise, the spatial/temporal evolution of disturbances no longer adhere to the structure and behaviour seen in the monochromatic case. In the case of low-level noise, the secondary wavepackets are introduced. These then become stronger than the daughter wavepackets causing the disturbance maximum to lie approximately in the centre of the disturbance in the case of significant noise. It is then possible that as this behaviour dominates it coincides with the breakdown of the family-tree structure. Documenting cases with δ between the values of 0.0008 and 0.001 would be necessary for a stronger statement to be made.

Again, having the disturbance maximum contained within the rest of the disturbance indicates that any movement of the maximum is representative of the movement of the entire impulse response. This suggests that the convective properties of this disturbance may be explored by tracing the location of the disturbance maximum (as will be seen later).

6.2.2 Temporal growth-rates

Both the temporal growth of the disturbance maximum and the temporal growth at some fixed streamwise locations are now measured in the same manner as in Section 3.4. The measured growth-rate of the disturbance maximum is compared against the growth-rate predicted by the eigenvalue problem and the differences in the growth-rate curves are discussed. The harmonic or subharmonic nature of the temporal evolution at fixed x is observed and the corresponding growth-rate is measured.

Low-level noise

Figure 6.5a shows the temporal growth-rates associated with a range of α when $\delta = 0.0002$ and $Re = 750$. Comparison with Figure 3.7a shows that for these parameters, very little has changed except that the maximum growth-rate has marginally increased ($\mu_r = 0.2072$ rather than $\mu_r = 0.2009$ in Figure 3.7a) as has the corresponding wavenumber ($\alpha = 0.3748$ rather than $\alpha = 0.3747$ in figure 3.7a). The growth-rate curve also appears more *jagged* than in the monochromatic case, but is otherwise very similar.

Figure 6.5b compares this predicted growth-rate with that measured from the time-history of the disturbance maximum at the start of each period by (4.3.14). The convergence is clear and occurs at a similar rate as for the monochromatic case.

The time-history of the logarithm of the wall vorticity envelope at fixed streamwise locations is shown in Figure 6.5c, showing a growing Floquet mode with a quasi-period twice the period of the underlying flow. That is, in the case of low-level noise the disturbance evolution for fixed x remains subharmonic in time.

Figure 6.5d shows the temporal growth-rates at three locations, measured by (4.3.23). Transient effects are significant for most of the time displayed, i.e. there is a less clear convergence to a single value than in the monochromatic case. However, the disordered behaviour present for most of the time does appear to settle down towards the end of the

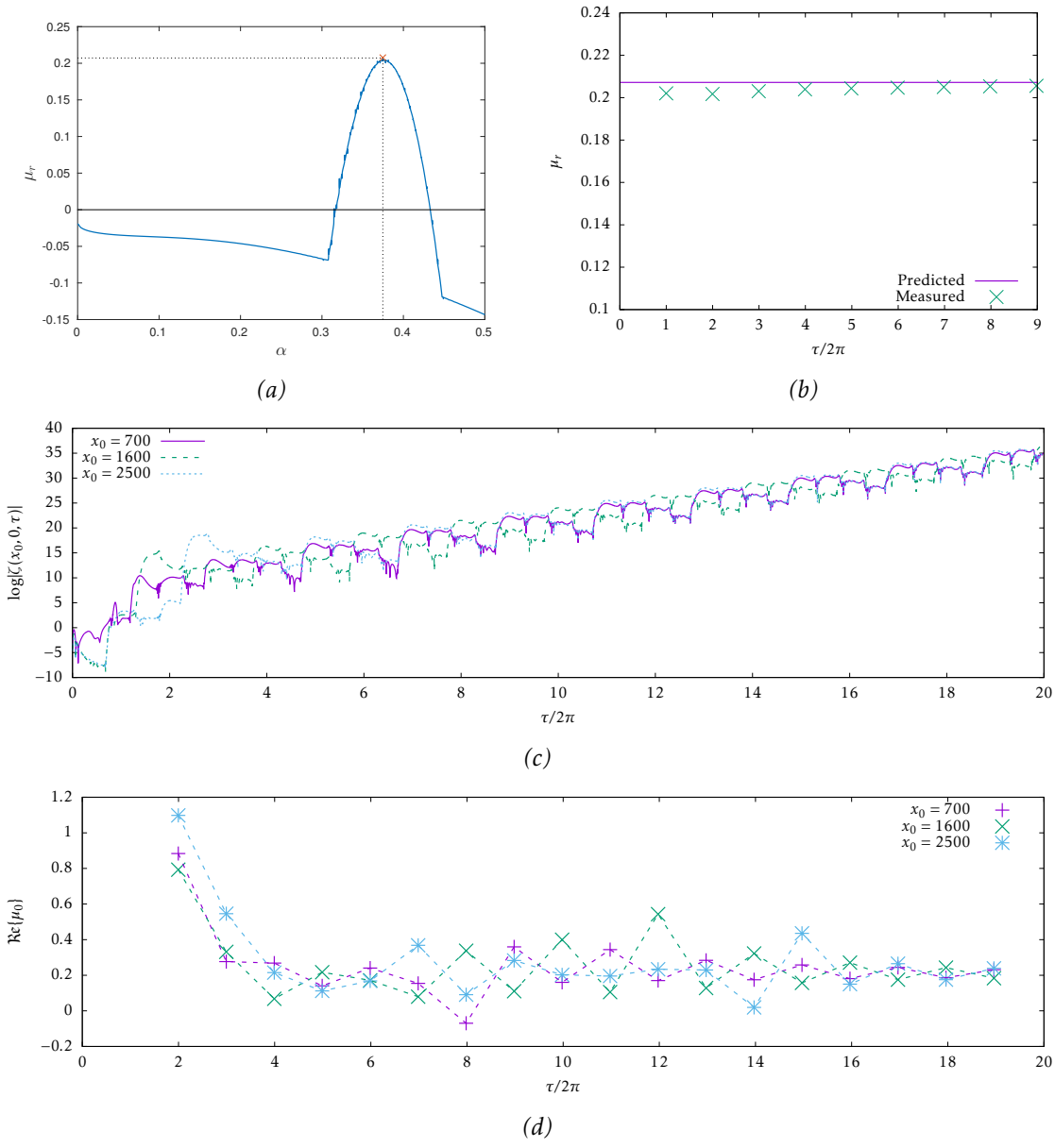

Figure 6.5: The Stokes layer with $\delta = 0.0002$, $p = 60$ and $(a_p, b_p) = (1, 0)$ at $Re = 750$ (low-level noise). In (a) the growth-rate associated with a selection of α are plotted and the most unstable mode is selected ($\alpha = 0.3748$ and $\mu_r = 0.2072$). In (b) the temporal growth-rate of the disturbance maximum is calculated with (4.3.14) at the beginning of each period and compared with the predicted value. In (c) the logarithm of the wall vorticity envelope at $x = 700, 1600, 2500$ displays subharmonic temporal growth as in Figure 3.11a. In (d) the temporal growth-rates are calculated at the beginning of each period using (4.3.23) for $x_0 = 700$ (+), $x_0 = 1600$ (×) and $x_0 = 2500$ (∗), showing convergence to a single positive value, though this is slower than for the monochromatic case (Figure 3.11b).

simulation. As for the pure Stokes layer, the temporal growth-rate at fixed x appears to be approaching a value very close to that of the disturbance maximum.

Significant noise

Figure 6.6a shows the growth-rates associated with a range of α as found from Floquet theory when $\delta = 0.0008$ and $Re = 700$. This figure is drastically different to Figure 3.8a which, aside from the small-scale protrusions, has a single peak at the dominant mode (as do Figure 3.7a and Figure 6.5a). In this case there are multiple peaks and the growth-rate is highly sensitive to the choice of α.

Figure 6.6b compares the predicted growth-rate with that measured using (4.3.14) and the convergence to the predicted value is significantly slower than in the monochromatic case (note that Figure 3.7b shows only ten periods of wall oscillation whereas Figure 6.5b shows 20). This slower convergence may be a manifestation of the multiple local maxima in the growth-rate curve (Figure 6.6a), suggesting that the impulse response remains a complicated superposition of several distinct modes for longer.

Figure 6.6c shows the time-history of the logarithm of the wall vorticity envelope at the approximate locations of local maxima. This figure indicates that the temporal evolution at these locations displays a quasi-periodic time-history with period equal to that of the underlying basic state. In this case the subharmonic temporal variation has thus been replaced by a harmonic temporal variation. This has coincided with the strengthening of the secondary wavepacket and the disturbance maximum moving between two locations with a period equal to that of the underlying oscillation.

High-level noise

The growth-rate curve for wavenumbers $0 \leq \alpha \leq 0.5$ is given in Figure 6.7a when $\delta = 0.01$ and $Re = 500$. The maximum growth-rate is noticeably larger than in the previous two cases at $\mu_r = 0.8447$ and the corresponding wavenumber is much closer to that for the monochromatic and low-level noise cases than for that of significant noise. The larger growth-rate was anticipated from Figure 6.4 but the curve has a distinct shape unlike any observed so far. There are two clear peaks of the growth-rate appearing at distinct wavenumbers and in this case there is no evidence of the fingers protruding from the curve.

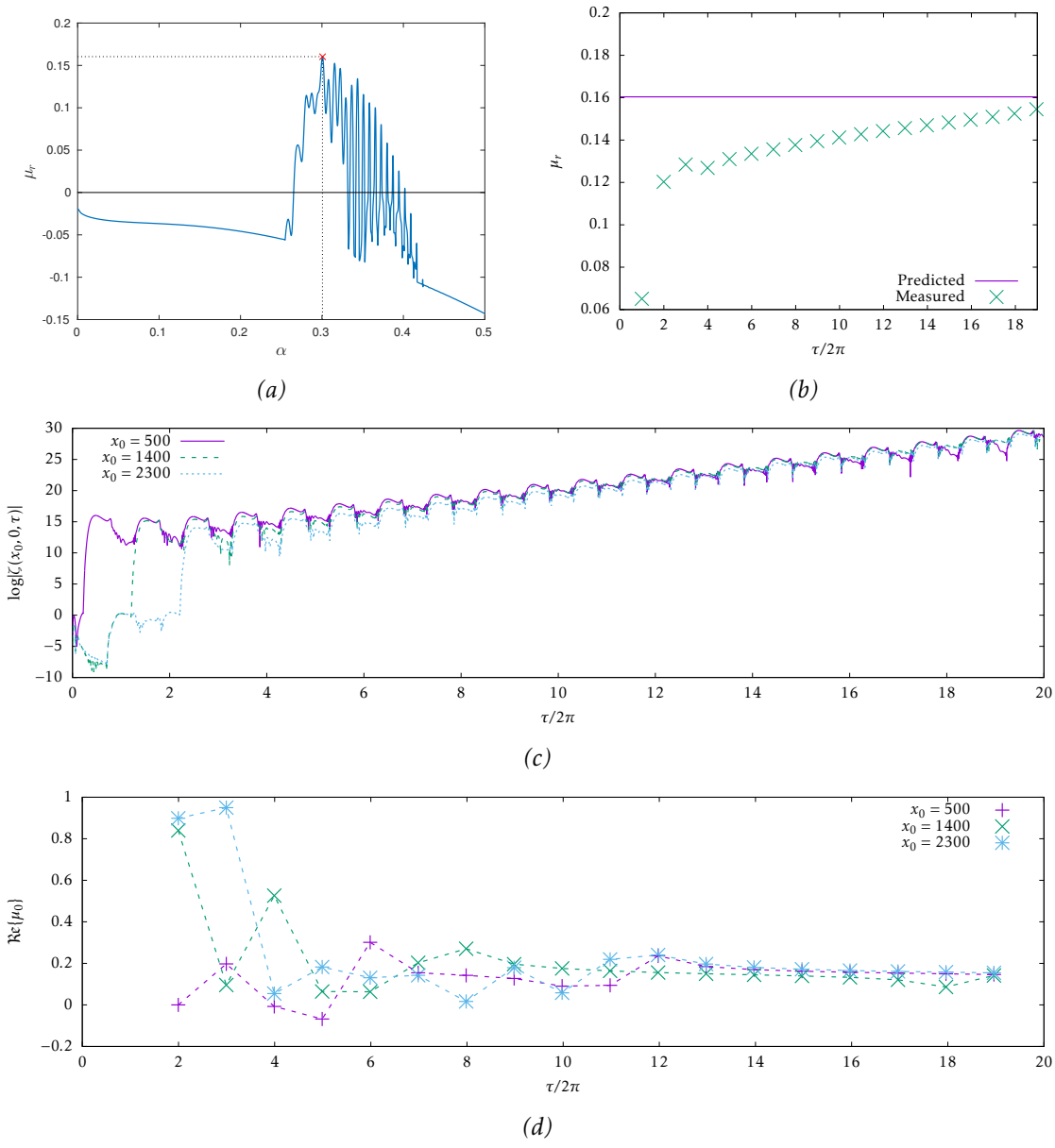

Figure 6.6: The Stokes layer with $\delta = 0.0008$, $p = 60$ and $(a_p, b_p) = (1, 0)$ at $Re = 700$ (significant noise). In (a) the growth-rates associated with a selection of α are plotted and the one expected to be most dominant is selected ($\alpha = 0.3006$ and $\mu_r = 0.1604$). In (b) the temporal growth-rate of the disturbance maximum is calculated with (4.3.14) at the beginning of each period and compared with the predicted value. In (c) the logarithm of the wall vorticity envelope at $x = 500, 1400, 2300$ reveals harmonic growth. In (d) the temporal growth is measured at the same streamwise locations using (4.3.23) at the beginning of each period, $x_0 = 500$ (+), $x_0 = 1400$ (×) and $x_0 = 2300$ (∗), showing convergence to a single positive value, though this is again slower than for the monochromatic case.

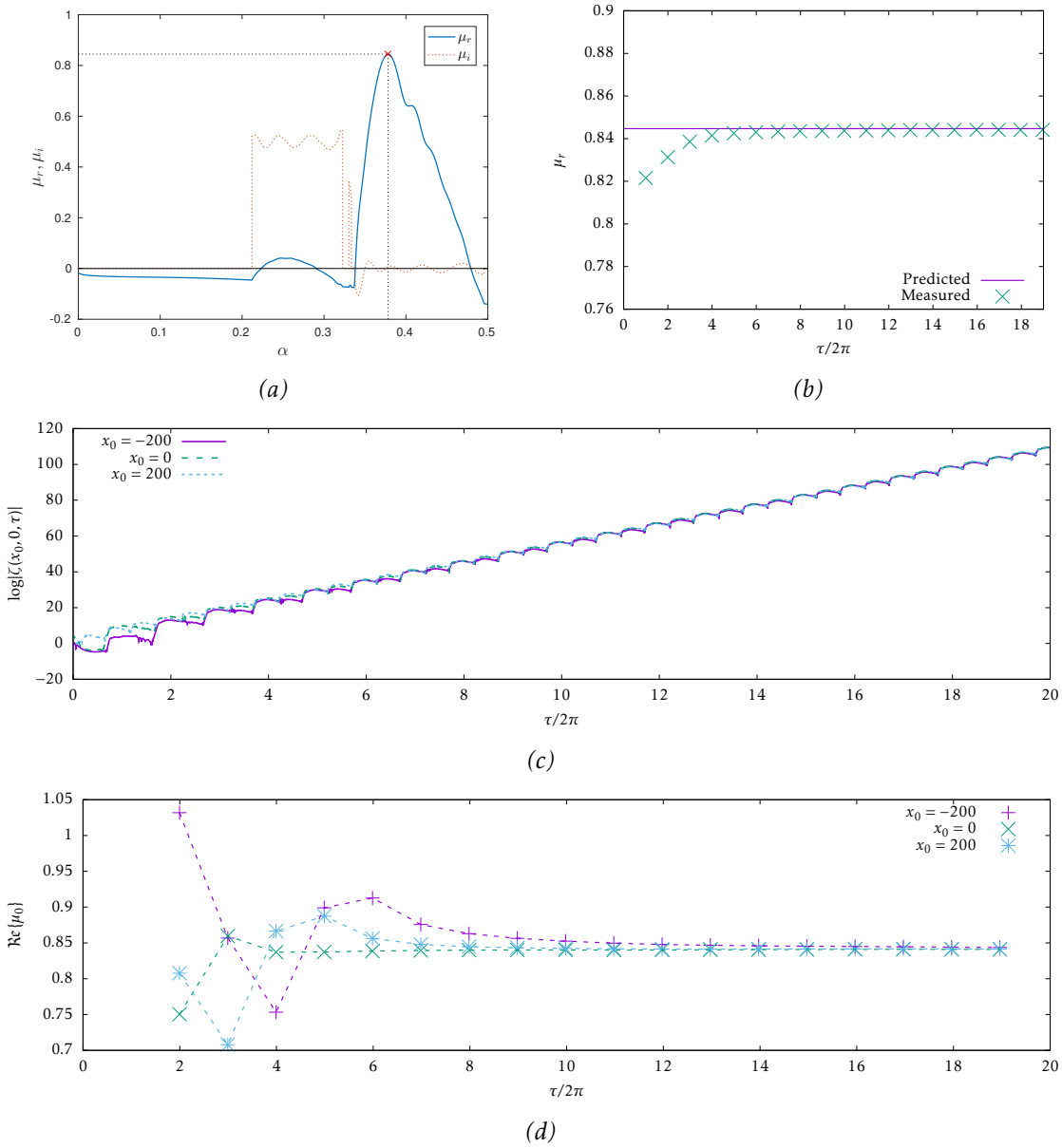

Figure 6.7: The Stokes layer with $\delta = 0.01$, $p = 60$ and $(a_p, b_p) = (1, 0)$ at $Re = 500$ (high-level noise). In (a) the growth-rate associated with a selection of α are plotted and the one expected to be most dominant is selected ($\alpha = 0.3783$ and $\mu_r = 0.8447$). The imaginary part of μ is also plotted showing that the lower peak corresponds to $\mu_i \sim 1/2$ and the higher peak corresponds to $\mu_i \sim 0$. In (b) the temporal growth-rate of the disturbance maximum is calculated with (4.3.14) at the beginning of each period and compared with the predicted value. In (c) the logarithm of the wall vorticity envelope at $x = -200, 0, 200$ reveals harmonic growth. In (d) the temporal growth-rates at these spatial locations are calculated at the beginning of each period using (4.3.23) for $x_0 = -200$ (+), $x_0 = 0$ (×) and $x_0 = 200$ (∗), showing convergence to a single positive value.

The imaginary part of the eigenvalue is also plotted in Figure 6.7a, revealing that the two peaks also correspond to distinct values of μ_i. The peak observed at lower α corresponds to $\mu_i \sim 1/2$ while the peak at larger α has $\mu_r \sim 0$. The imaginary part is not plotted for other cases since this value is known to move between 0 and 1/2 over the distance between fingers, i.e. at a fine scale not easily depicted in these figures.

In this case, near harmonic $\mu_i \sim 0$ and near subharmonic $\mu_i \sim 1/2$ behaviour is associated with distinct wavenumbers. Furthermore, the difference in the size of these peaks indicates that cusps corresponding to near harmonic temporal behaviour will dominate over those corresponding to near subharmonic temporal behaviour which is consistent with the apparently harmonic temporal growth at every fixed x in the contour plot Figure 6.4.

It is important to note that the vertical lines in the μ_i curve of Figure 6.7a indicate that different modes become dominant as α is changed. For instance, a mode with $\mu \in \mathbb{R}$ is dominant from $\alpha = 0$ to approximately $\alpha = 0.21$, then a mode with $\mu_i \sim 1/2$ moves further right in the complex plane. This mode moves into the unstable region ($\mu_r > 0$), causing the first peak, and then returns to the stable region of the complex plane. Then, at approximately $\alpha = 0.34$ a mode with $\mu_i \sim 0$ becomes dominant and moves into (then out of) the unstable region, creating the second peak.

Figure 6.7b compares the predicted growth-rate of $\mu_r = 0.8447$ against the temporal growth-rates of the disturbance maximum measured from the simulation at the start of each period using (4.3.14). This plot indicates much faster convergence to the asymptotic value than for significant noise.

In Figure 6.7c, the logarithm of the wall vorticity envelope is given at three locations and, as would be anticipated from the larger growth-rate, the slope of this curve is much steeper than in the previous two cases. The disturbance displays two peaks each period and provides the clearest evidence that the temporal variation of the disturbance at each of these spatial locations is harmonic.

Figure 6.7d shows the instantaneous temporal growth-rates at these streamwise locations, measured by (4.3.23), and it is immediately clear that transient effects are prevalent for a much shorter time than for the case of significant noise (see Figure 6.6d). In this case, the convergence to the asymptotic temporal behaviour is faster with regards to the temporal evolution of both the disturbance maximum and at any fixed spatial location.

Note that, for this case, the locations of local maxima are less clear due to the extent

to which the family-tree structure has broken down. For this example, the streamwise locations of interest were chosen as the initial point of excitation, $x = 0$, and one location on either side, $x = \pm 200$.

6.2.3 Cusp maps

Cusps will now be found for the three cases of interest and, since p is even, these are no longer expected to correspond to real α. As a result, the temporal growth-rate associated with any fixed streamwise location is expected to be less than that of the disturbance maximum. This feature will be explored in more detail later.

Low-level noise

A search for cusps in the vicinity of the real line was carried out for the case of low-level noise ($\delta = 0.0008$, $Re = 750$). It is anticipated that the cusps will be in a neighbourhood of the real line because the behaviour in this case is similar to the monochromatic Stokes layer.

Four cusps were found in this case and two of these are presented in Figure 6.8. Two of these cusps contribute to near harmonic temporal behaviour at all spatial locations and the others correspond to near subharmonic temporal variation (one of each is shown in Figure 6.8). These plots are similar to those for the pure Stokes layer (see Figure 5.6 and Figure 5.7), though the curves are somewhat deformed compared to the noise-free case. The most significant difference between these cusps and those of the monochromatic Stokes layer is that the locations have been shifted away from the real α-axis as anticipated by the failure of the symmetry arguments in the case that p is even.

Remembering that the locations of these cusps will only be approximate due to the limitations of the grid method, the locations of all four cusps found in this case are given in Table 6.1. It is immediately apparent that not only are the values of $\mathfrak{Im}\{\alpha_*\}$ nonzero in all cases, but that this value is close in all four cases. It is therefore possible that the actual cusp locations correspond to the same value of $\mathfrak{Im}\{\alpha_*\}$. This suggestion is explored in Figure 6.9.

Furthermore, comparison of the cusp locations in this case with those presented in Table 5.1 reveals that the cusps found in this case are located at the same $\mathfrak{Re}\{\alpha_*\}$ as those for the monochromatic case up to four decimal places. The cusp spacing is therefore

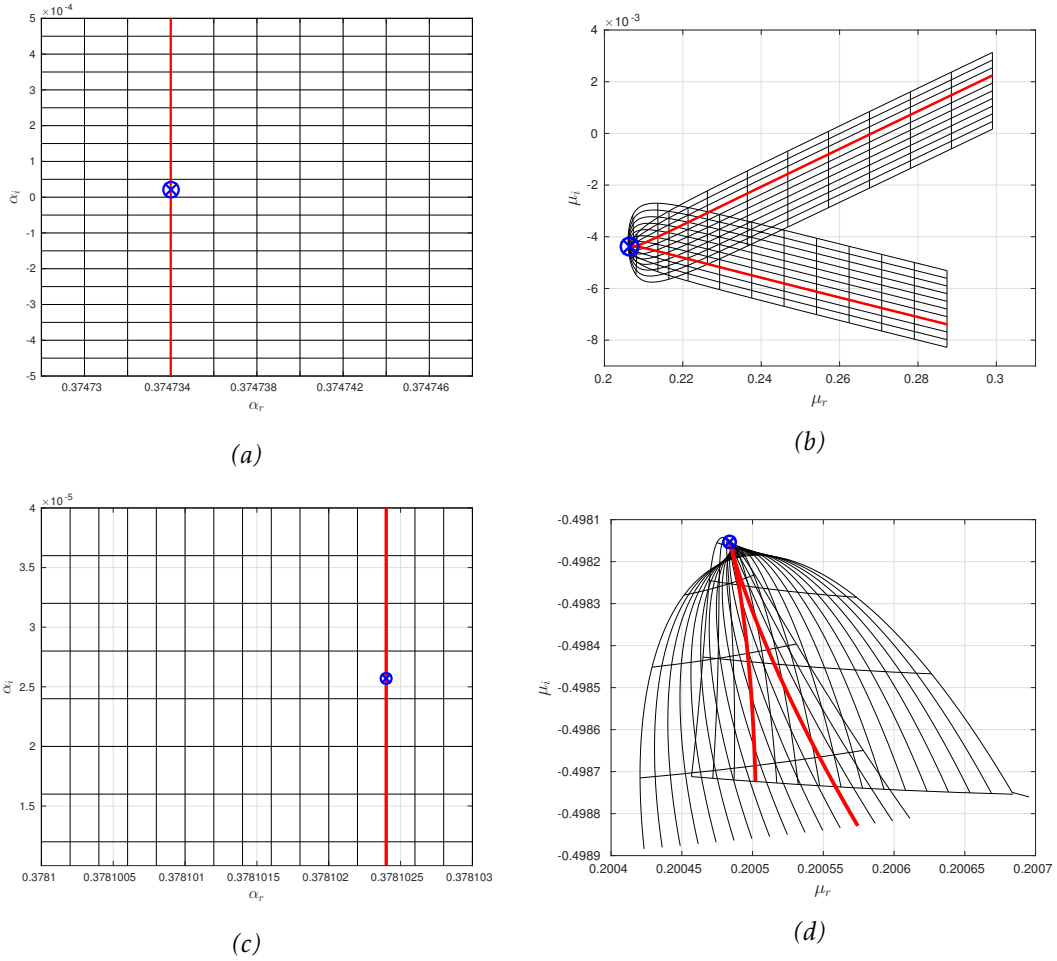

Figure 6.8: Cusp maps in the case of low-level noise, i.e. $Re = 750$, $\delta = 0.0002$, $p = 60$ and $(a_p, b_p) = (1, 0)$. The features of these cusps are similar to those for the pure Stokes layer (see Figure 5.6) except that they do not correspond to $\alpha \in \mathbb{R}$. In (a) and (c), the straight grids in the α-plane are shown and the corresponding curves in the complex μ-plane are shown in (b) and (d), respectively. In (b), $\mathrm{Im}\{\mu_*\} \sim 0$ which corresponds to near harmonic temporal growth. In (d), $\mathrm{Im}\{\mu_*\} \sim 1/2$ which corresponds to near subharmonic temporal growth.

Figure	$\mathfrak{Re}\{\alpha_*\}$	$\mathfrak{Im}\{\alpha_*\}$	$\mathfrak{Re}\{\mu_*\}$	$\mathfrak{Im}\{\mu_*\}$
6.8a,6.8b	0.374734	0.000022	0.206471	-0.004381
Not shown	0.368010	0.000026	0.201348	-0.003401
6.8c,6.8d	0.3781024	0.0000257	0.2004840	-0.4981533
Not shown	0.3713668	0.0000254	0.1989642	0.4883578

Table 6.1: The values of α_* and μ_* shown in Figure 6.8. Notice that for cusps that describe near subharmonic temporal variation, the values are given to an extra decimal place due to the finer grids used.

in good agreement, being $\Delta_\alpha^c = 0.003364$ in this case. This might have been anticipated from the observation that the streamwise separation of wavepackets is equal in these two cases.

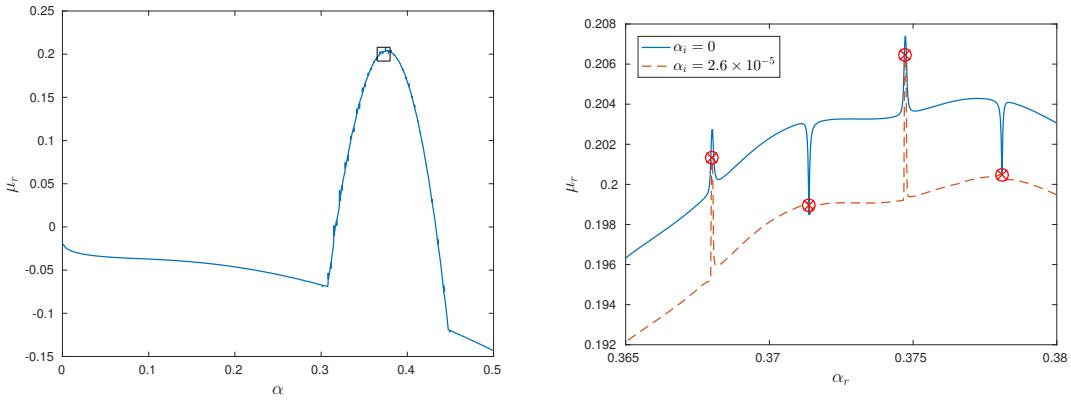

(a) *(b)*

Figure 6.9: The growth-rate curve for $\alpha \in \mathbb{R}$ for the case of low-level noise. In (a) the curve is produced for $0 \leq \alpha \leq 0.5$ and in (b) as small portion of this curve (indicated by a box) is presented. Aside from the destabilisation the main difference compared to the monochromatic case (see Figure 5.8) is that the subharmonic modes now lie on inverted fingers. The growth-rate curve when $\alpha_i = 0.000026$ is also shown in (b). This curve is qualitatively similar to Figure 5.8 and the cusps roughly correspond to this value of α_i.

While $\mathrm{Im}\{\mu_*\}$ is noticeably nonzero in Table 6.1 (compared to Table 5.1), justifying the description of these cusps as near harmonic, in the near subharmonic cases $\mathrm{Im}\{\mu_*\}$ is actually closer to 1/2 than in the monochromatic case. Therefore, while these cusps are described as near subharmonic due to the anticipated symmetry breaking, it cannot be ruled out that these are numerical approximations to exactly subharmonic cusps.

Figure 6.9 shows a small section of the growth-rate curve for $\alpha \in \mathbb{R}$. This reveals that the finger-like protrusions are still present and recognisable in this case and, though not shown in the figure, they still correspond to harmonic modes with $\mu_i = 0$. Where Figure 6.9 differs from the monochromatic case (Figure 5.8) is in the inverted fingers that are now present when $\mu_i \sim 1/2$. These features are responsible for the more jagged appearance of the growth-rate curve in this case (compared to the monochromatic case).

Unlike the monochromatic case, the cusps do not correspond to real α so it would be misleading to mark the cusp locations against this growth-rate curve in isolation. For this reason Figure 6.9 also presents the growth-rate curve for nonreal α with $\alpha_i = 0.000026$. A value in this area was chosen from the values observed in Table 6.1. For this value of α_i the growth-rate curve qualitatively agrees much better with that seen in Figure 5.8. In particular, the cusps that correspond to near harmonic temporal growth lie on the protruding fingers while those corresponding to near subharmonic temporal behaviour

lie halfway between the fingers.

Physically, this suggests that the temporal growth of the disturbance at any streamwise location will be less than that of the disturbance maximum. However, this discrepancy will be incredibly small and difficult to ascertain by extraction from the time-histories. This is consistent with the similarities between this case and the monochromatic case.

Note that it is not immediately apparent, when p is even, whether the cusps satisfy the collision criteria or not. A definitive proof that this is the case would be time consuming and computationally demanding. Instead, it is noted that these cusps are located very close to those found for the pure Stokes layer and that the temporal evolution of wavepackets is also similar in these two cases. This suggests that introducing this form of noise has simply deformed cusps that are known to satisfy the collision criteria. It is conjectured from this observation that the cusps presented in Figure 6.8 satisfy the collision criteria.

This conjecture is supported by the agreement between the temporal growth-rates of the disturbance at fixed spatial locations shown in Figure 6.5d and the values of $\mathfrak{Re}\{\mu_*\}$ given in Table 6.1.

Significant noise

Presented in Figure 6.10 are two cusps corresponding to near harmonic temporal growth at every spatial location in the case of significant noise ($\delta = 0.0008$, $Re = 700$). As for the previous case, the cusps do not correspond to real α_*. In fact, in this case the cusps are further from the real line and now correspond to $\mathfrak{Im}\{\alpha_*\} \sim -0.00075$.

The locations of these cusps are indicated in Table 6.2 and it is also observed that $\mathfrak{Im}\{\mu_*\} \neq 0$ for either of the cusps shown so the temporal behaviour associated with these cusps is near harmonic. It is interesting to note that no evidence of near subharmonic cusps halfway between the two shown in Figure 6.10 was found.

Figure	$\mathfrak{Re}\{\alpha_*\}$	$\mathfrak{Im}\{\alpha_*\}$	$\mathfrak{Re}\{\mu_*\}$	$\mathfrak{Im}\{\mu_*\}$
6.10a,6.10b	0.300800	-0.000789	0.152140	0.011465
6.10c,6.10d	0.308088	-0.000726	0.123530	0.019133

Table 6.2: The values of α_* and μ_* shown in Figure 6.10. Notice that both cusps describe near harmonic temporal behaviour.

The growth-rate curve for significant noise is plotted again in Figure 6.11a. In this

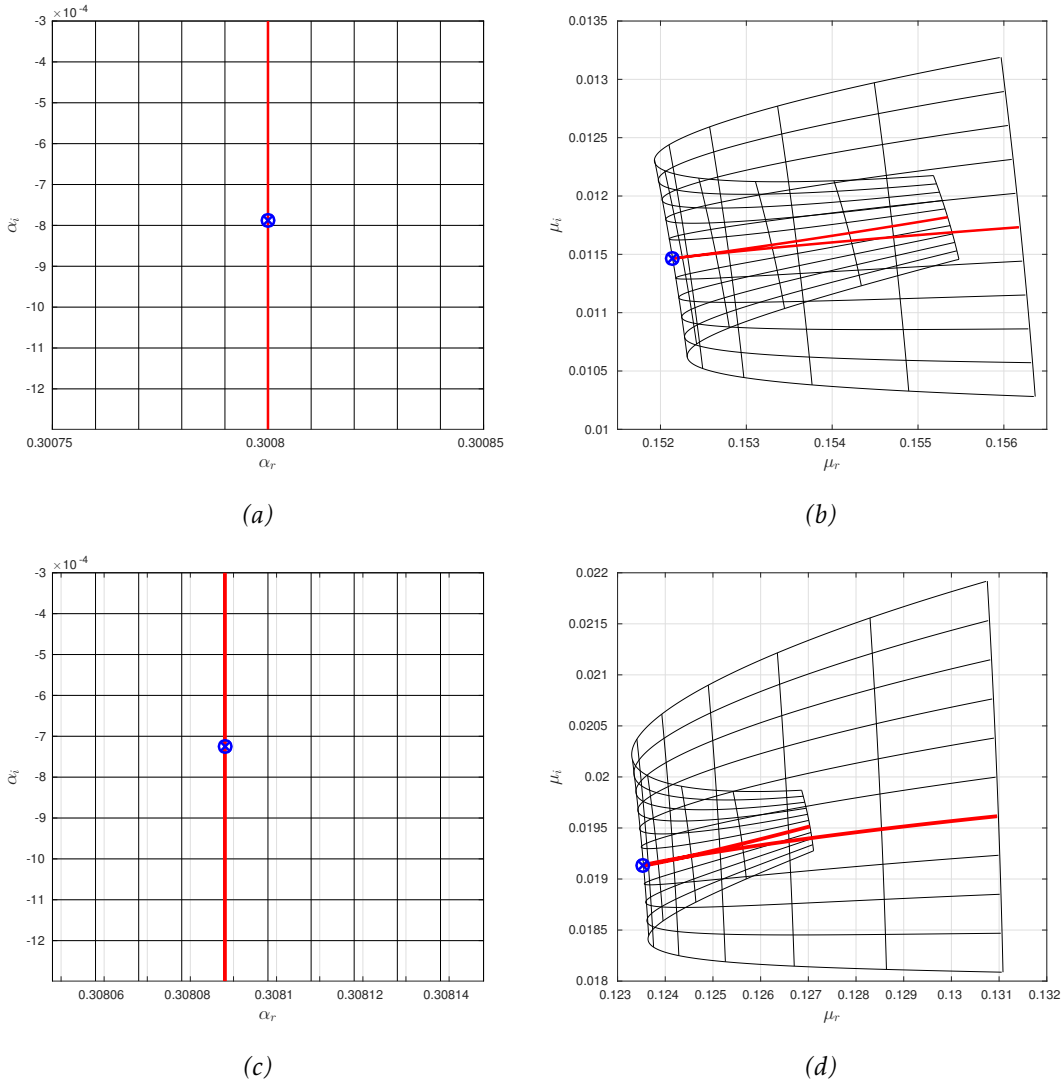

Figure 6.10: Cusp maps in the case of significant noise. That is $Re = 700$, $\delta = 0.0008$, $p = 60$ *and* $(a_p, b_p) = (1, 0)$. *In (a) and (c) the straight grids in the complex* α*-plane are shown and the corresponding curves in the* μ*-plane are shown in (b) and (d), respectively. Again, the locations of these cusps do not correspond to* $\alpha \in \mathbb{R}$.

case the imaginary part of the eigenvalue is also plotted. This curve is difficult to interpret as some of the vertical lines indicate a change in the dominant mode, while the actual curves of μ_i remain fairly steep. Interestingly, when $\alpha > 0.34$ the imaginary part is highly oscillatory, as has been discussed for the monochromatic and low-level noise cases, whereas for $\alpha < 0.34$ the imaginary part remains close to zero, as observed for one of the peaks in the high-level noise case.

An important feature of this curve is that the value of μ_i does not ever reach 1/2, so in this case the most unstable mode for all α is never subharmonic. When $\alpha \sim 0.41$ the

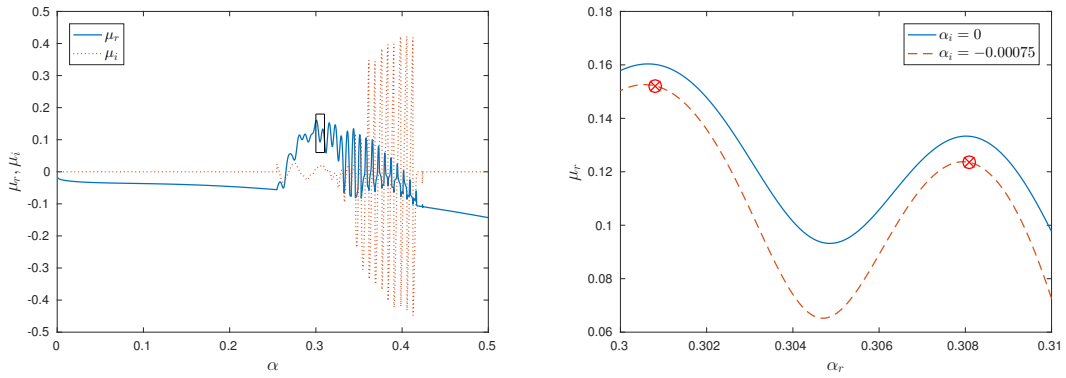

(a) *(b)*

Figure 6.11: The growth-rate curve for $\alpha \in \mathbb{R}$ for the case of significant noise. Plotting the real and imaginary parts of the most unstable eigenvalues in (a) reveals that there are no subharmonic modes when $\alpha \in \mathbb{R}$. In (b), the region near the cusps of Figure 6.10 is explored and in addition to the growth-rate curve for $\alpha_i = 0$ is the growth-rate curve for $\alpha_i = -0.00075$. This curve approximately passes through the cusps (marked by circled crosses) but there is no evidence of the fingers protruding from the curves in this case.

value of μ_i does come into proximity of 1/2, but these near subharmonic modes are either stable or only marginally unstable so will not be significant in the impulse response.

This supports the observation from Figure 6.7c that the temporal evolution at any given x is harmonic. In Figure 6.11b the locations of the cusps given in Figure 6.10 are marked against the curve with $\alpha_i = -0.00075$. This is chosen as the approximate value of $\mathrm{Im}\{\alpha_*\}$ for these cusps. Unlike the case of low-level noise, neither of these curves display the protruding fingers. However, it will later be seen that there are still features resembling the fingers at larger α in this case.

It is more difficult to ascertain whether the cusps shown in Figure 6.10 satisfy the collision criteria or not. Notionally, the cusp locations could be compared against the locations of cusps in the monochromatic case at the same Re, or for efficiency the locations of fingers. This is not directly suitable since the search for cusps was conducted near to the most unstable mode for $\alpha \in \mathbb{R}$ which, in this case, lies at a lower value of α than any fingers have been observed for the monochromatic case with $Re = 700$ (see Figure 3.8a). However, the distance between $\mathfrak{Re}\{\alpha_*\}$ suggests a separation of $\Delta_\alpha^c \sim 0.0073$, which is in agreement with the finger separation Δ_f^α found in the monochromatic case at this Re (Section 5.4).

Also, recall that for odd p it has been predicted that cusps will have $\alpha_* \in \mathbb{R}$. This means that for both $p = 59, 61$ there will be cusps that satisfy the collision criteria on

the real line, suggesting that cusps close to the real line when $p = 60$ (such as those presented in Table 6.2) may be deformations of these. Furthermore, the agreement with the temporal growth displayed at each location in Figure 6.6d suggests that these cusps may satisfy the collision criteria.

High-level noise

A search was also conducted in the case of high-level noise. Some cusps were found, but none that remotely agreed with the temporal growth associated with fixed spatial locations in Figure 6.7d. Some examples were found with $\mathfrak{Re}\{\mu_*\} > 0.85$ and it was concluded that these cusps do not satisfy the collision criteria since they display greater temporal growth than observed for $\alpha \in \mathbb{R}$ (for which the greatest growth observed is $\mu_r = 0.8447$, see Figure 6.7a).

It may be considered logical that cusps with greater growth-rate than that observed for $\alpha \in \mathbb{R}$ cannot satisfy the collision criteria as this would mean that the temporal growth of the disturbance at any fixed spatial location would exceed the temporal growth of the disturbance maximum. This should be an impossibility by the very nature of the disturbance maximum. In Section 5.2, an additional argument (in the framework of Briggs' method) as to why cusps with $\mathfrak{Re}\{\mu_*\} > \max_{\alpha\in\mathbb{R}} \mu_r$ do not satisfy the collision criteria is given. This argument is strongly related to the intuition described above.

Several cusps were also found with $\mathfrak{Re}\{\mu_*\} < 0.8$. It is unclear without a more in-depth analysis whether such cusps satisfy the collision criteria, since according to Figure 6.7a the most unstable cusp is expected to correspond to a temporal growth-rate much closer to that of the disturbance maximum, i.e. ~ 0.84.

None of these cusps were presented here since there was no evidence that they satisfy the collision criteria. It is important to note the significance of this criteria and not assume that it is satisfied for all cusps. Conveniently, for the monochromatic Stokes layer or the noisy Stokes layer with odd p, it has been shown that cusps satisfying $\mathfrak{Im}\{\alpha_*\} = 0$ and $\mathfrak{Im}\{\mu_*\} = k/2$ (with $k \in \mathbb{Z}$) should satisfy the collision criteria. When p is even, this is not the case.

The approach taken here has been to report cusps that describe a temporal variation at fixed streamwise locations that is in agreement with the simulation results. This does not mean that the cusps shown in Figure 6.8 and Figure 6.10 definitely satisfy the colli-

sion criteria, only that they are consistent with the observed behaviour. Any cusps that are not consistent with the observed behaviour are not included. This does not mean that these cusps definitely do not satisfy the collision criteria, as the simulations will only display the temporal growth associated with the cusp with greatest $\mathfrak{Re}\{\mu_*\}$.

6.2.4 Comparison of even and odd p

In all of the cases considered, the cusps found do not lie on the real line, as anticipated by the breaking of the flow symmetries when p is even. A direct result of this is that there exists some ray $x/\tau = V$ along which the disturbances experience greater temporal growth than at any given location $x/\tau = 0$. It is therefore anticipated that these disturbances exhibit some convective properties.

In each of the three cases of interest, comparison will be made against the disturbance evolution when $p = 59, 61$ since for odd p the cusps should correspond to $\alpha_* \in \mathbb{R}$. First, the features up to ten periods of wall-motion are compared showing broadly similar features, regardless of the choice of p. However, exploring the behaviour in more detail indicates that the disturbances display some convective properties when $p = 60$ but remain centred around the original mother wavepacket when $p = 59, 61$ in the manner observed for the monochromatic case.

Contour plots for the first ten periods of wall motion

Intuitively, it would be anticipated that changing p by 1 would leave the dynamics largely unchanged. However, since the antiperiodicity of the flow when p is odd breaks down when p is even, it is worth exploring how the behaviour of the disturbance when $p = 60$ compares to that when $p = 59$ and $p = 61$.

An immediate assessment of the qualitative difference between any disturbances can be made by observing the contour plots. Contour plots provide a means of establishing several important characteristics: existence of convective or absolute instability; harmonic or subharmonic temporal evolution at fixed x; whether the disturbance maximum is convected away or confined to a neighbourhood of the excitation; and also to what extent the family-tree structure is present.

An extended contour plot for the first ten periods of wall motion in the case of low-level noise ($\delta = 0.0002$, $Re = 750$) is shown in Figure 6.12a. This reinforces the conclusion

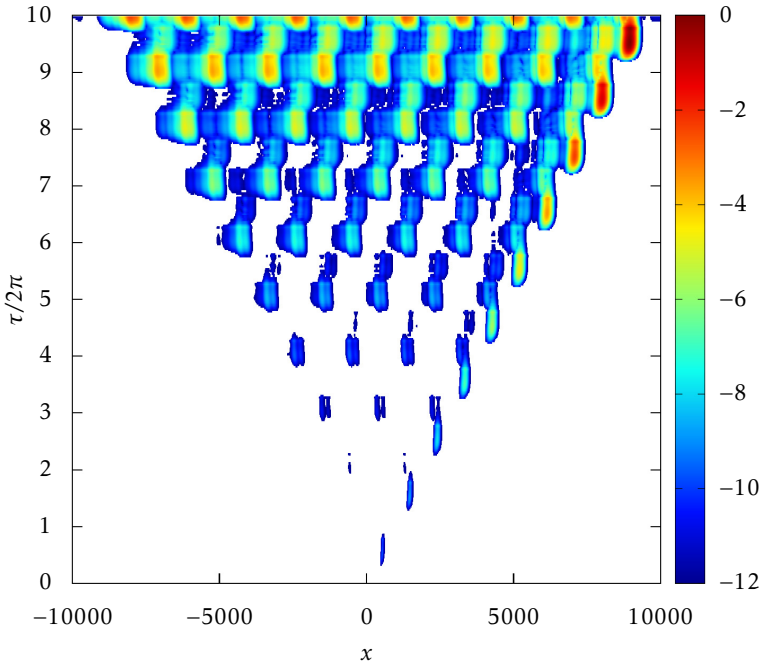

(a)

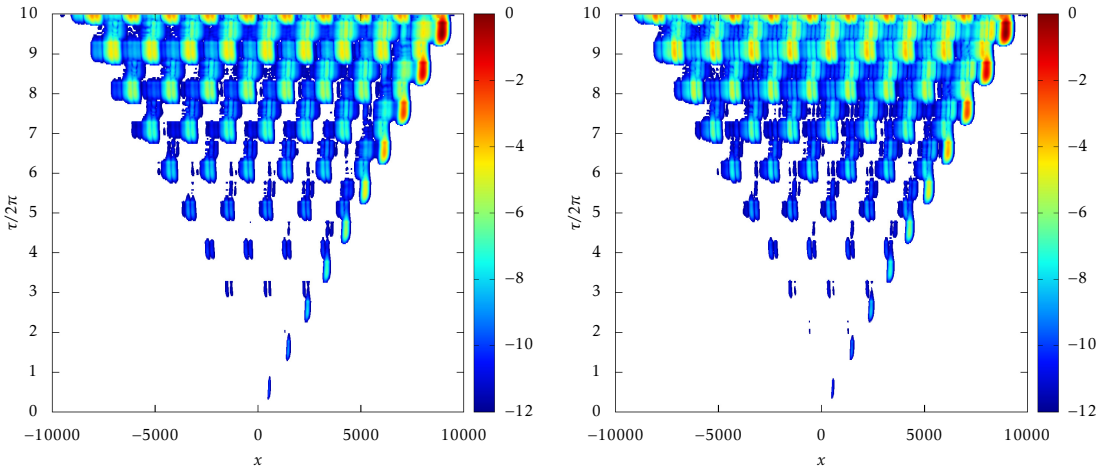

(b) (c)

Figure 6.12: Contour plot for the first ten periods of wall motion. Each case is for $Re = 750$, $\delta = 0.0002$ *with (a) corresponding to the case of low-level noise already discussed,* $p = 60$. *The cases* $p = 59$ *(b) and* $p = 61$ *(c) are compared showing strong qualitative agreement.*

already drawn that, aside from relatively minor qualitative changes, the disturbance evolution is largely unaffected by the presence of noise in this case. This contour plot can be compared with that for the pure Stokes layer in Figure 3.12 and the main difference is the magnitude of the disturbance in the regions between the wavepacket maxima.

Figure 6.12 also compares this contour plot against those for $p = 59$ and $p = 61$ with all other parameters kept the same. In these figures, the streamwise wavepacket separation appears equal which is consistent with the suggestion that this feature depends only on Re. Also, the temporal growth of each wavepacket is subharmonic in all three cases, as can be seen from their staggered arrangement.

The disturbance maximum is convected away from the point of excitation in all three cases in the same manner observed in the monochromatic case. It is interesting to observe no clear qualitative changes between these three cases according to Figure 6.12. This is to be expected in a case where the noise has had such little impact on the behaviour.

The equivalent contour plot in the case of significant noise is shown in Figure 6.13a and the disturbance maximum appears to remain confined to a region around the initial point of excitation. This is not what is anticipated from the cusp map method which suggests that the whole disturbance should display some convective properties. However, there is some suggestion at the top of this plot that the disturbance maximum has shifted slightly in the direction of positive x.

This plot is compared against the cases $p = 59, 61$ for which the temporal growth associated with any spatial location is expected to be equal to that of the disturbance maximum. These plots show no such sign of the maximum moving away from the initial point of excitation but otherwise show essentially the same behaviour with harmonic temporal variation at each x.

Recall that these plots are constructed by normalising the disturbance before cutting off the lower magnitudes and taking the logarithm. This means that the apparent thinning of the wavepacket extent as p is increased is the manifestation of a greater growth-rate. In this case the unitary shift in p is responsible for a noticeable change in the growth characteristics, but the qualitative behaviour of these disturbances is broadly similar.

Figure 6.14 presents the contour plot after ten periods of wall motion for the case of high-level noise ($\delta = 0.01$, $Re = 500$) which is compared against the cases $p = 59, 61$. In this case, the low-amplitude cut-off is taken to be smaller due to the greater tem-

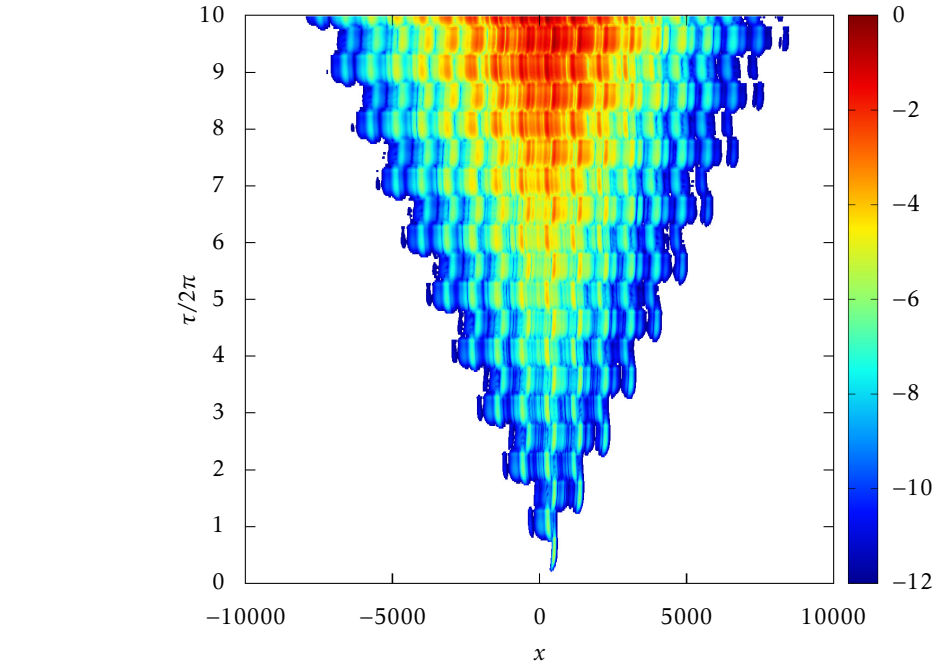

(a)

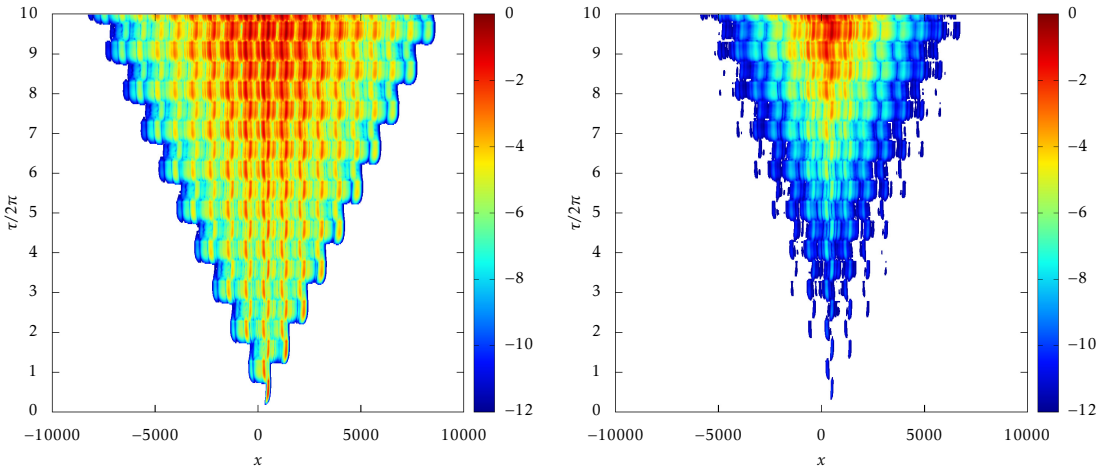

(b) (c)

Figure 6.13: Contour plot for the first ten periods of wall motion. Each case is for Re = 700, δ = 0.0008 with (a) corresponding to the case of significant noise already discussed, p = 60. The cases p = 59 (b) and p = 61 (c) are compared showing qualitative agreement. In this case the growth-rate appears to increase with increasing p.

poral growth-rate of the disturbance maximum. These contour plots are virtually indistinguishable; in all three cases the growth-rate appears approximately equal and the family-tree structure has completely broken down. In this figure there is no evidence of the disturbance maximum convecting away from the initial point of excitation.

Evidence of convection

Earlier, it was stated for the cases of significant and high-level noise that having the disturbance maximum contained within the body of the disturbance (approximately in the centre) means that the movement of the maximum should be representative of the movement of the disturbance. For this reason, the convective properties of these disturbances will be explored by tracing the location of the disturbance maximum.

Consider the time halfway through each period of wall motion $\tau/2\pi \in \{0.5, 1.5, 2.5, ...\}$. The location of the disturbance maximum can be found at each of these times. No staggering of this location is expected since the temporal behaviour associated with any fixed spatial location appears to be harmonic (or at least near harmonic) in these cases.

It is anticipated that when $p = 60$ the disturbance maximum will be slowly convected away from the initial point of excitation since there should be some ray $x/\tau = V_{max}$ along which the disturbance displays greater temporal growth than it does for any fixed x, $x/\tau = 0$. In the cases $p = 59, 61$ it is anticipated that the disturbance maximum at this selection of times will remain confined to the same location since the greatest growth is associated with the ray $x/\tau = 0$. These predictions are made based on whether the cusps correspond to $\alpha \in \mathbb{R}$ or not and are discussed near the end of Section 6.1.

In Figure 6.15, the locations of the disturbance maximum are plotted against time for the three choices of p in the cases of significant and high-level noise. The anticipated convection of the disturbance maximum is observed when p is even while this location remains fixed when p is odd.

Notice that there is a jump in the location of the disturbance maximum near the end of the simulation in the case of significant noise. This is due to the magnitude of a different wavepacket becoming greater than the previous maximum. This is supposedly a remaining manifestation of the family-tree structure and is noticeably absent in the case of high-level noise for which the disturbance maximum moves approximately the same distance each period.

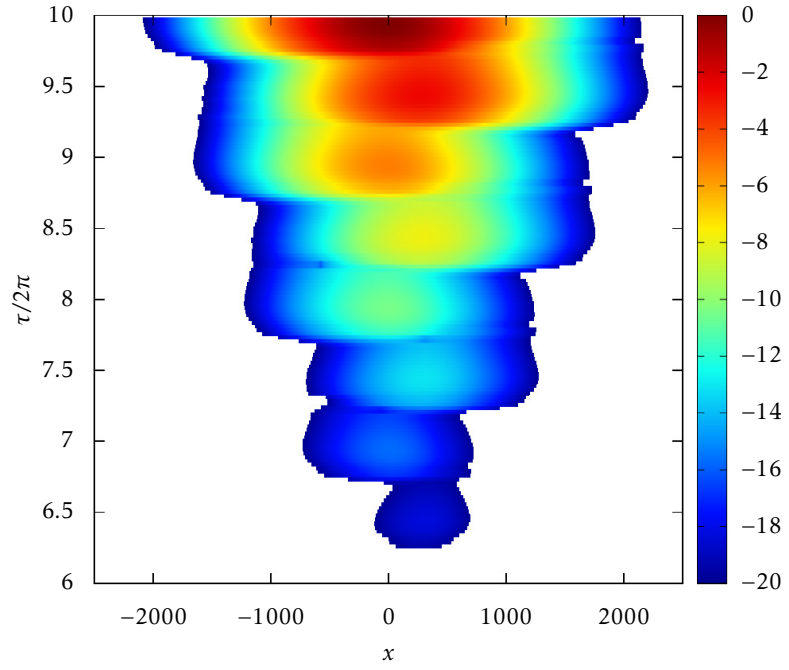

(a)

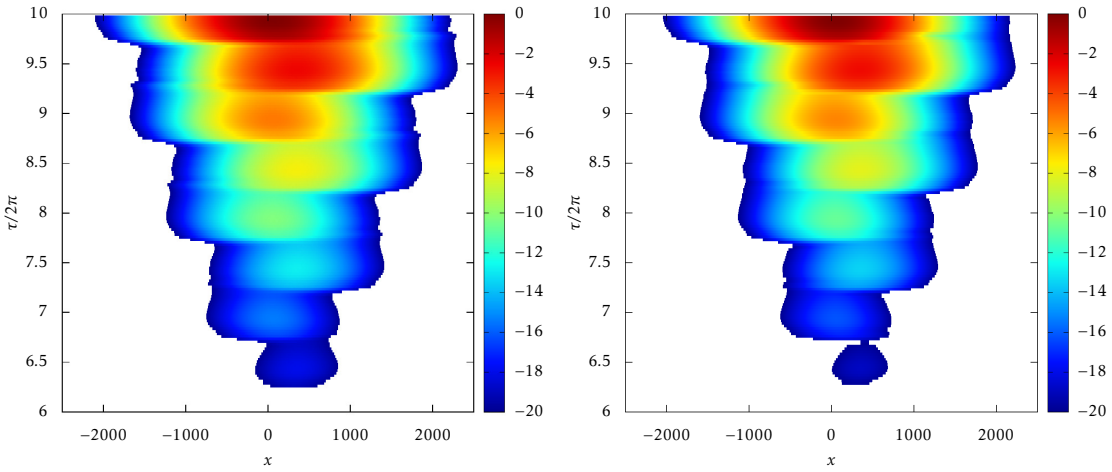

(b) (c)

Figure 6.14: Contour plot for the first ten periods of wall motion. Each case is for Re = 500, $\delta = 0.01$ with (a) corresponding to the case of high-level noise case already discussed, $p = 60$. The cases $p = 59$ (b) and $p = 61$ (c) are compared showing strong qualitative agreement.

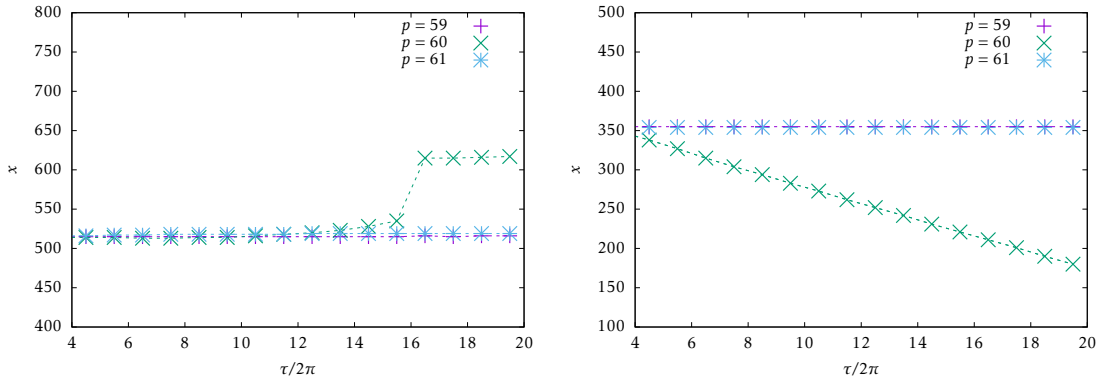

Figure 6.15: The location of the disturbance maximum when $\tau/2\pi = 0.5, 1.5, 2.5, \ldots$ for the cases of significant and high-level noise. In (a), $Re = 700$ and $\delta = 0.0002$ (significant noise). In (b), $Re = 500$ and $\delta = 0.001$ (high-level noise). In both cases, the disturbance maximum for $p = 59, 61$ remains in the same location for each time whereas for $p = 60$ the disturbance maximum begins to move away from this location. In (a) this convection only becomes apparent in the last 5 periods of wall motion, while in (b) the convection is immediately apparent.

It is interesting to note that the convection of the disturbance maximum is much stronger in the case of high-level noise than for significant noise even though there was no evidence of this in the contour plot, Figure 6.14. This is because the contours are much wider in Figure 6.14 so the location of the disturbance maximum is more difficult to deduce than in Figure 6.13 where there are still distinct local maxima present in a shape that still resembles the family-tree structure to some extent.

In the case of low-level noise, the family-tree structure is retained and the disturbance maximum is immediately convected downstream so is not representative of the general movement of the disturbance. In this case the convective properties of the disturbance will instead be investigated by plotting the local maxima of the disturbance at a selection of times. The equivalent plot for the monochromatic Stokes layer is given in Figure 3.13 (and reproduced in Figure 5.10).

In Figure 6.16 the locations of maxima are plotted against the logarithm of their amplitudes for $p = 60$ and $p = 61$. When $p = 61$, the structure is qualitatively similar to the monochromatic case. In particular, the wavepackets at each time are approximately equal in size as indicated by the dashed lines at the average value. This was anticipated from the flow symmetries that constrain the locations of cusps to real α and hence exhibit greatest temporal growth along the ray $x/\tau = 0$.

When $p = 60$, some other ray exhibits the greatest temporal growth since the cusps

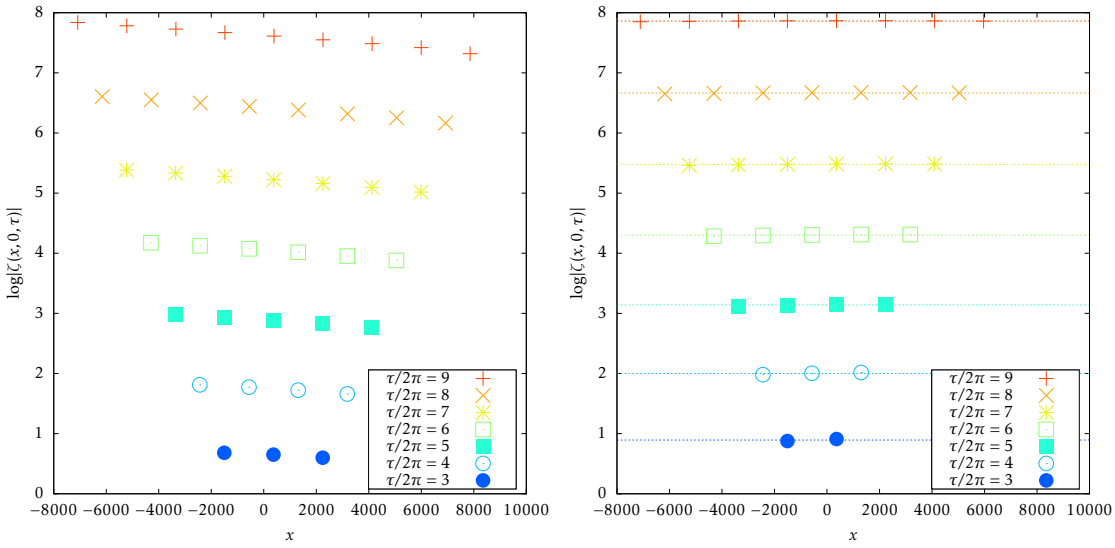

(a) *(b)*

Figure 6.16: The logarithm of the magnitude of the local maxima are plotted against the locations of these maxima at a selection of times (not including the global maxima which are convected downstream) when $Re = 750$ and $\delta = 0.0002$ (i.e. low-level noise). In (a), $p = 60$ is chosen and when compared to the monochromatic case (Figure 5.10) there is a clear tilting of the structure: more negative x is associated with larger magnitudes at later times. In (b), $p = 61$ is chosen and this plot is characteristically very similar to Figure 5.10, with dashed lines indicating the average size of the maxima at each time instance.

do not correspond to real α (see Table 6.1). In this case the wavepackets on the left-hand side of the plot become increasingly dominant over those on the right-hand side over time. This indicates that the disturbance does indeed display convective properties as anticipated.

It has now been shown that even when the impulse response is absolutely unstable the disturbance can display convective properties. This is what is generally expected of absolute instabilities since it is only in special cases that the cusps will have $\alpha_* \in \mathbb{R}$. Note that the immediate convection of the disturbance maximum in the low-level noise and monochromatic cases is an unrelated feature.

Finally, it is noted that when p is even and the temporal growth along the ray $x/\tau = 0$ (fixed spatial location) is less than the temporal growth along the ray $x/\tau = V_{max}$, it should be possible to select the parameters so that the disturbance decays with time at every spatial location while the disturbance maximum displays temporal growth. Such a disturbance would be convectively unstable. The possibility of the existence of convective instabilities in the noisy Stokes layer is not explored here but is suggested as future work.

Growth-rate curves for even and odd p

To conclude the comparison between even and odd p, a segment of the growth-rate curves for all of the cases discussed in this section are presented in Figure 6.17. In each plot, δ and Re are fixed and the variation of μ_r with α in the range $0.365 \leq \alpha \leq 0.385$ is presented for the three cases $p = 59, 60, 61$. These plots are accompanied by the corresponding variation of μ_i.

The values of μ_i were manipulated for graphical clarity. In the case of $p = 60$ this was generally achieved by plotting μ_i modulo 1 (except for in Figure 6.17d) and for odd p use was made of the fact that for any μ-root of the dispersion relation, $\bar{\mu}$ is also a root at the same α. In these cases $|\mu_i|$ was plotted. The manner in which μ_i was manipulated was to ensure the clearest comparison between the curves for each p shown. This is why $0 < \mu_i < 1$ in all cases except for Figure 6.17d where it was concluded that the curve was better represented crossing the real axis.

First, observe that in the case of low-level noise, the μ_r curves for odd p are qualitatively very similar to those explored for the monochromatic Stokes layer (Figure 6.17a). There are fingers protruding from the curve at regular intervals of α and it can be seen from Figure 6.17b that these correspond to $\mu_i = 0$, furthermore, $\mu_i = 1/2$ approximately halfway between each of these fingers (note that the vertical lines in Figure 6.17b are a manifestation of a sudden change in the location of μ_i). For all three values of p, and for the monochromatic Stokes layer at the same Re, the fingers are found in the same locations. This suggests that in each case the streamwise separation of wavepackets is the same. As noted before, when p is even there are inverted fingers corresponding to $\mu_i = 1/2$.

In the case of significant noise, there is still evidence of the evenly spaced fingers for all three choices of p, but these are significantly broader than in the previous case (Figure 6.17c). Note that this selection of α is greater than that considered in Figure 6.11 for which no fingers were observed and corresponds to the region with greatest variation in μ_i. The distance between the tips of these protrusions seems to be lower than in Figure 6.17a and to the eye is consistent with the value of $\Delta_f^\alpha = 0.0073$ found for the monochromatic Stokes layer at this Re (see Section 5.4).

It has already been notice in the case of significant noise, and is evident from Figure 6.17d, that for no choice of p is there an α corresponding to $\mu_i = 1/2$. The closest

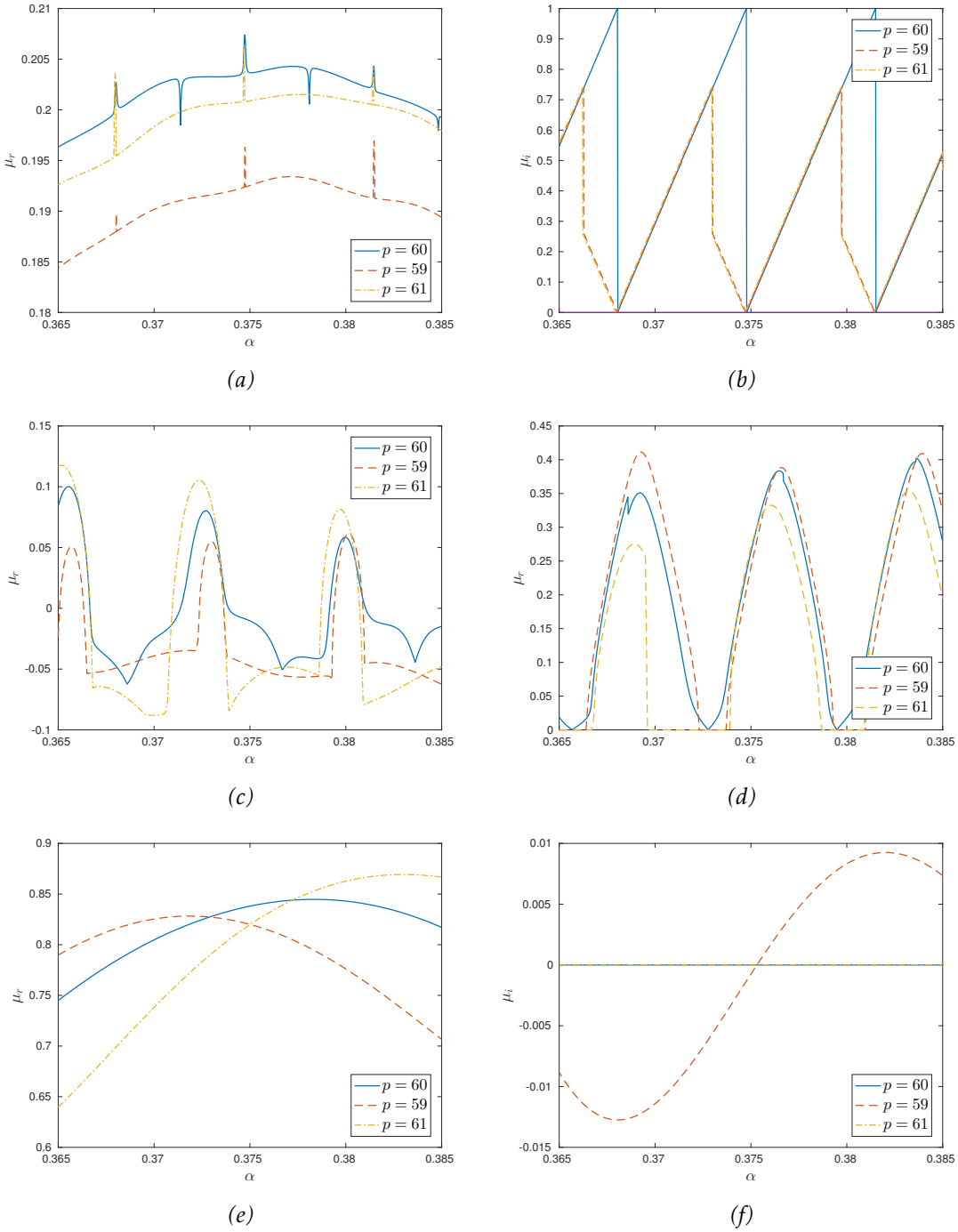

Figure 6.17: The variation of μ_r with α is plotted for $p = 60$ (solid line), $p = 59$ (dashed line) and $p = 61$ (chain) in (a), (c), (e). The corresponding variation of μ_i (modulo 1) is given in (b), (d), (f). The plots (a) and (b) correspond to the case of low-level noise ($\delta = 0.0002$, $Re = 750$). The plots (c), (d) correspond to the case of significant noise ($\delta = 0.0008$, $Re = 700$). The plots (e), (f) correspond to the case of high-level noise ($\delta = 0.001$, $Re = 500$).

μ_i gets to this value seems to be approximately halfway between the fingers and, with $\mu_i \sim 0.4$, these modes could be said to display near subharmonic behaviour.

In the cases of $p = 59, 61$, this means that the types of cusps that are constrained by the flow symmetries cannot appear between each finger (though this does not mean that there are no cusps at these locations) and for $p = 60$ no cusps were found here. In the case of odd p, the entire extent of the fingers still corresponds to $\mu_i = 0$, whereas for $p = 60$ the fingers correspond to $\mu_i \sim 0$ and it appears that $\mu_i = 0$ only at the tips of these protrusions (to the accuracy of these plots).

Finally, in Figure 6.17e the variation of μ_r with α for the case of high-level noise shows little evidence of the finger structures observed in the other cases. It is, however, intriguing to note from Figure 6.17f that for this range of α, all of the modes plotted have $\mu_i = 0$ when p is odd. This means that the curves shown display one of the main features of the fingers. Having observed the broadening of fingers with increased noise, it is possible that in this case the fingers have broadened to such an extend that they are no longer discernible at this scale.

In the case that $p = 60$, $\mu_i = 0$ at only one point in this range of α. This is consistent with the observation in the previous case that $\mu_i = 0$ across the entire extent of the fingers for odd p but only at a single α for even p. However, in this case it is evident that the wavenumber for which $\mu_i = 0$ when $p = 60$ does not correspond with the local maximum of μ_r. In the case of high-level noise in particular, exploration of a greater range of α would be more informative.

6.2.5 Discussion

The evolution of disturbances in three different examples of the Stokes layer modified by low-amplitude, high-frequency noise was explored. It was shown that for the cases considered, an increase in δ was capable of drastically destabilising the flow and that such destabilisation was associated with a change in the temporal evolution of the disturbance at fixed streamwise locations from subharmonic (with quasi-period twice the period of the basic state) to harmonic (with quasi-period equal to the period of the basic state).

For the lower levels of noise considered, this change in temporal variation appeared to coincide with the introduction and then strengthening of secondary wavepackets that are generated much closer to their respective mother wavepacket than the daughter

wavepackets discussed in the monochromatic case. For the case of high-level noise, the impulse response displayed a spatial/temporal evolution that was not at all comparable to the family-tree structure.

The cusp map method was applied in these cases and it was shown that, as was asserted based on symmetry arguments, for the choice of $p = 60$ there was no evidence of cusps with $\alpha \in \mathbb{R}$. This meant that, since $\alpha \in \mathbb{R}$ correspond to the greatest temporal growth along any ray $x/\tau = V$ (see Section 4.3), there is some ray along which the disturbance undergoes temporal growth greater than that displayed at any fixed spatial location. It was predicted, based on this observation, that when $p = 60$ the disturbance would display some convective properties while also growing at each spatial location. This was confirmed to hold for the three cases considered here.

Recalling that when p is odd, the symmetry arguments deployed for the pure Stokes layer apply and ensure the existence of cusps with $\alpha_* \in \mathbb{R}$, the same cases were considered but with $p = 59, 61$. As anticipated, it was seen that the disturbances did not display such convective properties in these cases.

Throughout this section, the Floquet eigenvalue method was applied and compared against the simulation results. It was seen that the breakdown of the family-tree structure coincided with the breakdown of the fingers protruding from the growth-rate curves. This is consistent with Section 5.4 where it was shown that the spacing of the fingers in α is consistent with the streamwise separation of wavepackets in the streamwise direction.

There was no evidence of cusps with $\mathrm{Im}\{\mu_*\} = 1/2$ in the case of significant noise, and it was seen that in the case of high-level noise the modes corresponding to harmonic and subharmonic temporal evolution (with $\mu_i = 0, 1/2$, respectively) are associated with distinct wavenumbers and display significantly different growth-rates.

6.3 Parametric investigation

Having discussed in some detail the effect that high-frequency noise in the basic state can have on the spatial/temporal evolution of disturbances, a broader investigation into the effects of noise can be carried out. Due to the many parameters controlling the form of the noise, this investigation will by no means be comprehensive and the focus will be on the destabilisation that has been observed as δ is increased (Thomas *et al.* , 2015). As discussed earlier, the dramatic change in Re_c that comes about for $\delta = \mathcal{O}(0.01)$ is consistent

with experimental observations but the other parameters, namely the noise frequency p and phase (a_p, b_p), are more difficult to extract from experiments. Indeed, in experiments the noise is expected to take a much more complicated form with a superposition of many harmonics and the possibility of breaking the exact periodicity that is central to the current approach.

The intention is to explore some of the observations reported by Thomas *et al.* (2015) in more detail. First, it will be shown that the problem is fairly insensitive to the choice of parameter pair (a_p, b_p), then the destabilisation will be explored for some choices of p. Finally, a brief investigation into the sensitivity of the problem to the precise choice of p will be presented.

6.3.1 Insensitivity to the phase of noise, (a_p, b_p)

The dependence of the problem on the phase of the noise will now be considered. Take the parameter pair (a_p, b_p), related by $a_p^2 + b_p^2 = 1$. First, it will be shown that there appear to be phase symmetries under which the asymptotic behaviour is unchanged which will be presented and discussed. Evidence will then be provided to suggest that, aside from these symmetries, the system is not particularly sensitive to the precise choice of (a_p, b_p).

Speculative phase symmetries

In addition to the symmetry between upstream and downstream, there is the possibility of an additional symmetry in this flow that comes about through modification of the parameters that control the phase of the noise. No mathematical argument has been found that utilises time shifts to show that such a symmetry must exist, but the eigenvalue solver provides anecdotal evidence.

Consider first an even value of p. Let $\alpha \in \mathbb{R}$ and set some (a_p, b_p). Fixing α, Re and p (even) it conjectured that

$$\Big((a_p, b_p) \to (b_p, -a_p)\Big) \quad \text{results in} \quad \Big(\mu \to \bar{\mu}\Big),$$

with $\bar{\mu}$ being the complex conjugate of μ. Notice that under this transform the relation $a_p^2 + b_p^2 = 1$ still holds and that this transformation amounts to a quarter-period shift in

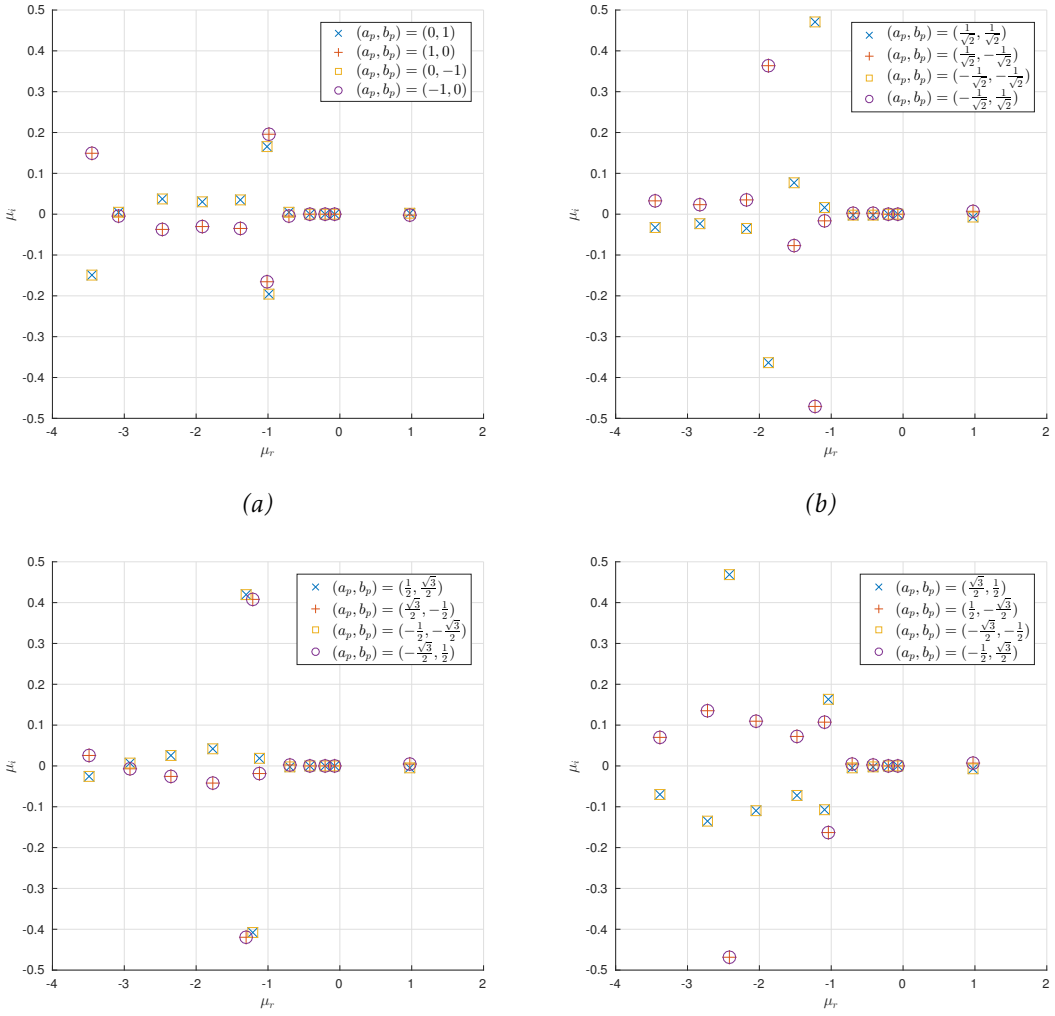

Figure 6.18: Fixed parameters $p = 70$, $\delta = 0.001$, $Re = 700$ and $\alpha = 0.34$. The eigenvalues are plotted for a selection of initial (a_p, b_p) and compared against those when $(a_p, b_p) \to (b_p, -a_p)$. For each case this transform is performed 3 times and this has the effect of conjugating the set of eigenvalues μ each time. The initial (a_p, b_p) are $(0,1)$ in (a), $(1/\sqrt{2}, 1/\sqrt{2})$ in (b), $(1/2, \sqrt{3}/2)$ in (c) and $(\sqrt{3}/2, 1/2)$ in (d). In all cases $a_p^2 + b_p^2 = 1$.

the phase of the noise. Performing this transformation again yields

$$\Big((a_p, b_p) \to (-a_p, -b_p)\Big) \quad \text{results in} \quad \Big(\mu \to \mu\Big),$$
$$\Big((a_p, b_p) \to (-b_p, a_p)\Big) \quad \text{results in} \quad \Big(\mu \to \bar{\mu}\Big).$$

This behaviour is consistent for all even values of p that were explored.

Some of the cases explored that displayed this symmetry are shown in Figure 6.18

where four different initial values of (a_p, b_p) are taken and this transform is performed three times. This supports the proposition stated above and highlights that performing this transform twice gives $(a_p, b_p) \to (-a_p, -b_p)$ and leaves the eigenvalues unchanged.

Table 6.3 shows the growth rates of the most unstable modes in Figure 6.18 for each of the four cases considered. Note that for each plot in Figure 6.18 there is only one choice of dominant growth-rate. This table shows that while this value is different in the four cases considered it does not differ much, suggesting that the precise choice of (a_p, b_p) is much less important than the choice of δ or p.

	(a)	(b)	(c)	(d)
$\Re\mathfrak{e}\{\mu\}$	0.974299	0.974986	0.975197	0.974430

Table 6.3: A comparison of the growth-rate of the most unstable modes associated with the different choices of (a_p, b_p). The letters (a), (b), (c) and (d) indicate which subfigure in Figure 6.18 the values correspond to, noting that complex conjugation does not effect the growth-rate. In each case, the growth-rates are similar but not equal.

Consider now odd values of p. No plots are presented for this case but it is observed that although the complex conjugation under $(a_p, b_p) \to (b_p, -a_p)$ no longer holds, the set of eigenvalues remain unchanged under a reversal of sign, i.e.

$$\Big((a_p, b_p) \to (-a_p, -b_p)\Big) \quad \text{results in} \quad \Big(\mu \to \mu\Big).$$

Noting that $(a_p, b_p) \to (-a_p, -b_p)$ is equivalent to $\delta \to -\delta$, this shows that a reversal in the sign of the noise (half-period shift in the phase) seems to leave the eigenvalues unchanged for both odd and even p. Only in the case of even p does a quarter-period shift in the phase appear to correspond to complex conjugation of the eigenvalues.

It is noted that this relationship breaks down when α is complex. The possibility that the relationship might hold for complex α provided $\alpha \to \bar{\alpha}$ was investigated and it was found that this was not the case.

While the suggestion that there is a shift in the phase of the noise that leaves the asymptotic behaviour unchanged is intriguing, no mathematical argument was found to support the existence of any such symmetry.

Simulation under different noise phases

Aside from the speculation that there is some form of symmetry under certain phase-shifts of the noise, it was also noted that the growth-rates for a selection of (a_p, b_p) differ only a little. This effect will now be explored through simulation results. The following four cases will be discussed: $(a_p, b_p) = (0,1), (1,0), (-1,0), (1/\sqrt{2}, 1/\sqrt{2})$. The noise level will be fixed at $\delta = 0.01$ so that the noise is of an amplitude that has significantly altered the stability of the flow and the three cases $p = 50, 60, 70$ will be considered. The Reynolds number will also be fixed at $Re = 500$, resulting in disturbances that are unstable for all choices of p at this δ and Re.

Consider $p = 50$. Figure 6.19 shows the contour plots for the four choices of (a_p, b_p). First, observe that these figures are not identical. However, in all four plots the growth over the six periods shown appears approximately equal, the observable width of the disturbances are approximately equal, and the disturbance maxima are confined to a corridor near the point of excitation.

Figure 6.20 shows equivalent plots in the case $p = 60$ and the agreement is even more striking. In this case there is little evidence left of the multiple wavepacket evolution observed for the monochromatic Stokes layer and few discernible differences between the figures. The same contour plots were constructed for $p = 70$, but these were virtually indistinguishable from Figure 6.20 so are not shown.

Now that it has been observed that the current choices of (a_p, b_p) have had little effect on the qualitative behaviour of disturbances, the temporal growth-rate of the disturbance maximum can be compared in each case. Table 6.4 presents the values measured using (4.3.14) and shows that for the choices of (a_p, b_p) considered, these growth-rates are in agreement to at least 2 decimal places for all three choices of p.

	(a_p, b_p)			
p	$(0,1)$	$(1,0)$	$(-1,0)$	$(1/\sqrt{2}, 1/\sqrt{2})$
50	0.3384	0.3356	0.3366	0.3334
60	0.8436	0.8437	0.8438	0.8439
70	0.7917	0.7935	0.7942	0.7931

Table 6.4: Comparison of the growth-rates for four different choices of (a_p, b_p). Here, $Re = 500$ and $\delta = 0.01$ in every case and $p = 50, 60, 70$ are considered. The growth-rates, measured from the simulations using (4.3.14) at the final time-step, generally agree to at least 2 decimal places for all values of (a_p, b_p) considered.

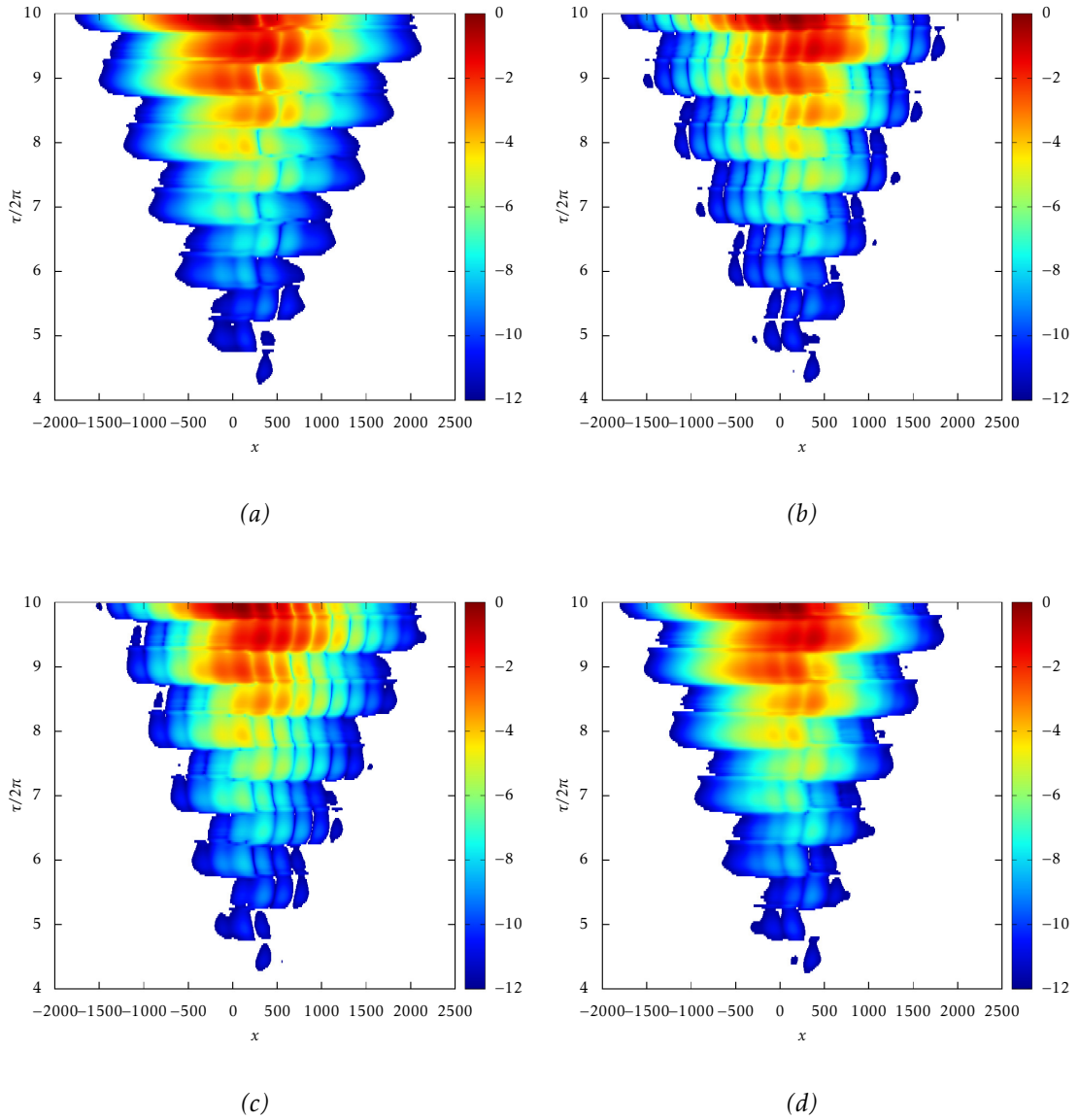

(a) (b)

(c) (d)

Figure 6.19: Space/time contour plots of $\log|\zeta(x,0,\tau)|$ *for* $Re = 500$, $\delta = 0.01$ *and* $p = 50$ *for four different choices of* (a_p, b_p)*: in (a)* $(a_p, b_p) = (0,1)$*, in (b)* $(a_p, b_p) = (1,0)$*, in (c)* $(a_p, b_p) = (-1,0)$*, and in (d)* $(a_p, b_p) = (1/\sqrt{2}, 1/\sqrt{2})$*. While the parameter choice clearly has some effect on the spatial/temporal evolution, the features of these plots are broadly similar.*

Notice that none of these values are as similar as might be suggested by the speculated symmetries. In particular, the growth-rates when $(a_p, b_p) = (-1,0), (0,1), (1,0)$ should be indistinguishable if this symmetry does indeed hold. The fact that the growth-rates in these cases are not particularly closer in value than they are to the case $(a_p, b_p) = (1/\sqrt{2}, 1/\sqrt{2})$ could either be due to the finite time of the simulations or might suggest that the observed symmetry does not actually hold.

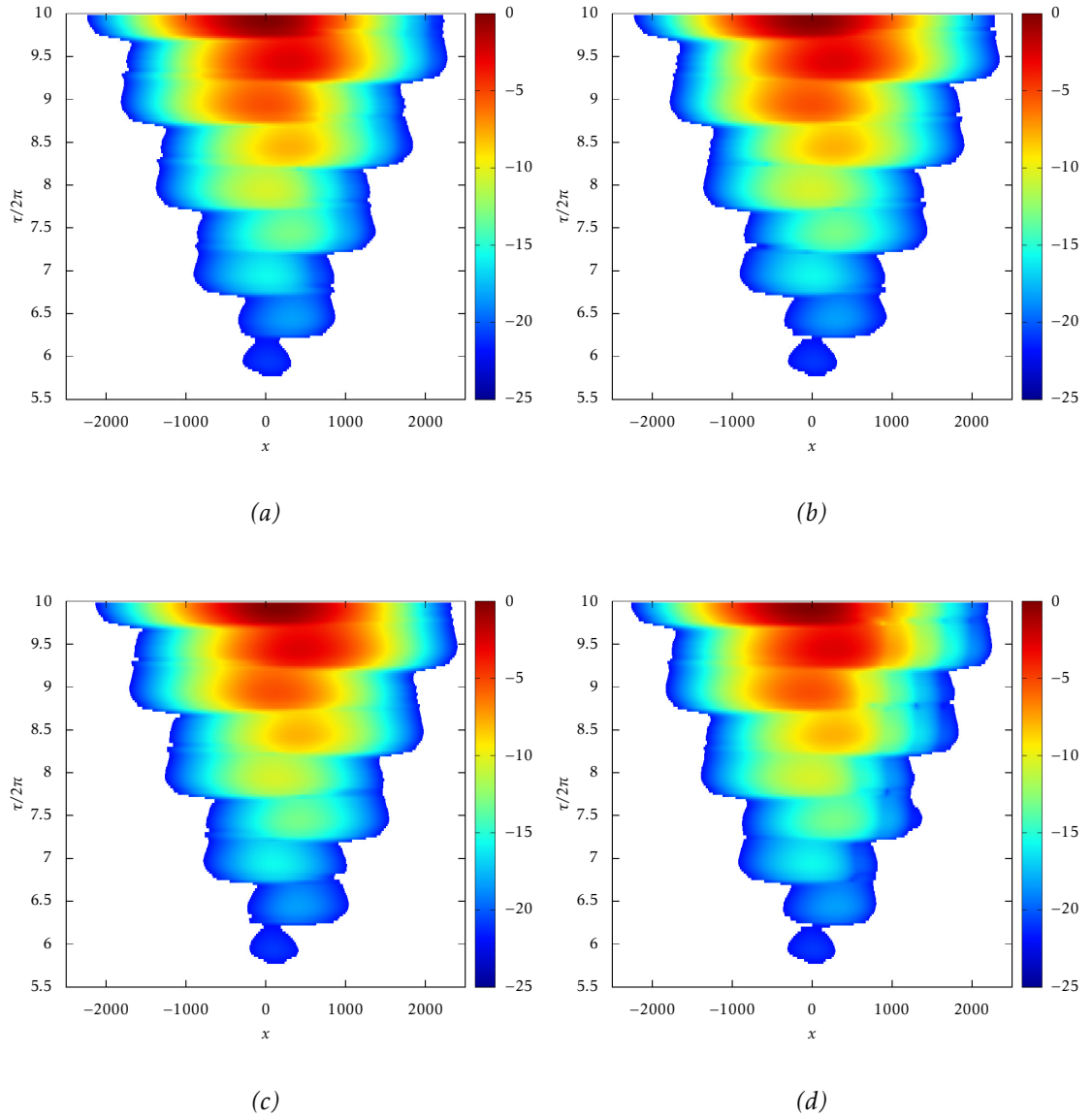

Figure 6.20: Space/time contour plots of $\log|\zeta(x,0,\tau)|$ *for* $Re = 500$, $\delta = 0.01$ *and* $p = 60$ *for four different choices of* (a_p, b_p)*: in (a)* $(a_p, b_p) = (0,1)$*, in (b)* $(a_p, b_p) = (1,0)$*, in (c)* $(a_p, b_p) = (-1,0)$*, and in (d)* $(a_p, b_p) = (1/\sqrt{2}, 1/\sqrt{2})$*. The parameter choice has little effect on the spatial/temporal evolution.*

These results suggest that the evolution of disturbances in the Stokes layer modified by high-frequency noise is relatively insensitive to the choice of parameter pair (a_p, b_p). This is not definitive since a limited choice of parameters were considered. However, these results do justify the decision to fix $(a_p, b_p) = (1,0)$ for the following investigation so as to reduce the parameter space with a minimal risk of missing important behaviour.

6.3.2 Destabilisation with δ

In order to quantify the destabilisation caused by the introduction of noise, the critical Reynolds number will be used. The critical Reynolds number Re_c is defined as the largest Reynolds number below which all disturbances are stable (i.e. the minimum point of the neutral stability curve). In order to deduce Re_c, the growth of modes for all $\alpha \in \mathbb{R}$ need to be considered at any given Re. Then, Re_c is the choice of Reynolds number for which the most unstable mode has a growth-rate of zero. In terms of the eigenvalue solver, the growth-rates can be calculated for a selection of α and the peak of this curve represents the most unstable mode. In terms of the simulations, the disturbance maximum will display temporal growth (or decay) equal to the growth of the most unstable (or least stable) mode.

While the asymptotically approached growth-rate cannot be deduced from the simulations, it is not necessarily more convenient to deduce Re_c from the eigenvalue problem. Both approaches are computationally expensive but the benefit of utilising the simulations is that the least stable (or most unstable) mode is found automatically, without having to search across a range of α. It will be seen that this is a useful feature for this particular flow.

Tracing the critical Reynolds number

Let $(a_p, b_p) = (1, 0)$, then for every choice of p and δ there will exist a critical Reynolds number Re_c, below which all disturbances are stable. It has already been shown by Thomas *et al.* (2015) that $\delta = \mathcal{O}(0.01)$ can result in Re_c less than half that of the monochromatic Stokes layer, bringing the value in line with that observed in experiments. Due to the simplicity of the noise model used, it is impossible to select a value of p that will allow a direct comparison with experiments so a selection of values will be chosen and the variation of Re_c with δ will be explored for each of these cases.

It has been shown that some disturbances take longer than ten periods to settle to a value near that predicted asymptotically. However, after this length of time the measured growth-rate is usually a reasonably good approximation. Furthermore, it has already been observed that for some values of Re there are several peaks in the growth-rate curve and so the dominant mode may move around in wavenumber-space (this consideration will be discussed in more detail later). This and the speed with which these simula-

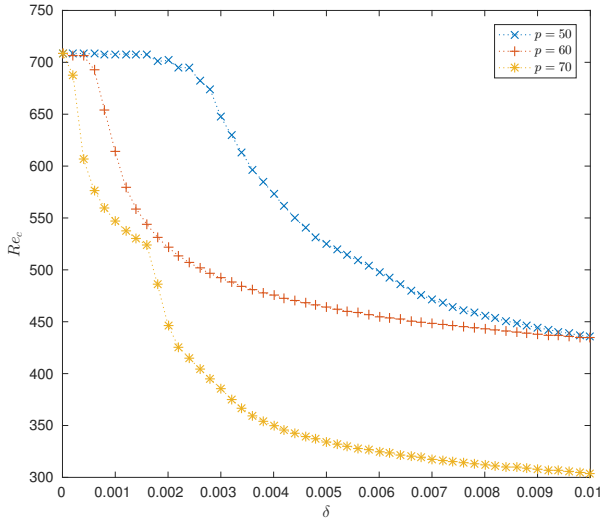

Figure 6.21: The effect of δ on Re_c for $p = 50$, $p = 60$ and $p = 70$. The value of Re_c was approximated from the simulations by measuring the growth rates at the end of ten periods of wall oscillation and performing a bisection method to find the Re for which the growth rate is approximately zero. In all three cases there is a dramatic reduction in Re_c by the time $\delta = 0.01$, with the greatest reduction being in the case $p = 70$.

tions can be run using parallel computing means that simulation better lends itself to a parametric investigation into Re_c than the Floquet method.

The values of Re_c were found to two decimal places. This was generally sufficient to give a reasonable estimate of the zero growth-rate. The values were found by a bisection method where the temporal growth-rate of the disturbance maximum was found for both a stable and unstable choice of Re, and the neutrally stable point is predicted linearly between them. The growth-rate at this Re is then measured and the process repeated. Several predicted values of Re_c were then compared with the Floquet method and were found to be good approximations of neutral conditions.

Shown in Figure 6.21 is the result of this investigation for $p = 50, 60, 70$ showing that there is a dramatic destabilisation in all three cases. In all three cases, an increase in δ is associated with a decrease in Re_c. According to Figure 6.21 a larger value of p also corresponds to a lower value of Re_c, but this observation should be viewed with caution, particularly since it is possible that a fairly modest increase in δ could result in the curves for $p = 50$ and $p = 60$ crossing one another. More insight into the variation of growth-rates with p will be provided later.

Consistently for all three values of p, the Re_c curves appear to be flattening out for

larger δ. This suggests that further increases in δ would have a comparatively small effect on the critical Reynolds number.

Switch in dominance of two modes

In Figure 6.21 there is a *kink* in the Re_c curve for $p = 70$ at $\delta = 0.0016$. This feature will now be explored further.

Given the manner in which these curves are found from the simulations and thus only provide approximations to Re_c, it is important to rule out the possibility that this kink is spurious. One of the reasons for utilising the simulations over Floquet theory was that the disturbance maximum will always grow in time as the most unstable mode, whereas any efficient method of tracing Re_c from the eigenvalue solver will involve following a particular mode (similar to the arclength continuation methods of Section 1.3).

It is anticipated that if there are two or more distinct modes that can become unstable, the point at which they swap dominance could manifest like this kink. It has already been noted that in the case of high-level noise there are two distinct modes at different wavenumbers with different values of μ_i.

The possibility that the kink in Figure 6.21 is a manifestation of one mode becoming dominant over another can be explored by investigating the behaviour of disturbances on each side of the kink, just above the Re_c curve to ensure disturbances are unstable.

Consider the two cases $\delta = 0.0014$, $Re = 535$ and $\delta = 0.0018$, $Re = 490$. In Figure 6.22 the growth-rates of a selection of modes are shown for $0 \leq \alpha \leq 0.5$ in both of these cases (found from the Floquet eigenvalue problem). It is immediately apparent in Figure 6.22a that the growth-rate curve displays two peaks for distinct wavenumbers. In Figure 6.22b the previously larger peak has virtually vanished. This figure suggests that the kink in Figure 6.21 is a manifestation of a change in dominant mode from that at the larger wavenumber ~ 0.4 to that at the lower wavenumber ~ 0.3.

The values of μ_i are also plotted against α in Figure 6.22, revealing that the locations of the peaks in μ_r correspond to distinct values of μ_i, which is consistent with what was observed for the case of high-level noise. That is, the peak at the lower wavenumber corresponds to $\mu_i \sim 1/2$ (near subharmonic) and the peak at the larger wavenumber corresponds to $\mu_i \sim 0$ (near harmonic).

For the two cases shown here, an increase in δ has resulted in the near subharmonic

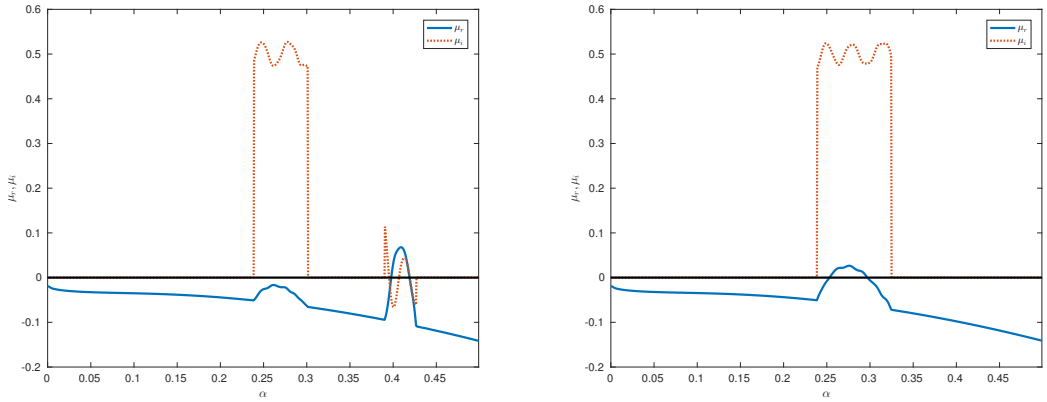

(a) *(b)*

Figure 6.22: In (a) the real and imaginary parts of μ are shown for a range of α with fixed $Re = 535$, $\delta = 0.0014$ and $p = 70$. In (b) this is shown for $Re = 490$ and $\delta = 0.0018$. The peaks in μ_r support the behaviour observed in the simulations, and it is revealed that in both cases the peaks found at $\alpha \sim 0.27$ correspond to $\mu_i \sim 1/2$, whereas the peak at larger α in (a) corresponds to $\mu_i \sim 0$.

behaviour becoming dominant over the near harmonic behaviour. However, this is only the case near the Re_c curve since the critical Reynolds number for the harmonic peak would presumably be described by a fairly smooth continuation of the first part of this curve, before the kink (this would be close to the curve for $p = 60$).

The kink observed in Figure 6.21 is consistent with being a manifestation of a switch in dominance of two modes. There is no evidence of such a switch for $p = 50$ or $p = 60$, though it is possible that such a feature occurs outside of the range of δ shown in Figure 6.21. It has already been observed that the disturbance at $Re = 500$ when $p = 60$ and $\delta = 0.01$ is dominated by the harmonic modes so if such a kink occurs when $p = 60$ it most likely does so outside of the range of this plot.

6.3.3 Noise frequency, p

Aside from the comparison made between the even case of $p = 60$ against the odd cases of $p = 59, 61$, only the three choices of $p = 50, 60, 70$ have been explored. While the problem is less sensitive to the choice of p than to the noise level δ, the evidence suggests that the value of p can have a significant effect on the disturbance evolution.

A thorough investigation into the sensitivity of disturbances to this parameter would be time consuming and computationally expensive. However, it is necessary to ensure that the features discussed above are consistent for a range of p. For this reason, a selec-

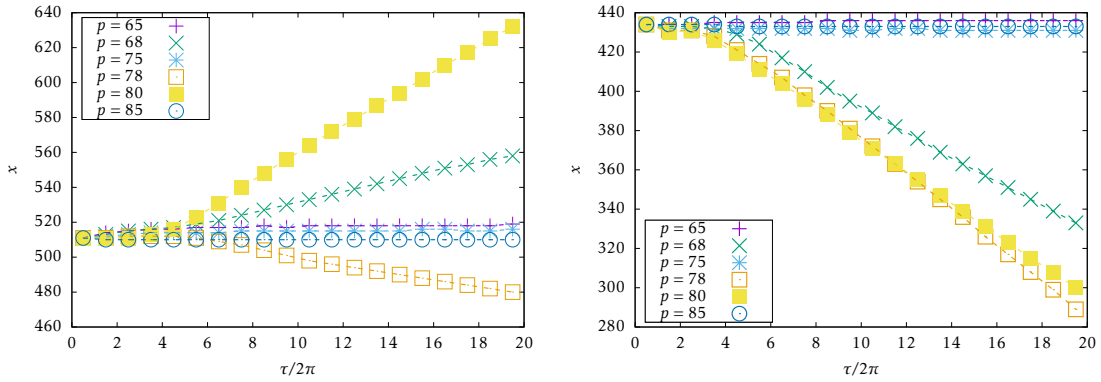

Figure 6.23: The location of the disturbance maximum is plotted against time for a range of p. In (a) the other parameters are fixed at $Re = 700$, $\delta = 0.001$ and $(a_p, b_p) = (1, 0)$. In (b) these parameters are fixed at $Re = 600$, $\delta = 0.005$ and $(a_p, b_p) = (1, 0)$. In both cases, the disturbance maximum remains in approximately the same place when p is odd, near $x = 510$ in (a) and near $x = 425$ in (b), but moves away from this location when p is even.

tion of p will be considered (with an equal number of even and odd values and excluding the values already explored) and simulations will be run in these cases for $\delta = 0.001$, $Re = 700$ and $\delta = 0.005$, $Re = 600$.

First, note that in all these cases the disturbance maximum lies within the structures of the disturbance rather than being immediately convected away (not shown). The location of said maximum will be treated as being representative of the general movement of the disturbance. In Figure 6.23 the location of the disturbance maximum is plotted against time, confirming that the disturbance displays convective properties when p is even but not when p is odd. This is consistent with the behaviour discussed in Section 6.2.

It is interesting to note from observing Figure 6.15 and Figure 6.23 is that the direction in which the disturbance moves (for even p) is not the same for all cases considered. In fact, there is little evidence that this direction can easily be predicted.

A brief investigation into the effect of p on the growth of the disturbance maximum was carried out. The temporal growth-rate of each disturbance maximum was calculated from the time-history of the simulations by (4.3.14) for $p = 55, 56, 57, ..., 85$, since this process is computationally much faster than plotting the growth-rate curves at a suitable resolution. The growth-rate is then plotted against p in several cases in Figure 6.24.

In Figure 6.24a, the Reynolds number is fixed at $Re = 500$ and μ_r is plotted against

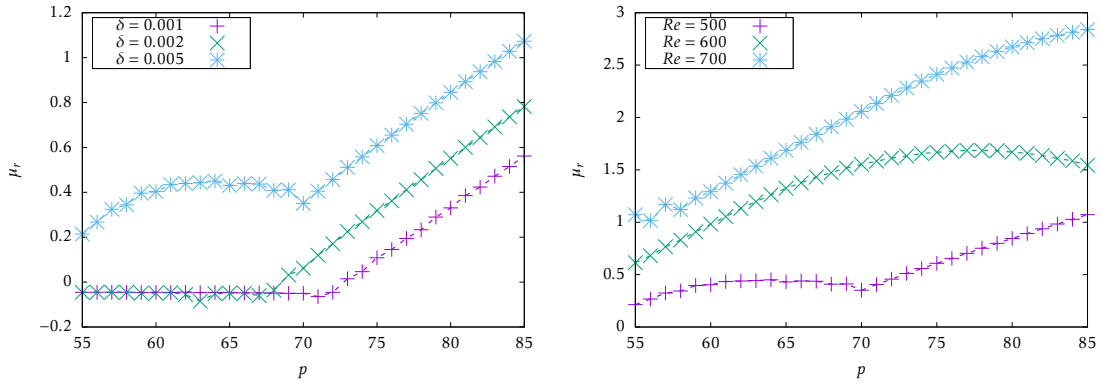

(a) (b)

Figure 6.24: The temporal growth-rate μ_r of the disturbance maximum is measured from the simulation time-history using (4.3.14)*. In (a), $Re = 500$ is fixed and three choices of δ are explored. In (b), $\delta = 0.005$ is fixed and three choices of Re are explored. In each case the variation of μ_r with p is shown.*

p for $\delta = 0.001, 0.002, 0.005$. In Figure 6.24b, the level of noise is fixed at $\delta = 0.005$ and μ_r is plotted against p for $Re = 500, 600, 700$. The case $\delta = 0.005$, $Re = 500$ is plotted in both figures for reference. Note that for all Re considered the pure Stokes layer is asymptotically stable, meaning that $\mu_r > 0$ in Figure 6.24 indicates destabilisation.

In all cases shown in Figure 6.24, an increase in δ or Re results in an increase in the growth of the disturbance maximum. However, the value of p corresponding to the peak growth-rate is not at all consistent. When $Re = 500$, it is not until p reaches ~ 70 that there is significant destabilisation. However, for larger Re, there are unstable disturbances for all p considered, with a relatively steep variation.

For $Re = 600$ there is a local maximum of μ_r when $p \sim 78$. The reducing gradient for $Re = 700$ suggests that if there is a local maximum in this case it corresponds to p larger than 85. There is also a local maximum around $p \sim 63$ in the case $\delta = 0.005$ and $Re = 500$.

Finally, observe that in all five cases shown, the problem is relatively insensitive to a small change in p, though a large change in p can have a significant effect on the growth-rate and spatial/temporal characteristics of a disturbance.

Summary

In this chapter, a simple model of noise was incorporated into the basic state to crudely replicate that reported in experiments. The results presented here broadly agree with those of Thomas *et al.* (2015): noise can have a destabilising effect on disturbances. The

spatial/temporal features of impulse responses in several cases were explored, revealing that under a sufficient level of noise the family-tree structure is disrupted and in many cases the multiple-wavepacket structure observed for the pure Stokes layer is replaced with a single-wavepacket response.

The focus of the current work has been on the temporal behaviour of the disturbance at fixed streamwise locations through the application of the cusp map method, and it has been shown that when p is odd the disturbance exhibits greatest temporal growth at a fixed streamwise location, $x/\tau = 0$. It has also been shown that when p is even, a ray exists that undergoes greater temporal growth than at any fixed streamwise location, resulting in a convection of the impulse response. It is noted that this effect appears to intensify with larger δ.

Aside from these convective properties, the structural features of the disturbances were found to be relatively insensitive to the choice of p in the limited cases considered in this chapter, though the growth of a disturbance can change significantly with p.

The destabilisation of the flow with increasing δ was documented when $p = 50, 60, 70$, suggesting that the variation of Re_c with δ becomes less pronounced for larger δ. The dependence of the problem on the parameter p was also briefly explored. Due to time restraints a more thorough investigation into the p-dependence of the problem is considered outside of the scope of this work.

It was also confirmed in several cases that the phase of the noise, dictated by the parameter pair (a_p, b_p), had a limited effect on the stability of the flow and the qualitative features of the disturbance.

Future work and conclusions

The main focus of this work has been to compile and extend the existing work on the stability of Stokes layers. In particular, the application of Briggs' method (Briggs, 1964) to show that the semi-infinite Stokes layer is subject to absolute instability has been a constructive contribution to this body of work. In general, the investigation has centred around the comparison between the linear stability analysis and simulations of disturbance evolution to develop a deeper understanding of the features and structures associated with this flow.

Future work

Due to a limit in resources and time there is a significant amount of work on this subject still to be explored. In this section, suggestions for future work (alluded to throughout) will be compiled in some detail.

Three-dimensional boundary layers

While the linear stability of three-dimensional boundary layers (unaligned composite flow) was explored in Section 1.5, no further use of these results is made in the present study. It would be interesting to explore the stability of this family of flows.

In particular, the stability of a mean flow modified by an oscillation in the direction perpendicular to the main flow would be of interest since it has been shown in some cases that in turbulent boundary layers a spanwise oscillation can reduce drag (Choi, 2005; Quadrio & Ricco, 2010; Touber & Leschziner, 2012; Blesbois *et al.* , 2013). The present work suggests that the stability of such a flow would be dictated by the stability of a turbulent boundary layer with streamwise oscillation. Some insight into the behaviour of such a flow could be provided by considering the simpler, laminar model of, say, the

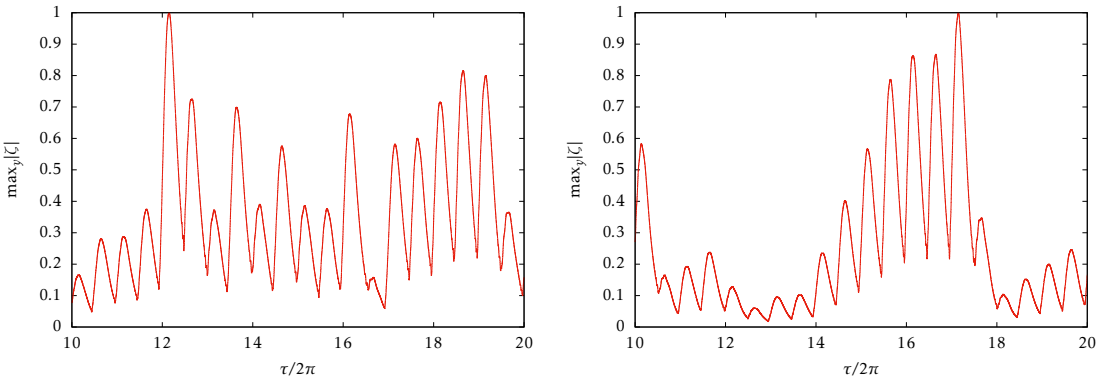

Figure 6.25: The single-wavenumber simulation is run in the cases: $Re = 1224$, $\alpha = 0.52$ in (a); $Re = 1300$, $\alpha = 0.55$ in (b). In each case the absolute value of the vorticity ζ is taken and the maximum value over the wall-normal direction is plotted. There is no clear indication of growth or decay in either case.

Blasius boundary layer modified by a perpendicular Stokes layer. While it would be informative to perform such an investigation regardless, there is some evidence to suggest that a linear model is capable of reproducing the turbulent drag reduction (Duque-Daza *et al.* , 2012).

Large wavenumbers

The linear stability analysis described in Chapter 1 fails to pick up some unexpected behaviour for larger values of α. This issue is demonstrated in the work of Kong & Luo (2016) where the stability of disturbances with α in this region is approximated in an ad hoc manner. The simulations of the present study are broadly in agreement with regards to the evolution of disturbances with these larger wavenumbers: even for large times the growth/decay appears random.

Presented in Figure 6.25 are the time-histories of the maximum vorticity (over y) and there is no clear growth or decay in either of the cases shown. This is consistent with the behaviour observed by Kong & Luo (2016). It is less clear from the 10-period snapshots whether some more regular behaviour is approached for longer times. It would be interesting to deduce some means of quantifying the asymptotic behaviour in these cases, be it through the Floquet method, frozen flow analysis or some other approach. Interestingly, when larger wavenumbers were incorporated into the impulse response, this had virtually no effect on the disturbance evolution.

The ability to extend the neutral curves to larger α would mean a more thorough investigation of the stability of this flow could be conducted, though there is currently no clear explanation for why this is not possible. It would be particularly interesting if there was evidence of the neutral curve turning and closing around itself, i.e. if there is a value of α for which an increase in Re first results in a transition from stability to instability and then a further increase in Re makes the disturbance once again stable. Such behaviour would be expected since it was shown by Hall (1978) that the Stokes layer is linearly stable in the limit $Re \to \infty$.

Nonlinearity

One of the main drawbacks of the Floquet method is that due to the large instantaneous growth-rates within each period of oscillation it is possible that nonlinearity can set in before the first period has even completed. Therefore, since the linear problem does not experience the periodicity of the flow, the Floquet assumption breaks down. While a nonlinear stability analysis is a challenging prospect, it is relatively straightforward (albeit more computationally expensive) to include the effects of nonlinearity in the disturbance simulations.

Consider the nondimensional Navier–Stokes equations with the incompressibility condition. The process implemented in Section 2.1 to deduce the equations governing disturbance evolution (2.1.7) can be applied, but with the nonlinear terms retained. This results in the modified governing equations

$$\frac{1}{Re}\frac{\partial \zeta}{\partial \tau} + U_S\frac{\partial \zeta}{\partial x} + U_S''v + \frac{\partial (u\zeta)}{\partial x} + \frac{\partial (v\zeta)}{\partial y} = \frac{1}{2Re}\left(\frac{\partial^2}{\partial x^2} + \frac{\partial^2}{\partial y^2}\right)\zeta, \tag{6.3.2a}$$

$$\left(\frac{\partial^2}{\partial x^2} + \frac{\partial^2}{\partial y^2}\right)v = -\frac{\partial \zeta}{\partial x}, \tag{6.3.2b}$$

$$u = -\int_y^\infty \left(\zeta + \frac{\partial v}{\partial x}\right)\mathrm{d}y. \tag{6.3.2c}$$

In the finite-difference formulation, the additional nonlinear terms can be calculated at each time-step and incorporated into the solver for the vorticity transport equation (6.3.2a) within the explicit terms E^n (2.4.12). In the spectral formulation this is more difficult since the individual Fourier modes no longer evolve independently. This means that every time-step involves a transformation into physical space, so that the nonlinear terms can be calculated, and then a transformation back into Fourier space to continue

the simulation as before. This makes the spectral method significantly slower since the Fourier transforms are computationally expensive. Whichever approach is taken, a much finer temporal and spatial resolution is required for nonlinear problems. This further increases computational expense and run-time.

In the nonlinear regime, Squire's theorem no longer applies, so a fully nonlinear simulation would have to be three-dimensional. In this case the governing equations can be deduced in essentially the same way. This again compounds the complexity of the problem so it would be logical to begin a nonlinear investigation with the two-dimensional problem (6.3.2).

Such an investigation would be mainly concerned with disturbances that are linearly highly damped. This would mean that nonlinear effects are fairly weak, though presumably still important. Of particular interest would be whether the family-tree structure is maintained, as this would provide a great deal of insight into experimental results. The two-dimensional nonlinear problem was considered in Thomas *et al.* (2014) but due to time restraints the current study did not investigate this extension.

The study of the stability of pulsatile flow in a channel is extended to the nonlinear regime by Pier & Schmid (2017). Two regimes are reported that display distinct behaviours. In the *cruising* regime, once nonlinear effects become important, the nonlinear behaviour dominates the disturbance evolution for all subsequent times. In the *ballistic* regime, nonlinear effects are important during the times that the eigenvector displays significant amplitude and linear effects dominate when the amplitude is small. That is, the disturbance passes in and out of the nonlinear regime within each period of wall motion. As the relative magnitude of the periodic flow component increases, it is noted that the cruising regime ceases to be important. This suggests that the pure Stokes layer may only exhibit the ballistic regime. It would be of great interest to explore whether this is indeed the case.

Transient, non-modal growth

It was noted when discussing the simulation results in Chapter 3 and Chapter 6 that there is a length of time over which the impulse settles down before beginning to approach the asymptotic behaviour. It may be of interest to explore this behaviour in more detail.

It is common for disturbances to undergo growth during this time, even in the cases

where they are asymptotically stable. In general, this growth is not of exponential form but rather it is algebraic and is thus referred to as non-modal. This behaviour is a direct result of nonorthogonal eigenvectors, meaning that the resultant of two exponentially decaying modes can exhibit growth for a short time (Schmid, 2007).

The investigation of the transient behaviour of disturbances in the Stokes layer could provide insight into the experimentally observed behaviour since the large instantaneous growth rates associated with disturbances in this flow combined with transient non-modal growth could cause early onset of nonlinear saturation. A consideration of transient effects would therefore be an informative component of any further studies of this flow. There has already been some work in this area (Hack & Zaki, 2015).

Absolute instabilities in other temporally periodic flows

One of the main motivators for the study of the Stokes layer is as a paradigm example through which methods can be developed that are applicable to periodic flows in general. For this reason, it would be interesting to see the present work extended to other examples of periodic flows.

A particularly relevant family of flows to the present work is that in which the oscillatory flow is modified by a mean flow. In the special case of a purely oscillatory flow there would be only absolute instability and in the limiting case of a purely steady unidirectional flow there would be only convective instability. It would be interesting to investigate the transition from one to the other and whether the mean flow could be used to hold off the onset of absolute instability.

Such an investigation would be conducted over a large parameter space and so is beyond the scope of this work. It is also interesting to note that the case in which the mean flow is at some angle to the oscillatory flow could easily be investigated as a straightforward extension, based on the transform discussed in Section 1.5.

The Stokes layer subject to noise

Due, in part, to the large parameter space associated with the noisy Stokes layer explored in Chapter 6, only a limited investigation could take place. Several possible extensions of the work presented here remain.

A more thorough investigation

The focus of the present study has been on the destabilising effect of δ and an in-depth investigation into the spatial/temporal behaviour of three cases, including application of the cusp map method. It would be of great interest to see the same level of depth extended to more cases.

The possibility that the flow is subject to convective instabilities, which temporally decay at every spatial location, was noted. A future investigation could explore this possibility in detail. Additionally, a more thorough pinch-point analysis could be explored, with possible aims being the prediction of the ray along which the disturbance is convected when p is even and a detailed confirmation of whether the cusps presented here do indeed satisfy the collision criteria.

It would also be interesting to explore a noise model that is not high-frequency or low-amplitude. Taking $p \sim 10$ and $\delta \sim 1$ would transform the problem from one with a fundamental oscillation modified in some way to a superposition of two oscillations of similar amplitude with related frequencies. It is unclear what effect this could have on disturbance evolution.

Finally, the noise model could be implemented when investigating the stability of composite flows (as described in Chapter 1). This would allow the impulse response in such flows to be modelled in a more realistic manner for better comparison against experiments.

Random noise simulations

In experiments, the form the noise takes is generally going to be much more complicated than the model used here. While it would be computationally demanding to reformulate the Floquet eigenvalue problem for a more random noise model (since the presence of more frequencies results in more nonzero entries in the matrix), it would be relatively straightforward to implement a more complex model in the linear simulations.

The wall motion could be given the form

$$U_w(\tau) = \cos(\tau) + \delta \sum_{p=0}^{P} \left[a_p \cos(p\tau) \pm \sqrt{1 - a_p^2} \sin(p\tau) \right] \tag{6.3.3}$$

which would generate a basic state

$$U_B(y,\tau) = \mathrm{e}^{-y}\cos(\tau - y) + \delta \sum_{p=0}^{P} \mathrm{e}^{-\sqrt{p}u}\left[a_p \cos(p\tau - \sqrt{p}y) \pm \sqrt{1-a_p^2}\sin(p\tau - \sqrt{p}y)\right] \quad (6.3.4)$$

The incorporation of multiple different frequencies would make the noise model much more realistic and it would be possible to generate the values of a_p randomly at the start of the simulation to determine whether the precise form of the noise has a significant effect on the stability.

It would also be interesting to introduce a noise model that breaks the periodicity of the problem. Again, this would be more realistic as there is no reason the mechanically generated noise in experiments would be identical each period. The linear stability analysis in this case would be possible if a subharmonic noise was introduced as this would retain the periodicity, but the period of the flow would be a multiple of the period of the fundamental oscillation. Alternatively, the periodicity could be properly broken with relatively little effort in the simulations. For instance, the values of a_p could be generated randomly as each period completes (with care taken to ensure continuity) to generate a highly random model of noise.

Carefully constructed experiments

While the destabilisation of the Stokes layer through the introduction of noise is consistent with the experimentally observed behaviour in principle, the discrepancy between the noise model and the real noise means that no direct comparisons can be made. Even making changes to the noise model to make it more realistic, such as those discussed above, would not give directly comparable results as the noise in experiments is incredibly difficult to measure.

It may be interesting for an experiment to be constructed in which the noise is purposely generated to have a form easily implemented in a linear stability analysis. This would provide a means of validating the linear stability analysis against experiments which, if successful, would mean that the Floquet approach is an appropriate means of modelling oscillatory flows.

Conclusions and final remarks

In Chapter 1, the current theoretical work on the linear stability of periodic flows (and in particular Stokes layers) is compiled in a manner akin to the work on steady flows, such as in Schmid & Henningson (2001). This proceeds from the derivation of linear disturbance equations (from the Navier–Stokes equations) to the application of Squire's theorem in the unsteady case, reducing the stability problem to the eigenvalue problem associated with a single equation (analogous to the Orr–Sommerfeld equation). The numerical methods used to solve this eigenvalue problem are also discussed.

In addition, the work was extended to the consideration of three-dimensional boundary layers. Influenced by Blennerhassett & Bassom (2007), it was found that an argument similar to that required for Squire's theorem held in such cases. Interest was restricted to the case of a mean flow modified by oscillation at some angle to it and it was shown that any case in which the flows are not aligned can be reduced to an equivalent aligned problem with lower Reynolds numbers. The particular presentation of Squire's theorem for unsteady flows made the analogy between these transforms clear. This relationship between the two-dimensional and three-dimensional boundary layers could prove useful in future studies.

The reproduction in Chapter 1 of existing results from Blennerhassett & Bassom (2002, 2006) and Thomas *et al.* (2011) not only serves to validate the existing work but also provides an independent verification of their results. This is particularly relevant since the use of Floquet theory to study the stability of periodic flows is a relatively recent addition to the field and remains novel. This makes the present work significant as one of only a few successful attempts at utilising this approach.

Some important results concerning the semi-infinite Stokes layer were the determination of the critical Reynolds number of $Re_c \sim 707.8$, in agreement with Blennerhassett & Bassom (2002), and a discussion on the eigenfunction structure associated with Floquet modes. The fingers protruding from the growth-rate curves for fixed Re and neutral curves in the (α, Re)-plane were documented and discussed. These features were revisited in Chapter 5 where their physical significance became apparent.

The finite-difference method described in Chapter 2 uses an almost identical formulation to Togneri (2011), further developed by Duval (2012), and is adapted from the same source code. This is due, mainly, to the significant amount of work required to

independently develop a code that elegantly deals with this computationally demanding problem. The spectral method used in the remainder of this work differs in the treatment of the streamwise co-ordinate and allows for the code to be naturally adapted for parallel computing, drastically reducing running times.

In the spectral method, the streamwise variation of the excitation is incorporated through a transformation to Fourier space. The evolution of each Fourier component of the disturbance (i.e. each choice of wavenumber α) is independent of the others and so this problem lends itself to parallelisation. This approach was found to have significantly greater computational speed than the finite-difference formulation. It is this spectral formulation that distinguishes the present approach to linear simulation from the numerical approach of Togneri (2011) on which it is based.

In Chapter 3, the methods of linear simulation allow for an investigation into the spatial/temporal structure of disturbances generated by impulsive forcing. The localisation of the forcing in space is not permitted by the single wavenumber approach of the Floquet method since the underlying assumption is spatial homogeneity. However, as the impulsive forcing passes and the spatial homogeneity returns, the response becomes a superposition of all the wavenumbers seeded in the initial excitation.

The running-time benefits of the spectral method allowed for the behaviour to be documented for an unprecedented twenty periods of wall motion when utilising the computational resources of the Raven cluster (courtesy of ARCCA). Having reproduced the family-tree structure reported in Thomas *et al.* (2014) in the first three periods, it was observed that as time progresses this structure evolves into a pattern of staggered wavepackets that spread out from the point of excitation in a dispersive manner (with the disturbance maximum consistently on one side of the disturbance). It was illustrated that in the case of an unstable disturbance this structure appeared to be associated with subharmonic temporal growth at every spatial location, i.e. absolute instability. Furthermore, it was shown that even for near-critical values of Re, the temporal growth-rate of the disturbance at several fixed streamwise locations approaches a value similar to that of the disturbance maximum.

Throughout this chapter, comparison was made between the temporal evolution of the disturbance maximum and the asymptotic behaviour predicted by Floquet theory. The agreement of these growth-rates was demonstrated and the Fourier spectrum of the

impulse response was explored, indicating that as time progresses the wavenumber expected to correspond to the temporal growth of the disturbance maximum becomes increasingly dominant.

In Chapter 4, the leading-order behaviour of the solution integral was determined by two methods. Briggs' method (Briggs, 1964) was found to be appropriate for periodic flows with some minor adjustments, as was the method of steepest-descent (Huerre, 2002).

The resulting conditions agree with those reported by Brevdo & Bridges (1997) except that more detail has been provided in the asymptotic evaluation through adaptation of the methods utilised in the steady case (Lingwood, 1997). Through this framework it was straightforward to clearly define convective and absolute instability as well as deducing an appropriate means of measuring, from the simulation results, the temporal growth associated with both the disturbance maximum and the disturbance at any fixed streamwise location. The main purpose of this detailed discussion was to ensure that the application to the semi-infinite Stokes layer is appropriate and well informed.

Described in Chapter 4 is the pinch-point condition on the dispersion relation. In summary, this condition is the collision of two α-roots of $D(\alpha, \mu)$ as μ undergoes a horizontal movement across the original integration contour L. Such a collision contributes to the asymptotic temporal behaviour of a disturbance at every streamwise location provided these α-roots originate in opposite half-planes (this is called the collision criteria). It was observed that this results in a saddle point of the dispersion relation in α which must be of pinch-type (i.e. with branches originating in opposite half-planes).

In general, the location of such saddle points is explored by mapping a straight grid in the complex μ-plane to the complex α-plane through $D(\alpha, \mu) = 0$. Due to the computational infeasibility of this approach, it was deemed more appropriate for the present study to instead perform the mapping of a straight grid in the α-plane to the μ-plane. In this case, the locations of cusps in the μ-plane indicate a saddle point of the dispersion relation. It then remains to ensure that any cusp corresponds to a saddle point of pinch-type.

Perhaps the main results of this work are contained within Chapter 5. First, it was observed that the antiperiodicity of the Stokes layer can be used to indicate that the existence of collisions that satisfy the collision criteria must occur for $\alpha \in \mathbb{R}$ and $\mu =$

$\mu_r + ik/2$ (with $k \in \mathbb{Z}$).

The eigenvalue solver developed in Chapter 1 was then adapted for the locating of cusps in the complex μ-plane and it was shown that those found satisfied the conditions predicted by the symmetry analysis. The cusps also had an even spacing in α and alternated between those that contributed a harmonic temporal variation and those that contributed a subharmonic temporal variation. Intriguingly, the harmonic cusps were located at the tips of the protruding fingers while the subharmonic cusps were located halfway between each of these.

The features of the disturbance evolution discussed in Chapter 3 were then revisited to illustrate that both methods are in good agreement. In particular, it was found that a simple function constructed from the superposition of six modes (with the characteristics of the cusps) was capable of displaying behaviour similar to the family-tree structure of the Stokes layer. This model was able to predict the streamwise separation of wavepackets from the separation of the cusps in α. Furthermore, through the summation of alternating harmonic and subharmonic modes, the staggered wavepacket structure was reproduced.

The observation reported in Thomas *et al.* (2015) that the introduction of noise to the wall motion is associated with a destabilisation of the flow is supported in Chapter 6. It was found that for all the cases considered an increase in noise level (δ) past a certain point resulted in a dramatic reduction of the critical Reynolds number. In some cases (in particular when $p = 70$) this could result in $Re_c \sim 300$ when $\delta = 0.01$, which is broadly in agreement with experiments. For smaller values of δ, the critical Reynolds number remained practically unchanged. There were no cases found for which an increase in δ noticeably stabilised the flow.

It was also shown that while modest levels of noise leave many features of the disturbance evolution unchanged, increasing the noise level can result in a spatial/temporal development completely unlike the family-tree structure observed in the pure Stokes layer. In the case for which the noise level is large enough to have significantly altered this behaviour, the multiple-wavepacket response is replaced with a single-wavepacket response, the disturbance maximum is confined to lie within the body of the disturbance, and a harmonic temporal behaviour is observed at every spatial location (in addition to the destabilisation). Two other cases were explored that showed some of the gradual

change that presumably leads to this new behaviour as δ is increased.

This chapter also included the application of the cusp map method to provide insight into the effect of noise on the dispersion relation and the effect this has on the disturbance evolution. It was seen that while this flow is subject to the same symmetries as the pure Stokes layer when p is odd, this symmetry breaks down when p is even. As a result of this symmetry breaking, there exists some spatial/temporal ray over which greater temporal growth is observed than at any fixed spatial location when p is even. When p is odd (as in the pure Stokes layer), no such ray existed. This proposition was demonstrated in several cases by showing that the disturbance undergoes convection along such a ray when p is even but not when p is odd. For all of the cases explored here the disturbance grows with time at every spatial location, so all of the disturbances are absolutely unstable even when they exhibit some convective properties.

Overall, the linear development of disturbances in the semi-infinite Stokes layer were explored through a Floquet stability analysis and a spectral (in the streamwise direction) method of linear simulation. These two approaches were compared in some detail, and the application of Briggs' method ensured that this comparison was as rigorous as appropriate. Some previous results were reproduced and insight was provided into some of the more intriguing features such as the wavepacket spacing and the protrusion of fingers from the growth-rate curves. Of great significance was the provision of evidence that the semi-infinite Stokes layer is subject to absolute instability.

The same methods applied to the semi-infinite Stokes layer were then applied to a modification that incorporated a simple model of noise. The effects that increasingly large levels of noise can have on the disturbance evolution were documented. It was shown that increasing the level of noise could be associated with a destabilisation of the flow as well as a breakdown of the spatial/temporal structures that characterise disturbance evolution in the pure Stokes layer.

Appendices

Appendix A

The Ginzburg–Landau equation with periodic coefficients

Introduction

The Ginzburg–Landau equation is one of the simplest PDEs that incorporates convection, diffusion and growth/decay (the features associated with hydrodynamic stability) and as such is an interesting model problem to provide insight into the behaviour of more complicated systems. This section will be concerned with the study of the Ginzburg–Landau equation with periodic coefficients

$$\frac{\partial u}{\partial t} = \frac{\partial^2 u}{\partial x^2} + a(t)\frac{\partial u}{\partial x} + b(t)u, \quad \text{for} \quad t > 0 \quad \text{and} \quad -\infty < x < \infty, \tag{A.1}$$

where it will be assumed that a and b are T-periodic so that Floquet theory can be applied. This problem lends itself well to the development of the tools required to locate the threshold between convective and absolute instability for periodic flows, as detailed in Brevdo & Bridges (1997), because of the comparative simplicity and the existence of an exact solution.

Much of the work presented here is a reproduction of that discussed in Brevdo & Bridges (1997). Furthermore, the conditions for absolute instability are the same as those discussed in Chapter 4, so will not be derived again here.

The term *pointwise* will be used throughout to refer to the temporal growth at all fixed spatial locations.

Analytic solution with global and pointwise growth-rates

This section follows exactly from the work of Brevdo & Bridges (1997). Consider the initial condition

$$u(x,0) = \mathrm{e}^{-\frac{px^2}{4}}, \tag{A.2}$$

for $p > 0$. The exact solution of (A.1) subject to this condition can be written as

$$u(x,t) = \frac{\mathrm{e}^{\beta(t)}}{\sqrt{1+pt}} \mathrm{e}^{\left(-\frac{p(x+\alpha(t))^2}{4(1+pt)}\right)}, \tag{A.3}$$

where

$$\alpha(t) = \int_0^t a(s)\,\mathrm{d}s, \quad \beta(t) = \int_0^t b(s)\,\mathrm{d}s. \tag{A.4}$$

The solution is subject to growth if the size of the integral across the spatial domain increases with time. Integration of (A.3) leads to

$$\int_{-\infty}^{\infty} u(x,t)\,\mathrm{d}x = \mathrm{e}^{\beta(t)} \int_{-\infty}^{\infty} u_0(x)\,\mathrm{d}x = \mathrm{e}^{t\frac{\beta(t)}{t}} \int_{-\infty}^{\infty} u_0(x)\,\mathrm{d}x, \tag{A.5}$$

so provided the integral of u_0 is finite, growth is observed if $\beta(t)/t$ gives a positive contribution over a period. Hence define

$$\bar{b} = \frac{\beta(T)}{T} = \frac{1}{T}\int_0^T b(s)\,\mathrm{d}s. \tag{A.6}$$

The solution (A.3) is exponentially stable if $\bar{b} < 0$ and exponentially unstable if $\bar{b} > 0$.

To distinguish between absolute and convective instability, consider the solution at some spatial location x_0 and rearrange (A.3) to get

$$u(x_0,t) = \frac{1}{\sqrt{1+pt}} \mathrm{e}^{t\gamma(x_0,t)} \tag{A.7}$$

where

$$\gamma(x_0,t) = \frac{\beta(t)}{t} - \left(\frac{\alpha(t)}{2t}\right)^2 - \frac{x_0\left(x_0+2\alpha(t)\right) - \frac{\alpha^2(t)}{pt}}{4t^2\left(1+\frac{1}{pt}\right)}. \tag{A.8}$$

So, again considering the net contribution over the period of α and β, by defining

$$\bar{a} = \frac{\alpha(T)}{T} = \frac{1}{T}\int_o^T a(s)\,\mathrm{d}s, \tag{A.9}$$

it can be seen that the solution has a pointwise growth-rate of

$$\bar{b} - \frac{\bar{a}^2}{4}. \tag{A.10}$$

The solution is absolutely unstable if $\bar{a}^2 < 4\bar{b}$ (with $\bar{b} > 0$) and convectively unstable if $\bar{a}^2 > 4\bar{b}$ (with $\bar{b} > 0$).

Condition for absolute instability

Let $D(k, \mu)$ denote the dispersion relation associated with (A.1) with wavenumber k and Floquet exponent μ. As has been seen in Chapter 4 and Brevdo & Bridges (1997), there is absolute instability if there is some k_0 and μ_0 that correspond to a saddle point of D, that is

$$D(k_0, \mu_0) = 0, \tag{A.11a}$$

$$\frac{\partial D}{\partial k}(k_0, \mu_0) = 0. \tag{A.11b}$$

It is also necessary that the branches of this saddle point originate in opposite halves of the complex k-plane (this is the collision criteria).

By performing the process detailed in Brevdo & Bridges (1997) and Chapter 4 to the Ginzburg–Landau equation with periodic coefficients, the dispersion relation is found to be

$$D(k, \mu) = -k^2 + ik\bar{a} + \bar{b} - \mu, \tag{A.12}$$

using the same definitions of $\bar{a}$ and $\bar{b}$ from (A.9) and (A.6), respectively. Hence, the roots of the dispersion relation satisfy

$$\mu = \bar{b} - k^2 + ik\bar{a}. \tag{A.13}$$

Instability is present if there exists a single k for which $\mu_r > 0$. According (A.13), the solution is stable for all $\bar{b} \leq 0$. When $\bar{b} > 0$ the solution is unstable for all k in the range $-\sqrt{\bar{b}} < k < \sqrt{\bar{b}}$. Over all k, the most unstable normal mode corresponds to $k = 0$ and in this case there is instability for $\bar{b} > 0$ and stability otherwise.

Absolute instability will be found for a complex pair (k_0, μ_0) that produce a saddle

point in the complex k-plane, so consider

$$D(k_0, \mu_0) = -k_0^2 + ik_0\bar{a} + \bar{b} - \mu_0 = 0, \tag{A.14a}$$

$$\frac{\partial D}{\partial k}(k_0, \mu_0) = -2k_0 + i\bar{a} = 0. \tag{A.14b}$$

This gives

$$k_0 = i\frac{\bar{a}}{2}, \tag{A.15a}$$

$$\mu_0 = \bar{b} - \frac{\bar{a}^2}{4}. \tag{A.15b}$$

Finally, the condition that the colliding k-roots originate from different half-planes (collision criteria) must be checked. An expression for k in terms of μ can be found from rearranging (A.13) to give

$$k_{1,2}(\mu) = \frac{i\bar{a}}{2} \pm \sqrt{-\frac{\bar{a}^2}{4} + \bar{b} - \mu}. \tag{A.16}$$

Fixing $\mu_i = \mathfrak{Im}\{\mu_0\} = 0$ and thus letting $\mu = \mu_r$, the origin of the colliding roots can be found as μ is moved away from μ_0 towards the right-half of the complex plane (and so past the original contour for the Laplace integral). That is, by letting $\mu_r \to \infty$. Taking this limit gives

$$k_1 \to +i\sqrt{\mu_r}, \tag{A.17a}$$

$$k_2 \to -i\sqrt{\mu_r}. \tag{A.17b}$$

Therefore, k_1 and k_2 originated in opposite half-planes so the collision criteria is met, and it can be concluded that (A.1) has absolutely unstable solutions if this collision corresponds to $\mathfrak{Re}\{\mu_0\} > 0$, i.e.

$$\bar{b} - \frac{\bar{a}^2}{4} > 0. \tag{A.18}$$

Note that the conditions for instability and for absolute instability found using this method are in perfect agreement with the conditions found from inspecting the analytic solution. This is not surprising since both methods are exact.

Floquet method

Eigenvalue problem to determine stability

Here, a Floquet eigenvalue problem will be constructed in a manner analogous to that presented in Chapter 1. The numerical methods implemented in Chapter 5 can then be explored for the Ginzburg–Landau equation with periodic coefficients to show that this approach is consistent with the exact methods discussed above.

Consider the equation (A.1). It will now be assumed that the differential operator is 2π-periodic and that the coefficients have the form

$$a(t) = U_a \cos(t) + \bar{a}, \tag{A.19a}$$

$$b(t) = U_b \cos(t) + \bar{b}, \tag{A.19b}$$

for real U_a and U_b. It can be easily verified by taking the integrals over a period and dividing by $T = 2\pi$ that $\bar{a}$ and $\bar{b}$ play the same role in this example as in the general case. It is expected that U_a and U_b will have no effect on the stability of the flow so both will be set to 1.

Assume a Floquet normal-mode of the form

$$u(x,t) = \mathrm{e}^{\mu t} Q(t) \mathrm{e}^{ikx}, \tag{A.20}$$

where Q is 2π-periodic. This results in the equation

$$\frac{\mathrm{d}Q}{\mathrm{d}t} = -k^2 Q + ika(t)Q + b(t)Q - \mu Q. \tag{A.21}$$

The periodicity of Q allows a harmonic decomposition of the form

$$Q(t) = \sum_{n=-\infty}^{n=\infty} q_n \mathrm{e}^{int}. \tag{A.22}$$

Furthermore, the periodic coefficients can be written in exponential form

$$a(t) = \frac{U_a}{2}\left[\mathrm{e}^{it} + \mathrm{e}^{-it}\right] + \bar{a}, \tag{A.23a}$$

$$b(t) = \frac{U_b}{2}\left[\mathrm{e}^{it} + \mathrm{e}^{-it}\right] + \bar{b}. \tag{A.23b}$$

Substitution of these into (A.21) and comparing coefficients of $\exp(int)$ results in an infinite system of equations satisfying, for each n,

$$\frac{1}{2}[U_b + ikU_a]q_{n-1} + [ik\bar{a} + \bar{b} - k^2 - in]q_n + \frac{1}{2}[U_b + ikU_a]q_{n+1} = \mu q_n. \tag{A.24}$$

Truncating this system by assuming $q_n = 0$ for $|n| > N$ and collecting the remaining harmonics into the vector

$$\boldsymbol{\psi} = (q_{-N}, q_{-N+1}, \ldots, q_{N-1}, q_N)^T \tag{A.25}$$

allows for this problem to be written as the eigenvalue problem $\boldsymbol{A}\boldsymbol{\psi} = \mu\boldsymbol{\psi}$ for the tridiagonal matrix defined as

$$\boldsymbol{A} = \begin{pmatrix} C_{-N} & B & 0 & \ldots & 0 \\ B & C_{-N+1} & B & & \vdots \\ 0 & \ddots & \ddots & \ddots & 0 \\ \vdots & & B & C_{N-1} & B \\ 0 & \ldots & 0 & B & C_N \end{pmatrix} \tag{A.26}$$

where

$$B = \frac{1}{2}[U_b + ikU_a], \tag{A.27a}$$

$$C_n = \bar{b} - k^2 + i(k\bar{a} - n). \tag{A.27b}$$

This eigenvalue problem can easily be solved in Matlab with $N = 10$ large enough to make results insensitive to a larger choice of N. For every complex eigenvalue μ, $\mu \pm ik$ will also be an eigenvalue because the k can be absorbed into the n of the harmonic decomposition. The problem will thus be restricted to μ satisfying $0 < \mu_i < 1$. The growth of the solution manifests as μ_r, and this can be plotted against $-1 \leq k \leq 1$ for comparison with the analytic solution.

The numerically calculated growth-rate for this range of k is shown in Figure A.1a. The theory predicts that $\mu_r = \bar{b} - k^2$ and the agreement is excellent. Furthermore, the theory predicts that the maximum growth over all k is equal to $\bar{b}$ (this corresponds to $k = 0$). Figure A.1b also shows excellent agreement between the numerical method and the exact solution.

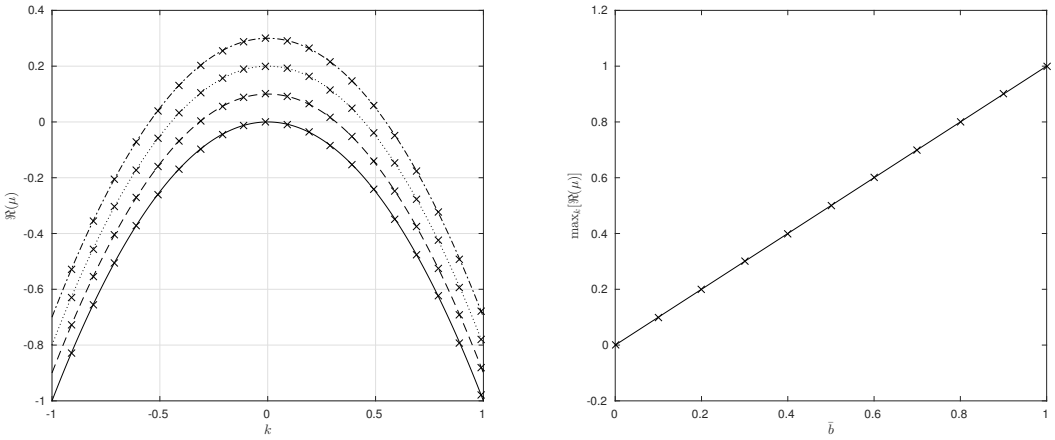

(a) *(b)*

Figure A.1: Growth-rates μ_r for $-1 < k < 1$ with $U_a = U_b = \bar{a} = 1$. (a) shows curves for $\bar{b} = 0, 0.1, 0.2, 0.3$ with $\bar{b} = 0$ on the bottom and $\bar{b}$ increasing as the curves move up the plot. The lines correspond to the exact value predicted by theory and the crosses correspond to the numerically calculated values. (b) shows the maximum growth over all k for several $\bar{b}$. Again, the line corresponds to the exact values and the crosses correspond to numerically calculated values.

In Figure A.1, results are given for fixed U_a, U_b and $\bar{a}$ since the theory suggests that μ_r is independent of these parameters. A brief parametric investigation was carried out to confirm the invariance of results with respect to U_a and U_b and μ_i was found to depend on $\bar{a}$ in the expected way, that is $\mu_i = k\bar{a}$ for each k.

Cusp map method

This approach describes a method by which the nature of an unstable solution can be determined (be it absolute or convective) from the dispersion relation. If the dispersion relation has a saddle point for some k_0, μ_0 that satisfies the collision criteria, then there is a contribution to the temporal asymptotics of the solution at any fixed spatial location. For a numerical approximation to the dispersion relation, as described by the Floquet formulation, such a saddle point can be found by mapping a straight grid in the complex μ-plane to the complex k-plane through roots of the dispersion relation. This involves solving the eigenvalue problem for a given μ to ascertain k.

In general, this is a more computationally demanding method than finding k for a given μ. Instead, a straight grid in the complex k-plane will be mapped through roots of the dispersion relation to the complex μ-plane. It is shown in Kupfer *et al.* (1987) that

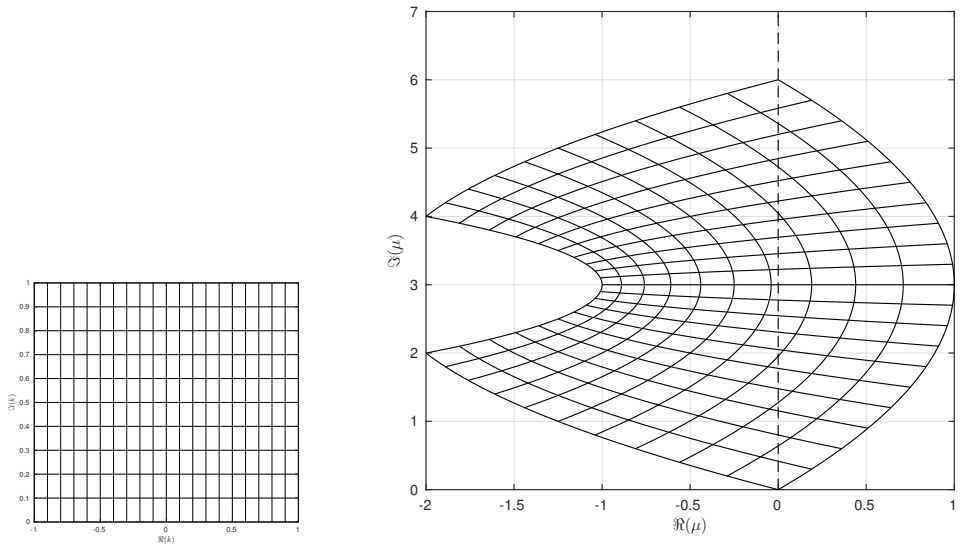

(a) *(b)*

Figure A.2: $\bar{a} = 3$ and $\bar{b} = 1$. The grid in the complex k-plane (a) is mapped by the dispersion relation to the complex μ-plane (b) and no cusp is observed. Solution is absolutely stable.

the existence of a cusp in the μ-plane is equivalent to the existence of a saddle point in the k-plane. The cusp map method was utilised in Chapter 5 for the pure Stokes layer and in Chapter 6 for the noisy Stokes layer.

Presented in Figure A.2 is an example of a mapping from a straight grid in the complex k-plane to a curved shape in the complex μ-plane through the dispersion relation. In this case there is no cusp so the solution is absolutely stable. This is consistent with the theory since in this case $\bar{b} - \bar{a}^2/4 < 0$.

In Figure A.3, the parameters were chosen so that according to the theory the solution would exhibit a pointwise growth of zero (i.e. $\bar{b} - \bar{a}^2/4 = 0$) and it can be seen that this manifests as a cusp for which $\mu_r = 0$. An absolutely unstable example is shown in Figure A.4, in which the cusp is located in the unstable region $\mu_r > 0$. Note that the theoretically predicted pointwise growth-rate corresponds to the location of the real part of the cusp. For the parameters used in Figure A.4, the pointwise growth is $\bar{b} - \bar{a}^2/4 = 0.75$.

The final example, shown in Figure A.5, reveals that it is possible for a cusp to exist while the solution is absolutely stable. The cusp is in the region $\mu_r < 0$ so pointwise decay is observed. This is expected for all unstable solutions to (A.1), and for Figure A.2 it is expected the the cusp would exist at $\mu_r = \bar{b} - \bar{a}^2/4 = -1.25$ which is outside of the range considered.

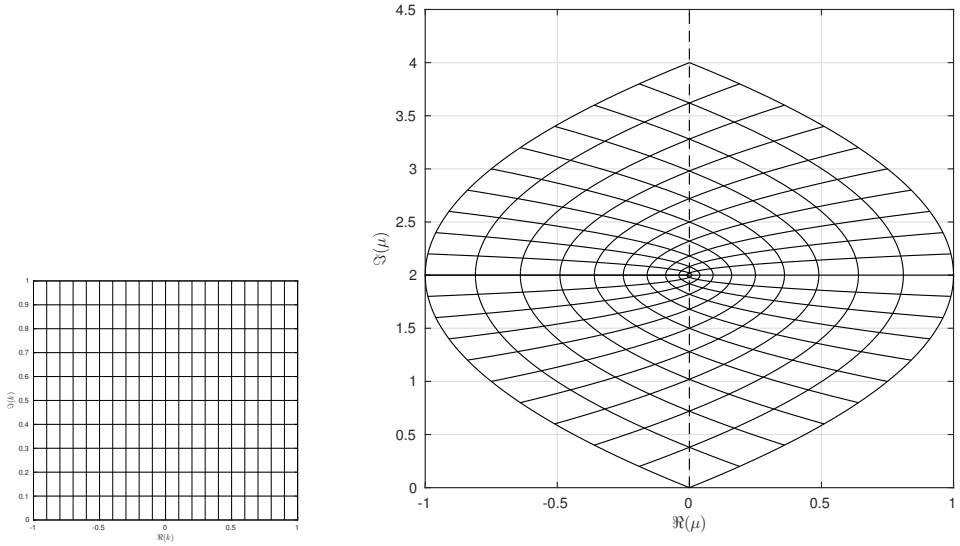

(a) *(b)*

Figure A.3: $\bar{a} = 2$ and $\bar{b} = 1$. The grid in the complex k-plane (a) is mapped by the dispersion relation to the complex μ-plane (b) and a cusp is observed at $\mathfrak{Re}(\mu) = 0$. Solution exhibits neutral pointwise stability.

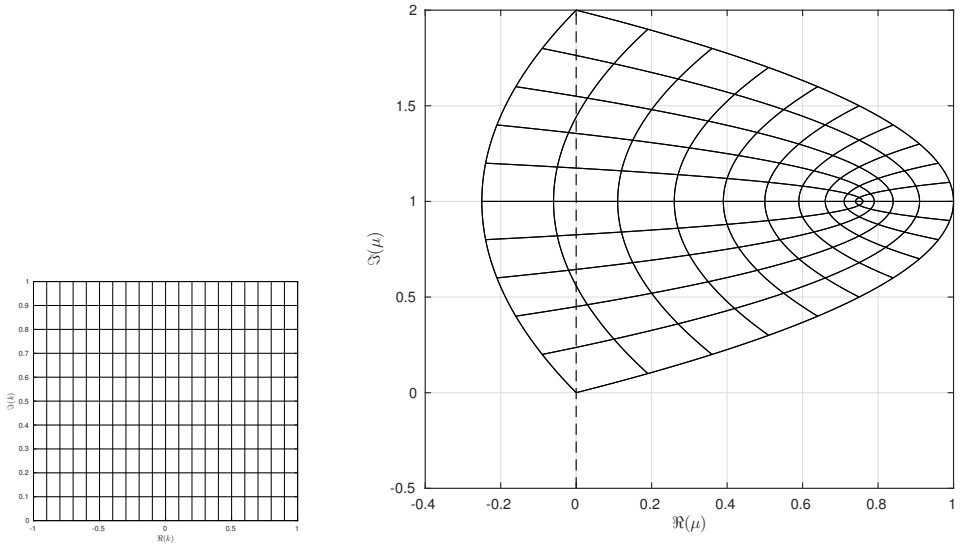

(a) *(b)*

Figure A.4: $\bar{a} = 1$ and $\bar{b} = 1$. The grid in the complex k-plane (a) is mapped by the dispersion relation to the complex μ-plane (b) and a cusp is observed with $\mathfrak{Re}(\mu) > 0$. Solution is absolutely unstable.

Note that for all the cases shown, $\bar{b} > 0$ so the solution is unstable and thus experiences global growth. It is also worth considering that for the cases in which a cusp exists in the range considered, some of the grid lines in the k-plane overlap existing lines in

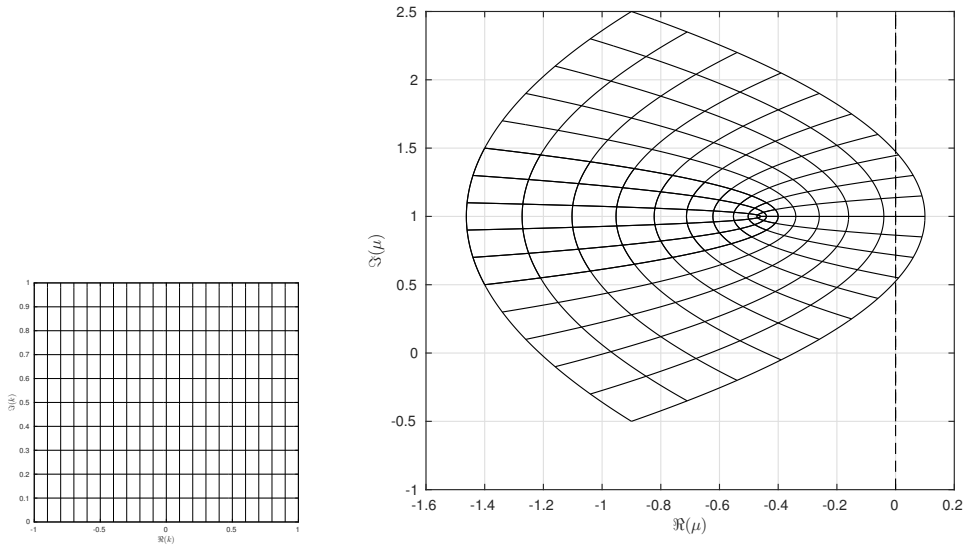

(a) *(b)*

Figure A.5: $\bar{a} = 1.5$ and $\bar{b} = 0.1$. The grid in the complex k-plane (a) is mapped by the dispersion relation to the complex μ-plane (b) and no cusp is observed with $\mathfrak{Re}(\mu) < 0$. Solution is absolutely stable.

μ-space. Another interesting feature is that the imaginary part of μ is only important modulo 1 so any of the pictures can be vertically shifted by whole numbers in either direction and still have the same meaning. Note that μ has not been restricted to $0 \leq \mu_i < 1$ as this would make the structures almost impossible to interpret.

Saddle points

Due to the comparatively simple nature of the problem, it can easily be reformulated as a quadratic eigenvalue problem in k so that the saddle point method outline above can be performed.

The formulation is identical up to (A.24), which can be written as

$$\left[\frac{1}{2}U_b q_{n-1} + \left(\bar{b} - in - \mu\right)q_n + \frac{1}{2}U_b q_{n+1}\right] + k\left[\frac{i}{2}U_a q_{n-1} + i\bar{a}q_n + \frac{i}{2}U_a q_{n+1}\right] - k^2 q_n = 0. \quad \text{(A.28)}$$

Concatenating the harmonic coefficients as in (A.25) results in the polynomial eigenvalue problem

$$A_0\psi + kA_1\psi + k^2 A_2\psi = 0 \quad \text{(A.29)}$$

where

$$A_0 = \begin{pmatrix} C_{-N} & \frac{1}{2}U_b & 0 & \dots & 0 \\ \frac{1}{2}U_b & C_{-N+1} & \frac{1}{2}U_b & & \vdots \\ 0 & \ddots & \ddots & \ddots & 0 \\ \vdots & & \frac{1}{2}U_b & C_{N-1} & \frac{1}{2}U_b \\ 0 & \dots & 0 & \frac{1}{2}U_b & C_N \end{pmatrix} \tag{A.30}$$

with $C_n = \bar{b} - in - \mu$,

$$A_1 = \begin{pmatrix} i\bar{a} & \frac{i}{2}U_a & 0 & \dots & 0 \\ \frac{i}{2}U_a & i\bar{a} & \frac{i}{2}U_a & & \vdots \\ 0 & \ddots & \ddots & \ddots & 0 \\ \vdots & & \frac{i}{2}U_a & i\bar{a} & \frac{i}{2}U_a \\ 0 & \dots & 0 & \frac{i}{2}U_a & i\bar{a} \end{pmatrix} \tag{A.31}$$

and

$$A_0 = \begin{pmatrix} -1 & 0 & \dots & 0 \\ 0 & -1 & & \vdots \\ \vdots & & \ddots & 0 \\ 0 & \dots & 0 & -1 \end{pmatrix}. \tag{A.32}$$

This problem can be solved in Matlab using the polyeig routine or alternatively through construction of a companion matrix. This numerical approximation to the dispersion relation can be used to map the effect that the motion of a straight line in the complex μ-plane has on the complex k-plane. If a saddle point is formed, the collision criteria is met and this point corresponds to μ with positive real part (growth), it is concluded that there is absolute instability. If any of these conditions do not hold, there is either convective instability or stability.

Presented in Figure A.6, Figure A.7, Figure A.8 and Figure A.9 are the mappings found for the same parameters as Figure A.2, Figure A.3, Figure A.4 and Figure A.5, respectively. It is comforting to see that the same conclusions can be drawn. For Figure A.6 and A.8, only μ in the unstable region ($\mu_r \geq 0$) are used, and the presence (Figure A.8) or absence (Figure A.6) of the saddle point indicates whether the solution is absolutely stable or not (provided the collision criteria is met).

The saddle points in Figure A.7 and Figure A.9 do not indicate absolute instability. This is because the saddle point in Figure A.9 is found from a grid in the complex μ-plane

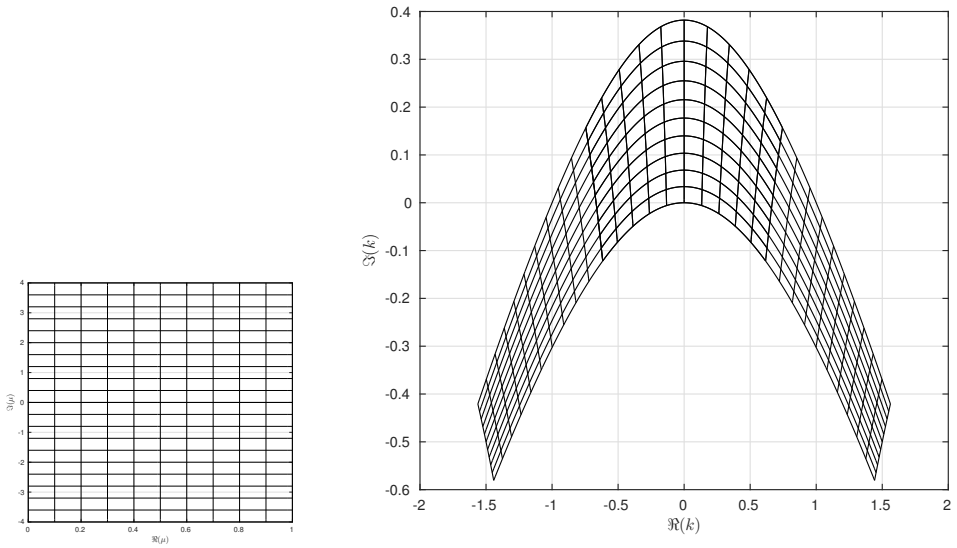

(a) *(b)*

Figure A.6: $\bar{a} = 3$ and $\bar{b} = 1$. The grid in the complex μ-plane (with $\mathfrak{Re}(\mu) \geq 0$) (a) is mapped by the dispersion relation to the complex k-plane (b) and no saddle point is observed. Solution is absolutely stable.

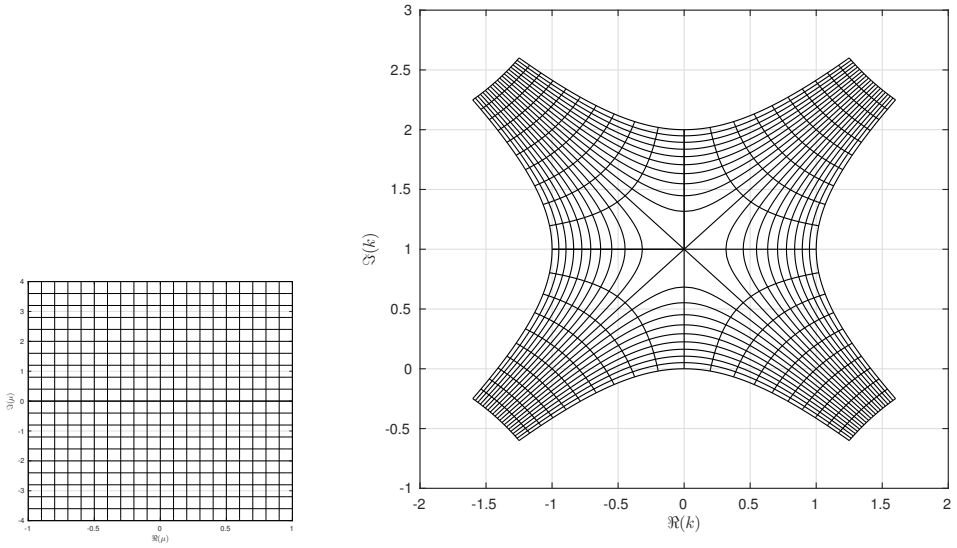

(a) *(b)*

Figure A.7: $\bar{a} = 2$ and $\bar{b} = 1$. The grid in the complex μ-plane (a) is mapped by the dispersion relation to the complex k-plane (b)and a saddle point is observed. Further inspection reveals that this saddle point corresponds to $\mathfrak{Re}(\mu) = 0$ so solution exhibits neutral pointwise stability.

in the region $\mu_r \leq 0$. Similarly, though it is difficult to tell from Figure A.7, this saddle point corresponds to $\mu_r = 0$ (in fact it actually corresponds to $\mu = 0$). Though not shown, the map formed using the same straight grid in the μ-plane as Figure A.6 and Figure A.8

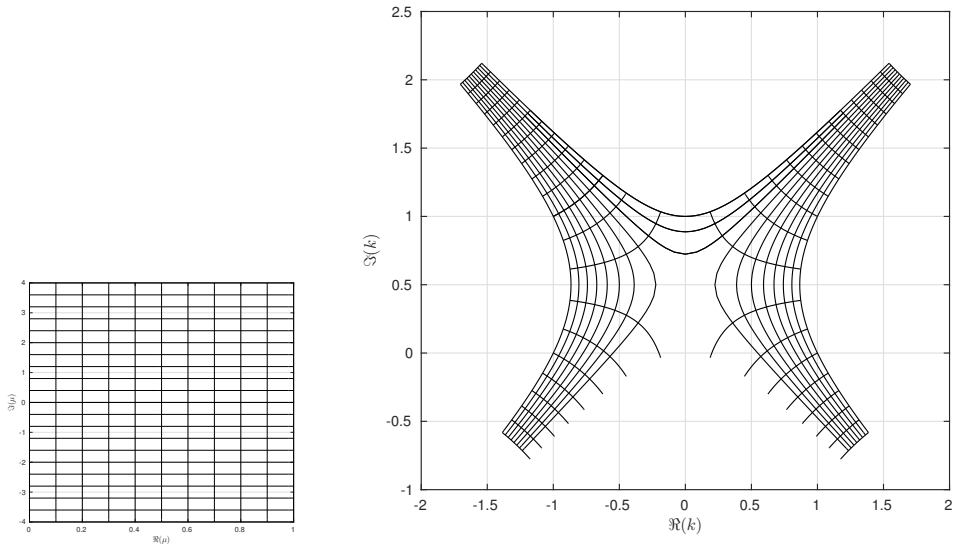

(a) *(b)*

Figure A.8: $\bar{a} = 1$ and $\bar{b} = 1$. The grid in the complex μ-plane (with $\mathfrak{Re}(\mu) \geq 0$) (a) is mapped by the dispersion relation to the complex k-plane (b) and a saddle point is observed. Solution is absolutely unstable.

(i.e. $\mu_r \geq 0$) does not result in a saddle point when the parameters of A.9 are taken. This is in agreement with the results of the cusp method.

Ultimately, the plots shown can not be used in isolation to locate absolute instability since it has been shown that saddle points can exist in the case of absolute stability. This problem is in some way tackled by the consideration of only the unstable region of μ-space ($\mu_r > 0$) but the collision criteria still needs to be met. Furthermore, these figures do not indicate the location in the μ-plane that corresponds to the saddle point. This can only be observed as the process is conducted (it is through this observation that it is known that the saddle point in Figure A.7 corresponds to $\mu = 0$). Similarly, it can only be seen if the collision criteria is met by observing the process to ensure that for a fixed μ_i, for large μ_r the two corresponding k (those that are least stable) appear both above and below the real k-axis. This is indeed the case for Figure A.8 so in this case the solution is absolutely unstable.

When using the cusp map method, it is not clear in the same way how it can be assured that the collision criteria are met.

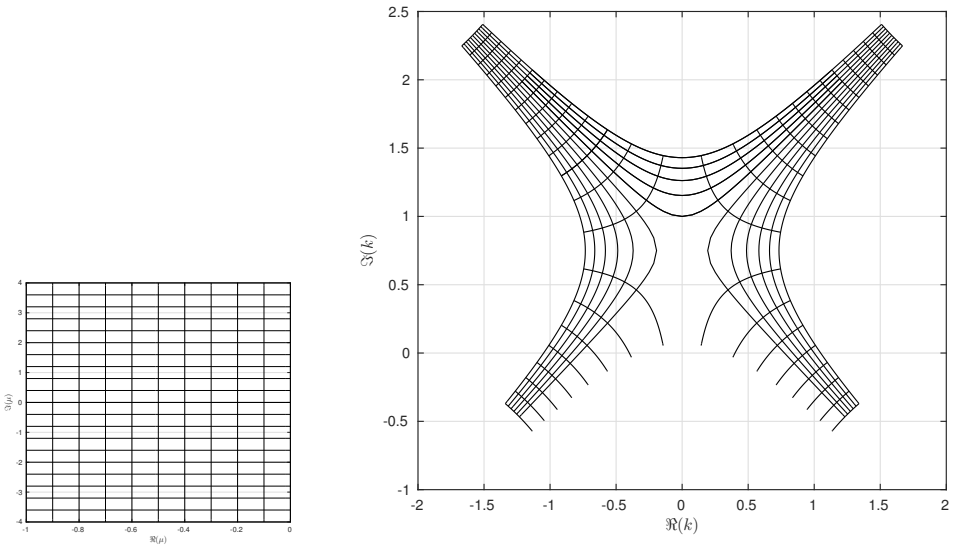

(a) *(b)*

Figure A.9: The grid in the complex μ-plane (with $\mathfrak{Re}(\mu) \leq 0$) (a) is mapped by the dispersion relation to the complex k-plane (b) for $\bar{a} = 1.5$ and $\bar{b} = 0.1$. Though a saddle point exists, $\mathfrak{Re}(\mu) \leq 0$ suggests the solution is absolutely stable. Indeed, there is no saddle point for $\mathfrak{Re}(\mu) \geq 0$.

Summary

A variety of different methods have been used to deduce whether an unstable solution to the Ginzburg–Landau equation with periodic coefficients (A.1) is absolutely or convectively unstable. These methods have included inspection of the exact analytic solution and a pinch-point analysis conducted exactly (supporting the inspection of the exact solution) and numerically (from the viewpoint of both saddle points and cusp maps in the complex plane). All of these methods are in good agreement as to whether a solution for a particular choice of parameters is absolutely or convectively unstable.

Appendix B

Model dispersion relation with fingers

Introduction

While the fingers protruding from the growth-rate curves for the pure Stokes layer are intriguing features, in this appendix it will be seen that such features can be seen in a simple analytic dispersion relation.

When discussing the form of the fingers in Chapter 1, it is shown that as α is increased, the complex conjugate pairs of μ meet at the real axis, move along the real line in opposite directions, return to the same location and move away from the real axis again in complex conjugate pairs. Such behaviour could be considered generic.

Take, for example, a quadratic curve that is dependent on some parameter. If, by varying this parameter, the turning point of the quadratic repeatedly crosses the real axis of the independent variable, three states are moved between:

- No real roots, in this case the quadratic curve does not cross the real axis. In this case there are two complex roots that are complex conjugates of one another,
- A single repeated root, in this case the curve touches the real axis at a single location,
- Two real roots, in this case the curve crosses the real axis twice.

It is not difficult to see how this can cause behaviour like that discussed for the fingers, and such behaviour will now be demonstrated for a simple example.

Simple dispersion relation

Take a dispersion relation that is quadratic in μ,

$$D(\mu) = \mu^2 + B\mu + C, \tag{B.1}$$

which has been normalised so that the μ^2 coefficient is 1. This means that the curve has a single turning point that is a minimum. Introducing a parameter, α, that moves the location of this minimum past the real μ-axis allows for transition between the three states discussed above. Therefore, the dispersion relation of interest will be

$$D(\alpha, \mu) = \mu^2 + \cos(6\alpha)\mu + \cos(50\alpha). \tag{B.2}$$

The trigonometric form of the coefficients B and C was chosen so that the three states are moved between repeatedly and the numbers 6 and 50 were selected based on the desired scaling with α. In particular, $0 \leq \alpha \leq 1$ will be of interest here.

Since (B.2) is of quadratic form in μ, the roots of D can be written exactly as

$$\mu_{1,2} = \frac{-\cos(6\alpha) \pm \sqrt{\cos^2(6\alpha) - 4\cos(50\alpha)}}{2}. \tag{B.3}$$

Variation of μ with α

Consider the μ-roots of the dispersion relation (B.2). These are the values of μ that satisfy

$$D(\alpha, \mu) = 0 \tag{B.4}$$

for some given α. In this section, the behaviour of the μ-roots will be explored for $\alpha \in \mathbb{R}$.

The μ-roots with the largest real part can be plotted against α using (B.3) with the positive square root selected. The variation of the real and imaginary parts of μ with α are presented in Figure B.1. It is immediately apparent that this curve displays behaviour analogous to the fingers first seen in Chapter 1. Over this range of α, μ_r follows a gentle curve that peaks around $\alpha = 0.3$ and this curve is periodically interrupted by protrusions. These protrusions correspond to $\mu_i = 0$ and in between these locations μ_i varies between 0 and 1.

Also marked in Figure B.1 are eight crosses that span one of these fingers. These

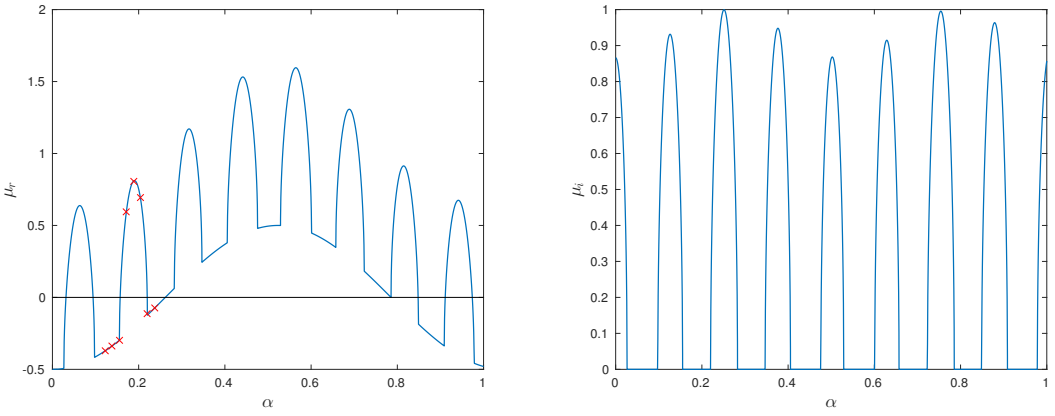

(a) *(b)*

Figure B.1: The μ-roots of D (B.2) *for* $0 \leq \alpha \leq 1$. *In (a) the real part* μ_r *is shown and in (b) the imaginary part* μ_i *is shown. Crosses indicate the choices of* α *explored further in Figure B.2.*

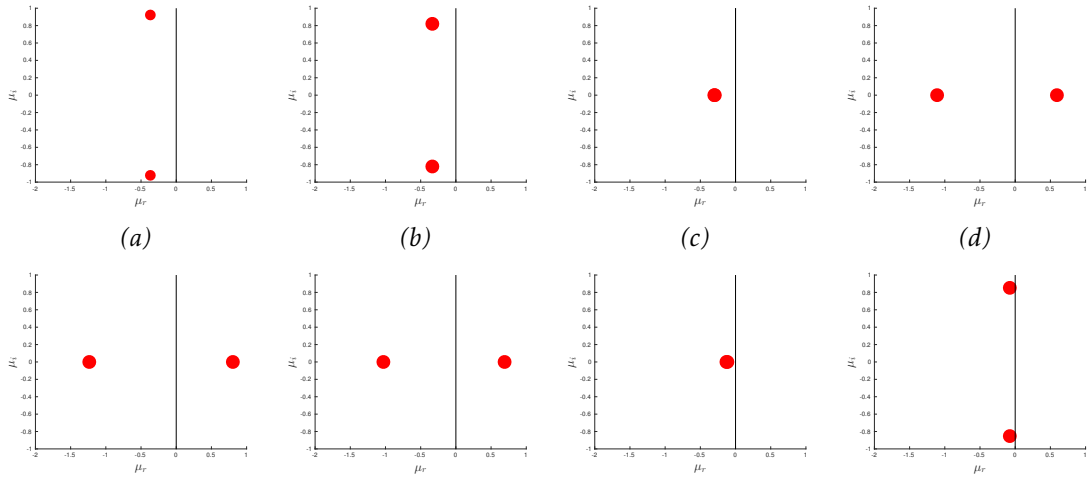

(a) *(b)* *(c)* *(d)*

(e) *(f)* *(g)* *(h)*

Figure B.2: The behaviour of the μ-roots pairs for each of the α *marked with* (×) *in Figure B.1. In (a)* $\alpha = 0.122841$ *and* α *is incremented by* 0.016229 *between plots. As* α *is increased, the complex conjugate pairs of μ-roots move towards the real axis and converge at a point. The two μ-roots then move in opposite directions along the real axis, turn around and converge back to a single point. Two complex conjugate μ-roots then move away from the real axis. This is directly comparable to Figure 1.8.*

points have an equal spacing in α of 0.016229 and range from $\alpha = 0.122841$ to $\alpha = 0.236444$. It can be seen from Figure B.2 that the behaviour of the pair of μ-roots at each of these α is directly comparable with that seen in the pure Stokes layer in Figure 1.8.

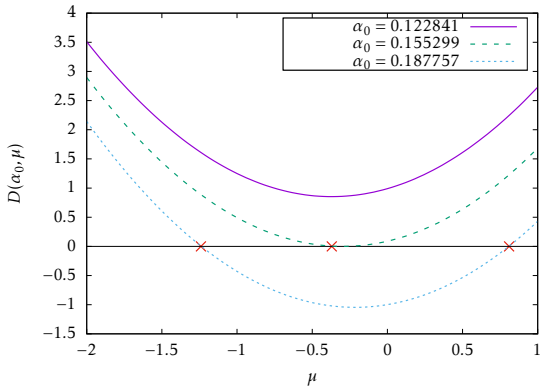

Figure B.3: The dispersion relation (B.2) *is plotted against $\mu \in \mathbb{R}$ for three choices of α_0. In (a), $\alpha_0 = 0.122841$ and the curve $D(\alpha_0, \mu)$ does not cross the μ axis so there are complex conjugate roots. In (b), $\alpha_0 = 0.155299$ and the curve $D(\alpha_0, \mu)$ has a single repeated real root. In (c), $\alpha_0 = 0.18775$ and the curve $D(\alpha_0, \mu)$ has two real roots. The points indicated by (×) are the locations of the real roots taken from Figure B.2.*

Dispersion relation with α treated as a parameter

In order to provide additional insight into this behaviour, the dispersion relation (B.2) will be explored for a selection of fixed, real α. Note that when μ is real, so is D. For this section, the variation of D along the real line will therefore be considered.

Remember that D has been constructed so that it is a quadratic curve in μ whenever α is fixed. Here, three choices of α will be made to demonstrate the transition between the three states discussed above. Based on the eigenvalues observed in Figure B.2, the wavenumbers of interest here will be: $\alpha_0 = 0.122841$, corresponding to complex conjugate roots; $\alpha_0 = 0.155299$, approximately corresponding to a repeated root; and $\alpha_0 = 0.18775$, corresponding to two real roots.

In Figure B.3, the quadratic curve $D(\alpha_0, \mu)$ is plotted against μ for these three choices of α_0. This demonstrates that for real μ, the parameter α has the effect of moving the minimum of D over the μ-axis. When this minimum corresponds to $D > 0$, there are no real roots and the complex roots are complex conjugates of one another. When the minimum corresponds to $D < 0$, there are two real roots. When $D = 0$ there is a single repeated real root.

Summary

It has been shown here that the intriguing feature of fingers protruding from the growth-rate curves of the semi-infinite Stokes layer can be reproduced using a significantly simpler model. This illustrates that the behaviour is in some sense generic.

Bibliography

Akhaven, R., Kamm, R. D., & Shapiro, A. H. 1991. An investigation of transition to turbulence in bounded oscillatory flows. Part 1. Experiments. *Journal of Fluid Mechanics*, **225**, 395–422.

Atobe, T. 2014. Primary mode changes due to longitudinal wall oscillation in two-dimensional channel flow. *Fluid Dynamics Research*, **46**, 025502.

Bers, A. 1983. Space-time evolution of plasma instabilities - absolute and convective. *Chap. 3, pages 451–517 of:* A. A. Galeev, R. N. Sudan (ed), *Hanbook of Plasma Physics*, vol. 1. North-Holland.

Blennerhassett, P. J., & Bassom, A. P. 2002. The linear stability of flat Stokes layers. *Journal of Fluid Mechanics*, **464**, 393–410.

Blennerhassett, P. J., & Bassom, A. P. 2006. The linear stability of high-frequency oscillatory flow in a channel. *Journal of Fluid Mechanics*, **556**, 1–25.

Blennerhassett, P. J., & Bassom, A. P. 2007. A note on the linear stability of a two-dimensional stokes layer. *The Quarterly Journal of Mechanics and Applied Mathematics*, **60**(3).

Blesbois, O., Chernyshenko, S. I., Touber, E., & Leschziner, M. A. 2013. Pattern prediction by linear analysis of turbulent flow with drag reduction by wall oscillation. *Journal of Fluid Mechanics*, **724**, 607–641.

Brevdo, L., & Bridges, T. J. 1996. Absolute and convective instabilities of spatially periodic flows. *Philosophical Transactions of the Royal Society of London A*, **354**, 1027–1064.

Brevdo, L., & Bridges, T. J. 1997. Absolute and convective instabilities of temporally oscillating flows. *Zeitschrift für angewandte Mathematik und Physik*, **48**, 290–309.

Bridges, T. J., & Morris, P. J. 1983. Differential eigenvalue problems in Which the parameter appears nonlineraly. *Journal of Computational Physics*, **55**, 437–460.

Briggs, R. J. 1964. *Electron-stream interaction with plasmas*. MIT Press.

Carpenter, M. H., Gottlieb, D., & Abarbanel, S. 1993. Stable and accurate boundary treatments for compact, high-order finite-difference schemes. *Applied Numerical Mathematics*, **12**, 55–87.

Carpenter, P. W., Kudar, K. L., Ali, R., Sen, P. K., & Davies, C. 2007. A deterministic model for the sublayer streaks in turbulent boundary layers for application to flow control. *Philosophical Transactions of the Royal Society A*, **365**, 2419–2441.

Choi, K. S. 2005. Near-wall structure of turbulent boundary layer with spanwise-wall oscillation. *Physics of Fluids*, **14**, 2530–2542.

Clamen, M., & Minton, P. 1977. An experimental investigation of flow in an oscillating pipe. *Journal of Fluid Mechanics*, **81**(7), 421–431.

Conrad, P. W., & Criminale, W. O. 1965. The stability of time-dependent laminar flow: Parallel flows. *Zeitschrift fur Angewandte Mathematik*, **16**, 233–254.

Criminale, W. O., Jackson, T. L., & Joslin, R. D. 2003. *Theory and computation of hydrodynamic stability*. Cambridge University Press.

Davies, C., & Carpenter, P. 2001. A Novel velocity-vorticity formulation of the Navier-Stokes equations with applications to boundary layer disturbance evolution. *Journal of Computational Physics*, **172**, 119–165.

Drazin, P. G. 2002. *Introduction to hydrodynamic stability*. Cambridge University Press.

Duque-Daza, C. A., Baig, M. F., Lockerby, D. A., Chernyshenko, S. I., & Davies, C. 2012. Modelling turbulent skin-friction control using linearized Navier-Stokes Equations. *Journal of Fluid Mechanics*, **702**, 403–414.

Duval, M. 2012. *Modelling turbulent boundary layer control using wall oscillations*. Project Report, Department de Genie Mathematique, Toulouse and School of Mathematics, Cardiff University.

Eckmann, D. M., & Grotberg, J. B. 1991. Experiments on transition to turbulence in oscillatory pipe flow. *Journal of Fluid Mechanics*, **222**, 329–350.

Hack, M. J. P., & Zaki, T. A. 2015. Modal and non-modal stability of boundary layers forced by spanwise wall oscillations. *Journal of Fluid Mechanics*, **778**, 389–427.

Hall, P. 1978. The linear stability of flat Stokes layers. *Proceedings of the Royal Society of London, A*, **359**, 151–166.

Herbert, T. 1988. Secondary instability of boundary layers. *Annual Review of Fluid Mechanics*, **20**, 487–526.

Hino, M., Sawamoto, M., & Takasu, S. 1976. Experiments on transition to turbulence in an oscillatory pipe flow. *Journal of Fluid Mechanics*, **75**, 193–207.

Huerre, P. 2002. Open shear flow instabilities. *Chap. 4, pages 159–229 of:* G. K. Batchelor, H. K. Moffatt, M. G. Worster (ed), *Perspectives in Fluid Dynamics*. Cambridge University Press.

Kelley, C. T. 2005. *Arclength continuation and bifurcation*. Tech. rept. Technical report, North Carolina State University.

Kong, W., & Luo, J. 2016. Global instability of Stokes layer for whole wave numbers. *Applied Mathematics and Mechanics (English Edition)*, **37**, 999–1012W.

Kupfer, K., Bers, A., & Ram, A. K. 1987. The cusp map in the complex-frequency plane for absolute instabilities. *Physics of Fluids*, **30**, 3075–3082.

Lele, S. K. 1992. Compact finite difference schemes with spectral-like resolution. *Journal of Computational Physics*, **103**, 16–42.

Lingwood, R. J. 1997. On the applications of the Briggs' and steepest-descent methods to a boundary-layer flow. *Studies in Applied Mathematics*, **98**, 213–254.

Luo, J., & Wu, X. 2010. On the linear instability of a finite Stokes layer: Instantaneous versus Floquet modes. *Physics of Fluids*, **22**, 054106.

Pier, B. 2003. Finite amplitude crossflow vortices, secondary instability and transition in the rotating disk boundary layer. *Journal of Fluid Mechanics*, **487**, 315–343.

Pier, B., & Schmid, P. J. 2017. Linear and nonlinear dynamics of pulsatile channel flow. *Journal of Fluid Mechanics*, **815**, 435–480.

Quadrio, M., & Ricco, P. 2010. The laminar generalized Stokes layer and turbulent drag reduction. *Journal of Fluid Mechanics*, **667**, 135–157.

Rohatgi, A. 2010. WebPlotDigitizer. *http://arohatgi.info/WebPlotDigitizer (Accessed: 12-07-2016)*.

Schmid, P. J. 2007. Nonmodal stability theory. *Annual Review of Fluid Mechanics*, **39**, 129–162.

Schmid, P. J., & Henningson, D. S. 2001. *Stability and transition in shear flows*. Springer-Verlag, New York.

Squire, H. B. 1933. On the stability for three-dimensional disturbances of viscous fluid flow between parallel walls. *Proceedings of the Royal Society of London Series A*, **147**, 621–628.

Tennekes, H., & Lumley, J. L. 1972. *A first course in turbulence*. Nassachusetts Institute of Technology Press.

Thomas, C. 2016. personal communication.

Thomas, C., Bassom, A. P., Blennerhassett, P. J., & Davies, C. 2010. Direct numerical simulations of small disturbances in the classical Stokes layer. *Journal of Engineering Mathematics*, **68**, 327–338.

Thomas, C., Bassom, A. P., Blennerhassett, P. J., & Davies, C. 2011. The linear stability of oscillatory Poiseuille flow in channels and pipes. *Proceedings of the Royal Society A*, **467**, 2643–2662.

Thomas, C., Davies, C., Bassom, A. P., & Blennerhassett, P. J. 2014. Evolution of disturbance wavepackets in an oscillatory Stokes layer. *Journal of Fluid Mechanics*, **752**, 543–571.

Thomas, C., Blennerhassett, P. J., Bassom, A. P., & Davies, C. 2015. The linear stability of a Stokes layer subjected to high frequency perturbations. *Journal of Fluid Mechanis*, **764**, 193–218.

Togneri, M. 2011. *A high-order finite difference investigation of boundary layer perturbation*. Ph.D. thesis, School of Mathematics, Cardiff University.

Togneri, M., & Davies, C. 2011. A high order finite-difference solver for investigation of disturbance development in turbulent boundary layers. *Computers & Fluids*, **46**, 472–478.

Touber, E., & Leschziner, M. A. 2012. Near-wall streak modification by spanwise oscillatory wall motion and drag reduction mechanisms. *Journal of Fluid Mechanics*, **693**, 150–200.

Trefethen, L. N. 2000. *Spectral methods in MATLAB*. Society for Industrial and Applied Mathematics.

Tsigklifis, K., & Lucey, A. D. 2017. Asymptotic stability and transient growth in pulsatile Poiseuille flow through a compliant channel. *Journal of Fluid Mechanics*, **820**, 370–399.

Von Kerczek, C., & Davis, S. H. 1974. Linear stability theory of oscillatory Stokes layers. *Journal of Fluid Mechanics*, **62**, 753–773.